



**HAL**  
open science

# Analysis of the degradation in solid oxide cells operated in fuel cell and electrolysis modes: microstructural evolution and stability of the electrodes materials

Federico Monaco

► **To cite this version:**

Federico Monaco. Analysis of the degradation in solid oxide cells operated in fuel cell and electrolysis modes: microstructural evolution and stability of the electrodes materials. Materials Science [cond-mat.mtrl-sci]. Université Grenoble Alpes [2020-..], 2020. English. NNT: 2020GRALI034. tel-02971294

**HAL Id: tel-02971294**

**<https://theses.hal.science/tel-02971294v1>**

Submitted on 19 Oct 2020

**HAL** is a multi-disciplinary open access archive for the deposit and dissemination of scientific research documents, whether they are published or not. The documents may come from teaching and research institutions in France or abroad, or from public or private research centers.

L'archive ouverte pluridisciplinaire **HAL**, est destinée au dépôt et à la diffusion de documents scientifiques de niveau recherche, publiés ou non, émanant des établissements d'enseignement et de recherche français ou étrangers, des laboratoires publics ou privés.

## THÈSE

Pour obtenir le grade de

### **DOCTEUR DE L'UNIVERSITE GRENOBLE ALPES**

Spécialité : **Matériaux, Mécanique, Génie civil, Electrochimie**

Arrêté ministériel : 25 mai 2016

Présentée par

### **Federico MONACO**

Thèse dirigée par **M. Jérôme LAURENCIN**, Docteur, CEA-LITEN, et  
codirigée par **Mme. Florence LEFEBVRE-JOUD**, Docteure, CEA-LITEN

préparée au sein du **CEA-LITEN**  
dans l'**École Doctorale I-MEP<sup>2</sup>**

# **Analyse de la dégradation des cellules à oxydes solides fonctionnant en mode pile à combustibles et électrolyse : Évolution microstructurale et stabilité des matériaux d'électrodes**

Thèse soutenue publiquement le « **23/07/2020** »,  
devant le jury composé de :

#### **Mme. Elisabeth SIEBERT**

Directrice de recherche, Laboratoire d'Electrochimie et de Physicochimie des  
Matériaux et des Interfaces (LEPMI) de Grenoble (Présidente de jury)

#### **M. Ming CHEN**

Professeur, Danish Technical University (DTU) (Rapporteur)

#### **Mme. Aline LÉON**

Docteure, European Institute for Energy Research (EIFER) (Rapporteure)

#### **Mme. Armelle RINGUEDE**

Directrice de recherche, École Nationale Supérieure de Chimie de Paris (ENSCP)  
(Examinatrice)

#### **M. Jérôme LAURENCIN**

Docteur, CEA-LITEN (Membre, directeur de thèse)

#### **Mme. Florence LEFEBVRE-JOUD**

Docteure, CEA-LITEN (Invitée, co-directrice de thèse)

#### **M. Bertrand MOREL**

Docteur, CEA-LITEN (Invité, co-encadrant de thèse)

#### **Mme. Marie PETITJEAN**

Docteure, CEA-LITEN (Invitée, co-encadrante de thèse)





“Il tempo non è mai perso, è sempre relativo.  
Dipende da te, non dall’orologio”

*Wu Ming*, Proletkult (2018)



# Acknowledgements

This work was almost entirely carried out at the “Laboratoire des Technologies Hydrogène” (LTH) which is part of the “Service des Technologies Hydrogène et Bioressources” (STHB) of the French Alternative Energies and Atomic Energy Commission (CEA) here in Grenoble. For this reason, I would like to thank Ms. Julie Mougin and Ms. Isabelle Maillot, heads of the Laboratory and the Service, respectively, for allowing me to be part of this amazing research team.

Moreover, during these years, I participated to the KIC Innoenergy PhD School, in which the scientific work of a PhD student is successfully complemented by a formation focused on the industrial innovation. In this context, I would like to thank Ms. Isabelle Schuster, Ms. Christine Dominjon and Ms. Scarlett Tukunaga for admitting me in the program and giving me all the help that I needed.

Thanks to the founding provided by the KIC, I also had the opportunity to spend a four-month period at the microXAS beamline of the Swiss Light Source (SLS) of the Paul Scherrer Institute (PSI). Therefore, I would like to thank Mr. Daniel Grolimund and Mr. Dario Ferreira-Sanchez for accepting me during my mobility and for their help during those months.

I would also like to thank the members of the jury for my PhD defense, those who were able to attend in person and those who were connected in remote. In particular, Mr. Ming Chen from the Danish Technical University (DTU) and Ms. Aline Léon from the European Institute for Energy Research (EIFER) for their contribution in the reviewing of the manuscript, Ms. Armelle Ringuède from the École Nationale Supérieure de Chimie de Paris (ENSCP) for accepting to be examiner of the work, and, finally, Ms. Elisabeth Siebert from the Laboratoire d'Electrochimie et de Physicochimie des Matériaux et des Interfaces (LEPMI) for being the president of the jury, but also for the inspiring meetings that we had during the PhD. Thank you all for having dedicated your time to my work and for the interesting discussions that have followed the dissertation.

A special thanks goes to my main supervisor during this work, Mr. Jérôme Laurencin, it was a privilege to work with you and to witness your competence and moral integrity. I would also like to thank my co-supervisors, Ms. Florence Lefevbre-Joud, Ms. Marie Petitjean and Mr. Bertrand Morel, for their help during these years. I know that we did not worked always together but knowing that you were there if needed, helped me a lot.

This work would not have been possible without external collaborations. Therefore, I would like to thank Mr. Maxime Hubert, Mr. Julio Da Silva and Mr. Peter Cloetens from the ID16A beamline of the European Synchrotron Radiation Facility (ESRF) for their 3D reconstructions. I would also thank Mr. Julien Vulliet from the CEA Le Ripault and Mr. Dario Montinaro from SOLIDPower S.p.A. for giving me their aged samples in order to analyze them. In addition, I would like to thank Ms. Elisabeth Djurado from the LEPMI for her willingness to host me after the end on my three-year contract and for the useful exchanges that we were able to have.

I would like to thank all the people working at the LTH: Pascal, Pierre, Bastien, Bruno, Thibault M. Thibault D., Jérôme A., Karine, Stephane, Geraud, Eric, Denis, Philippe, Géraldine, Livia, Lionel, Benjamin, Manon, Simon, Sarah, Eglantine, Olivier, Nathalie and the others (I am sure I forgot someone, please excuse me for that). I am also glad of meeting all the others PhD students and Post-docs: Elisa, Hamza, Youcef, Rakesh, Amira, Sergii, Vlad, Pauline, Lydia, Veronica, Tika, Paul and Delphine, sharing the work with you during these years was a pleasure and I really appreciate all of you.

Finally, I would like to thank all my friends here in Grenoble, but also those scattered across Europe: I feel like one of the luckiest people in the world for having you. Last but not least, I would like to thank my family for their endless support, I would not be here without you.

*Insomma, grazie di cuore a tutti.*

# Abstract English

This work was dedicated to the analysis of the degradation of solid oxide cells operated in electrolysis and fuel cell modes. A threefold methodology has been applied by coupling (i) electrochemical tests, (ii) advanced post-test analyses and (iii) multi-scale modeling. Long-term durability experiments have been carried out on standard cells (Ni-YSZ/YSZ/GDC/LSCF) to investigate the performance loss as a function of the operating conditions. Specimens, which have been extracted from the pristine and aged samples, have been characterized to evaluate the microstructural and physico-chemical evolutions occurring at the two electrodes. In parallel, detailed micro-kinetic models for the hydrogen electrode (Ni-YSZ cermet) and for the oxygen electrode (LSCF/LSCF-GDC) have been developed and experimentally validated before being integrated into a macro-scale model for the complete cell. The multi-scale numerical tool has been used to propose a better understanding of the underlying forces driving the degradation. Moreover, the impact on the cell performances has been simulated and discussed as a function of the operating conditions. Based on the results presented in this work, it has been confirmed that the degradation of SOCs is significantly larger in electrolysis mode with respect to fuel cell operation under  $H_2$ . On the one hand, it has been shown that the difference in durability behavior can be ascribed to the effect of the cathodic overpotential on the nickel instability in the hydrogen electrode. On the other hand, it has been observed and demonstrated that the destabilization of the LSCF is favored by both the anodic current and the high operating temperature.

# Résumé Français

Ce travail a été dédié à l'étude de la dégradation des piles à oxyde solide fonctionnant en mode électrolyse et pile à combustibles. Une approche intégrée couplant (i) des caractérisations électrochimiques, (ii) des analyses post-test avancées et (iii) une modélisation multi-échelle a été adoptée. Des tests de longue durée ont été menés avec des cellules standards (Ni-YSZ/YSZ/GDC/LSCF) pour évaluer la dégradation des performances en fonction des conditions de fonctionnement. Des échantillons, extraits de cellules initiales et après test, ont été finement caractérisés pour déterminer les évolutions microstructurales et physico-chimiques des deux électrodes en fonctionnement. En outre, des modèles de cinétiques élémentaires ont été développés et validés expérimentalement pour l'électrode à hydrogène (cermet Ni-YSZ) et pour l'électrode à oxygène (LSCF/LSCF-GDC) avant d'être intégrés dans un modèle de cellule à l'échelle macroscopique. L'outil numérique multi-échelle a été utilisé pour étudier les mécanismes sous-jacents contrôlant les phénomènes de dégradation. Par ailleurs, leurs effets sur les performances de la cellule en fonction des conditions de fonctionnement ont été évalués et discutés grâce au modèle. Sur la base des résultats présentés dans ce travail, il a été confirmé que la dégradation des SOCs est nettement plus importante en mode électrolyse par rapport à un fonctionnement en pile à combustibles fonctionnant sous  $H_2$ . Cette différence peut être attribuée d'une part, à l'effet des surtensions cathodiques sur l'instabilité du nickel dans l'électrode à hydrogène. D'autre part, il a été observé et démontré que la déstabilisation du LSCF est favorisée sous fort courant anodique à haute température.



# Contents

<b>Acknowledgements</b> .....	<b>i</b>
<b>Abstract English</b> .....	<b>iii</b>
<b>Résumé Français</b> .....	<b>iii</b>
<b>Contents</b> .....	<b>v</b>
<b>List of Figures</b> .....	<b>ix</b>
<b>List of Tables</b> .....	<b>xv</b>
<b>List of Symbols</b> .....	<b>xvii</b>
Chemical Species.....	xvii
Roman Symbols.....	xvii
Greek Symbols .....	xviii
Abbreviations.....	xix
<b>General Introduction</b> .....	<b>1</b>
1. Motivation.....	1
2. General Objective .....	3
3. Layout of the Manuscript.....	4
<b>I. Literature Review on Solid Oxide Cells: Technology Fundamentals and Degradation Phenomena</b> .....	<b>7</b>
I.1 Solid Oxide Cells: Basic Operating Mechanisms and Materials.....	8
I.1.1 SOCs Principle.....	8
I.1.2 SOCs Architecture .....	9
I.1.3 Materials Selection .....	11
I.1.4 Thermodynamic Description of SOCs and Nernst Equation.....	13
I.1.5 Losses at the Cell Level and Impact on Cell's Performances .....	16
I.2 Literature Review on the Reaction Mechanisms for the Two Electrodes .....	20
I.2.1 Reaction Mechanism for the Hydrogen Electrode.....	20
I.2.2 Reaction Mechanism for the Oxygen Electrode .....	22
I.3 Durability of SOCs .....	23
I.3.1 Durability Results Reported in Literature.....	23
I.3.2 Main Degradation Mechanisms.....	25
I.3.3 Concluding Remarks .....	30

I.4	Conclusions of This Chapter: Objectives and Methodology of the Thesis .....	31
<b>II.</b>	<b>Durability Experiments and Post-Test Characterization Techniques ....</b>	<b>33</b>
II.1	Long-term Tests in Electrolysis Mode at Different Operating Temperature .....	34
II.1.1	Cell Description .....	35
II.1.2	Description of the Test Benches .....	36
II.1.3	Experimental Techniques .....	37
II.1.4	Testing Protocols .....	40
II.1.5	Tests Results .....	43
II.2	Long-term Tests in Collaboration with External Partners.....	50
II.2.1	Cells Description .....	51
II.2.2	Durability Tests .....	52
II.3	Physico-Chemical Characterizations and 3D Reconstructions .....	54
II.3.1	Sample Selection .....	54
II.3.2	Sample Preparation.....	55
II.3.3	Characterization Techniques .....	58
II.4	Conclusion of This Chapter .....	61
<b>III.</b>	<b>Development and Validation of the Multi-Scale Modeling Tools .....</b>	<b>63</b>
III.1	Micro-Scale Models for the Hydrogen Electrode.....	64
III.1.1	Models Description.....	64
III.1.2	Experimental Characterization .....	75
III.1.3	Models Validation and Discussion .....	82
III.1.4	Concluding Remarks and Model Adaptation for the Degradation Studies .....	94
III.2	Micro-Scale Model for the Oxygen Electrode .....	96
III.2.1	Experimental Characterization .....	97
III.2.2	Microstructural Reconstruction for Cell I.....	104
III.2.3	Description of the Modeling Tools.....	105
III.2.4	Model Validation and Discussion.....	109
III.2.5	LSCF-GDC Composite Electrodes.....	116
III.2.6	Concluding Remarks .....	116
III.3	Macro-Scale Model at the Cell level and Multi-Scale Integration.....	118
III.3.1	Macro-Scale Model Description.....	118
III.3.2	Multi-Scale Integration .....	119
III.3.3	Multi-Scale Model Validation .....	120

III.4	Conclusion of This Chapter .....	122
<b>IV.</b>	<b>Hydrogen Electrode Degradation: Impact of Polarization and Initial Microstructure on the Ni Evolution .....</b>	<b>123</b>
IV.1	3D Reconstructions and Image Processing Techniques for Microstructural Computations.....	124
IV.1.1	Samples Extracted from Cell-A and Cell-B .....	124
IV.1.2	Methodology for the Determination of the Microstructural Parameters .....	126
IV.2	Results of the Microstructural Analysis .....	127
IV.2.1	Microstructural Properties of the Reference Cells.....	127
IV.2.2	Microstructural Evolution of the Aged Cells.....	129
IV.3	Impact of Ni Evolution on the Cell Performances .....	133
IV.3.1	Preliminary Remark: Adaptation of the H <sub>2</sub> Electrode Model.....	134
IV.3.2	Role of Ni Agglomeration on Degradation .....	134
IV.3.3	Role of Ni Depletion on Degradation.....	136
IV.4	Suggested Mechanism of Ni Depletion .....	138
IV.5	Conclusion of This Chapter .....	142
<b>V.</b>	<b>Oxygen Electrode Degradation: LSCF Demixing and Interdiffusion at the GDC/8YSZ Interface.....</b>	<b>145</b>
V.1	Characterization of the Pristine Cell.....	146
V.1.1	Detection of SrZrO <sub>3</sub> After Sintering.....	146
V.1.2	Inter-Diffusional Layer Between the GDC and the YSZ .....	147
V.1.3	Crystalline Phases Distribution Across the Electrolyte and Barrier Layer.....	149
V.2	Characterization of the Aged Cells.....	149
V.2.1	Preliminary Remark: Proposed Mechanism for the LSCF Destabilization.....	150
V.2.2	LSCF Destabilization: Sr Release from the Material as a Function of Temperature and Polarization.....	152
V.2.3	Evolution of the IDL After Aging in Electrolysis Mode: Preliminary Characterizations and Discussion.....	155
V.3	Conclusion of This Chapter .....	158
<b>VI.</b>	<b>Conclusions and Perspectives .....</b>	<b>161</b>
VI.1	General Conclusions .....	161
VI.2	Perspectives .....	166

<b>Appendix A</b> .....	<b>171</b>
Cells Description and Experimental Conditions .....	171
<b>Appendix B</b> .....	<b>173</b>
Development of the Micro-Kinetic Model for the Hydrogen Electrode Reaction Mechanism: Model I Based on the Oxygen Spillover Mechanism.....	173
<b>Appendix C</b> .....	<b>177</b>
Development of the Micro-Kinetic Model for the Hydrogen Electrode Reaction Mechanism: Model II Based on the Hydrogen Spillover Mechanism .....	177
<b>Bibliography</b> .....	<b>181</b>

# List of Figures

Figure 0-1: Increase in electricity production worldwide (data from [IEA 2019]).	1
Figure 0-2: Global temperature increase associated to the anthropogenic CO <sub>2</sub> emissions and reduction strategies [IPCC 2018].	2
Figure 0-3: Schematic representation of the threefold methodology adopted in this work.	4
Figure I-1: Solid Oxide Cells operating principle.	8
Figure I-2: Different architectures for SOCs: a) Tubular design [Larminie 2003] – b) Planar design.	10
Figure I-3: Ionic conductivity of 8YSZ and 3YSZ as a function of the operating temperature [Lay-Grindler 2013].	12
Figure I-4: Illustration of the thermodynamically reversible operation of a SOC operating in fuel cell mode.	14
Figure I-5: Schematic representation of an i-V curve in SOFC and SOEC at H <sub>2</sub> /H <sub>2</sub> O = 50/50 vol.% with an illustration of the overpotentials arising in the two operating modes.	16
Figure I-6: Schematic representation of the phenomena associated to the performances degradation in solid oxide cells (from [Yokokawa 2008]).	25
Figure II-1: Schematic representation of the tested cells ( <i>Cell-A1</i> and <i>Cell-A2</i> ): a) Button cell geometry – b) Oxygen electrode architecture.	35
Figure II-2: Experimental setups: a) Ceramic housing – b) Metallic housing.	36
Figure II-3: Classical representation of the impedance spectra: a) Nyquist plot – b) Bode plot of the real and imaginary part of the impedance.	39
Figure II-4: Illustration of the procedure for the determination of R <sub>s</sub> and R <sub>pol</sub> from the experimental EIS data: a) Equivalent Circuit Model used – Nyquist (b) and partial Bode (c) plots of the experimental data – Nyquist (d) and partial Bode (e) plots of the spectrum fitted with the inductive contribution – Nyquist (f) and partial Bode (g) plots of the simulated spectrum without the inductive contribution.	41
Figure II-5: Comparison of the initial performances in SOFC mode at 800°C (with Q <sub>air</sub> = 62 Nml·min <sup>-1</sup> ·cm <sup>-2</sup> and Q <sub>H<sub>2</sub></sub> = 12 Nml·min <sup>-1</sup> ·cm <sup>-2</sup> ): a) <i>Cell-A1</i> – b) <i>Cell-A2</i> – c) ASR as a function of the current density for the two cells.	44
Figure II-6: Initial performances in SOEC mode for <i>Cell-A1</i> and <i>Cell-A2</i> with H <sub>2</sub> O/H <sub>2</sub> = 90/10 vol.% and T = 850°C (Q <sub>air</sub> = 62 Nml·min <sup>-1</sup> ·cm <sup>-2</sup> and Q <sub>fuel</sub> = 12 Nml·min <sup>-1</sup> ·cm <sup>-2</sup> ): a) i-U curves – b) EIS at OCV – c) EIS at i = -0.75 A·cm <sup>-2</sup> .	45
Figure II-7: Degradation curves for the two cells aged in electrolysis mode with H <sub>2</sub> O/H <sub>2</sub> = 90/10 vol.% at i <sub>DC</sub> = -0.75 A·cm <sup>-2</sup> (corresponding to a SC of 50%).	46

Figure II-8: Final performances in SOEC mode for *Cell-A1* and *Cell-A2* with  $H_2O/H_2 = 90/10$  vol.% and  $T = 850^\circ C$  ( $Q_{air} = 62 \text{ Nml}\cdot\text{min}^{-1}\cdot\text{cm}^{-2}$  and  $Q_{fuel} = 12 \text{ Nml}\cdot\text{min}^{-1}\cdot\text{cm}^{-2}$ ): a) i-U curves – b) EIS at OCV – c) EIS at  $i_{DC} = -0.75 \text{ A}\cdot\text{cm}^{-2}$ . ..... 48

Figure II-9: Comparison between the EIS acquired under polarization ( $i_{DC} = -0.75 \text{ A}\cdot\text{cm}^{-2}$ ) at the beginning and at the end of the two long term tests with  $H_2O/H_2 = 90/10$  vol.% and  $T = 850^\circ C$  ( $Q_{air} = 62 \text{ Nml}\cdot\text{min}^{-1}\cdot\text{cm}^{-2}$  and  $Q_{fuel} = 12 \text{ Nml}\cdot\text{min}^{-1}\cdot\text{cm}^{-2}$ ): a) Nyquist and partial Bode plots for *Cell-A1* – b) Nyquist and partial Bode plots for *Cell-A2*. ..... 49

Figure II-10: Schematic description of the cells coming from partners: a) Dimensions and configuration of *Cell-A3* and *Cell-A4* – b) Illustration of the sectors for *Cell-A3* – c) Dimensions and configuration of *Cell-B*. ..... 51

Figure II-11: Experimental results for *Cell-A3* aged in fuel cell mode for 15'000 hour with  $H_2/N_2 = 60/40$  vol.% and  $T = 780^\circ C$  ( $Q_{air} = 110 \text{ Nml}\cdot\text{min}^{-1}\cdot\text{cm}^{-2}$  and  $Q_{fuel} = 7 \text{ Nml}\cdot\text{min}^{-1}\cdot\text{cm}^{-2}$ ): a) Local voltages and b) Local current densities as a function of time for the three segments analyzed. .... 52

Figure II-12: Experimental results for *Cell-B* aged in electrolysis mode for 1'000 hours with  $H_2O/H_2 = 90/10$  vol.% and  $T = 800^\circ C$  (with  $Q_{air} = 112 \text{ Nml}\cdot\text{min}^{-1}\cdot\text{cm}^{-2}$  and  $Q_{fuel} = 24 \text{ Nml}\cdot\text{min}^{-1}\cdot\text{cm}^{-2}$ ): a) Durability curve at  $800^\circ C$  and  $i_{DC} = -0.5 \text{ A}\cdot\text{cm}^{-2}$  – b) Comparison of the polarization curves recorded after the reduction and at the end of the experiment. .... 54

Figure II-13: Schematic representation of the lamellae preparation procedure: a) Protective Pt deposition on ROI – b) FIB milling around the ROI – c) Isolated lamella – d) Extraction of the sample from the cell – e) Sample mounted on the Al pin. .... 56

Figure II-14: Schematic representation of the micro-pillar preparation procedure: a) Protective Pt deposition on ROI – b) Elliptic FIB milling around the ROI – c) Extraction of the sample from the cell – d) Sample mounted on the Al pin with refined shape. .... 57

Figure II-15: Schematic illustration of the  $\mu$ XRD/ $\mu$ XRF experiment: a) Basic principle of scattering in XRD [Willmott 2011] – b) Characteristics of powder XRD [Willmott 2011] – c) Lines of emission for XRF – d) Experimental setup at the microXAS beamline at the PSI..... 58

Figure II-16: Schematic illustration of the X-ray nano-holotomography experiment: a) ID16A Beamline – b) Experimental setup. .... 61

Figure III-1: Illustration of the Ni-YSZ cermet modeling in electrolysis mode: a) Scheme of the electrode containing part of the electrolyte (EL), the functional layer (FL) and part of the current collector layer (CC) – b) Representation of the oxygen spillover mechanism implemented in Model I – c) Representation of the hydrogen spillover mechanism implemented in Model II. .... 65

Figure III-2: Symmetric cell used for the experimental characterization of the hydrogen electrode. 76

Figure III-3: Illustration of validity of the measurements for the symmetric cell in the three-electrode setup (with  $H_2/H_2O = 50/50$  vol.% and  $T = 700^\circ C$ ): a)  $\eta$ -i curves recorded for the WE and the CE vs the RE – b) EIS diagrams at OCP recorded for the two half-cell and the complete cell. .... 78

Figure III-4: Experimental and simulation results at  $700^\circ C$ : a) Experimental and simulated  $\eta$ -i curves with  $H_2/H_2O = 50/50$  vol.%– b) Experimental and simulated  $\eta$ -i curves with  $H_2/H_2O = 25/75$  vol.% and  $H_2/H_2O = 75/25$  vol.%– Experimental Nyquist plot (c) and partial Bode plot (d) of the EIS diagrams at OCP measured at different  $H_2/H_2O$  ratios (20/80, 30/70, 40/60, 50/50, 60/40, 70/30, 80/20 vol.%). .... 79

Figure III-5: Determination of the cermet microstructural parameters: a) Pillar extracted from the reduced cell containing the electrode – b) 2D cross-section extracted from the raw reconstruction – c) 2D cross-section taken from the filtered reconstruction – d) Segmented cross-section – e) Rendering of the segmented 3D volume..... 82

Figure III-6: Experimental and simulated impedance spectra at OCP with different  $p_{H_2}/p_{H_2O}$ : Nyquist (a) and partial Bode (b) plots with  $H_2/H_2O = 50/50$  vol.%– Nyquist (c) and partial Bode (d) plots with  $H_2/H_2O = 40/60$  vol.% – Nyquist (e) and partial Bode (f) plots with  $H_2/H_2O = 60/40$  vol.%. ..... 86

Figure III-7: Results of the simulation with Model II on the steam interaction with Ni and YSZ surfaces with  $H_2/H_2O = 50/50$  vol.%. a) Local kinetic rate of  $H_2O$  adsorption/desorption on Ni surface (CR1) – b) Local kinetic rate of  $H_2O$  adsorption/desorption on YSZ surface (CR3) – c) Kinetic rate of steam adsorption/desorption on Ni and YSZ integrated over the electrode thickness as a function of the overpotential – d) Schematic representation of the two parallel pathways for the electrode reaction with Model II (given in electrolysis mode)..... 88

Figure III-8: Kinetic rate of the charge transfer reactions at different polarizations with  $H_2/H_2O = 50/50$  vol.%. a) Local kinetic rate of the first charge transfer reaction (ER1) – b) Local kinetic rate of the second charge transfer reaction (ER2). ..... 90

Figure III-9: Local surface coverages at different polarizations with  $H_2/H_2O = 50/50$  vol.%. a) hydroxyl ions on the YSZ surface – b)  $H_2O$  on the YSZ surface – c)  $H_2O$  on the Ni surface. .... 91

Figure III-10: Results of the sensitivity analysis on the parameters of Model II at  $700^\circ C$ : a)  $\eta$ -i curve at  $H_2/H_2O = 50/50$  vol.% for the model limited by the incorporation/excorporation of oxygen ions in the YSZ (CR5) – b)  $\eta$ -i curve at  $H_2/H_2O = 50/50$  vol.% for the model limited by the dissociation of water adsorbed on the YSZ (CR3) – c)  $\eta$ -i curve at  $H_2/H_2O = 50/50$  vol.% for the model limited by the surface diffusion of hydroxyl ions on the YSZ – Nyquist (d) and partial Bode (e) plots of the EIS diagrams at OCP at  $H_2/H_2O = 50/50$  vol.%. ..... 93

Figure III-11: Adaptation of Model II to study the degradation considering water and hydroxyl dissociation on the surface of Ni..... 96

Figure III-12: Cell dimensions and experimental setups: a) Cell I – b) Cell II. .... 98

Figure III-13: Results for the WE of Cell I at  $700^\circ C$ ,  $750^\circ C$  and  $800^\circ C$  in air atmosphere ( $p_{O_2} = 0.21$  atm): a) Experimental and simulated  $\eta$ -i curves – b) Electrode polarization resistance..... 100

Figure III-14: Impedance spectra for Cell I at  $750^\circ C$  recorded at different current densities, Nyquist plot (left) and partial Bode plot (right): a)  $i_{DC} = 0$   $mA \cdot cm^{-2}$  – b)  $i_{DC} = 10$   $mA \cdot cm^{-2}$  – c)  $i_{DC} = 50$   $mA \cdot cm^{-2}$  – d)  $i_{DC} = 70$   $mA \cdot cm^{-2}$  (line=simulation, open symbols=experimental,  $i_{AC} = \pm 10$   $mA \cdot cm^{-2}$ ). ..... 101

Figure III-15: Impedance spectra for Cell I recorded at OCP and under anodic polarization at different temperatures, Nyquist plot (left) and partial Bode plot (right): a)  $700^\circ C$  – b)  $800^\circ C$  (lines= simulation, open symbols=experimental,  $i_{AC} = \pm 10$   $mA \cdot cm^{-2}$ ). ..... 102

Figure III-16: Results for Cell II at  $700^\circ C$  in air atmosphere ( $p_{O_2} = 0.21$  atm): a) Experimental and simulated  $\eta$ -i curves – b) Electrode polarization resistance..... 103

Figure III-17: Three-dimensional rendering volume for the LSCF electrode of Cell I. .... 104

Figure III-18: Illustration of the reaction pathways for the oxygen electrode (shown in electrolysis mode): *Bulk path*: oxygen ion migration in GDC (T1) – oxygen transfer across the LSCF/GDC interface (R1) – oxygen ion/vacancy diffusion in LSCF (T2) – oxygen excorporation from the bulk to the surface of LSCF (R2) – oxygen adsorbate diffusion on the surface of the LSCF (T3) – associative desorption of oxygen (R4) – gas diffusion (T4) – hole migration in the LSCF (T5). *Surface path*: oxygen ion migration in the GDC (T1) – direct oxidation at the TPBs (R3) – oxygen adsorbate diffusion on the surface of the LSCF (T3) – associative desorption of oxygen (R4) – gas diffusion (T4) – hole migration in the LSCF (T5). ..... 106

Figure III-19: Equivalent circuit used to fit the EIS of Cell II..... 107

Figure III-20: Results of the simulations: a) Ratio calculated with the model between the kinetic rate of R3 and R2 – b) Oxygen vacancies concentration in the LSCF lattice, ☆ = equilibrium concentration – c) Comparison of the ratio at OCP and under anodic polarization at different temperatures..... 113

Figure III-21: Illustration of the procedure to integrate the micro-scale models for the fuel and oxygen electrodes in the macro-scale model at the cell level..... 119

Figure III-22: Validation of the multi-scale modeling scheme on the initial performances of *Cell-A1* and *Cell-A2* (SOFC fuel composition: H<sub>2</sub>/H<sub>2</sub>O = 100/0 vol.%, SOEC fuel composition: H<sub>2</sub>/H<sub>2</sub>O = 10/90 vol.%): a) SOFC performances of *Cell-A1* at 800°C – b) SOEC performances of *Cell-A1* at 850°C – c) SOFC performances of *Cell-A2* at 800°C – d) SOEC performances of *Cell-A2* at 850°C. .... 121

Figure IV-1: Procedure for the sample preparation, reconstruction and analysis: a) Micro-pillar of *Cell-B Reference* prepared with the pFIB – b) Comparison of a 2D slice before and after the segmentation – c) 3D segmented volume – d) Illustration of the slice-by-slice approach for the computation of the local microstructural properties at the electrode/electrolyte interface..... 125

Figure IV-2: Illustration of the two samples taken from the aged cell of type *B* corresponding to *Cell-B Active* and *Cell-B Inactive*. ..... 125

Figure IV-3: Comparison of the microstructural properties between the two types of reference cells: 3D rendering and 2D cross-section of a) *Cell-A Reference* and b) *Cell-B Reference* (White: Ni, Grey: YSZ, Black: Pores) – c) Nickel particle size distribution for the two types of reference cells – d) Evolution of the Ni volume fraction for the two cells at the electrode/electrolyte interface. .... 128

Figure IV-4: 3D segmented rendering and 2D cross-sections extracted for the bulk reconstructions of the aged samples: a) *Cell-A3 Outlet* – b) *Cell-A4 Inlet* – c) *Cell-B Active* – d) *Cell-B Inactive* (White: Ni, Grey: YSZ, Black: Pores). ..... 130

Figure IV-5: 2D images from the segmented volumes extracted parallel and perpendicular to the electrode/electrolyte interface: a) *Cell-A Reference* – b) *Cell-A3 Outlet* – c) *Cell-A4 Inlet* – d) *Cell-B Reference* – e) *Cell-B Active* – f) *Cell-B Inactive* (White: Ni, Grey: YSZ, Black: Pores)..... 131

Figure IV-6: Local microstructural parameters at the electrode/electrolyte interface for *Cell-A* and *Cell-B*: (a, b) Nickel volume fraction – (c, d) Pores volume fraction – (e, f) TPBs density – (g, h) Ni specific surface area. .... 132

Figure IV-7: Effects of the hydrogen electrode microstructural evolution on the H<sub>2</sub> electrode and cell performances: a) Increase of the Ni mean particle diameter associated to the Ni agglomeration – b) Effect of the Ni agglomeration on the density of TPBs – c) Simulated voltage drop at 750°C and -0.5 A · cm<sup>-2</sup> caused by Ni agglomeration at 750°C and 850°C – Effect of the Ni depletion on the

hydrogen electrode activation overpotential (d) and on the cell performances (e) – f) Evolution of the EIS associated to the Ni depletion. .... 135

Figure IV-8: Simulation results for the hydrogen electrode at  $H_2O/H_2 = 50/50$  vol.% and  $750^\circ C$ : a) Steam partial pressure, b) hydroxyl Ni surface coverage and c) oxygen Ni surface coverage as a function of the position in the electrode at  $\pm 0.5 A \cdot cm^{-2}$ ..... 139

Figure IV-9: Mechanism for Ni depletion: a) Electrode overpotential as a function of the position in the electrode at  $\pm 0.5 A \cdot cm^{-2}$  – b) Normalized oxygen vacancies concentration in the YSZ at the electrode/electrolyte interface as a function of the applied current density – c) Proposed mechanism for the weakening of the Ni/YSZ interface. .... 141

Figure V-1: Analysis of the pristine oxygen electrode: a) 2D element distribution obtained from the XRF signal at the electrode/barrier layer/electrolyte interface – b) Local XRF intensity integrated over the horizontal direction – c) XRD pattern at the GDC/8YSZ interface..... 147

Figure V-2: Analysis of the XRD pattern at the interface for *Cell-A Reference*: a) Main crystalline phases identified at the barrier layer/electrolyte interface – b) 2D maps of the XRD showing the distribution of the crystalline phases..... 148

Figure V-3: Evolution of the oxygen atom concentration in the LSCF along the electrode thickness as a function of the overpotential (illustrated for a pure LSCF electrode operated at  $800^\circ C$ ). ..... 150

Figure V-4: 2D XRD maps of the LSCF phase and evolution of the LSCF Unit Cell Volume along the oxygen electrode thickness for the four samples analyzed: a) *Cell-A Reference* – b) *Cell-A1* – c) *Cell-A2* – d) *Cell-A3*. .... 152

Figure V-5: Analysis of the operated cells: a) 2D element distribution obtained from the XRF signal at the electrode/barrier layer/electrolyte interface for *Cell-A1*, *Cell-A2* and *Cell-A3* – b) Comparison of the integrated XRF signal of Sr between the pristine cell and the aged samples. .... 154

Figure V-6: XRD maps exhibiting the crystalline phases at the interface between the barrier layer and the electrolyte in the cells aged in electrolysis mode..... 156

Figure V-7: Evolution of the XRD pattern at the interface for the cells aged in electrolysis mode as a function of the operating temperature: a) *Cell-A1* (aged at  $850^\circ C$ ) vs *Cell-A Reference* – b) *Cell-A2* (aged at  $750^\circ C$ ) vs *Cell-A Reference*..... 157



# List of Tables

Table II-I: Summary of the experimental protocol for <i>Cell-A1</i> and <i>Cell-A2</i> (considering an active area for both cells of 9.08 cm <sup>2</sup> ).....	42
Table II-II: Evolution of cell voltage measured from the i-U curves and resistances obtained from the EIS for <i>Cell-A1</i> and <i>Cell-A2</i> at 850°C and $i_{DC} = -0.75 \text{ A}\cdot\text{cm}^{-2}$ (with H <sub>2</sub> O/H <sub>2</sub> = 90/10 vol.%).....	46
Table II-III: Summary of the electrochemical tests results and experimental characterizations .....	62
Table III-I: Reactions for Model I (expressed in electrolysis mode with the abbreviations CR and ER referring to the chemical and electrochemical reactions, respectively) .....	66
Table III-II: Reactions for Model II (expressed in electrolysis mode with the abbreviation CR and ER referring to the chemical and electrochemical reactions, respectively) .....	67
Table III-III: Thermodynamic data for the species used in the models at 700°C [Bessler 2007, Chase 1998] .....	70
Table III-IV: Diffusion coefficients and conductivities at T=700°C [Lay-Grindler 2013, Todd 2002, Vogler 2009] .....	73
Table III-V: Determination of the reaction order for H <sub>2</sub> and H <sub>2</sub> O at OCP from the experimental and simulated EIS with H <sub>2</sub> /H <sub>2</sub> O = 20/80, 30/70, 40/60, 50/50, 60/40, 70/30, 80/20 vol.% and T = 700°C .....	81
Table III-VI: Microstructural properties of the Ni-3YSZ cermet electrode extracted from the 3D reconstruction.....	83
Table III-VII: Parameters used in the simulations at 700°C .....	84
Table III-VIII: Parameters in the sensitivity analysis for Model II .....	92
Table III-IX: Reactions on Ni surface added in the hydrogen spillover micro-scale model to study the degradation.....	96
Table III-X: Microstructural parameters of Cell I reconstructed <i>via</i> FIB-SEM .....	105
Table III-XI: Equations of the physically-based model of the oxygen electrode made of porous LSCF (cf. List of symbols).....	108
Table III-XII: Parameters used in the model to fit the experimental data (fitted values in italic)...	111
Table III-XIII: Parameters for the computation of the exchange current densities for the fuel and oxygen electrodes fitted on the micro-scale models [Hubert 2018] .....	120
Table IV-I: Connected bulk properties of the Ni-YSZ extracted away from the electrode/electrolyte interface for the eight samples ( <i>Cell-A3</i> : aged SOFC – <i>Cell-A4</i> and <i>Cell-B Active</i> : aged SOEC)..	129



# List of Symbols

## Chemical Species

$h^{\bullet}$	Hole defect in LSCF	(-)
$H_2(gas)$	Gaseous H <sub>2</sub>	(-)
$H_{Ni}$	H attached on Ni surface	(-)
$H_2O(gas)$	Gaseous H <sub>2</sub> O	(-)
$H_2O_{Ni}$	H <sub>2</sub> O attached on Ni surface	(-)
$H_2O_{YSZ}$	H <sub>2</sub> O attached on YSZ surface	(-)
$O_2(gas)$	Gaseous O <sub>2</sub>	(-)
$O_{LSCF}$	Oxygen adsorbate on LSCF surface	(-)
$O_{Ni}$	O attached on Ni surface	(-)
$O_O^x$	Oxygen in the lattice	(-)
$O_{YSZ}^{2-}$	O <sup>2-</sup> attached on YSZ surface	(-)
$OH_{Ni}$	OH attached on Ni surface	(-)
$OH_{YSZ}^-$	OH <sup>-</sup> attached on the YSZ surface	(-)
$V_O^{\bullet\bullet}$	Oxygen vacancy	(-)

## Roman Symbols

$a_i$	Thermodynamic activity for the i-th species	(-) or (mol·m <sup>-2</sup> )
$A$	Electrode surface area	(m <sup>2</sup> )
$C_{dl}$	Double-layer capacitance	(F·m <sup>-2</sup> )
$C_i$	Concentration of the i-th species	(mol·m <sup>-3</sup> )
$\tilde{D}_{chem}$	Oxygen chemical diffusion coefficient in LSCF	(m <sup>2</sup> ·s <sup>-1</sup> )
$D_i$	Diffusion coefficient for the i-th species	(m <sup>2</sup> ·s <sup>-1</sup> )
$D_{i-j}$	Binary diffusion coefficient for the i-th and j-th species	(m <sup>2</sup> ·s <sup>-1</sup> )
$D_{K,i}$	Knudsen diffusion coefficient for the i-th species	(m <sup>2</sup> ·s <sup>-1</sup> )
$E_{act}$	Activation energy	(J·mol <sup>-1</sup> )
$E$	Electrode potential	(V)
$E^{eq}$	Equilibrium potential	(V)
$E^{meas}$	Measured potential	(V)
$F$	Faraday's constant	(C·mol <sup>-1</sup> )
$h_m^0$	Standard enthalpy of formation of the m-th species	(J·mol <sup>-1</sup> )
$i_0$	Exchange current density	(A·cm <sup>-2</sup> )
$i$	Current density	(A·cm <sup>-2</sup> )
$\vec{i}_{el/io}$	Local electronic/ionic current densities in the electrodes	(A·cm <sup>-2</sup> )
$K_i^{eq}$	Equilibrium constant of i-th reaction	(-)

$k_{jS}^i$	Kinetic constant for the $i$ -th reaction of the $j$ -th species on the surface $S$ for the hydrogen electrode micro-scale model	$(s^{-1})$ or $(m^2 \cdot s^{-1} \cdot mol^{-1})$
$k_i^{red/ox}$	Reduction/oxidation kinetic constant for the $i$ -th charge transfer reaction for the hydrogen electrode micro-scale model	$(m^3 \cdot s^{-1} \cdot mol^{-1})$
$k_+$	Forward reaction kinetic constants for R1 for the oxygen electrode micro-scale model	$(mol \cdot m^{-2} \cdot s^{-1})$
$k_{ox}^{LSCF/gas}$	Forward reaction kinetic constants for R2 for the oxygen electrode micro-scale model	$(m^8 \cdot mol^{-3} \cdot s^{-1})$
$k_{ox}^{TPB}$	Forward reaction kinetic constants for R3 for the oxygen electrode micro-scale model	$(m^3 \cdot mol^{-1} \cdot s^{-1})$
$k_{des}$	Forward reaction kinetic constants for R4 for the oxygen electrode micro-scale model	$(m^2 \cdot mol^{-1} \cdot s^{-1})$
$\ell$	Thickness	(m)
$m_i$	Molar mass of the $i$ -th species	$(g \cdot mol^{-1})$
$n$	Number of electrons exchanged in the charge transfer reaction	(-)
$N_a$	Avogadro's Number	$(atoms \cdot mol^{-1})$
$\vec{N}_i$	Molar flux of the $i$ -th species	$(mol \cdot m^{-2} \cdot s^{-1})$
$p_i$	Partial pressure of $i$ -th gas species	(atm)
$p_{ref}$	Reference pressure	(atm)
$P_{tot}$	Total pressure	(atm)
$q_i$	Stoichiometric coefficient of $i$ -th species	(-)
$q_{rev}$	Specific reversible heat generated in a SOC	$(J \cdot mol^{-1})$
$\bar{r}_a$	Mean radius of the $a$ phase	(m)
$R$	Universal gas constant	$(J \cdot mol^{-1} \cdot K^{-1})$
$R_{pol}$	Polarization resistance	$(\Omega \cdot cm^2)$
$R_s$	Serial resistance	$(\Omega \cdot cm^2)$
$s_m^0$	Standard entropy of formation of the $m$ -th species	$(J \cdot K^{-1} \cdot mol^{-1})$
$s_{Ni}$	Free surface site on Ni surface	(-)
$s_{YSZ}$	Free surface site on YSZ surface	(-)
$\hat{S}_i$	Source term for the $i$ -th species	$(mol \cdot m^{-3} \cdot s^{-1})$
$Sp_{a-b}$	Specific surface area between the $a$ and $b$ phases	$(m^{-1})$
$T$	Absolute temperature	(K)
$U$	Cell voltage	(V)
$V_i$	Fuller's volume for the $i$ -th species	(-)
$x_i$	Molar fraction of the $i$ -th species	(-)
$w_{rev}$	Specific reversible electrical work generated in a SOC	$(J \cdot mol^{-1})$

## Greek Symbols

$\alpha$	Hydrogen electrode reaction order for hydrogen	(-)
$\alpha_{red/ox}$	Reduction/oxidation transfer coefficients	(-)
$\beta$	Hydrogen electrode reaction order for steam	(-)
$\gamma$	Hydrogen electrode $i_0$ dependence on $H_2$	(-)
$\Gamma_S$	Total density of sites available for adsorption on the surface $S$	$(mol \cdot m^{-2})$

$\Delta g_i^0$	Standard Gibbs free energy variation for the i-th reaction	(J·mol <sup>-1</sup> )
$\varepsilon_a$	Volume fraction of the <i>a</i> phase	(%)
$\eta$	Electrode overpotential	(V)
$\eta_{ohmic}$	Cell's Ohmic overpotential	(V)
$\eta_{conc}$	Cell's concentration overpotential	(V)
$\eta_{act}$	Cell's activation overpotential	(V)
$\theta_{ads,iS}$	Surface coverage of i-th species on surface S	(-)
$\theta_s$	Fraction of empty surface sites on surface S	(-)
$\lambda$	Oxygen electrode $i_0$ dependence on O <sub>2</sub>	(-)
$\tilde{\mu}_i$	Electrochemical potential of the i-th species	(J·mol <sup>-1</sup> )
$v^i$	Kinetic rate of the i-th reaction	(mol·m <sup>-3</sup> ·s <sup>-1</sup> )
$\xi^{TPBs}$	Triple phase boundaries lengths density	(m <sup>-2</sup> )
$\sigma_i$	Ionic / Electronic conductivity	(S·m <sup>-1</sup> )
$\tau_a$	Apparent tortuosity factor of the <i>a</i> phase	(-)
$\varphi_i$	Local electronic / ionic potential	(V)
$\chi$	Hydrogen electrode $i_0$ dependence on H <sub>2</sub> O	(-)

## Abbreviations

3YSZ	Yttria Stabilized Zirconia with 3 mol.% of Yttria
6Sc1CeSZ	6/1 mol.% Scandia/Ceria-doped Zirconia
8YSZ	Yttria Stabilized Zirconia with 8 mol.% of Yttria
ASR	Area Specific Resistance
CC	Current Collector
CCD	Charge-Coupled Device
CE	Counter Electrode
CHP	Combined Heat and Power
CPE	Constant-Phase Element
CR	Chemical Reaction
DFT	Density Functional Theory
DGM	Dusty-Gas Model
ECM	Equivalent Circuit Model
EIS	Electrochemical Impedance Spectroscopy
ER	Electrochemical Reaction
ESRF	European Synchrotron Radiation Facility
FIB-SEM	Focused Ion Beam-Scanning Electron Microscopy
FL	Functional Layer
FLG	Finite-Length Gerischer
FRA	Frequency Response Analyzer
FU	Fuel Utilization
GDC	Gadolinium-doped Ceria
IDL	Inter-diffusional Layer
IPCC	International Panel on Climate Change
KB	Kirkpatrick-Baez
LSC	Lanthanum Strontium Cobaltite
LSCF	Lanthanum Strontium Cobaltite Ferrite
LSM	Lanthanum Strontium Manganite

MFC	Mass Flow Controller
MIEC	Mixed Ionic and Electronic Conductors
OCP	Open Circuit Potential
OCV	Open Circuit Voltage
P2G	Power-to-gas
PEMC	Proton Exchange Membrane Cells
pFIB	Plasma-Focused Ion Beam
PSD	Particle Size Distribution
PSI	Paul Scherrer Institute
RE	Reference Electrode
RES	Renewable Energy Sources
ROI	Region of Interest
RVE	Representative Volume Element
RU	Repeating Units
SC	Steam Conversion
SEM	Scanning Electron Microscopy
SIMS	Secondary-Ions Mass Spectrometry
SLS	Swiss Light Source
SOC	Solid Oxide Cell
SOEC	Solid Oxide Electrolysis Cell
SOFC	Solid Oxide Fuel Cell
TEC	Thermal Expansion Coefficient
TEM	Transmission Electron Microscopy
TPBs	Triple Phase Boundaries lengths
UCV	Unit Cell Volume
WE	Working Electrode
XRD	X-ray Diffraction
XRF	X-ray Fluorescence
YSZ	Yttria Stabilized Zirconia

# General Introduction

## 1. Motivation

Nowadays the energy sector is facing historical challenges related to the increase in consumption and the transitioning towards renewable energy sources (RES). Indeed, the energy demand is encountering a worldwide growth that is expected to rise of nearly 50% up to 2050 [IEO 2019]. In particular, the electrical demand is increasing steadily while a large part of the electricity is still produced in classical thermoelectric power plant using fossil fuels (Figure 0-1).

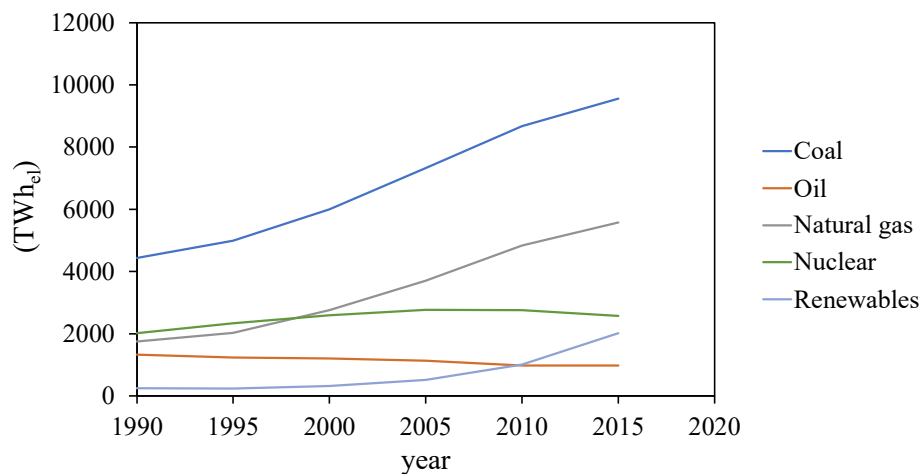
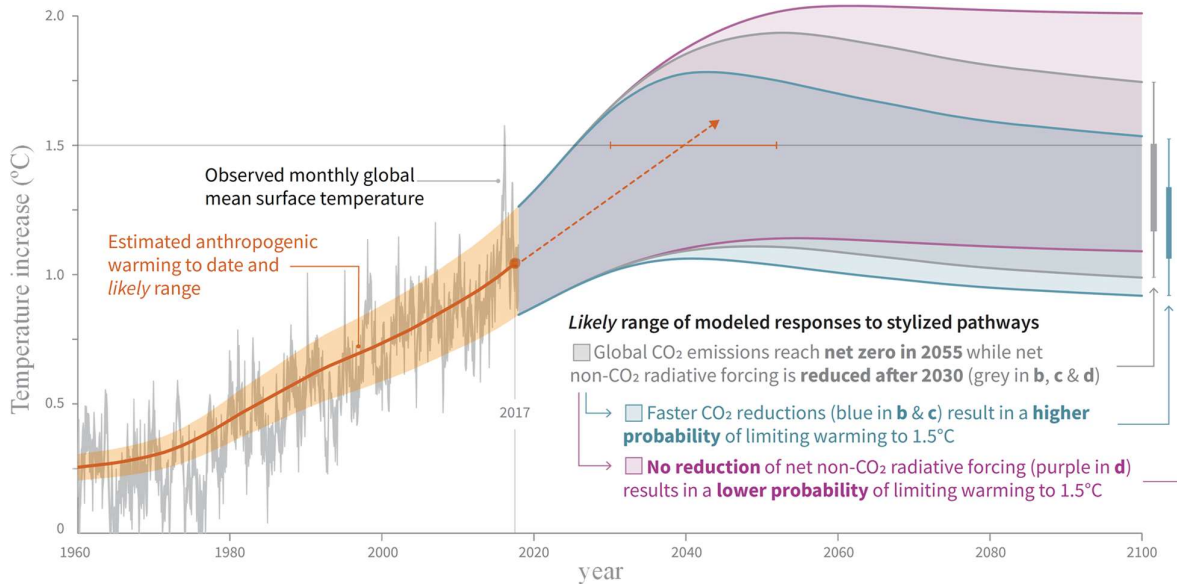


Figure 0-1: Increase in electricity production worldwide (data from [IEA 2019]).

In return, this accelerated consumption of oil, coal and natural gas has triggered an environmental crisis on a global scale due to the CO<sub>2</sub> emissions associated to their combustion. Indeed,

anthropogenic carbon dioxide in the atmosphere is known to be the main cause of the climate changes that will shape the future of our societies [IPCC 2018]. In particular, global warming of 1.5 – 2°C is expected to occur in the next 30 – 60 years with severe consequences on earth’s eco-systems. Therefore, to mitigate climate changes, an effort on reducing CO<sub>2</sub> emissions is needed as it is clearly stated by the International Panel on Climate Change (IPCC) [IPCC 2018] (cf. Figure 0-2).



**Figure 0-2: Global temperature increase associated to the anthropogenic CO<sub>2</sub> emissions and reduction strategies [IPCC 2018].**

With this objective, the transition towards a renewable-based energy system is required. In Europe, the European Commission targets to reach at least a 32% share of energy produced from renewable energy sources by 2030 [EU 2018]. However, one of the main difficulties for this transition relies on the intermittent nature of RES, such as solar and wind power. Therefore, it is also necessary to develop technologies able to store the overproductions of RES and to reinject them when the demand exceeds the production.

In this context, hydrogen appears as an interesting energy vector to be employed in a climate-neutral society. Indeed, the H<sub>2</sub> molecule presents the highest mass specific heating value of all ( $\approx 120 \text{ MJ}\cdot\text{kg}^{-1}$ ) and its consumption produces only water. However, to be relevant, the hydrogen must be produced using clean energy sources. To date, most of the hydrogen is obtained by steam reforming of natural gas generating carbon dioxide as a byproduct. To overcome this issue, the electrolysis of water combined with renewable energy sources could represent a promising solution to store renewable electricity by converting the electrical energy into chemical one (Power-to-Gas – P2G).

Several technologies exist to perform H<sub>2</sub>O electrolysis, such as Alkaline Cells, Proton Exchange Membrane Cells (PEMCs) and Solid Oxide Cells (SOCs). Among these technologies, the high-temperature SOCs are considered as the most promising in terms of electrical efficiency, hydrogen production rate, and cost. Indeed, thanks to the operation at high temperature (700-900°C), SOCs do not require the use of expensive electro-catalysts, such as platinum, and they can also be used to directly convert carbon containing fuels. Moreover, part of the energy necessary to perform the steam dissociation reaction in a SOC can be provided in the form of heat. Therefore, this technology allows to work at lower voltage and higher current density with respect to PEMCs and Alkaline Cells [Graves 2011]. This feature guarantees high rates of hydrogen production while keeping very high electrical efficiency. Finally, thanks to their reversibility, the same electrochemical device can be directly used to produce electricity in fuel cell mode (Solid Oxide Fuel Cell – SOFC) or hydrogen in electrolysis mode (Solid Oxide Electrolysis Cell – SOEC) making it even more suited for coupling with RES.

Despite all these advantages, the commercial attractiveness of SOCs technology is still limited by too high capital costs. These costs are principally due to the absence of a scale-economy and the relatively high degradation rates. Indeed, up to date the lifetime of SOCs remains insufficient for their industrial deployment. Therefore, the degradation of SOCs is considered as one of the main drawbacks of this technology and several efforts are made to limit it.

The high degradation is caused by several instabilities that arise during operation, such as chemical reactivities between components and microstructural evolutions. These phenomena cause a deterioration of the performances by decreasing the electrocatalytic activity of the electrodes and the ionic/electronic conductivities in the cell's components. In addition, after long-term operation the mechanical stability of the SOCs may also be compromised. All these degradation mechanisms are promoted by the high temperature and the polarization of the electrodes even if their underlying causes remain unclear. Consequently, it is necessary to understand the origins of these phenomena to develop solutions to avoid or minimize them in order to improve the attractiveness of this technology.

## **2. General Objective**

In this context, this thesis aims at investigating the degradation of classical SOCs during operation as a function of the operating conditions. The main focus will be on the study of the microstructural evolutions and the physico-chemical reactivity between the different elements at different operating temperatures and polarizations. With this objective, a threefold methodology is applied in this work

by coupling (i) electrochemical characterizations, (ii) advanced post-test analyses and (iii) multi-scale modeling as reported in Figure 0-3.

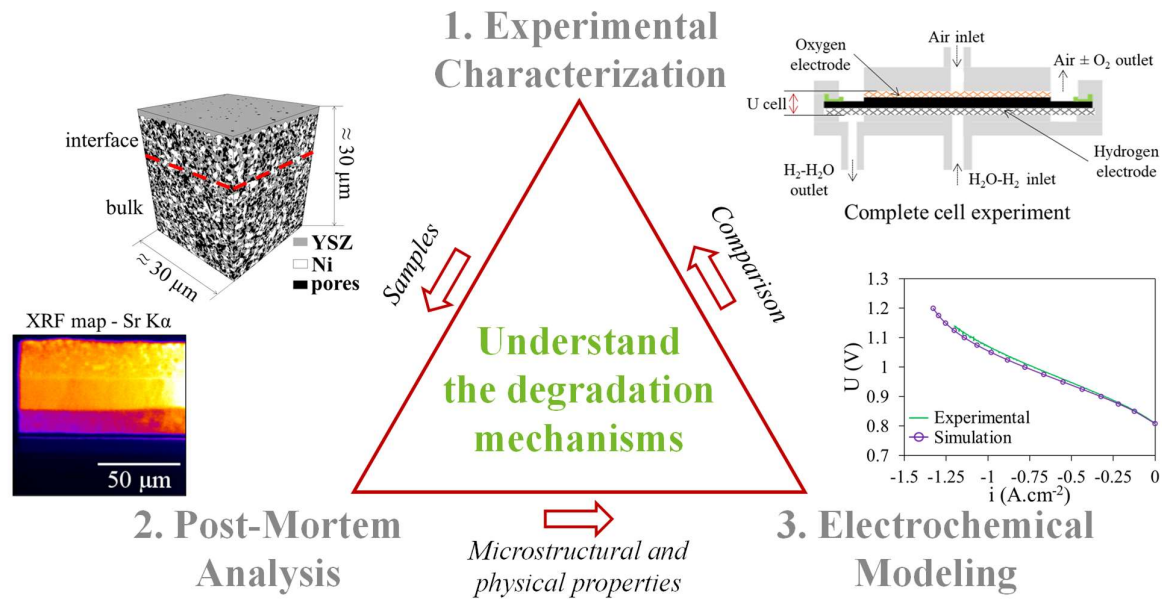


**Figure 0-3: Schematic representation of the threefold methodology adopted in this work.**

Long-term degradation tests are carried out to investigate the evolution of the electrochemical performances. After the durability experiments, specimens extracted from the pristine and aged cells are analyzed using synchrotron-based characterization techniques. Indeed, these techniques offer the possibility to analyze the evolutions in SOCs samples ensuring typical features that are required to obtain reliable results, such as fine spatial resolution while keeping large fields of view. In this frame, X-ray nano-holotomography has been adapted to investigate the microstructural evolutions in the hydrogen electrode (Ni-YSZ cermet) while X-ray micro-diffraction and micro-fluorescence are used to analyze the physico-chemical reactivity in the LSCF-based oxygen electrode. In parallel, a specific attention is given to the modeling of the detailed reaction mechanisms occurring in the two electrodes. With this purpose, elementary kinetic models for the two electrodes are discussed and validated thanks to specific experimental campaigns. Finally, the micro-kinetic models are integrated in a macro-scale model at the cell level. The numerical tool is used to investigate the causes of the degradation mechanisms and to quantify their impacts on the overall cell performances.

### 3. Layout of the Manuscript

In the first chapter of this thesis, the SOCs technology is reviewed. The operating principle, the types of architectures and the materials used in SOCs are discussed focusing on the intrinsic causes of the

performance losses arising in operation. Moreover, the existing literature on the detailed reaction mechanisms occurring in the two electrodes is reported highlighting the recent advances and the uncertainties still existing. Finally, the main causes of the degradation during operation are discussed in order to identify and select the main phenomena studied in this work.

The second chapter is dedicated to the analysis of the experimental results obtained at the complete cell level in the frame of this work. The analyzed cells as well as the experimental setups are described and the effects of the operating conditions on the degradation are discussed. With this purpose, the long-term performances of different types of cells aged in fuel cell and electrolysis mode at different operating temperatures are compared. In addition, the characterization techniques used to investigate the aged cells are described with a specific focus given to the sample preparation for the post-test analyses.

The third chapter describes the development and the validation of the micro-kinetic models at the electrode level and the integration in the multi-scale modeling tool. For the hydrogen electrode, the development of the kinetic model considering the detailed reaction mechanism is described. In this frame, two models have been built considering the two most typical charge transfer reactions (the oxygen spillover and the hydrogen spillover mechanisms). A specific experimental campaign carried out on a symmetric cell is described and it is employed to discriminate between the two mechanisms. Once validated, the micro-kinetic model is used to discuss the reaction mechanism as a function of the polarization. For the oxygen electrode, an existing micro-scale model is validated taking advantage of specific electrochemical tests. Once validated, the effects of the operating temperature are discussed. Finally, the micro-scale models for the two electrodes are integrated in the macro-scale model for the cell and the overall modeling scheme is validated on the performances of the complete cells analyzed in this work.

In chapter four, the results on the microstructural evolutions of nickel in the hydrogen electrode are discussed. The Ni agglomeration and the Ni depletion from the interface are analyzed as a function of operating conditions and initial electrode microstructure. Subsequently, the validated multi-scale modelling tool is used to quantify the effects of Ni instability on the electrode and cell performances. Moreover, the causes of the Ni migration are investigated, taking advantage of the micro-scale model for the hydrogen electrode, and a mechanism to explain the depletion of nickel from the interface as a function of the polarization is proposed.

Chapter five reports preliminary analyses on the physico-chemical reactivity at the oxygen electrode. Specimen extracted from the pristine cell and after aging in different operating conditions are analyzed. The characterization of the reference cell has allowed the determination of the initial reactivity between the electrode and the electrolyte materials. Subsequently, the effects of polarization and operating temperature are discussed from the analysis of the aged cells. The results are analyzed in the frame of a degradation mechanism based on the electrochemical reaction occurring at the electrode scale. Finally, a correlation between the electrode material instability and the interdiffusion of chemical elements at the barrier layer/electrolyte interface is suggested.

To conclude, in chapter six a summary of the main results obtained in this work is reported and some outlooks for future work are proposed.

# **I. Literature Review on Solid Oxide Cells: Technology Fundamentals and Degradation Phenomena**

This chapter is dedicated to the detailed description of the context in which the thesis has been carried out. A specific attention is given to the presentation of the fundamentals of Solid Oxide Cells (SOCs), including the state-of-the-art materials and architectures. Moreover, the basic operation with the physical processes occurring in SOCs are described as well as their impact on the performances during operation. Furthermore, the detailed reaction mechanisms for both electrodes are discussed analyzing the existing literature in terms of modeling and experimental results. Finally, the issues concerning the durability of SOCs are presented and the underlying causes of degradation are introduced and discussed. Based on this bibliography review, the objectives and the strategy adopted for the thesis are defined.

In the first section of the chapter, an overview of the technological, thermodynamic, and operational characteristics of SOCs is given. The second section is dedicated to the review of the detailed reaction mechanisms for the two electrodes, whereas the third section is devoted to the analysis of the degradation mechanisms for this type of technology. Finally, in the last section of this introduction, the justification of the applied approach is given.

# I.1 Solid Oxide Cells: Basic Operating Mechanisms and Materials

## I.1.1 SOCs Principle

SOCs are electrochemical devices that can directly convert fuel into electricity (fuel cell mode – SOFC) or electricity into fuel (electrolysis mode – SOEC). In recent years, the interest in SOCs has significantly grown thanks to their wide range of technological applications that could offer innovative solutions for the transition toward a renewable energy market. For example, when operated in electrolysis mode, these electrochemical devices could be coupled with wind turbines or solar panels for clean production of hydrogen [Godula-Jopek 2015, Lehner 2014]. Besides, in fuel cell mode, SOCs are typically used for the generation of heat and electricity for residential micro-Combined Heat and Power systems ( $\mu$ CHP) [Arsalis 2019, Kendall 2016].

The operating principle of SOCs is represented in Figure I-1.

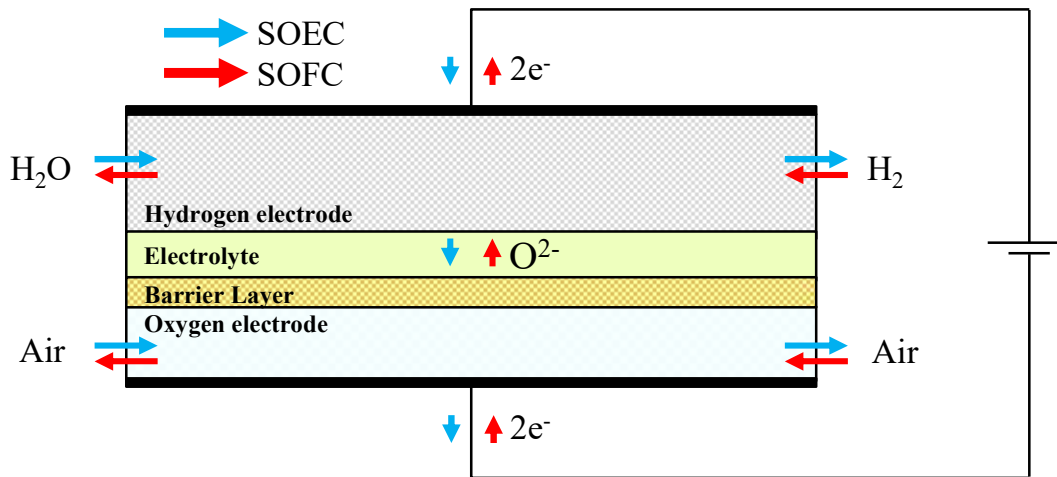
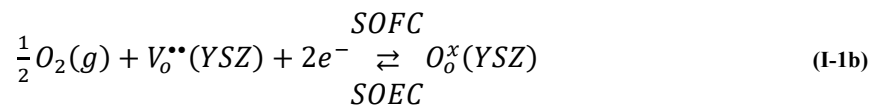
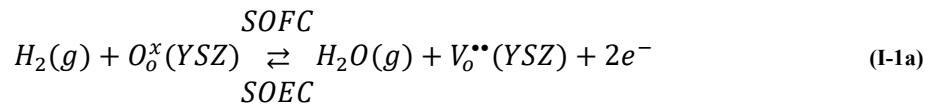
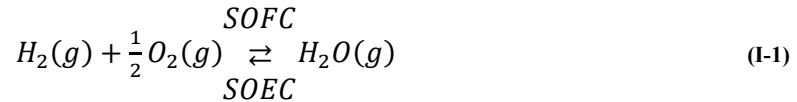


Figure I-1: Solid Oxide Cells operating principle.

The classical reactants and products are hydrogen, oxygen and steam according to the total reaction given in eq. (I-1), which is divided in the two semi-reactions reported in eqs. (I-1a) and (I-1b).



The main components of a SOC are the hydrogen electrode, in which the hydrogen oxidation/steam reduction reactions take place (eq. (I-1a)), and the oxygen electrode, in which oxygen is consumed in

SOFC mode and produced in SOEC mode (eq. (I-1b)). Between the two electrodes, the solid electrolyte ensures the migration of oxygen vacancies ( $V_o^{**}$ ) from one electrode to the other.

To increase the ionic conductivity in the solid electrolyte, SOCs are usually operated at high temperature (700°C – 900°C), which offers many advantages. Indeed, the high operating temperature allows the direct conversion of carbon-containing fuels so that SOCs can be directly used to produce electricity and heat from hydrocarbons, such as methane, in SOFC mode [Morel 2005] and to perform the co-electrolysis of steam and carbon dioxide in SOEC mode [Aicart 2014]. In addition, thanks to the high operating temperature, SOCs present very high efficiency [Godula-Jopek 2015] and allow the utilization of non-expensive catalysts [Shaikh 2015]. Moreover, in SOFC mode, this technology is especially relevant for cogeneration applications. Finally, as already mentioned, it can be noticed that SOCs can be also operated alternatively in fuel cell and electrolysis modes for reversible utilization.

### *1.1.2 SOCs Architecture*

Two main types of architectures have been proposed for SOCs: tubular and planar. In the tubular configuration, one of the electrodes is situated in the internal face of a cylinder and the other one on the external part (Figure I-2a). This configuration presents the advantages of having high mechanical robustness and simplicity in the sealing between the electrodes [Blum 2005, Larminie 2003]. Nevertheless, it has been shown that the performances for this type of architecture can be limited due to the difficulty for the reactants to reach the electrochemical active sites and to significantly high ohmic losses associated to the design and the complex connection between cells [Hino 2004].

Even if some projects on tubular SOCs are currently carried out [Yoshikawa 2017], nowadays the most common type of layout for this technology is the planar one [Wen 2002] (Figure I-2b). In this design, the manufacturing procedure is significantly simpler than the tubular one and the ohmic losses are much less pronounced. The cells are piled-up one on top of the other using metallic interconnects to form high power density stacks. The fuel and the air can be distributed in a cross-flow, a parallel co-flow or a counter-flow configuration. The main difficulty consists in ensuring the sealing between the different components to avoid any leakage especially from the hydrogen electrode side. Nevertheless, it has been shown that this type of configuration allows reaching the highest performances [Ni 2008].

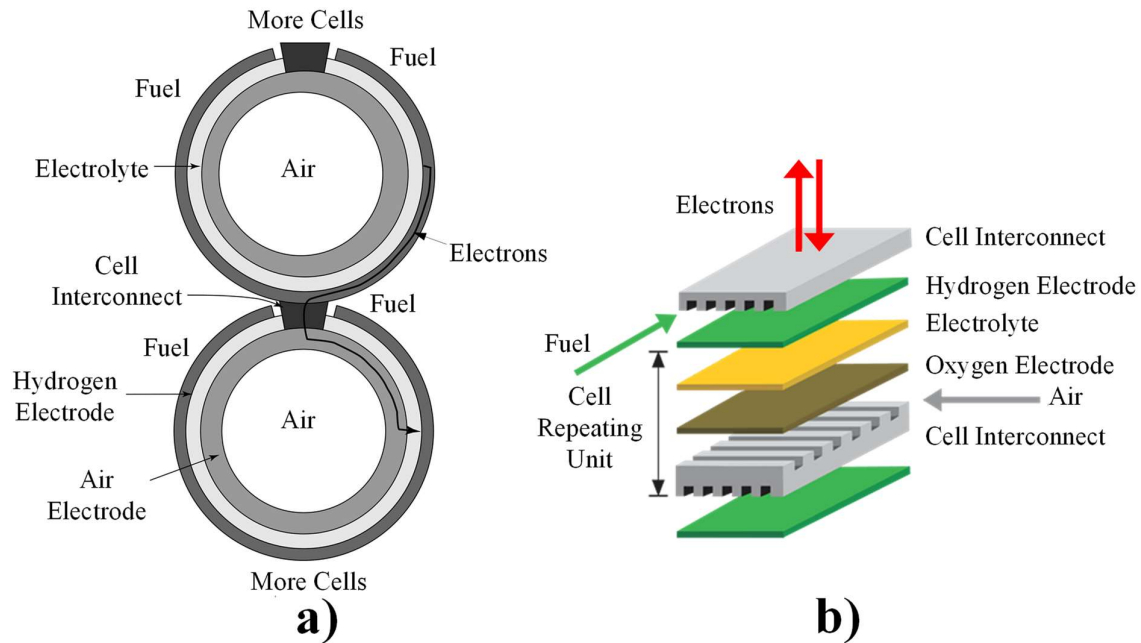


**Figure I-2: Different architectures for SOCs: a) Tubular design [Larminie 2003] – b) Planar design.**

To ensure the mechanical robustness in the planar configuration, different types of solutions have been found. In general, the thickness of one of the cell's layers is increased and the layer serves as support for the rest of the cell. Depending on which layer is used as a substrate it is possible to have: (i) oxygen or hydrogen electrode supported cells, (ii) electrolyte supported cells and (iii) metal interconnect supported cells. Each one of these solutions presents some advantages and drawbacks. Oxygen electrode supported cells have been reported to allow good performances, even if the specific cost is more elevated than in the other configurations [Irshad 2016]. Electrolyte supported cells are classically used at very high temperature ( $> 850 - 900^{\circ}\text{C}$ ) to limit the ohmic losses inside the electrolyte [Kendall 2016]. Very recently, this type of cells has attracted significant interest because of the relative simplicity in the manufacturing and the high mechanical strength. Moreover, the use of highly conductive materials for the electrolyte has allowed working at lower operating temperatures [Jais 2017] and new experimental results at the cell level show promising behaviors in terms of durability [Schefold 2020]. The metal supported cells consist in using porous metallic interconnects to increase the mechanical robustness and the resistance to thermal and redox cycling, while reducing the manufacturing costs. Promising performances have been obtained for this type of technology [Blennow 2011, Dogdibegovic 2019b], even if it remains still immature, especially in terms of durability [Brandon 2017, Dogdibegovic 2019a]. Finally, the hydrogen electrode supported cells have been reported to be a good compromise between manufacturing costs, performances, and mechanical robustness [Irvine 2013]. For this reason, nowadays, the most common design for planar

SOC is the hydrogen electrode supported cell configuration even if electrolyte supported cells and metal supported cells are being extensively studied as promising alternatives.

### 1.1.3 Materials Selection

To ensure the reliability of SOCs, the choice of the materials used for the two electrodes and the electrolyte is of central importance. Indeed, they must fulfill a large number of requirements such as:

- Compatibility on the thermal expansion coefficient (TEC) between the different layers,
- Chemical stability in the reducing and oxidizing environments of the cathode and the anode respectively,
- High electro-catalytic activity for the reactions taking place at the two electrodes,
- High ionic conductivity and negligible electronic conductivity for the electrolyte,
- Low chemical reactivity between the different layers (including the interconnectors),
- Mechanical robustness,
- Competitive fabrication costs with low environmental impact.

These strict requirements must be satisfied considering also the high operating temperature of SOCs making the selection of the materials even more complex.

#### 1.1.3.1 Electrolyte

The electrolyte in SOCs is classically made of fluorite-type ceramic oxides (e.g.  $ZrO_2$ ,  $CeO_2$ ,  $Bi_2O_3$  and  $ThO_2$ ). Di- or tri-valent rare-earth or alkaline-earth cations (such as Ce, Mg, Y, Nd, Sm, Yb and Sc) are used as substitution elements to stabilize the ceramic in the cubic crystalline phase throughout a large range of temperatures [Kharton 2004]. The substitution also creates oxygen vacancies in the lattice of the material leading to high ionic conductivities. With a fixed concentration of dopant, the evolution of the ionic conductivity can be described using a classical Arrhenius-type law as given in eq. (I-2).

$$\sigma_{io} = \sigma_{io}^0 \cdot \exp\left(-\frac{E_{act}}{R \cdot T}\right) \quad (I-2)$$

In which  $\sigma_{io}^0$  is a pre-exponential factor ( $S \cdot cm^{-1}$ ),  $E_{act}$  is the activation energy ( $J \cdot mol^{-1}$ ),  $R$  is the universal gas constant ( $J \cdot K^{-1} \cdot mol^{-1}$ ) and  $T$  is the operating temperature (K).

To date, the most typical electrolyte material for hydrogen electrode supported cells is Zirconia stabilized in the cubic phase adding 8 %mol. of Yttria ( $(ZrO_2)_{0.92}(Y_2O_3)_{0.08} - 8YSZ$ ) [Suciu 2018]. The choice of 8YSZ represents a good compromise between the ionic conductivity and the

mechanical robustness. Indeed, the ionic conductivity of YSZ exhibits a maximum around 8.5 – 9 %mol. of Yttria [Nakamura 1986], whereas lower doping levels, such as the tetragonal Zirconia doped with 3 %mol. of Yttria (3YSZ), correspond to higher mechanical strength [Ghatee 2009]. Typical evolutions of the ionic conductivity for the 8YSZ and 3YSZ as a function of the operating temperature are shown in Figure I-3 (considering  $\sigma_{io,3YSZ}^0 = 44.7 \text{ S}\cdot\text{cm}^{-1}$ ,  $\sigma_{io,8YSZ}^0 = 466 \text{ S}\cdot\text{cm}^{-1}$ ,  $E_{act,3YSZ} = 69'837 \text{ J}\cdot\text{mol}^{-1}$  and  $E_{act,8YSZ} = 82'616 \text{ J}\cdot\text{mol}^{-1}$  [Lay-Grindler 2013]).

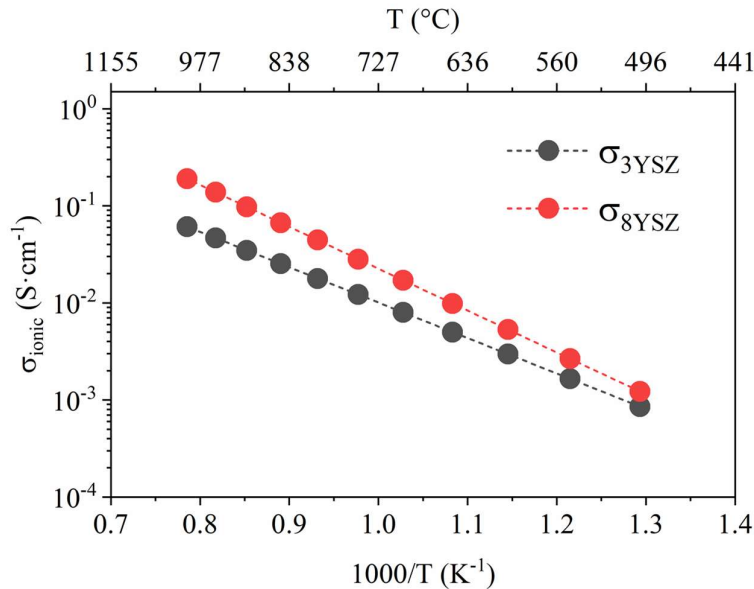


**Figure I-3: Ionic conductivity of 8YSZ and 3YSZ as a function of the operating temperature [Lay-Grindler 2013].**

### 1.1.3.2 Oxygen Electrode

The oxygen electrode was classically made of a porous composite of 8YSZ and Lanthanum Strontium Manganite (LSM) [Jiang 2008]. With these materials, the oxidation/reduction of oxygen occurs at the so-called Triple Phase Boundaries lines (TPBs) where the electronic, ionic and gas phases meet. Nowadays, this composite has been advantageously replaced by Mixed Ionic and Electronic Conductors (MIEC) for which the reaction can be extended from the vicinity of TPBs to the whole surface area of the porous electrode resulting in a substantial increase of the performances [Adler 2004]. Among the different compounds, the Lanthanum Strontium Cobaltite Ferrite ( $\text{La}_x\text{Sr}_{1-x}\text{Co}_y\text{Fe}_{1-y}\text{O}_{3-\delta}$  – LSCF) perovskite is the most employed material for SOCs application [Gómez 2016, Laguna-Bercero 2012, Menzler 2010]. In addition, it has been recently proposed to replace LSCF by a composite of LSCF and Gadolinium-doped Ceria Oxide ( $\text{Gd}_x\text{Ce}_{1-x}\text{O}_{2-\delta}$  – GDC) as an alternative oxygen electrode, in order to mitigate the mismatch in thermal expansion coefficients between the electrode and the electrolyte [Dusastre 1999] and to enhance the electrode performances, especially in electrolysis mode [Effori 2019].

To mitigate the reactivity of LSCF and YSZ, a barrier layer of GDC is usually added between the electrolyte and the electrode to avoid the direct contact between the two materials [Ferreira-Sanchez 2017, Knibbe 2010a, Laurencin 2017].

### *1.1.3.3 Hydrogen Electrode*

The typical hydrogen electrode is constituted of a porous cermet of nickel and YSZ, in which the Ni serves as electronic conductor/reaction catalyst, the YSZ as ionic conductor and the pores ensure the gas transport [Jiang 2004, Menzler 2010]. Porous cermet electrodes are used to extend the electrochemical active area in the thickness of the electrode. The hydrogen electrode is also used as mechanical support of the cell. Therefore, the electrode is usually structured into regions with different microstructures to separate the electrochemical and the mechanical functions.

In contact with the electrolyte, the thin functional layer (FL) presents a fine microstructure in which the electrochemical reactions take place at the TPBs. This layer is associated with a thick current collector substrate (CC) with a coarser microstructure which ensures the gas diffusion to the FL and guarantees the collection of electronic current. It can be noticed that in some cases pores formers are added in the substrate to favor the diffusion to the active sites [Moussaoui 2020, Pecho 2015]. In the functional layer of the cermet, the YSZ presents typically the same amount of Yttria as in the electrolyte (8YSZ). Nevertheless, in some cases 3YSZ is used to take advantage of the higher mechanical robustness [Ghatee 2009] even if in this case the electrode exhibits a lower ionic conductivity (cf. Figure I-3). It can be noticed that for the CC layer the choice of 3YSZ is the most common due to the better mechanical properties.

### *1.1.4 Thermodynamic Description of SOCs and Nernst Equation*

As a general matter, SOCs are electrochemical devices that allow the direct conversion of the chemical energy contained in the fuel in electricity and vice versa. To investigate the operation of SOCs it is important to obtain the standard voltage of the cell, corresponding to the difference between the standard potentials at the two electrodes. With this objective, it can be useful to analyze the thermodynamically reversible processes occurring in an ideal cell.

A solid oxide cell operating in SOFC mode can be described with the scheme reported in Figure I-4. Based on this representation, it is possible to apply the first law of thermodynamic to obtain an energy balance of the system as reported in eq. (I-3).

$$q_{rev} - w_{rev} = v_{prod} \cdot h_{prod}^0(T, p_0) - v_{ox} \cdot h_{ox}^0(T, p_0) - h_{fuel}^0(T, p_0) \quad (I-3)$$

In which all the quantities are referred to an unitarian molar flow of fuel ( $\text{mol} \cdot \text{s}^{-1}$ ).

In eq. (I-3),  $q_{rev}$  represents the specific reversible heat produced in the cell ( $\text{J} \cdot \text{mol}^{-1}$ ),  $w_{rev}$  the specific reversible electrical work delivered by the cell ( $\text{J} \cdot \text{mol}^{-1}$ ) and  $v_{prod} / v_{ox}$  the stoichiometric coefficients corresponding to one mole of fuel for the product and the oxidant, respectively. The terms  $h_{prod}^0$ ,  $h_{ox}^0$ ,  $h_{fuel}^0$  are the specific enthalpies of the product, the oxidant and the fuel as a function of the absolute temperature and at standard pressure of 1 atm (expressed in  $\text{J} \cdot \text{mol}^{-1}$ ).

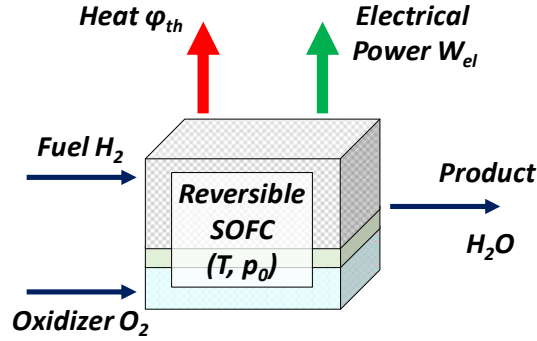


**Figure I-4: Illustration of the thermodynamically reversible operation of a SOFC operating in fuel cell mode.**

It can be noticed that the right-hand side of eq. (I-3) represent the standard variation of enthalpy of the reaction associated to one mole of fuel,  $\Delta h_{react}^0(T, p_0)$ , as given in eq. (I-4).

$$v_{prod} \cdot h_{prod}^0(T, p_0) - v_{ox} \cdot h_{ox}^0(T, p_0) - h_{fuel}^0(T, p_0) = \Delta h_{react}^0(T, p_0) \quad (I-4)$$

Moreover, as the process is considered reversible, the second law of thermodynamic can be written as reported in eq. (I-5).

$$\frac{q_{rev}}{T} = v_{prod} \cdot s_{prod}^0(T, p_0) - v_{ox} \cdot s_{ox}^0(T, p_0) - s_{fuel}^0(T, p_0) \quad (I-5)$$

In which  $T$  is the operating temperature (K) and the terms  $s_{prod}^0$ ,  $s_{ox}^0$ ,  $s_{fuel}^0$  are the specific entropies of the product, of the oxidant and of the fuel as a function of the absolute temperature and at standard pressure of 1 atm (expressed in  $\text{J} \cdot \text{K}^{-1} \cdot \text{mol}^{-1}$ ).

In this case, the right-hand side of eq. (I-5) corresponds to the standard variation of entropy for the reaction of one mole of fuel,  $\Delta s_{react}^0(T, p_0)$ , so that it can be rewritten as shown in eq. (I-6).

$$q_{rev} = T \cdot \Delta s_{react}^0(T, p_0) \quad (I-6)$$

Combining eqs. (I-3), (I-4) and (I-6) it is possible to express the specific electrical work produced by the cell as reported in eq. (I-7).

$$w_{rev} = -(\Delta h_{react}^0(T, p_0) - T \cdot \Delta s_{react}^0(T, p_0)) = -\Delta g_{react}^0(T, p_0) \quad (\text{I-7})$$

Where  $\Delta g_{react}^0(T, p_0)$  is the standard variation of the Gibbs free energy for the reaction considering one mole of fuel.

The total electrical power produced by the cell in reversible conditions can be obtained by the specific electrical work and the flow of fuel consumed in the reaction, as given in eq. (I-8).

$$W_{el} = i \cdot U^0 \cdot A = \dot{n}_{fuel\ consumed} \cdot w_{rev} \quad (\text{I-8})$$

In which  $i$  is the current density generated by the cell ( $A \cdot cm^{-2}$ ),  $U^0$  represents the standard cell potential (V) and  $A$  is the active area of the cell ( $cm^2$ ). Finally, considering the Faraday's law ( $i = n \cdot F \cdot \dot{n}_{fuel\ consumed} \cdot A^{-1}$ ) and combining eqs. (I-7) and (I-8), it is possible to obtain a thermodynamic definition of the standard voltage of the cell given in eq. (I-9).

$$U^0 = -\frac{\Delta g_{react}^0(T, p_0)}{n \cdot F} \quad (\text{I-9})$$

In which  $n$  is the number of electrons exchanged in the reaction and  $F$  is the Faraday's constant ( $C \cdot mol^{-1}$ ).

This definition of the standard cell voltage represents the ideal potential difference measurable in a cell operating in standard conditions of pressure ( $p_0 = 1 \text{ atm}$ ) for all the reactants and products and at a given operating temperature. Nevertheless, in real operation the pressures of reactants and products do not correspond to the standard pressure so that the Nernst equation is used to take into account this limitation and evaluate the real Open Circuit Voltage ( $U_{OCV}$ ) of the cell.

To introduce the Nernst equation, it is useful to start from the general form of a chemical reaction such as the one reported in eq. (I-10).



In this expression, each one of the involved species has an associated chemical activity ( $a_i$ ) that can be expressed as in eq. (I-11) in case of ideal solution of gaseous species.

$$a_i = \frac{p_i}{p_0} = x_i \cdot \frac{p_{tot}}{p_0} \quad (\text{I-11})$$

In which  $p_{tot}$  is the operating pressure of the cell and  $p_i$ ,  $x_i$  are the partial pressure (atm) and the molar fraction of the  $i$ -th species.

Based on thermodynamic considerations, it can be shown that the Gibbs free energy variation of a reaction such as the one given in eq. (I-10) is influenced by the activity of the species involved in the reaction according to eq. (I-12) [Atkins 2006].

$$\Delta g_{react}(T, p) = \Delta g_{react}^0(T, p_0) + R \cdot T \cdot \ln \left( \frac{a_C^{v_c} \cdot a_D^{v_d}}{a_A^{v_a} \cdot a_B^{v_b}} \right) \quad (\text{I-12})$$

Combining eqs. (I-9), (I-11) and (I-12) it is possible to express the Nernst potential of the reaction which depends on thermodynamic considerations and on the partial pressures of the reactants and products. Moreover, if the solid oxide cell operates at ambient pressure, the Nernst equation for the typical reaction in a SOC (eq. (I-1)) can be expressed as:

$$U_{OCV} = U^0 - \frac{R \cdot T}{2 \cdot F} \cdot \ln \left( \frac{x_{H_2O, hydrogen\ electrode}}{x_{H_2, hydrogen\ electrode} \cdot x_{O_2, oxygen\ electrode}^{0.5}} \right) \quad (\text{I-13})$$

In eq. (I-13) the molar fractions of hydrogen, oxygen and steam are taken at the interface between the corresponding electrode and the electrolyte and considering a nil current flowing in the cell.

It can be noticed that when the cell is operated, several reversible and irreversible phenomena arise under current inducing a modification of the cell voltage with respect to the OCV. To analyze these losses, polarization curves (i-U curves) are usually used. In these curves, the cell voltage is plotted as a function of the current density and the losses in operation are represented by the overpotentials arising in both polarizations (cf. Figure I-5).

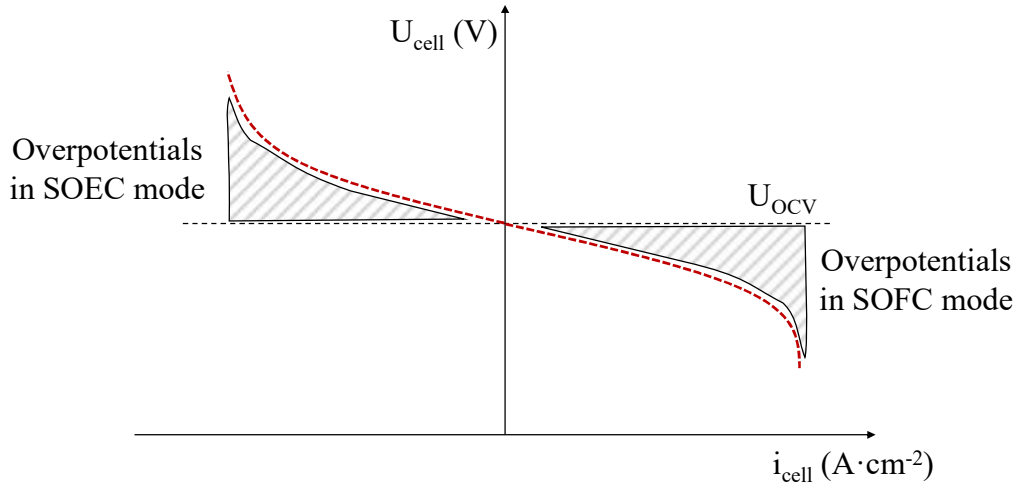


**Figure I-5: Schematic representation of an i-V curve in SOFC and SOEC at  $H_2/H_2O = 50/50$  vol.% with an illustration of the overpotentials arising in the two operating modes.**

### 1.1.5 Losses at the Cell Level and Impact on Cell's Performances

The overpotentials generated during the operation of the cell are associated to the concentration of the gases in both electrodes at the electrochemical active sites and to the nature of the electrochemical reactions in each electrode. In addition, the Ohmic losses generated by the current flow contribute to the overall decrease in performances so that the relation between the cell potential and the current density can be written as reported in eq. (I-14).

$$U_{cell} = U_{OCV} - \eta_{ohmic}(i) - \eta_{conc}^{O_2 electrode}(i) - \eta_{conc}^{H_2 electrode}(i) - \eta_{act}^{O_2 electrode}(i) - \eta_{act}^{H_2 electrode}(i) \quad (I-14)$$

In which  $i$  is the current density expressed in  $A \cdot cm^{-2}$ . The different overpotentials are  $> 0$  in SOFC mode and  $< 0$  in SOEC mode so that the cell voltage is always smaller than the OCV when operating in fuel cell mode whereas it is higher in electrolysis mode.

#### 1.1.5.1 Ohmic Overpotential

The Ohmic overpotential ( $\eta_{ohmic}(i)$ ) is caused by the material resistance to the passage of the ionic and electronic currents. In particular, it takes into account the resistance associated to the flow of electrons in the electrodes and the one related to the flow of ions in the electrolyte. Moreover, the contact resistance between the electrodes and the current collectors also contribute to the overall Ohmic resistance of the cell.

All these contributions are gathered together under a general resistance  $R_s$  expressed in  $(\Omega \cdot cm^2)$ , so that the Ohmic overpotential for the complete cell can be described using a classical Ohm's law (eq. (I-15)).

$$\eta_{ohmic}(i) = R_s \cdot i \quad (I-15)$$

The electronic conductivities of the electrodes are usually orders of magnitude higher than the ionic conductivity of the electrolyte, so that the latter term represents the most important part to the Ohmic resistance of the cell. It can be noticed that the second larger contribution is represented by the contact resistances [Liu 2008]. To limit these last phenomena, highly conductive grids or contact layers are usually used as current collectors in single cells experimental setups or stacks, respectively. Furthermore, compressive loads are applied on the system to maximize the contacts between the cell and the current collectors.

#### 1.1.5.2 Concentration Overpotentials

The concentration overpotentials in the oxygen electrode ( $\eta_{conc}^{O_2 electrode}$ ) and in the hydrogen electrode ( $\eta_{conc}^{H_2 electrode}$ ) are caused by the modification of the gases composition at the electrochemical active sites that arise when the cell is operated. For each electrode, the concentration overpotential can be expressed as a combination of two factors: The losses due to gas conversion ( $\Delta U_{rev}$ ) [Primdahl 1998] and the overpotential associated to gas diffusion ( $\eta_{diff}$ ) [Zhu 2003].

*Gas conversion losses* – The gas conversion losses are generated by the fact that when a current is passed through the cell, the gases composition is modified according to the Faraday’s law. They correspond to pure ‘reversible losses’ that will appear even for an ideal system without irreversible processes. Considering the classical operation in a SOC involving hydrogen, steam and oxygen (eq. (I-1)) the gas conversion losses are drawn from the Nernst equation as reported in eqs. (I-16a) and (I-16b) for the two electrodes [Godula-Jopek 2015]:

$$\Delta U_{rev}^{H_2 electrode} = \frac{R \cdot T}{2 \cdot F} \cdot \ln \left( \frac{a_{H_2}^{channel, i=0} \cdot a_{H_2O}^{channel, i \neq 0}}{a_{H_2}^{channel, i \neq 0} \cdot a_{H_2O}^{channel, i=0}} \right) \quad (I-16a)$$

$$\Delta U_{rev}^{O_2 electrode} = \frac{R \cdot T}{2 \cdot F} \cdot \ln \left( \frac{\sqrt{a_{O_2}^{channel, i \neq 0}}}{\sqrt{a_{O_2}^{channel, i=0}}} \right) \quad (I-16b)$$

In which the activities  $a_i^{channel, i=0}$  and  $a_i^{channel, i \neq 0}$  correspond to the activity of the  $i$ -th species in the gas channel in open circuit conditions and under current, respectively.

It can be pointed out that in fuel cell mode, the cell is normally operated with over-stoichiometric air flow in the oxygen electrode, so that the contribution of the  $\Delta U_{rev}^{O_2 electrode}$  remains limited. Moreover, it can be noticed that these losses are not related to the diffusion of gases in the electrodes, but they are only linked to the inlet gas composition and the current flowing through the cell.

The existence of the conversion losses implies the presence of a limiting current density, corresponding to the conditions in which all the reactants are consumed by the reaction ( $\dot{n}_{reactant consumed} = \dot{n}_{reactant inlet}$ ). Therefore, it can be useful to define the conversion rate ( $CR$ ) corresponding to the amount of reactant consumed by the reaction divided by the inlet flow of reactant entering the cell (eq. (I-17)).

$$CR = \frac{\dot{n}_{reactant consumed}}{\dot{n}_{reactant inlet}} = \frac{i \cdot A}{n \cdot F \cdot \dot{n}_{reactant inlet}} \quad (I-17)$$

For an operation in fuel cell mode, this parameter is called Fuel Utilization (FU) while for an operation in electrolysis mode it is normally named Steam Conversion (SC).

*Diffusion overpotentials* – The diffusion overpotentials are caused by the limitations induced by the gas transport inside the electrodes. Indeed, in order to sustain the electrochemical reactions at the active sites when the cell is operated, a flux of reactants and products arises in the electrodes. This transport phenomena are influenced by the microstructure of the electrodes. Therefore, the volume fraction and the ‘morphology’ of the pores play a central role in the diffusion of the gases from the channels to the electrochemical active sites [Holzer 2013]. Starting from these premises, the diffusion

overpotentials are defined as reported in eqs. (I-18a) and (I-18b) for the hydrogen electrode and the oxygen electrode, respectively [Laurencin 2011].

$$\eta_{diff}^{H_2 electrode} = \frac{R \cdot T}{2 \cdot F} \cdot \ln \left( \frac{a_{H_2}^{channel} \cdot a_{H_2O}^{active sites}}{a_{H_2}^{active sites} \cdot a_{H_2O}^{channel}} \right) \quad (I-18a)$$

$$\eta_{diff}^{O_2 electrode} = \frac{R \cdot T}{2 \cdot F} \cdot \ln \left( \frac{\sqrt{a_{O_2}^{active sites}}}{\sqrt{a_{O_2}^{channel}}} \right) \quad (I-18b)$$

In which the hydrogen, steam and oxygen activities are taken considering an operating cell ( $i \neq 0$ ).

### 1.1.5.3 Activation Overpotentials

The activation overpotentials ( $\eta_{act}$ ) represent the voltage losses due to the inherent irreversibilities related to all the processes occurring in both active functional layers including the electrochemical reactions and the mass and charge transfers. Considering a phenomenological approach, the current density can be expressed as a function of these overpotentials using a Butler-Volmer formalism as reported in eq. (I-19a) for the hydrogen electrode and eq. (I-19b) for the oxygen electrode [Godula-Jopek 2015, Virkar 2000].

$$i = i_0^{H_2 electrode} \cdot \left[ \exp \left( \frac{2\alpha_{H_2} F}{RT} \eta_{act}^{H_2 electrode} \right) - \exp \left( \frac{-2(1-\alpha_{H_2}) F}{RT} \eta_{act}^{H_2 electrode} \right) \right] \quad (I-19a)$$

$$i = i_0^{O_2 electrode} \cdot \left[ \exp \left( \frac{2\alpha_{O_2} F}{RT} \eta_{act}^{O_2 electrode} \right) - \exp \left( \frac{-2(1-\alpha_{O_2}) F}{RT} \eta_{act}^{O_2 electrode} \right) \right] \quad (I-19b)$$

In which  $i_0$  is the so-called ‘apparent’ exchange current density ( $A \cdot cm^{-2}$ ) and  $\alpha_{O_2, H_2}$  are the symmetry factors for both electrodes.

Recalling the definition of hyperbolic sine and taking the symmetry factor as 0.5 [Bard 2001], it is possible to express the activation overpotential for each electrode as a function of the operating current density as given in eqs. (I-20a) and (I-20b).

$$\eta_{act}^{H_2 electrode} = \frac{R \cdot T}{F} \cdot \sinh^{-1} \left( \frac{i}{2 \cdot i_0^{H_2 electrode}} \right) \quad (I-20a)$$

$$\eta_{act}^{O_2 electrode} = \frac{R \cdot T}{F} \cdot \sinh^{-1} \left( \frac{i}{2 \cdot i_0^{O_2 electrode}} \right) \quad (I-20b)$$

It can be noticed that these expressions have been derived with a purely ‘phenomenological’ approach considering an ‘overall’ charge transfer occurring at the electrodes/electrolyte interfaces. Indeed, these apparent exchange current densities for each electrode represent global parameters that include each elementary step of the reaction mechanisms (such as the charge transfers, the diffusion of surface-attached species and the adsorption/desorption reactions) [Godula-Jopek 2015]. These parameters are strongly dependent on the electrode microstructure [Connor 2018] and the gas

composition in electrochemical active areas. Moreover, they are also affected by the operating temperature [Virkar 2000].

The determination of the correct values for the exchange current densities, must rely on the identification of the detailed reaction mechanisms occurring at each electrode which are still not completely understood. Several works have been dedicated to investigate these reactions using experimental and modeling techniques. In the next section, a review of these contributions for each electrode is reported.

## **I.2 Literature Review on the Reaction Mechanisms for the Two Electrodes**

### *I.2.1 Reaction Mechanism for the Hydrogen Electrode*

Concerning the reaction mechanism in the Ni-YSZ cermet, several experimental works have characterized the electrode behavior using polarization curves and Electrochemical Impedance Spectroscopy (EIS) [Bieberle 2001, 2000, Dasari 2013, Doppler 2018, Grondin 2011, Holtappels 1999a, 1999b, Kek 2001, Luo 2017, Marina 2007, Mizusaki 1994b, 1994a, Pan 2016, Primdahl 1997, Shin 2016, Sonn 2008]. Nevertheless, it can be pointed out that most of the works presented in the literature are focused on the reaction for hydrogen oxidation in SOFC mode, whereas there is a lack of investigations in electrolysis conditions. For example, very few studies have been specifically devoted to the electrode response in cathodic polarization [Dasari 2013, Grondin 2011, Shin 2016] and even less have operated the electrode at high steam partial pressure ( $p_{H_2}/p_{H_2O} \ll 1$ ) [Shin 2016].

As a general matter for the Ni-8YSZ cermet, it has been shown that the electrode reaction is strongly thermally activated and its kinetic rate is proportional to the density of active TPBs [Bieberle 2000, Doppler 2018, Mizusaki 1994a, Pan 2016]. Based on these observations, it has been proposed that the charge transfer at the TPBs should limit the overall electrode response [Luo 2017]. Moreover, a strong dissymmetry in the two branches of the polarization curve has been highlighted [Dasari 2013, Holtappels 1999b, Luo 2017, Marina 2007, Mizusaki 1994b, Pan 2016] with an increase of the polarization resistance ( $R_{pol}$ ) in cathodic polarization (SOEC mode) compared to the anodic one (SOFC mode) [Pan 2016]. Finally, an important effect of  $p_{H_2O}$  on the kinetics has been found [Bieberle 2001, Dasari 2013, Grondin 2011, Holtappels 1999a, Luo 2017, Pan 2016, Shin 2016], while the impact of  $p_{H_2}$  remains less pronounced [Kek 2001]. Therefore, it has been inferred from these results that the interaction of steam molecules with the electrode surface could co-limit the global kinetics [Dasari 2013].

Complementary with the experimental approach, modeling is an efficient tool to propose and check the relevance of reaction mechanisms. In this frame, several authors have studied the steam and hydrogen interactions with Ni-YSZ using Density Functional Theory (DFT) to determine the most energetically favorable configuration [Cadi-Essadek 2016, Chaopradith 2015, Cucinotta 2011, Gorski 2011, Kresse 2000, Mohsenzadeh 2014, Raz 2001, Seenivasan 2017, Shishkin 2010]. These theoretical investigations showed that the interaction of hydrogen with the Ni-YSZ system results in dissociative adsorption of H<sub>2</sub> on the Ni surface [Cadi-Essadek 2016, Cucinotta 2011, Kresse 2000, Shishkin 2010], whereas steam molecules can be adsorbed on both surfaces. On Ni surface, the adsorbed H<sub>2</sub>O could dissociate into a hydroxyl and a surface-attached hydrogen [Mohsenzadeh 2014], while the dissociation in two hydroxyl ions would be promoted on YSZ surface [Raz 2001].

To account for both the experimental and DFT computational findings, mainly three reaction pathways divided in a sequence of elementary steps have been proposed in the literature. They differ from each other by the nature of the charge transfer across the Ni-YSZ interface with an interstitial process [Holtappels 1999a], an oxygen spillover mechanism [Mizusaki 1994b], and a hydrogen spillover mechanism [De Boer 1998]. These three reaction pathways have been implemented by several authors into micro-kinetic models and the simulations have been compared to the response of Ni patterned electrodes [Bessler 2007, 2010, Bieberle 2002, Goodwin 2009, Luo 2019, Vogler 2009]. The modeling results have suggested that the hydrogen spillover would be the most relevant reaction mechanism for the Ni-8YSZ electrode [Bessler 2010, Goodwin 2009, Luo 2019, Vogler 2009] even if some recent studies have suggested that the oxygen spillover mechanism could also be involved in the electrode response [Bredikhin 2018, Fu 2014, Ong 2017]. Moreover, it is worth mentioning that most of the simulations were focused on the steady-state behavior of the electrode whereas very few studies have simulated the dynamic response to take advantage of the EIS measurements [Bieberle 2002, Gewies 2008]. Besides, to the best of our knowledge, only one study has been dedicated to the micro-kinetic dynamic modeling of representative porous Ni-8YSZ cermet [Gewies 2008]. In that case, the simulations were carried out without knowing the exact microstructure of the cermet and considering a simplified charge transfer mechanism.

From this literature review, it appears that the detailed reaction mechanism of eq. (I-1a) remains unclear, especially for a cell operated in SOEC condition. Indeed, as pointed out by Hanna *et al.* [Hanna 2014], there is still a clear need for “more detailed experimental data and refinement of elementary kinetic and transport parameters to improve quantitative model prediction over a wide range of conditions”.

### 1.2.2 Reaction Mechanism for the Oxygen Electrode

For composite LSM-YSZ electrodes, it is generally accepted that the oxidation/reduction reactions (eq. (I-1b)) occur *via* the same reaction mechanism in opposite directions. In cathodic polarization (i.e. SOFC mode), the oxygen is adsorbed on the LSM surface and diffuses to the TPBs where the charge transfer reaction takes place, producing two electrons in the LSM and an oxygen ion in the YSZ. In anodic polarization (i.e. SOEC mode), the reverse mechanism occurs. It has been observed experimentally that the overall reaction rate would be proportional to the density of TPBs indicating that the charge transfer would control the reaction kinetics [Radhakrishnan 2005]. In addition, recent studies have pointed out that the surface diffusion of oxygen on the LSM could also contribute significantly to the electrode response [Banerjee 2017, Bertei 2017].

On the other hand, the reaction pathway for MIEC electrodes remains less understood. In fuel cell mode, it has been extensively studied experimentally [Baumann 2007, Grunbaum 2006, 2009, Kim 2017, Tietz 2006] and theoretically [Adler 1996, Deseure 2005, Fleig 2007, Hubert 2016, Laurencin 2015, Liu 1998b, Mortensen 2014, Prestat 2007, Simrick 2012, Yurkiv 2014]. Adler *et al.* [Adler 1996] have analyzed the impedance of porous LSCF electrodes with a model in which the polarization resistance is dominated by the so-called “chemical impedance” that takes into account the oxygen vacancies diffusion in the bulk of the LSCF and the reaction at the surface of electrode particles. The same mechanism has been used by Deseure *et al.* [Deseure 2005] to model the AC and DC response of a dense electrode in fuel cell mode. Prestat *et al.* [Prestat 2007] and Fleig *et al.* [Fleig 2007] have also proposed models for dense LSCF film. In their model, Fleig *et al.* [Fleig 2007] have refined the Adler’s approach with intermediate surface reactions of oxygen ionization leading to an electrostatic potential step across the LSCF surface. Besides, Yurkiv *et al.* [Yurkiv 2014] and Mortensen *et al.* [Mortensen 2014] have extended this modeling approach based on oxygen bulk diffusion and charge transfer at the LSCF surface to the LSCF-GDC composite electrodes.

For pure LSCF electrodes, several experimental results have confirmed the mechanism proposed by Adler *et al.* [Adler 1996] at the open circuit potential and under cathodic polarization [Adler 2004, Baumann 2006, 2007, Grunbaum 2009]. However, some authors [Liu 1998b, 1999, Siebert 2013], have suggested that the direct oxygen oxidation/reduction at TPBs could also participate to the electrode response, especially in anodic polarization for which the oxidation at TPBs could control the reaction mechanism [Laurencin 2015, Siebert 2011]. Similarly, for LSCF-GDC electrodes some authors [Hubert 2016, Kim 2017, Laurencin 2015] have suggested a significant contribution of the TPBs even under cathodic polarization.

Recently, our research group at CEA has investigated the oxidation/reduction process for pure LSCF and composite LSCF-GDC electrodes proposing a stationary and dynamic model taking into account the electrode microstructure properties as well as the most likely processes occurring therein [Hubert 2016, Laurencin 2015]. In this model, two parallel pathways have been considered for the reaction. On the one hand, the ‘bulk path’, corresponding to the oxygen vacancies diffusion in the bulk of the LSCF coupled with surface reactions. On the other hand, the ‘surface path’, in which the direct oxidation/reduction at the TPBs between the GDC and the LSCF is considered. Thanks to a preliminary validation [Laurencin 2015] and a microstructural sensitivity analyses [Hubert 2016], it has been proposed that the main reaction pathway could change as a function of the polarization and type of electrode. For a pure LSCF electrode, the reaction would be controlled by the ‘bulk path’ in cathodic polarization and at OCV, whereas in anodic polarization the ‘surface path’ would become dominant. For a LSCF-GDC composite electrode, the reaction mechanism would be always controlled by the oxidation/reduction at the TPBs (‘surface path’).

From this analysis of the literature on the oxidation/reduction at the oxygen electrode, it can be stated that the reaction mechanism of eq. (I-1b) remains partially unclear, especially in anodic polarization (i.e. SOEC mode) and for MIEC-based electrodes. Some theoretical results have suggested a modification in the reaction mechanism as a function of the polarization [Laurencin 2015], even if there is still a need of complete validation for this hypothesis.

### **I.3 Durability of SOCs**

Despite of their numerous advantages, the performance degradation of SOCs is still too high to envisage the industrial deployment of this technology [Irvine 2016, Sohal 2011]. Indeed, the voltage degradation rates are still in the range of  $\approx 0.5 - 3 \text{ \%}\cdot\text{kh}^{-1}$  in SOFC mode and between 0.6 and  $10 \text{ \%}\cdot\text{kh}^{-1}$  in SOEC operation at relatively low current densities ( $|i_{DC}| < 1 \text{ A}\cdot\text{cm}^{-2}$ ) [Skafta 2016]. These rather large degradation rates are caused by various aging phenomena activated by the high operating temperature and the polarization.

#### *I.3.1 Durability Results Reported in Literature*

To study the durability of SOCs, long-term tests are classically performed in which a cell or a stack is operated at constant current or potential and the evolution of the cell/stacks performances is measured over time. Typically, galvanostatic tests are carried out keeping a constant current density

and measuring the cell voltage over time. To obtain reliable information about the degradation phenomena occurring in a SOCs, the duration of these long-term tests is of central importance. Indeed, it has been recently pointed out that the degradation of SOCs could be strongly non-linear so that short-term degradation tests may be misleading [Fang 2018, 2019, Nguyen 2013].

In fuel cell mode, the durability experiments performed at the Forschungszentrum in Jülich are among the longest available in literature [Fang 2019]. After more than 100'000 hours of test, the authors have reported a degradation rate ranging from  $\approx 0.4 \text{ mV}\cdot\text{kh}^{-1}$  up to  $\approx 9 \text{ mV}\cdot\text{kh}^{-1}$  (with an average of  $0.5 \text{ }\%\cdot\text{kh}^{-1}$ ) operating a short-stack at  $0.5 \text{ A}\cdot\text{cm}^{-2}$  and  $700^\circ\text{C}$  (FU: 40%) [Fang 2019]. In general, the performance degradation in SOFC mode is reported in the range of  $0.5 - 3 \text{ }\%\cdot\text{kh}^{-1}$  [Blum 2016, 2020, Menzler 2018]. This rather low degradation rate remains too large with respect to target degradation rate of  $< 0.2 \text{ }\%\cdot\text{kh}^{-1}$  [DOE 2020].

In electrolysis mode, Schefold *et al.* have tested the durability of an hydrogen electrode supported cell and have reported a degradation rate of  $40 \text{ mV}\cdot\text{kh}^{-1}$  ( $3.8 \text{ }\%\cdot\text{kh}^{-1}$ ) after 9'300 hours of operation at  $-1 \text{ A}\cdot\text{cm}^{-2}$  and  $\approx 780^\circ\text{C}$  (SC: 36%) [Schefold 2012]. During the long-term test, several incidents occurred causing stepwise increases of the voltage and contributing to the high overall degradation rate. The same research group, has recently tested the durability of an electrolyte supported cell showing a voltage degradation of  $\approx 7.4 \text{ mV}\cdot\text{kh}^{-1}$  ( $\approx 0.6 \text{ }\%\cdot\text{kh}^{-1}$ ) after 20'000 hours of operation at  $-0.9 \text{ A}\cdot\text{cm}^{-2}$  and  $\approx 840^\circ\text{C}$  (SC: 51%) without major incidents [Schefold 2017]. Other authors have tested a short-stack containing two hydrogen electrode supported cells for more than 20'000 hours keeping the stack for  $\approx 16'000$  hours at  $-0.5 \text{ A}\cdot\text{cm}^{-2}$  and  $800^\circ\text{C}$  with a SC of 50% and observing an average degradation rate of  $\approx 6.5 \text{ mV}\cdot\text{kh}^{-1}$  ( $0.6 \text{ }\%\cdot\text{kh}^{-1}$ ) [Fang 2018, Frey 2018]. In literature, degradation rates from  $0.6$  to  $10 \text{ }\%\cdot\text{kh}^{-1}$  are reported for the operation in electrolysis mode at relatively low current densities [Brisse 2008, Ebbesen 2010, Fang 2015, Knibbe 2011, Nguyen 2013, Sun 2019, The 2015, Tietz 2013]. These degradation rates remain too high for the complete applicability of this technology. Indeed, for profitable application of SOCs for hydrogen production, electrolyzers are expected to work at high current densities to maximize the hydrogen production ( $|i_{\text{DC}}| > 1.2 \text{ A}\cdot\text{cm}^{-2}$ ) with target degradation rates limited to  $1 \text{ }\%\cdot\text{kh}^{-1}$  [FCH JU 2018]. In addition, the occurrence of incidents during operation can further limit the long-term behavior of the cells. In particular, steam starvation under current has been reported to cause re-oxidation of the Ni in the hydrogen electrode as well as the reduction of the zirconia in the electrolyte. Moreover, the volumetric change associated to the formation of NiO can favor the formation of cracks in the electrolyte and thus compromise the mechanical of the cell.

The higher degradation rate in electrolysis mode with respect to the fuel cell operation is confirmed by several experimental studies [Fang 2015, Frey 2018, Hubert 2017, 2018a, Laurencin 2017, Nguyen 2013, Trini 2020]. Similarly, it has been generally observed that the degradation rate would be accelerated operating the cell at high current densities (and overpotentials) [Chen 2013, Hagen 2006, Hauch 2006, Hoerlein 2018, Nguyen 2013]. Finally, it also appears that the fuel composition would play a role on the degradation, which is increased by a larger steam content [Hauch 2011b, Hoerlein 2018]. In contrast, the effects of the operating temperature are less clear with several authors reporting that the degradation rate would be lowered at high temperature [Fang 2015, Hagen 2006, Hauch 2006].

In conclusion, it can be stated that the influence of the operating parameters on the degradation remains not completely established. Nevertheless, it appears that the operation in electrolysis mode and at high current densities would accelerate the cells degradation. A detailed review of the most part of long-term tests for stacks and button cells experiments reported in literature can be found in [Blum 2020, Ploner 2017, Skafta 2016] for both operating modes.

### 1.3.2 Main Degradation Mechanisms

The degradation in performance is associated to morphological and chemical instabilities that are activated by the operating temperature and the polarization as schematically depicted in Figure I-6.

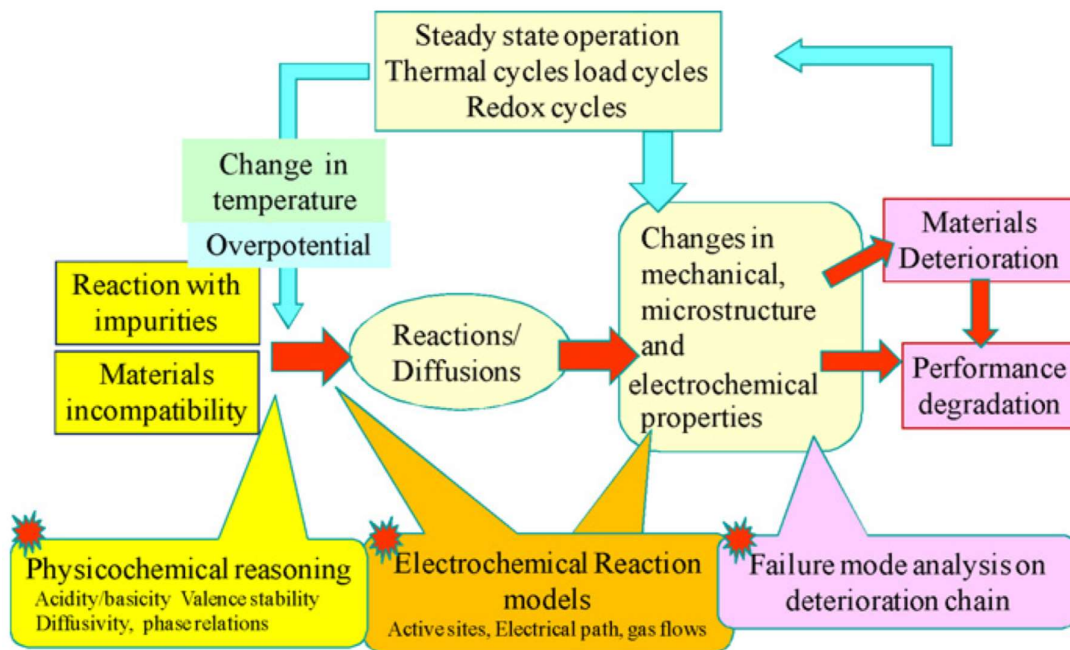


**Figure I-6: Schematic representation of the phenomena associated to the performances degradation in solid oxide cells (from [Yokokawa 2008]).**

These degradation mechanisms occur in each component of the stack. They can be summarized with mainly (i) the microstructural evolutions in the electrodes, (ii) the chemical instabilities of materials, (iii) the inter-diffusion of elements between the cell components, (iv) the electrode poisoning with ‘intrinsic’ or ‘extrinsic’ contaminants (impurities already present in the cell raw materials or coming from the environment such as Cr or Si, from interconnect plates or tubes and sealing), (v) oxidation of the metallic interconnect and (vi) mechanical damage [Chen 2016, Khan 2016, Moçoteguy 2013].

These phenomena can cause an increase in the ohmic or in the polarization resistances of the cell or stack and it appears that they can evolve differently according to the operating conditions. Furthermore, a decrease in the OCV is measured in case of severe damaging of the electrolyte (formation of micro-cracks), associated to the loss of tightness of the cell. Several degradation mechanisms have been proposed in literature and the main ones are discussed hereafter.

#### *1.3.2.1 Electrolyte Degradation*

*Phase transformation* – A decrease of the YSZ ionic conductivity has been reported in literature [Butz 2009, 2012, Kishimoto 2012b, Kondoh 1998, Shimonosono 2012]. This evolution has been ascribed to a modification of the crystalline phase of the doped-ZrO<sub>2</sub> from the cubic phase to the less conductive tetragonal or monoclinic phases [Shimonosono 2012]. To explain this phase transformation, it has been suggested that during the co-sintering of the hydrogen electrode with the YSZ electrolyte, nickel could dissolve in the electrolyte and subsequently the exsolution of Ni could induce the passage from the cubic to the tetragonal/monoclinic crystal [Kishimoto 2012b]. It can be noticed that the impact of this degradation mechanism has been reported to be quite limited after long-term tests [Liu 2012].

*Nano-porosities formation* – After long-term operation in SOEC mode, some authors have identified the presence on nano-porosities arising in the electrolyte in the vicinity of the oxygen electrode/electrolyte interface [Knibbe 2010b, Laurencin 2017, Rinaldi 2017a, The 2015, Tietz 2013]. It has been suggested that the chemical potential gradients for Zr<sup>4+</sup> and Y<sup>3+</sup> towards the interface with the barrier layer would promote the formation of these nano-porosities at the grain boundaries of the electrolyte [The 2015]. Alternatively, it has been recently proposed that these nano-pores may be originated from the loss of Zr<sup>4+</sup> associated to the formation of secondary phases at the oxygen electrode/electrolyte interface [Laurencin 2017]. However, the process related to the formation of these nano-porosities remains not completely established.

### 1.3.2.2 Oxygen Electrode Degradation

*Delamination* – The detachment of the oxygen electrode from the electrolyte remains an important degradation mechanism specifically for LSM-YSZ composite electrodes [Chen 2011, Knibbe 2011, Virkar 2010, Yokokawa 2008]. In literature it is reported that this phenomenon is favored in electrolysis mode and two main mechanisms have been proposed to explain it: On the one hand, it has been suggested that the formation of secondary phases at the interface would induce micro-cracks and eventually complete delamination [Chen 2011]. On the other hand, it has been proposed that an increase of internal oxygen pressure would occur in the electrolyte at the interface with the oxygen electrode during electrolysis operation, leading to the delamination [Virkar 2010]. Nevertheless, it can be pointed out that this type of degradation mechanism is quite specific for LSM-YSZ composite electrodes.

*Chromium poisoning* – Aside from the delamination, the poisoning of the oxygen electrode caused by the deposition of chromium coming from the interconnectors has also been reported to contribute significantly to the degradation [Blum 2020, Groß-Barsnick 2019, Jiang 2014, Liu 2010b, Schuler 2012]. Indeed, it has also been suggested that this phenomenon could represent a significant contribution to the overall degradation in stacks if not controlled using appropriate coatings [Blum 2020].

It has been shown that chromium would diffuse through the electrode *via* volatile species and deposit on the electrode surface forming insulating phases such as chromium oxide ( $\text{Cr}_2\text{O}_3$ ) [Liu 2010b]. Moreover, it has also been reported that the Cr could react with the strontium contained in the electrode material to form  $\text{SrCrO}_x$  reducing even more the electrode performances [Schuler 2012]. It appears that this phenomenon could be limited by using dry air in the gas flow as the formation of volatile chromium-based species would be favored by the presence of steam [Chen 2010].

*LSCF demixing and reactivity at the electrode/barrier layer/electrolyte interface* – It is well recognized that the release of strontium from the LSCF in the oxygen electrode coupled with the reactivity at the electrolyte interface are among the main contributions to the overall degradation of SOCs [Knibbe 2010b, Kostogloudis 2000, Liu 2014, Oh 2012, Tietz 2013]. It has been reported the demixing of the LSCF under operation would be associated to a passivation layer on the LSCF surface [Baqué 2017] and to the formation of insulation phases such as strontium zirconates ( $\text{SrZrO}_3$ ) at the barrier layer/electrolyte interface [Knibbe 2011, Morales 2017, The 2015]. Moreover, it has been recently pointed out that the oxygen electrode degradation could be significantly accelerated in electrolysis mode [Finsterbusch 2012, Laurencin 2017, Mahmoud 2017, Rinaldi 2017b]. Based on

this observation, it has been proposed that this behavior could be associated to the depletion of oxygen vacancies in the LSCF material due to the anodic polarization [Finsterbusch 2012, Laurencin 2017]. In particular, it has been suggested that the accumulation of oxygen in the LSCF under electrolysis current could be the driving force for Sr segregation and the formation of strontium oxide on the electrode surface [Laurencin 2017]. This should explain the formation of zirconates in the porosity of the GDC barrier layer and the precipitation of nano-porosities in the electrolyte, which have been observed to be strongly accelerated under electrolysis current. However, for a full validation of this mechanism there is not yet a direct and clear experimental evidence showing that the LSCF phase demixing is aggravated under electrolysis condition.

As introduced previously, to limit the reactivity between the LSCF and the YSZ, a GDC layer is added at the interface. As a consequence, an inter-diffusional layer (IDL) has been detected between the GDC and the YSZ [Szász 2018, Tsoga 2000] which is reported to have a lower ionic conductivity [Zhou 2004]. Nevertheless, the formation of  $\text{SrZrO}_3$  is still detected in aged [Endler 2010] and pristine cells [Ferreira-Sanchez 2017] especially in the porosities of the barrier layer [Matsui 2016]. Moreover, the effect of the IDL on the cell's performances and its evolution during operation are also unclear. It has been proposed that the IDL could be formed exclusively during sintering [Morales 2017, Xu 2019] and it could even act as a protective layer to prevent the formation of strontium zirconate [Szász 2018, Wankmüller 2017, Wilde 2018] whereas some other authors have suggested that the evolution in operation of the IDL could contribute to the increase of the Ohmic losses in SOCs [Matsui 2019, Shimura 2019].

### 1.3.2.3 Hydrogen Electrode Degradation

*Impurities segregation* – The presence of impurities has been reported to be a possible reason for the hydrogen electrode degradation [Ebbesen 2010, Hauch 2008, 2011a, Mogensen 2002]. Indeed, it has been shown that trace elements present in the gas stream can deposit in the active sites of the Ni-YSZ cermet hindering the electrochemical reactions [Ebbesen 2010, Mogensen 2002]. In addition, the deposition at the TPBs of silica ( $\text{SiO}_2$ ) contained in the glass sealing has also been reported [Hauch 2008]. Based on these observations, it can be stated that to limit the deposition of impurities a specific attention must be dedicated to the inlet gas cleaning [Ebbesen 2010] and to the pretreatment of the seal.

*Ni morphological evolution* – The Ni-YSZ cermet is subjected under operation to a Ni agglomeration resulting in a phase coarsening and a migration changing the Ni distribution in the electrode [De

Angelis 2018, Faes 2009, Fang 2018, Frey 2018, Hagen 2006, Hoerlein 2018, Hubert 2018a, Jiao 2011, Kennouche 2016a, 2016b, Lay-Grindler 2014, Lee 2014, Rinaldi 2017a, Tanasini 2009, Trini 2019, 2020].

The Ni agglomeration is characterized by an increase of the Ni mean particle diameter due to the sintering of the smallest particles. This phenomenon yields a loss of active TPBs [De Angelis 2018, Faes 2009, Lay-Grindler 2014] inducing a significant decrease in cell performance that could explain around 30% of the total cell degradation after 2'000 hours [Hubert 2018a]. It has been shown by several authors that this phenomenon is purely thermally activated and independent on the electrode polarization [Faes 2009, Hagen 2006, Hubert 2018a, Kennouche 2016b, Lee 2014]. Indeed, it has been proposed that Ni coarsening is ascribed to an Arrhenius-type Ostwald ripening process that could be associated to surface diffusion of Ni [Hubert 2018a]. However, the role of the electrode microstructure remains nowadays unclear. Indeed, it has been suggested that the YSZ backbone could limit the Ni coarsening [Faes 2009, Hubert 2018a, Jiang 2003]. This inhibiting effect of the YSZ network could be explained by the interfacial adhesion between Ni and YSZ that could stabilize the nickel and prevent a massive agglomeration at high temperature [Hubert 2018a].

In parallel to the agglomeration, a process of Ni migration has also been observed leading to change the Ni repartition within the electrode. This phenomenon is restricted to the electrode active layer where the electrochemical reactions take place. It is associated to a migration of Ni towards the bulk of the electrode and results in a significant Ni depletion at the electrolyte interface. The Ni depletion is accompanied by a loss of active TPBs that can induce a significant degradation of the electrode and cell performances. However, despite its critical importance, the contribution of Ni depletion on the electrode and cell degradation rates has never been quantified precisely.

In terms of operating conditions, Ni migration has been observed after aging in SOEC operation [Frey 2018, Hoerlein 2018, Mogensen 2017, Rinaldi 2017a, Trini 2020] and in SOFC mode [Hagen 2006, Hauch 2011a]. However, some experimental results suggest that the severity of the phenomenon could be aggravated under electrolysis conditions because of the high cathodic overpotential [Frey 2018, Nakajo 2020, Trini 2020]. In addition, it has been reported that the high steam partial pressures could accelerate the process [Chen 2012]. To date, the role of temperature or the initial cermet microstructure remains unclear and even contradictory with the statements observed for the Ni coarsening in the bulk. For instance, a fine microstructure in the active layer could help to mitigate the rate of Ni migration [Hauch 2016].

For all these reasons, the origin of Ni migration remains not completely understood. Nevertheless, it has been proposed that the mechanism is based on the formation of  $\text{Ni(OH)}_x$  gaseous species to take into account the role of high steam partial pressure [Hauch 2008, Holzer 2011, Jiao 2011]. Furthermore, in order to explain the depletion in the active layer observed especially in electrolysis mode, it has been proposed that Ni migration could be triggered by high cathodic overpotential [Mogensen 2017, Nakajo 2020, Trini 2020]. In particular, Trini *et al.* [Trini 2020] have recently analyzed the microstructural evolutions occurring in the Ni-8YSZ cermet after aging in SOFC and SOEC conditions (this work was carried out in parallel to this study). In their work, they have observed a clear Ni depletion from the electrode/electrolyte interface only for the cell aged in electrolysis mode. To explain this behavior, it has been proposed that the main driving force for the loss of nickel from the interface could be the gradient in Ni wettability arising between the electrode/electrolyte interface and the electrode bulk as a function of the local oxygen partial pressure. Based on this mechanism, the minimization of the free energy of the system would lead to the migration of Ni toward the bulk of the electrode in SOEC mode. The reverse should be obtained in SOFC mode. However, thanks to the significant lower overpotentials under anodic polarizations, the process could be very limited in SOFC condition. This behavior could explain why no Ni enrichment is observed at the electrolyte interface after operation in fuel cell mode. Nevertheless, in spite of these very recent studies, the mechanism triggering the Ni instability is still unclear.

### 1.3.3 Concluding Remarks

Based on this analysis of the degradation phenomena for SOCs operated in fuel cell or electrolysis mode it is clear that the performance losses are highly dependent on the operating conditions (such as local gas compositions, currents and overpotentials). As an example, the destabilization of the LSCF in the oxygen electrode appears to be linked to the local concentration of oxygens in the material which depends directly on the reaction mechanism of the electrode. Moreover, it has been proposed that the Ni depletion from the hydrogen electrode/electrolyte interface would be favored in electrolysis condition due to the local overpotential. Therefore, the knowledge of the detailed reaction mechanisms at the two electrodes is essential to understand the intrinsic causes of these degradation phenomena.

Among these reviewed degradation mechanisms, it is nowadays widely accepted [Frey 2018] that the two most impacting processes are the Ni morphological evolution in the hydrogen electrode and the chemical destabilization in the oxygen electrode coupled with the reactivity with the electrolyte.

Indeed, these mechanisms are suspected to contribute significantly to the degradation measured during SOCs operation. Furthermore, experimental and theoretical investigations have shown that the severity of these phenomena would be strongly aggravated by an operation in SOEC mode explaining the higher degradation rates measured for cells operated under electrolysis current.

#### **I.4 Conclusions of This Chapter: Objectives and Methodology of the Thesis**

In this chapter, the state-of-the-art of SOCs technology has been given. The operating principle as well as the typical architecture and the materials used in solid oxide cells have been described. Moreover, the evolution of the cell performances in operation has been discussed focusing on the irreversibilities that are generated in fuel cell and electrolysis mode. It has been also shown that the knowledge of the exact reaction mechanisms for the two electrodes remains an open question and represents a key objective to better understand the behavior of SOCs in operation.

In addition, the durability of solid oxide cells has been discussed highlighting the need to have long-term tests to better understand the loss of performances over time. The specific degradation mechanisms hindering the commercial attractiveness of this technology have been discussed for the various components of the cell. Moreover, it has been shown that the nature of these phenomena is strongly related to the detailed reaction mechanisms that control the local parameters (such as current density and overpotential). Therefore, a deep understanding of the oxidation/reduction reactions for the two electrodes represents a fundamental step in the analysis of the performance deterioration.

The analysis of the degradation mechanisms occurring in SOCs has revealed that the morphological evolutions of Ni in the hydrogen electrode and the destabilization of the oxygen electrode material are amongst the most important causes of the degradation. In addition, it appears that these phenomena could be activated in electrolysis mode whereas their severity could be limited during fuel cell operation. Furthermore, it can be noticed that the impact of the operating temperature and of the initial electrodes microstructures remains unclear.

Based on these premises, this thesis aims to study the morphological evolutions of nickel in the hydrogen electrode as a function of the initial microstructure of the cermet and the polarization. In addition, the destabilization of the LSCF-based oxygen electrode and the evolution of the IDL as a function of the operating conditions is analyzed and discussed.

With this objective, long-term tests have been carried out in electrolysis and fuel cell modes either directly or in collaboration with partners. The durability experiments have allowed to investigate the performances evolution as a function of the operating conditions. Specimens extracted from the aged and pristine cells have been characterized focusing on the nickel evolution in the cermet and on the chemical reactivity at the oxygen electrode/barrier layer/electrolyte interface. Furthermore, a micro-scale model describing the detailed reaction mechanism for the hydrogen electrode has been developed and validated, whereas the existing model for the oxygen electrode has been validated. These models have been used in a multi-scale modeling scheme to investigate the underlying mechanisms for the hydrogen and oxygen electrodes degradations.

## II. Durability Experiments and Post-Test Characterization Techniques

SOCs under operation are subjected to several degradation phenomena arising in the electrodes and in the electrolyte. As discussed in chapter I, the degradation in performances is dependent on many parameters such as the operating mode (i.e. fuel cell or electrolysis), the current density and the operating temperature. As mentioned in the introduction, the precise role of these operating conditions is not precisely understood yet. For example, it seems that the degradation under electrolysis current is more severe than in fuel cell mode, whereas the role of temperature is still unclear. Moreover, it appears that the degradation of SOC's could be strongly non-linear so that short-term degradation tests should be avoided [Fang 2018, 2019, Nguyen 2013, Schefold 2017]. Finally, it is also reminded that the electrode microstructures could play a key role, not only on the initial cell performances, but also on its stability.

In this context, different durability experiments using classical hydrogen electrode supported cells have been analyzed in the frame of this thesis. First, two durability experiments have been performed to investigate the influence of the operating temperature on the degradation. The two button cells have been aged for the same operating time ( $\approx 1'800$  hours) and in the same experimental conditions so that only the operating temperature was changed between the two tests. At the end of durability experiments, the cells performances have been measured in the same conditions to quantify the 'intrinsic' degradation in the two cases. To complement these two tests, three additional cells, which

were aged by partners, have also been studied. These cells present different hydrogen electrode microstructures and were operated in fuel cell or electrolysis mode with aging times ranging from 1'000 to 15'000 hours. Therefore, the effect of electrode microstructure, test duration and operating mode have been also analyzed in this work.

To better understand the phenomena underlying the degradation, specimens have been extracted from the aged and pristine cells and advanced post-mortem characterizations have been carried out to assess the evolution of the electrode microstructure upon operation and the chemical reactivity between the components. In particular, micro X-ray Diffraction ( $\mu$ XRD) and micro X-ray Fluorescence ( $\mu$ XRF) maps have been acquired focusing on the crystallographic modification of the oxygen electrodes and the chemical reactivity at the oxygen electrode/electrolyte interface. Moreover, X-ray nano-holotomography has been used to obtain 3D reconstructions of the hydrogen electrode to investigate the microstructural evolutions in the Ni-YSZ cermet.

In the first section of this chapter, the long-term tests performed at different operating temperatures are described and the results of the electrochemical characterizations are discussed. The second section is dedicated to the experimental results related to the cells aged by partners in fuel cell and electrolysis mode. Finally, in the last part of this chapter, the post-mortem techniques used to characterize the aged cells as well as the procedures to prepare the samples for post-test analyses are introduced.

## **II.1 Long-term Tests in Electrolysis Mode at Different Operating Temperature**

In the frame of this thesis, two long-term tests have been performed keeping the same aging conditions in terms of gas compositions and current densities, whereas the temperature has been varied between the two tests. These durability experiments have been carried out in order to investigate the influence of the operating temperature on the cell degradation. Indeed, as already mentioned in the first chapter, it has been reported in literature that the degradation would be lowered at high operating temperature [Fang 2015, Hagen 2006, Hauch 2006]. Nevertheless, as pointed out in [Badwal 2001, Hubert 2018] this statement appears to be contradictory with the thermal activation of the aging phenomena, such as the agglomeration of Nickel in the cermet [Hubert 2018a, Kröll 2017] that would aggravate the degradation at higher temperature.

Therefore, to establish the effect of temperature on the degradation and to discriminate between 'intrinsic' and apparent degradations, the two cells were aged for approximately the same time

( $\approx 1'800$  hours) at different temperatures. The tests were performed in galvanostatic mode keeping a constant current density and measuring the evolution of the cell voltage over the time. The electrochemical characterizations at the beginning and at the end of the test were performed in order to analyze the ‘intrinsic’ degradation as a function of the operating temperature as suggested in [Fang 2018, Hubert 2018, 2018a].

### II.1.1 Cell Description

It is worth noting that material and geometrical characteristics of all the cells analyzed in the frame of this thesis are summarized in Appendix A.

For these two long-term experiments, two cells coming from the same batch were used and are referred as *Cell-A1* and *Cell-A2* thereafter. In Figure II-1a, a schematic representation of the cells is given. They present a circular geometry with an active area of  $9.08 \text{ cm}^2$  and are composed of standard materials.

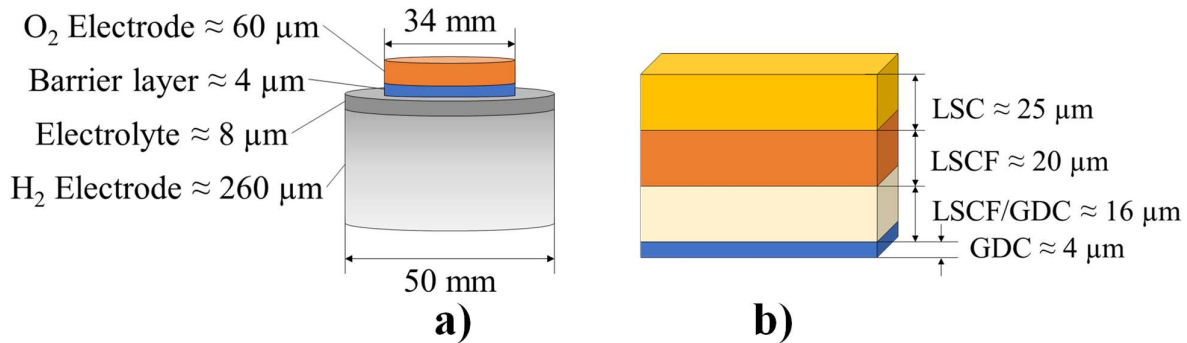


**Figure II-1: Schematic representation of the tested cells (*Cell-A1* and *Cell-A2*): a) Button cell geometry – b) Oxygen electrode architecture.**

A dense electrolyte made of Zirconia Stabilized with 8 %mol. of Ytria (8YSZ) having a thickness of  $\approx 8 \mu\text{m}$  is sandwiched between the two electrodes. The hydrogen electrode consists in a thick Ni-YSZ porous cermet that also serves as mechanical support ( $\approx 260 \mu\text{m}$ ). The oxygen electrode has a multilayer structure with a total thickness of  $\approx 60 \mu\text{m}$ . This assembly is composed of a LSCF ( $\text{La}_{0.6}\text{Sr}_{0.4}\text{Co}_{0.2}\text{Fe}_{0.8}\text{O}_{3-\delta}$ ) – GDC ( $\text{Gd}_{0.2}\text{Ce}_{0.8}\text{O}_{2-\delta}$ ) composite ( $\approx 16 \mu\text{m}$ ) associated to a LSCF layer ( $\approx 20 \mu\text{m}$ ) topped with a current collector made of Lanthanum Strontium Cobaltite ( $\text{La}_{0.5}\text{Sr}_{0.5}\text{CoO}_3$ , LSC) (cf. Figure II-1b). Finally, a barrier layer of GDC of  $\approx 4 \mu\text{m}$  is added between the oxygen electrode and the electrolyte to limit the reactivity between the two.

### II.1.2 Description of the Test Benches

The two cells (*Cell-A1* and *Cell-A2*) have been tested in two equivalent test benches that have been previously validated to ensure the relevance of the experimental results.

Both setups are equipped with an oxygen diffuser made of Crofer22APU which is positioned on top of the oxygen electrode. The oxygen diffuser serves also as current collector as can be seen from Figure II-2. To ensure a good electrical contact and a homogeneous flow path, a gold grid of 100 meshes·cm<sup>-2</sup> with a diameter of 34 mm was inserted between the diffuser and the oxygen electrode surface. A gold wire welded directly to the grid was used as a probe for the cell voltage measurement whereas the current was applied directly on the metallic tube supplying air (cf. Figure II-2). Finally, a total weight of 0.4 kg·cm<sup>-2</sup> (i.e. 3.6 kg) has been applied on the cell to minimize the contact resistances.

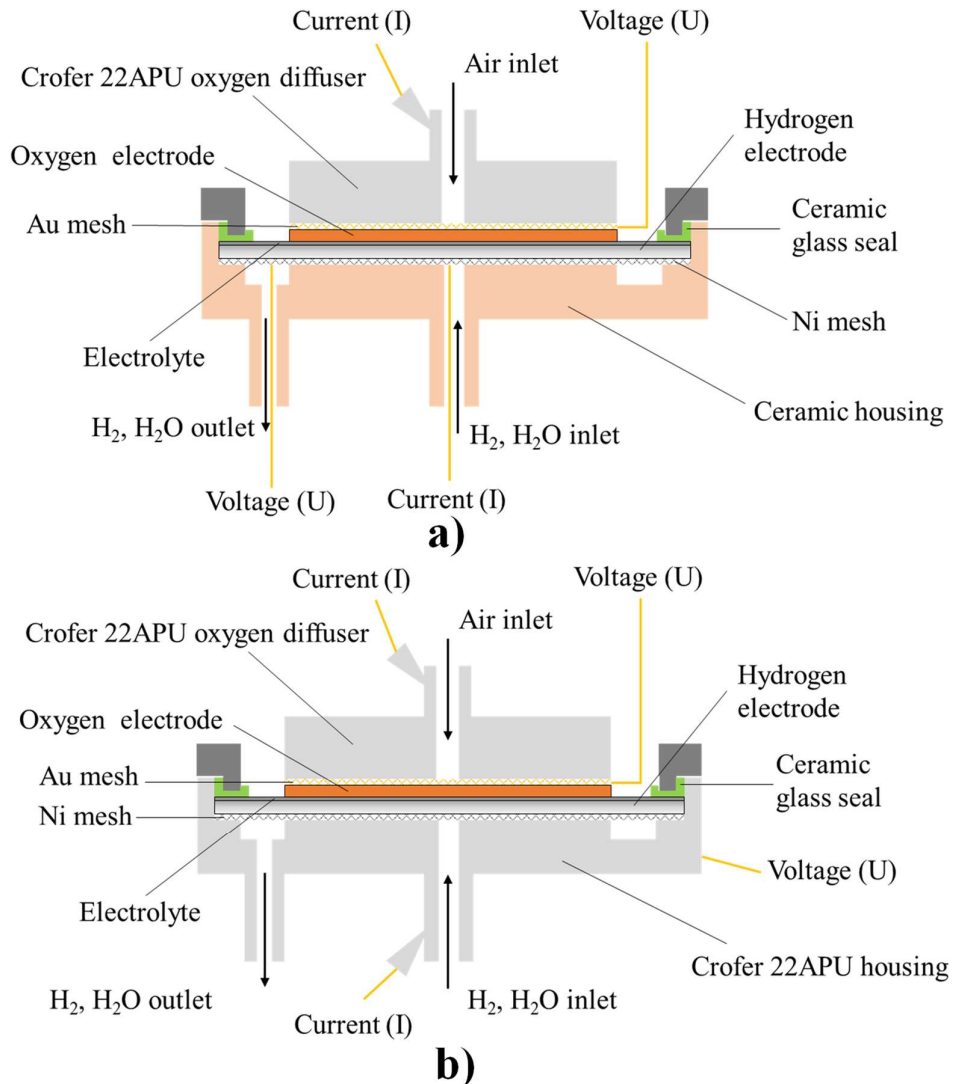


Figure II-2: Experimental setups: a) Ceramic housing – b) Metallic housing.

The two setups differ in terms of material used for the cell holder at the hydrogen side: In one case a ceramic material ( $\text{Al}_2\text{O}_3$ ) was utilized while in the other case the housing was made of Crofer22APU. In both setups, a Ni grid of  $100 \text{ meshes} \cdot \text{cm}^{-2}$  has been chosen as current collector in contact with the hydrogen electrode. For the ceramic housing, two wires have been welded to the Ni mesh to apply the current and measure the cell voltage (Figure II-2a). Whereas for the metallic housing the two measurements were performed welding the gold wires directly to the support in Crofer22APU (Figure II-2b).

In the two test benches, the gases are introduced from the center of the cell and distributed radially. On the oxygen electrode, the air flow was controlled using a Mass Flow Controller (MFC) while the outlet flow was evacuated directly in the furnace. On the hydrogen electrode two different ways to produce the steam were used. In the setup consisting in the ceramic housing, the steam was produced sending  $\text{H}_2$  and  $\text{O}_2$  through an oxy-combustion chamber in stoichiometric quantities to obtain the desired composition in terms of hydrogen and water. In the setup with the metallic housing, the steam was produced using a steam generator ( $T = 106\text{-}108^\circ\text{C}$ ,  $p = 1,3\text{-}1,4 \text{ bar}$ ). The steam was regulated downstream thanks to a modified MFC, allowing its operating temperature to be higher than  $100^\circ\text{C}$  (usually maximum temperature of MFC is  $60^\circ\text{C}$ ). A second mass flow controller was used for hydrogen, and the two fluxes were mixed in the inlet pipe before entering the chamber. In both test benches, all the tubes entering the hydrogen electrode were kept at  $\approx 130^\circ\text{C}$  to avoid any condensation. Finally, the outlet gas was sent to a heat exchanger to separate the water from the dry gas. To ensure the gas tightness between the two electrodes, a ceramic glass seal is applied at the periphery of the electrolyte in both test benches, guaranteeing a sealed fuel chamber.

It can be noticed that all the MFCs as well as the heating of the furnace were controlled by the supervision software RSView<sup>®</sup> which was also employed to save the data each 0.2 seconds. The temperatures were measured using K-type thermocouples positioned close to the tested cell (in one case in the cell housing, in the other in the fuel outlet tube). All the temperature variations were performed with a heating/cooling rate of  $\approx 1^\circ\text{C} \cdot \text{min}^{-1}$  to avoid any thermal damaging of the cells and the sealing.

### *II.1.3 Experimental Techniques*

The electrochemical behavior of both cells has been characterized using polarization curves (i-U curves) and Electrochemical Impedance Spectroscopy (EIS). These two methods are often used to

characterize SOCs but also other types of electrochemical devices [Bard 2001]. The first technique provides an overall information about the steady-state operation of the analyzed device, whereas the EIS allows obtaining its frequency response. The details of the two techniques are briefly reported hereafter.

### II.1.3.1 Polarization curves

For the polarization curve, the cell voltage is plotted as a function of the current density passing through the cell. As shortly described in chapter I, the  $i$ - $U$  curves allow obtaining the cell overpotentials for a stationary operation. From the  $i$ - $U$  curves, it is possible to draw the Area Specific Resistance (ASR,  $\Omega \cdot \text{cm}^2$ ) as a function of the current density defined using eq. (II-1).

$$ASR(i_{DC}) = abs\left(\frac{dU}{di}\right)_{i_{DC}} \quad (\text{II-1})$$

In which  $i_{DC}$  is the operating current density in  $\text{A} \cdot \text{cm}^{-2}$  and  $U$  is the cell voltage (V).

In this thesis, the  $i$ - $U$  curves have been measured in galvanostatic mode with a sweep rate of  $2.2 \text{ mA} \cdot \text{s}^{-1} \cdot \text{cm}^{-2}$  (i.e.  $20 \text{ mA} \cdot \text{s}^{-1}$ ) which represents a good compromise between sufficiently low scanning rate (to fulfill the steady-state condition) and fast enough data acquisition.

### II.1.3.2 Electrochemical Impedance Spectroscopy

The EIS method takes advantage of the fact that the phenomena occurring in a SOCs differ in their characteristic time constants and frequency responses [Huang 2007, Nechache 2014]. The EIS is based on the application of a small sinusoidal perturbation to the system and the measurement of the output signal which will have the same frequency ( $f$ ) but a phase shift ( $\varphi$ ) and a different amplitude with respect to the input. As an example, if a sinusoidal perturbation is superimposed to the stationary current, it is possible to express the input and the output of the system according to eq. (II-2).

$$i(t) = i_{DC} + i_{AC} \cdot \sin(2\pi ft) \text{ and } U(t) = U_{DC} + U_{AC} \cdot \sin(2\pi ft + \varphi) \quad (\text{II-2})$$

In which the subscript DC indicates the steady-state operating point and the subscript AC indicates the amplitude of the sinusoidal. If the absolute value of the perturbation is sufficiently low to maintain a linear response of the system, for each frequency of the input it is possible to determine the impedance of the cell ( $Z(f)$ ) which is defined as reported in eq. (II-3) taking advantage of the Euler's relation.

$$Z(f) = \frac{U(t)}{i(t)} = |Z| \exp(j\varphi) = Z_{real}(f) + j \cdot Z_{imag}(f) \quad (\text{II-3})$$

In which  $j$  is the imaginary unit.

Sweeping over different frequencies, it is possible to display the evolution of the impedance using the classical Nyquist and Bode plots as shown in Figure II-3a and Figure II-3b, respectively.

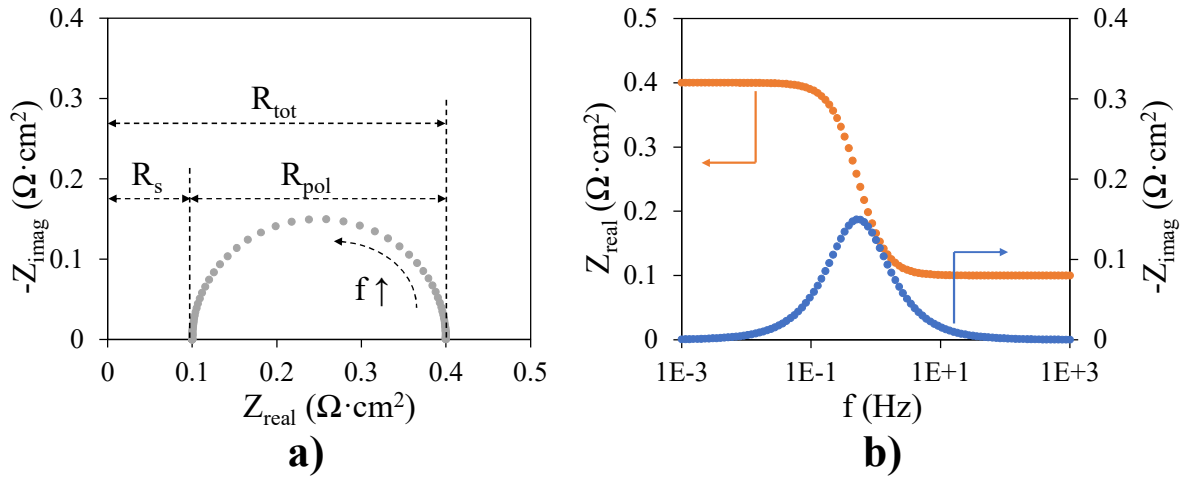


**Figure II-3: Classical representation of the impedance spectra: a) Nyquist plot – b) Bode plot of the real and imaginary part of the impedance.**

From the Nyquist plot, it is possible to identify the serial resistance ( $R_s$ ), the total resistance ( $R_{tot}$ ) and the polarization resistance ( $R_{pol}$ ) (cf. Figure II-3a). The first one is defined as the high frequency intercept of the Nyquist plot with the real axis and represents the Ohmic contribution to the cell resistance [Nechache 2016]. Similarly, the total electrode resistance is given by the intercept with the real axis at low frequency and corresponds to the steady-state resistance of the system (equivalent to the ASR). Finally, the polarization resistance is obtained by subtracting the serial resistance to the total resistance and represents a convolution of all the resistive processes occurring in the two electrodes [Montinaro 2014].

In this thesis, the impedance spectra at Open Circuit Voltage (OCV) and under polarization have been measured in the frequency range between  $10^{-2}$  and  $10^5$  Hz in galvanostatic mode with an amplitude of  $\pm 8 \text{ mA}\cdot\text{cm}^{-2}$  at OCV and of  $\pm 40 \text{ mA}\cdot\text{cm}^{-2}$  under polarization. In both cases, the amplitude of the sinusoidal current has been selected paying a specific attention to check the linearity condition and to optimize the signal-to-noise ratio.

It can be noticed that, since SOCs operate at high temperature, an inductive effect of the wires is measured at high frequencies modifying the shape of the impedance spectra and hindering the determination of the serial resistance [Caliandro 2019, Shin 2013]. To overcome this limitation, one classical approach is to fit the impedance spectra using an Equivalent Circuit Model (ECM) representative of the cell response (i.e. with an inductive contribution) and to re-simulate the

impedance without this inductive component [Caliandro 2019, Liu 2010a]. This methodology has been used in this thesis employing the software Zview to obtain the experimental serial and polarization resistances.

A similar ECM to the one reported in [Liu 2010a, Nechache 2016] has been employed (Figure II-4a). It consists of an inductance (L), that considers the contribution of the wires, an Ohmic resistance ( $R_s$ ), two Resistance-Capacitance elements (R-C) and two Resistance-Constant Phase Element groups (R-CPE). The two R-Cs are used to simulate the low-frequency contributions in the diagram whereas the R-CPEs represent the phenomena at medium/high frequencies. As an example, the application of this procedure to one of the impedance spectra measured at the beginning of the durability experiment is shown in Figure II-4.

As it can be seen in Figure II-4, it is possible with the selected ECM to fit accurately the shape and the frequency distribution of the experimental impedance spectrum. Therefore, this ECM can be used to decorrelate the contribution of the inductive elements by re-simulating the cell impedance without the artifact related to the L component (Figure II-4f and Figure II-4g).

#### II.1.4 Testing Protocols

The protocol of the two tests for *Cell-A1* and *Cell-A2* is summarized in Table II-I.

At the beginning of each test, the ceramic glass seal was solidified following the procedure reported in the manuscript of M. Hubert [Hubert 2018] with  $N_2$  sent to the hydrogen electrode and air to the oxygen electrode. Subsequently, the NiO in the cermet was reduced at 800°C progressively increasing the  $H_2$  content in the fuel flow until 100% was reached. Once the measured OCV was consistent with the fuel composition (at 800°C with  $\approx 100\%$   $H_2$  the expected OCV is  $\approx 1.2$  V in our testing conditions), the electrochemical characterization of the cells started.

As a first step of the test, the *i-U* curve at 800°C was measured in fuel cell mode sending 100%  $H_2$  at the hydrogen electrode. Ambient air was sent to the oxygen electrode and its flowrate was chosen in such a way to have an equivalent air utilization factor of 20% at  $|i_{DC}| = 0.75 \text{ A}\cdot\text{cm}^{-2}$  for the entire duration of the test. For the hydrogen side, a nominal flowrate of  $12 \text{ Nml}\cdot\text{min}^{-1}\cdot\text{cm}^{-2}$  was sent.

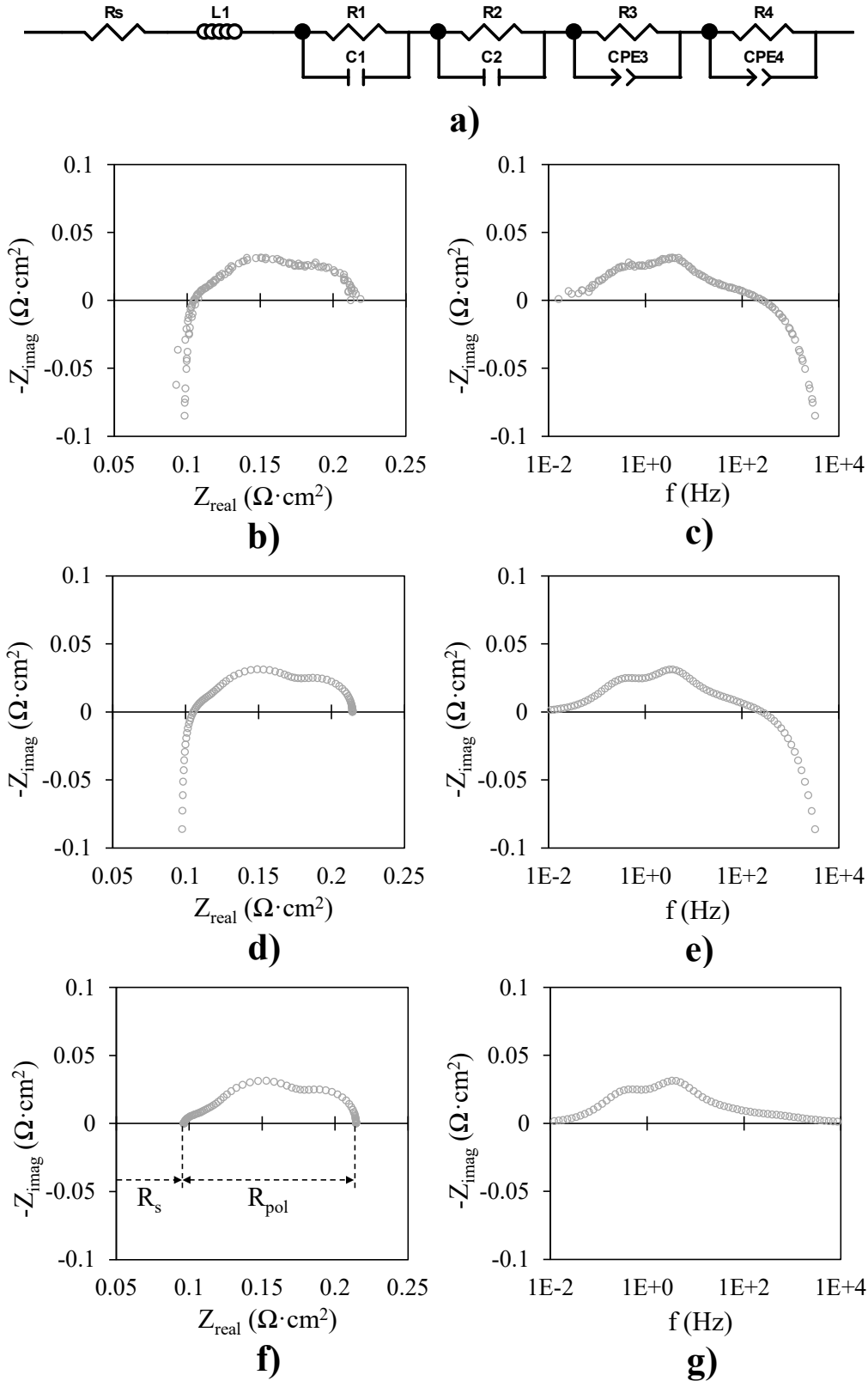


**Figure II-4: Illustration of the procedure for the determination of  $R_s$  and  $R_{pol}$  from the experimental EIS data: a) Equivalent Circuit Model used – Nyquist (b) and partial Bode (c) plots of the experimental data – Nyquist (d) and partial Bode (e) plots of the spectrum fitted with the inductive contribution – Nyquist (f) and partial Bode (g) plots of the simulated spectrum without the inductive contribution.**

**Table II-I: Summary of the experimental protocol for *Cell-A1* and *Cell-A2* (considering an active area for both cells of 9.08 cm<sup>2</sup>)**

	<i>Cell-A1</i> (ceramic housing)	<i>Cell-A2</i> (metallic housing)
Glass seal solidification	Protocol reported in [Hubert 2018]	
NiO reduction	T = 800°C oxygen side: air (Q <sub>air</sub> = 7.3 Nml·min <sup>-1</sup> ·cm <sup>-2</sup> ) hydrogen side: N <sub>2</sub> /H <sub>2</sub> ↑ %H <sub>2</sub> up to 100% (Q <sub>tot</sub> = 7.3 Nml·min <sup>-1</sup> ·cm <sup>-2</sup> )	
Initial characterization in SOFC mode (i-U curve)	T = 800°C oxygen side: air (Q <sub>air</sub> = 62 Nml·min <sup>-1</sup> ·cm <sup>-2</sup> ) hydrogen side: 100% H <sub>2</sub> (Q <sub>tot</sub> = 12 Nml·min <sup>-1</sup> ·cm <sup>-2</sup> )	
Initial characterization in SOEC mode (i-U curve, EIS at OCV and at i <sub>DC</sub> = -0.75 A·cm <sup>-2</sup> )	T = 850°C oxygen side: air (Q <sub>air</sub> = 62 Nml·min <sup>-1</sup> ·cm <sup>-2</sup> ) hydrogen side: H <sub>2</sub> O/H <sub>2</sub> = 90/10 vol.% (Q <sub>tot</sub> = 12 Nml·min <sup>-1</sup> ·cm <sup>-2</sup> )	
Durability experiment (Voltage evolution at i = -0.75 A·cm <sup>-2</sup> with SC ≈ 50%)	T = 850°C same gas flowrates same compositions	T = 750°C same gas flowrates same compositions
Final characterization in SOEC mode (i-U curve, EIS at OCV and at i <sub>DC</sub> = -0.75 A·cm <sup>-2</sup> )	T = 850°C oxygen side: air (Q <sub>air</sub> = 62 Nml·min <sup>-1</sup> ·cm <sup>-2</sup> ) hydrogen side: H <sub>2</sub> O/H <sub>2</sub> = 90/10 vol.% (Q <sub>tot</sub> = 12 Nml·min <sup>-1</sup> ·cm <sup>-2</sup> )	
Shutdown	oxygen side: air (Q <sub>air</sub> = 3.7 Nml·min <sup>-1</sup> ·cm <sup>-2</sup> ) hydrogen side: N <sub>2</sub> /H <sub>2</sub> = 97/3 vol.% (Q <sub>tot</sub> = 3.7 Nml·min <sup>-1</sup> ·cm <sup>-2</sup> )	

After this preliminary characterization, the temperature was increased to 850°C and the gas composition was changed to H<sub>2</sub>O/H<sub>2</sub> = 90/10 vol.% in the hydrogen side keeping the same total flowrates for both electrodes. Once the OCV was stabilized, the i-U curves in electrolysis mode, the EIS at OCV and the EIS at i<sub>DC</sub> = -0.75 A·cm<sup>-2</sup> have been measured.

Subsequently the two durability experiments have been conducted. For *Cell-A1*, the temperature was kept at 850°C and the current was set to -6.81 A (corresponding to -0.75 A·cm<sup>-2</sup>). For *Cell-A2*, instead, the temperature was lowered to 750°C keeping the cell at OCV. After the stabilization of the temperature and the OCV, the same current than *Cell-A1* was applied (-6.81 A).

It can be noticed that the operating current density of -0.75 A·cm<sup>-2</sup> was chosen in order to have a Steam Conversion (SC) of 50% during the aging period, considering the nominal flowrate of steam sent to the hydrogen electrode (10.8 Nml·min<sup>-1</sup>·cm<sup>-2</sup>). Subsequently, the two cells have been operated in galvanostatic mode for ≈ 1'800 hours and the evolution of the voltage in each experiment has been measured every 15 minutes.

Finally, at the end of the durability experiments, the two cells have been characterized again at 850°C performing the i-U curves in electrolysis mode, the EIS at OCV and the EIS at i<sub>DC</sub> = -0.75 A·cm<sup>-2</sup>. For *Cell-A2*, the heating from 750°C to 850°C was done keeping the cell at OCV.

All the electrochemical characterizations have been conducted using a potentiostat/galvanostat (Autolab PGSTAT-302N) equipped with a Frequency Response Analyzer module (FRA) and a 10 A current booster. All the experimental data have been collected using the NOVA software and analyzed using Zview.

When the final characterization was completed, the two furnaces were cooled down to room temperature. During this step, the gas flowrates for the two electrodes have been lowered to  $3.7 \text{ Nml}\cdot\text{min}^{-1}\cdot\text{cm}^{-2}$  by keeping an air sweeping condition for the oxygen electrode whereas a mixture of nitrogen and hydrogen with a  $\text{N}_2/\text{H}_2$  ratio of 97/3 vol.% was sent at the hydrogen electrode. Thanks to this shutdown procedure, the nickel of the cermets for the two cells was kept in its reduced state without any re-oxidation. Finally, the two cells were removed from the support by cutting the border with a diamond pen.

### II.1.5 Tests Results

In this paragraph the results of the durability tests of *Cell-A1* at  $850^\circ\text{C}$  and *Cell-A2* at  $750^\circ\text{C}$  are reported analyzing the initial performances of the two cells, the degradation curves and the performances at the end of the tests.

#### II.1.5.1 Performances in Fuel Cell Mode

To ensure the same starting point between the two durability experiments, it has been checked that the two cell presents the same initial performances. For this purpose, the i-U curves obtained in SOFC at  $800^\circ\text{C}$  after the reduction of the NiO in the cermet are compared in Figure II-5.

The two i-U curves are well superposed indicating that the two cells in the two experimental setups exhibit very similar performances (Figure II-5a and Figure II-5b). Moreover, in Figure II-5c the evolution of the ASR evaluated from the i-U curves using eq. (II-1) is also reported. The two curves show the same behavior confirming that the two experimental setups and cells are entirely comparable. It can be noticed that the slight oscillations observed at high current density are related to the sampling rate used to obtain the experimental curves, which influenced the evaluation of the derivative (eq. (II-1)). Finally, it can be noticed that the value of the OCV obtained in the two cases is very close to the theoretical one ( $\approx 1.2 \text{ V}$  at  $800^\circ\text{C}$  and  $\approx 100\%$  of  $\text{H}_2$ ) indicating that no gas leakage is present between one electrode and the other. After this preliminary characterization, the temperature was increased to  $850^\circ\text{C}$  and the performances in electrolysis mode have been measured for both cells.

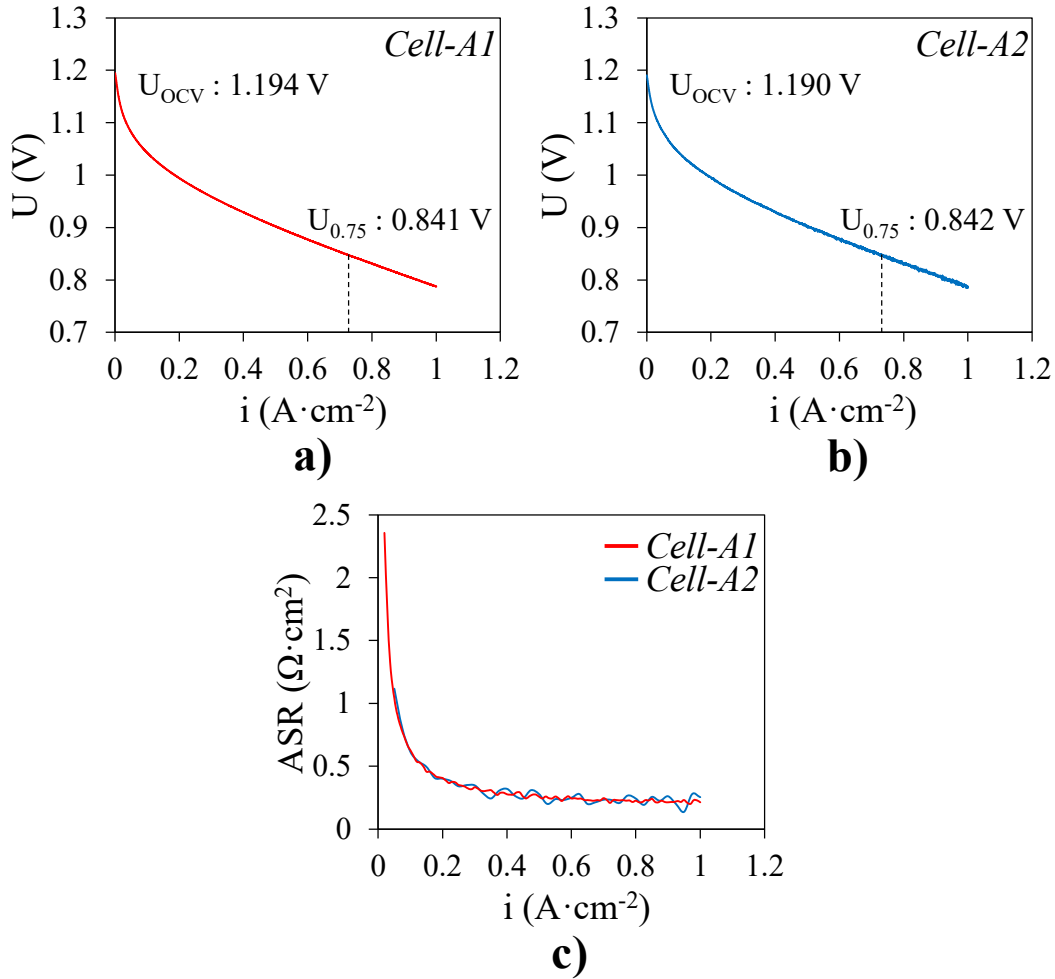


**Figure II-5: Comparison of the initial performances in SOFC mode at 800°C (with  $Q_{air} = 62 Nml \cdot min^{-1} \cdot cm^{-2}$  and  $Q_{H_2} = 12 Nml \cdot min^{-1} \cdot cm^{-2}$ ): a) *Cell-A1* – b) *Cell-A2* – c) ASR as a function of the current density for the two cells.**

### II.1.5.2 Comparison of the Initial Performances in SOEC Mode

In Figure II-6 the comparison of the  $i$ - $U$  curves measured in electrolysis mode and the EIS for the two cells at the beginning of the durability tests are reported.

From Figure II-6a, it can be noticed that the two cells exhibit similar behaviors in terms of polarization curves at 850°C with  $H_2O/H_2 = 90/10$  vol.%. In addition, the two cells present very similar values for OCV (0.807 V for *Cell-A1* and 0.805 for *Cell-A2*) while only a minor difference is found for the voltages at  $i_{DC} = -0.75 A \cdot cm^{-2}$  (cf. Table II-II,  $t = 0$  hours). Analyzing the polarization curves in Figure II-6a, it can be noticed that *Cell-A2* presents slightly better performances (at  $i_{DC} = -0.75 A \cdot cm^{-2}$ ,  $U_{Cell-A2}$  is  $\approx 2\%$  lower than  $U_{Cell-A1}$ ). To analyze this difference the experimental EIS have been collected for both cells at OCV and at  $i_{DC} = -0.75 A \cdot cm^{-2}$ .

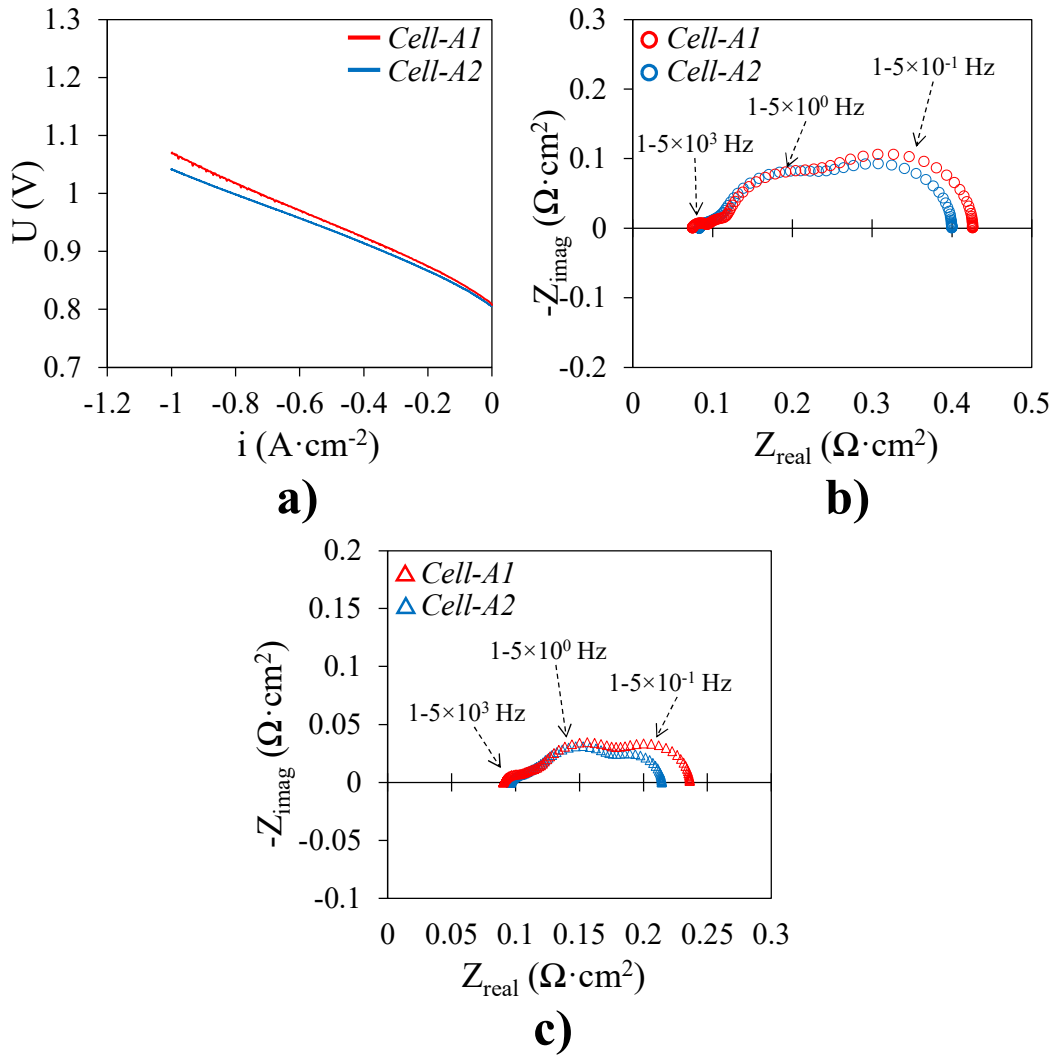


**Figure II-6: Initial performances in SOEC mode for *Cell-A1* and *Cell-A2* with  $\text{H}_2\text{O}/\text{H}_2 = 90/10$  vol.% and  $T = 850^\circ\text{C}$  ( $Q_{\text{air}} = 62 \text{ Nml}\cdot\text{min}^{-1}\cdot\text{cm}^{-2}$  and  $Q_{\text{fuel}} = 12 \text{ Nml}\cdot\text{min}^{-1}\cdot\text{cm}^{-2}$ ): a)  $i$ - $U$  curves – b) EIS at OCV – c) EIS at  $i = -0.75 \text{ A}\cdot\text{cm}^{-2}$ .**

The impedance spectra have been treated as described in section II.1.3.2 to remove the inductance (cf. Figure II-4). From the analysis of the diagrams at OCV (Figure II-6b) and at  $i_{\text{DC}} = -0.75 \text{ A}\cdot\text{cm}^{-2}$  (Figure II-6c), the difference in the performances between the two cells could be attributed to the low-frequency processes. Indeed, the response at high and medium frequencies appears to be well superposed between the two cells, and only the contribution at low frequencies ( $< 1 \text{ Hz}$ ) is slightly larger for *Cell-A1* at OCV and under polarization. This phenomenon may be attributed to the gas diffusion in the electrodes [Caliandro 2019, Leonide 2008] that could be associated to some minor differences in the electrodes microstructures. Nevertheless, it can be pointed out that the two cells present very similar performances at the beginning of the durability experiments.

**Table II-II: Evolution of cell voltage measured from the i-U curves and resistances obtained from the EIS for *Cell-A1* and *Cell-A2* at 850°C and  $i_{DC} = -0.75 \text{ A}\cdot\text{cm}^{-2}$  (with  $\text{H}_2\text{O}/\text{H}_2 = 90/10 \text{ vol.}\%$ )**

		t = 0 hours	t ≈ 1'800 hours	$\Delta$ ( $\text{mV}\cdot\text{kh}^{-1}$ ) or ( $\text{m}\Omega\cdot\text{cm}^2\cdot\text{kh}^{-1}$ )	% $\Delta$ (%initial $\cdot\text{kh}^{-1}$ )
U at $i_{DC} = -0.75 \text{ A}\cdot\text{cm}^{-2}$ (V)	<i>Cell-A1</i>	1.005	1.031	≈ 14	1.4%
	<i>Cell-A2</i>	0.988	1.021	≈ 18	1.8%
$R_s$ ( $\text{m}\Omega\cdot\text{cm}^2$ )	<i>Cell-A1</i>	90	117	15	17%
	<i>Cell-A2</i>	96.2	112	9	9%
$R_{tot}$ ( $\text{m}\Omega\cdot\text{cm}^2$ )	<i>Cell-A1</i>	236	295	33	14%
	<i>Cell-A2</i>	214	280	37	17%

### II.1.5.3 Durability Results

After the characterization of the two cells in electrolysis mode, the durability experiments were started by keeping *Cell-A1* at 850°C and lowering the operating temperature of *Cell-A2* to 750°C. In Figure II-7 the degradation curves are reported, in which the evolution of the cell voltage (at  $-0.75 \text{ A}\cdot\text{cm}^{-2}$ ) is plotted as a function of the aging time. It can be noticed that the evolution of the curves is significantly less noisy for *Cell-A2*, aged in the metallic test bench in which the steam was produced using a steam generator. This indicates that this technique allows stable operations with very small fluctuations in the steam flow with respect to other solutions (such as the oxy-combustion of  $\text{H}_2$  or the use of a bubbler).

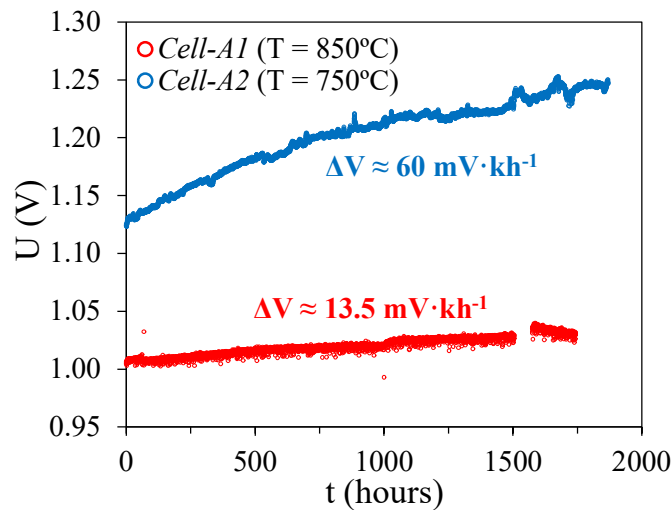


**Figure II-7: Degradation curves for the two cells aged in electrolysis mode with  $\text{H}_2\text{O}/\text{H}_2 = 90/10 \text{ vol.}\%$  at  $i_{DC} = -0.75 \text{ A}\cdot\text{cm}^{-2}$  (corresponding to a SC of 50%).**

As it can be seen from Figure II-7, the ‘apparent’ degradation measured as the slope of the durability curves ( $U=f(t)$ ) is significantly higher for *Cell-A2* aged at 750°C with an overall degradation rate of

$\approx 60 \text{ mV}\cdot\text{kh}^{-1}$ . In addition, it appears that the degradation rate for this test follows two slightly different trends in the first 500 hours and for  $t > 500$  hours. This confirms that extrapolating the degradation rate from short durability experiments could be misleading as suggest by [Fang 2019, Nguyen 2013].

On the other hand, the ‘apparent’ degradation rate of *Cell-A1* at  $850^\circ\text{C}$  is substantially lower ( $\approx 13.5 \text{ mV}\cdot\text{kh}^{-1}$ ). Moreover, the degradation rate in this case appears to be more linear along the entire duration of the test. It can be pointed out that after  $\approx 1'500$  hours of operation a problem with the electrical power supply of the test bench has caused the temporary interruption of the degradation test for approximately 100 hours. Nevertheless, it can be noticed that when the test was restarted, after a stabilization period, the cell performances were in the same range as during the first 1'500 hours of aging.

From the comparison between the two durability curves it appears that the degradation of *Cell-A2* (aged at lower operating temperature) would be substantially higher than that of *Cell-A1* tested at higher temperature. Nevertheless, in order to evaluate the ‘intrinsic’ degradation in the two cases it is necessary to compare the performances at the end of each test in the same experimental conditions. Indeed, independently of the aging conditions, the degradation rates have to be measured using a reference condition of temperature, current density and gas feeding as pointed out by M. Hubert [Hubert 2018]. With this method, all the internal voltage loss affected by the aging can be directly compared to each other and a ‘true’ or ‘intrinsic’ degradation rate can be measured in the reference condition chosen for the evaluation.

#### *II.1.5.4 Comparison of the Performances at the End of the Test in SOEC Mode*

After the durability experiments, the two cells have been characterized at  $850^\circ\text{C}$  to verify the evolution of the ‘intrinsic’ degradation in the two cases (Figure II-8). To investigate these evolutions, the cell voltages and the resistances obtained from the EIS under polarization at the same operating point (i.e.  $-0.75 \text{ A}\cdot\text{cm}^{-2}$ ) measured at the beginning and at the end of the durability experiments are given in Table II-II for the two tests.

Interestingly, the comparison of the polarization curves for *Cell-A1* and *Cell-A2* indicates that the difference in the ‘intrinsic’ degradation rates is much less pronounced than what the analysis of the durability curves has suggested. Indeed, when operating the two cells in the same conditions at the end of the tests, the two curves are almost superposed (Figure II-8a). This is confirmed by the degradation rates, obtained from the *i-U* curves measured in the same conditions, reported in Table

II-II ( $\approx 14 \text{ mV}\cdot\text{kh}^{-1}$  for *Cell-A1* vs  $\approx 18 \text{ mV}\cdot\text{kh}^{-1}$  for *Cell-A2*) reinforcing the statement that the ‘true’ degradation for the two tests is quite similar. These results are consistent with those reported by Fang *et al.* who have found a higher measured degradation rates at lower temperature but comparable ASR degradations operating a short-shack at  $700^\circ\text{C}$ ,  $750^\circ\text{C}$  and  $800^\circ\text{C}$  [Fang 2018]. Only a minor difference can be noticed with the performances of *Cell-A1* slightly worse than those of *Cell-A2* consistently with the difference in the initial *i-U* curves (Figure II-8a).

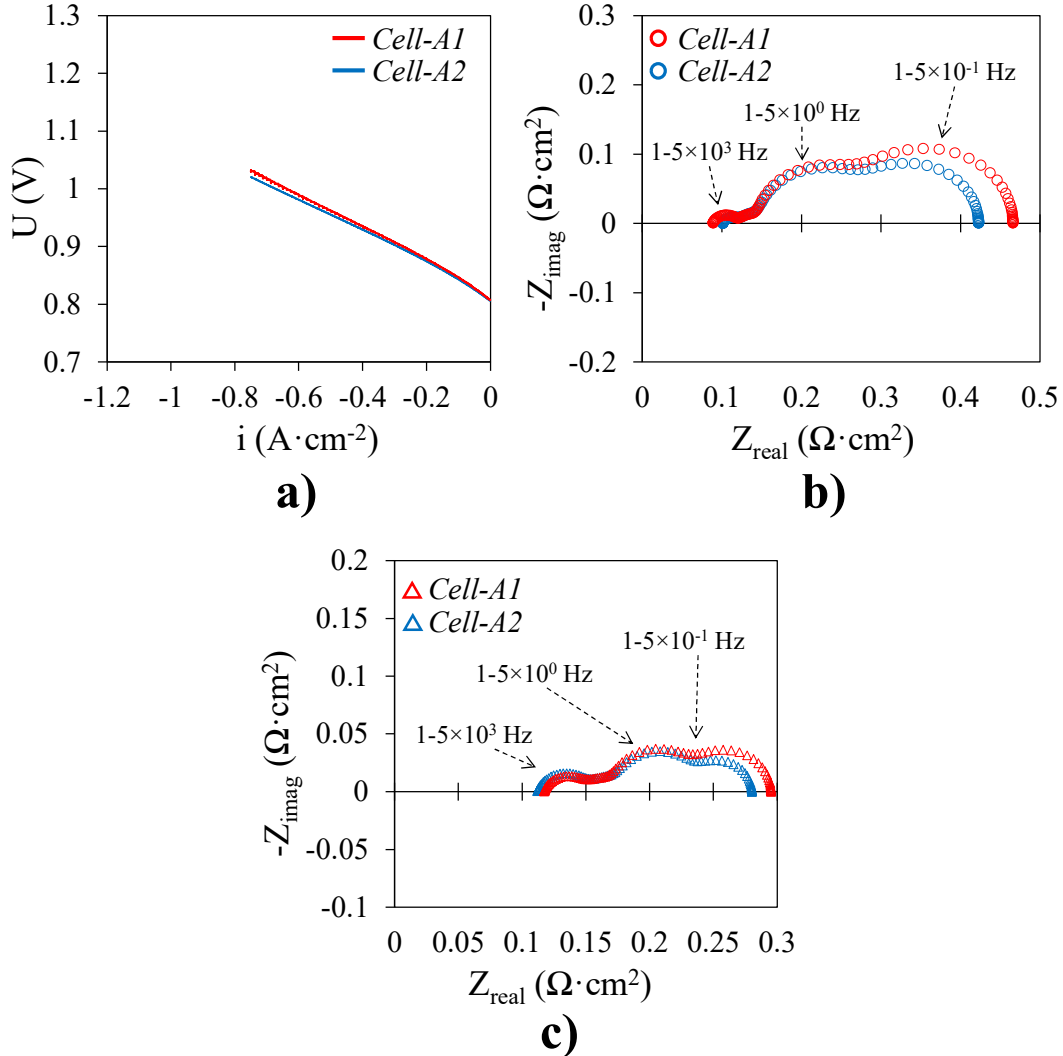


**Figure II-8:** Final performances in SOEC mode for *Cell-A1* and *Cell-A2* with  $\text{H}_2\text{O}/\text{H}_2 = 90/10$  vol.% and  $T = 850^\circ\text{C}$  ( $Q_{\text{air}} = 62 \text{ Nml}\cdot\text{min}^{-1}\cdot\text{cm}^{-2}$  and  $Q_{\text{fuel}} = 12 \text{ Nml}\cdot\text{min}^{-1}\cdot\text{cm}^{-2}$ ): a) *i-U* curves – b) EIS at OCV – c) EIS at  $i_{\text{DC}} = -0.75 \text{ A}\cdot\text{cm}^{-2}$ .

From the analysis of the EIS at OCV (Figure II-8b) and under polarization (Figure II-8c) it can be seen that the most impacted contributions to the impedance diagrams are the serial resistances and the high frequency arc ( $> 10^3 \text{ Hz}$ ). This statement is also confirmed by the comparison of the EIS obtained at  $i_{\text{DC}} = -0.75 \text{ A}\cdot\text{cm}^{-2}$  at the beginning and at the end of each test (Figure II-9). A noticeable

increase in the serial resistance can be detected as reported in the Table II-II. Moreover, this increase is higher for the cell aged at 850°C (*Cell-A1*) than the one aged at 750°C (*Cell-A2*). Besides, it is also clear that the convoluted semi-circle at high frequencies is increased after both durability experiments. Nevertheless, it is worth noting that the resistance associated to this contribution cannot be precisely drawn from the ECM fitting as it is strongly convoluted with the second semi-circle at intermediate frequencies. Therefore, its relative evolution and comparison between the two tests cannot be reasonably obtained here.

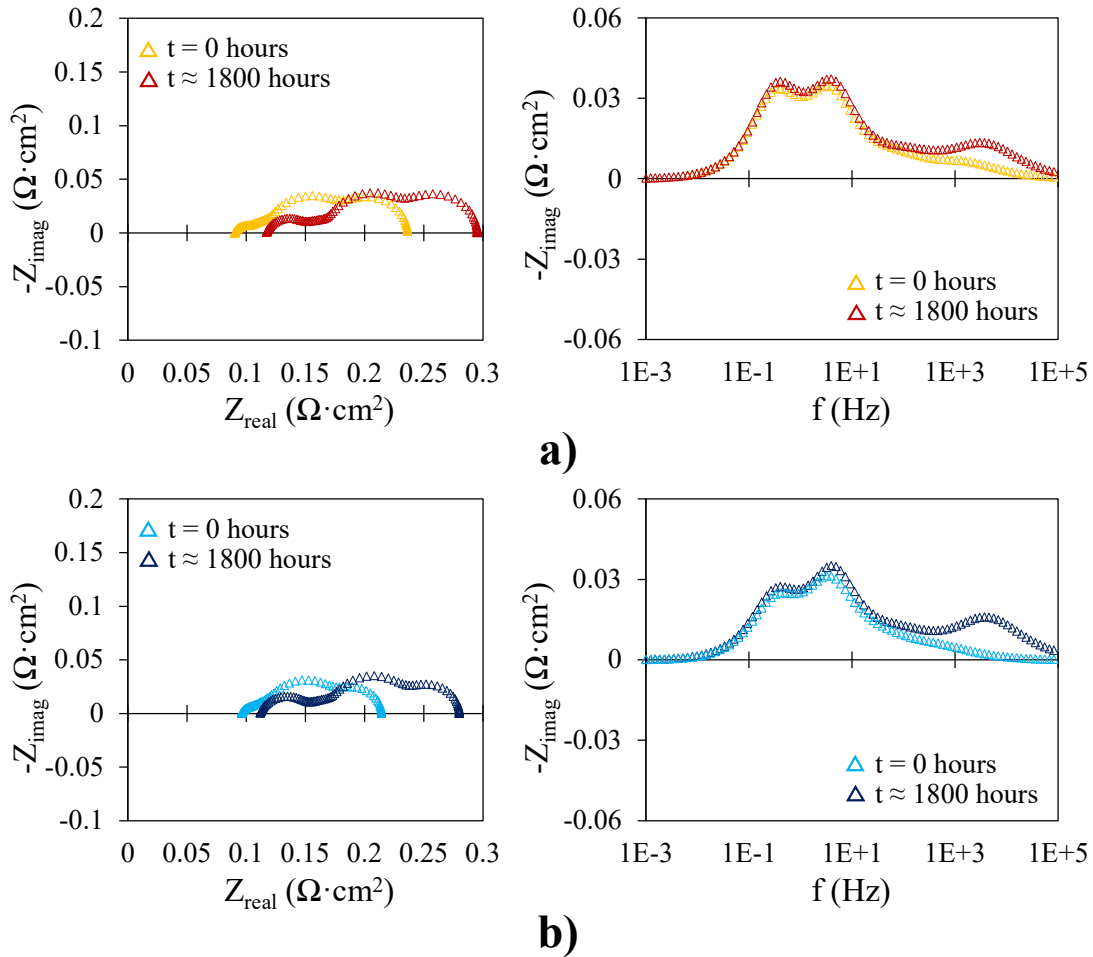


**Figure II-9: Comparison between the EIS acquired under polarization ( $i_{DC} = -0.75 \text{ A} \cdot \text{cm}^{-2}$ ) at the beginning and at the end of the two long term tests with  $\text{H}_2\text{O}/\text{H}_2 = 90/10 \text{ vol.}\%$  and  $T = 850^\circ\text{C}$  ( $Q_{air} = 62 \text{ Nml} \cdot \text{min}^{-1} \cdot \text{cm}^{-2}$  and  $Q_{fuel} = 12 \text{ Nml} \cdot \text{min}^{-1} \cdot \text{cm}^{-2}$ ): a) Nyquist and partial Bode plots for *Cell-A1* – b) Nyquist and partial Bode plots for *Cell-A2*.**

The increase in the  $R_s$  indicates an evolution of the Ohmic resistance of the cells. This deterioration of the Ohmic resistance is a general trend, which is usually observed for cells tested in electrolysis condition [Fang 2015]. As discussed in the introduction, this degradation may originate from different phenomena. It could be mainly ascribed to either a full Ni depletion at the  $\text{H}_2$  electrode or an evolution of the inter-diffusional layer at the oxygen electrode/electrolyte interface. In good consistency with

the work of M. Hubert *et al.* [Hubert 2018a], which was performed on the same type of cells, and with the post-test characterization of *Cell-A3* and *Cell-A4* (cf. chapter IV), some Scanning Electron Microscopy (SEM) observations have revealed that there is no complete depletion of nickel at the hydrogen electrode/electrolyte interface after the test. This result would indicate that the increase in the Ohmic resistance could be mainly due to an evolution of the inter-diffusional layer during aging in electrolysis mode (cf. chapter V).

On the other hand, as shown in the third chapter dedicated the electrodes kinetics, the high-frequency contribution at around  $2\text{-}5 \times 10^3$  Hz must be ascribed to the charge transfer reaction occurring in the hydrogen electrode [Caliandro 2019, Montinaro 2014, Nechache 2016]. Without a significant Ni depletion for this particular type of cell, this evolution can thus be associated to the degradation phenomenon of Ni agglomeration detailed in chapter IV.

Based on these results it can be said that the voltage evolution measured on the durability curves could be misleading for the determination of the intrinsic degradation of the cells. Indeed, in our experimental conditions, the intrinsic degradation appear to be very similar between the two long-term tests whereas the apparent degradation is significantly larger at lower temperature. Moreover, it has been clearly established that a part of the degradation is explained by a significant increase of the ohmic resistance. This degradation seems to be aggravated at high temperatures and it could be ascribed to an evolution of the inter-diffusional layer in relation with the deterioration of the oxygen electrode. To investigate this possibility, the oxygen electrode and the electrolyte of these two cells have been characterized by local  $\mu$ XRD and the local  $\mu$ XRF. The results of these characterizations are reported in chapter V.

## **II.2 Long-term Tests in Collaboration with External Partners**

In parallel to the long-term tests described in the previous section, two other cells (*Cell-A3* and *Cell-A4*) coming from the same manufacturer and tested by partners have been characterized after durability experiments in fuel cell and electrolysis modes. In addition, a last cell, prepared and tested in electrolysis mode at CEA by the group lead by J. Vulliet (*Cell-B*) has also been analyzed. These two types of cells (*Cell-A* and *Cell-B*) present different cermet microstructures (cf. Appendix A) and the cells were tested with aging times ranging from 1'000 to 15'000 hours. In this section, the description of the cells is given as well as the results of the durability experiments.

## II.2.1 Cells Description

The two cells, *Cell-A3* and *Cell-A4*, present the same type of electrolyte and hydrogen electrode as *Cell-A1* and *Cell-A2* consisting in a dense electrolyte in 8YSZ ( $\approx 8 \mu\text{m}$ ) and a porous Ni-YSZ cermet hydrogen electrode ( $\approx 260 \mu\text{m}$ ). For the thin oxygen electrode, two variants are considered: On the one hand, the oxygen electrode of *Cell-A3* presents the same multilayer structure as the two cells described in the previous section (*Cell-A1* and *Cell-A2*). On the other hand, *Cell-A4* presents an oxygen electrode constituted by a single layer in LSC ( $\approx 75 \mu\text{m}$ ) and a barrier layer of GDC ( $\approx 4 \mu\text{m}$ ). Both cells are rectangular as shown in Figure II-10a with an active surface area of  $\approx 70 \text{ cm}^2$  and  $48 \text{ cm}^2$ , for *Cell-A3* and *Cell-A4* respectively. Moreover, the oxygen electrode of *Cell-A3* is segmented in 20 sectors as depicted in Figure II-10b with the external sectors of  $3.17 \text{ cm}^2$  and the central ones of  $3.79 \text{ cm}^2$ . Three samples have been taken at the inlet, center and outlet of this segmented cell for characterization (Figure II-10b). Although their oxygen electrodes are different, it is worth noting that the cermets of *Cell-A1*, *Cell A2*, *Cell-A3* on the one hand, and *Cell-A4* on the other hand have been produced by using the same manufacturing protocol and are almost identical in terms of composition and microstructure.

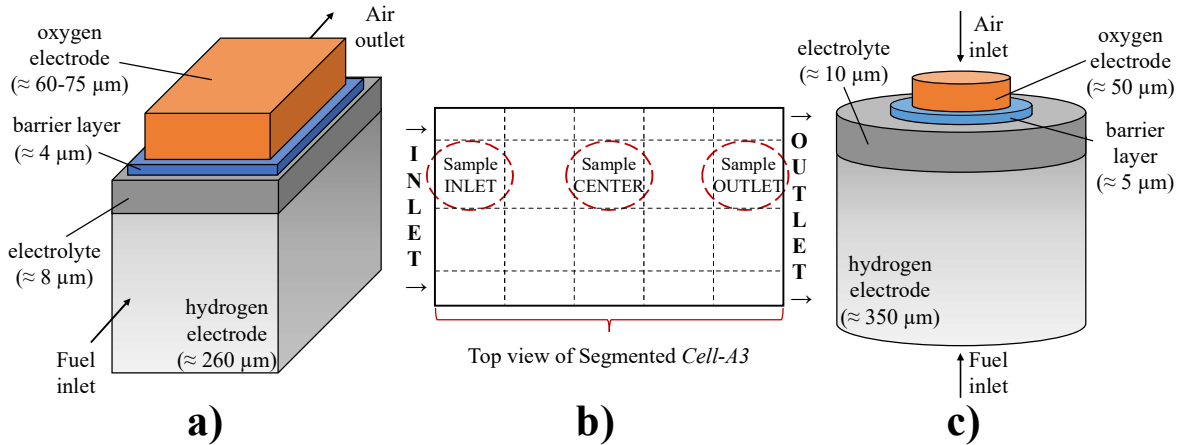


**Figure II-10: Schematic description of the cells coming from partners: a) Dimensions and configuration of *Cell-A3* and *Cell-A4* – b) Illustration of the sectors for *Cell-A3* – c) Dimensions and configuration of *Cell-B*.**

The other type of cell (*Cell-B*) is a circular button cell with an active area of  $3.14 \text{ cm}^2$  (Figure II-10c). In this case, the porous hydrogen electrode is a Ni-8YSZ cermet that serves as mechanical support ( $\approx 350 \mu\text{m}$ ) while the electrolyte is made of 8YSZ ( $\approx 10 \mu\text{m}$ ). The oxygen electrode is a single layer of porous LSCF with a thickness of  $\approx 50 \mu\text{m}$ . It can be noticed that also for *Cell-B*, a barrier layer of GDC ( $\approx 5 \mu\text{m}$ ) is added between the oxygen electrode and the electrolyte in order to limit their reactivity. Finally, aside from the oxygen electrode, it is worth noting that *Cell-B* differs from *Cell-A* with a coarser Ni-YSZ cermet microstructure (as it is presented and analyzed in detail in chapter IV).

## II.2.2 Durability Tests

The segmented cell (*Cell-A3*) was aged for 15'000 hours in fuel cell mode at an operating temperature of 780°C. A nominal flowrate of  $\approx 7 \text{ Nml}\cdot\text{min}^{-1}\cdot\text{cm}^{-2}$  composed of diluted hydrogen was used to supply the hydrogen electrode ( $\text{H}_2/\text{N}_2 = 60/40 \text{ vol.}\%$ ), while ambient air was sent to the oxygen electrode (flowrate  $\approx 110 \text{ Nml}\cdot\text{min}^{-1}\cdot\text{cm}^{-2}$ ). During the durability experiment, the cell was kept at OCV or operated in potentiostatic mode. The test was conducted in a specific setup with a longitudinal co-flow configuration similar to the one reported by Wuillemin *et al.* [Wuillemin 2008]. In this setup, the different sectors of the oxygen electrode have been connected to a metallic plate presenting the same segmentation. The insulation between the different metallic sectors has been obtained using a non-conductive glue to avoid their electrical contact. In this way, the local voltages and current densities for each sector of *Cell-A3* have been measured independently and their evolution has been recorded. In the frame of this thesis, three samples coming from the inlet, the center and the outlet of the cell have been analyzed (cf. Figure II-10b). For these three segments, the evolution of voltages and current densities during the aging test are shown in Figure II-11a and Figure II-11b, respectively.

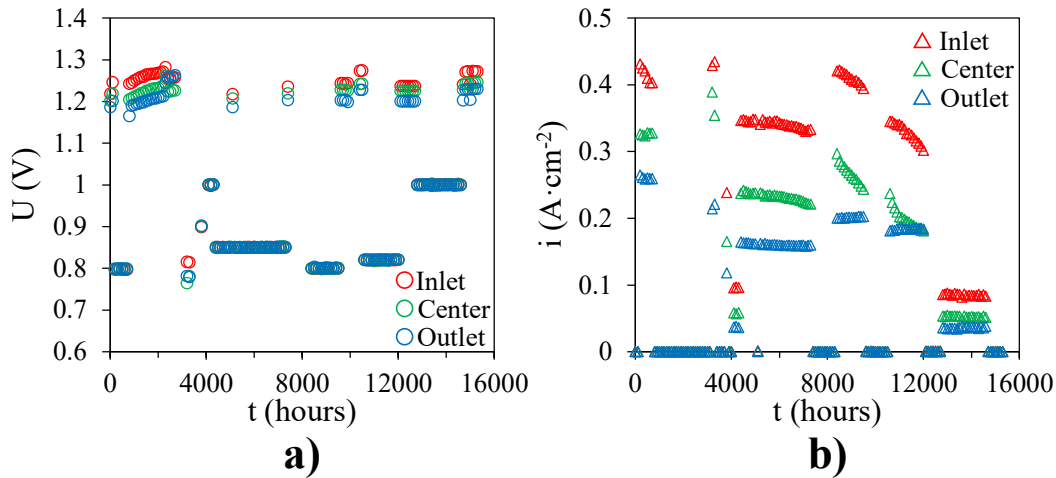


**Figure II-11: Experimental results for *Cell-A3* aged in fuel cell mode for 15'000 hour with  $\text{H}_2/\text{N}_2 = 60/40 \text{ vol.}\%$  and  $T = 780^\circ\text{C}$  ( $Q_{\text{air}} = 110 \text{ Nml}\cdot\text{min}^{-1}\cdot\text{cm}^{-2}$  and  $Q_{\text{fuel}} = 7 \text{ Nml}\cdot\text{min}^{-1}\cdot\text{cm}^{-2}$ ): a) Local voltages and b) Local current densities as a function of time for the three segments analyzed.**

As expected, a higher current density is measured at the inlet of the cell, related to the higher concentration of hydrogen. Moreover, the evolution of the local currents during the experiment is quite limited indicating a good stability of the cell. The degradation of the cell was also measured analyzing the evolution of global ASR at a current density of  $\approx 0.25 \text{ A}\cdot\text{cm}^{-2}$  corresponding to a fuel utilization (FU) of  $\approx 40\%$ . An overall increase of  $\approx 130 \text{ m}\Omega\cdot\text{cm}^2$  (i.e.  $\approx 9 \text{ m}\Omega\cdot\text{cm}^2\cdot\text{kh}^{-1}$ ) was measured corresponding to a degradation rate of  $\approx 3 \text{ mV}\cdot\text{kh}^{-1}$ . This rather low value obtained for an operating time of 15'000 hours is in good agreement with the typical degradation rates measured on classical

SOFCs over shorter aging periods [Skafte 2016]. This good durability behavior of *Cell-A3* indicates that its electrodes microstructures and interfaces must be stable upon SOFC operation, especially for the Ni-YSZ cermet. Finally, it can be noticed that during the long-term test no significant accidents were reported although, as already stated the cell was kept at the OCV for a fraction of the operating time.

The other cell of the same type (*Cell-A4*) was aged in electrolysis mode for 10'700 hours in a short stack configuration containing six repeating units (RU). All the details of the stack aging, as well as the data analyses have been already published by Rinaldi *et al.* [Rinaldi 2017a]. The gas composition at the hydrogen electrode inlet was  $\text{H}_2\text{O}/\text{H}_2 = 90/10$  vol.%, while the oxygen electrode compartment was swept under ambient air (flowrate at the hydrogen electrode  $\approx 10 \text{ Nml}\cdot\text{min}^{-1}\cdot\text{cm}^{-2}$  – flowrate at the oxygen electrode  $\approx 15 \text{ Nml}\cdot\text{min}^{-1}\cdot\text{cm}^{-2}$ ). The cells in the stack were maintained at a temperature ranging between  $710^\circ\text{C}$  and  $730^\circ\text{C}$  and were operated in galvanostatic mode at  $-0.6 \text{ A}\cdot\text{cm}^{-2}$  (SC  $\approx 45$  %) for the first 3'250 hours and then at  $-0.5 \text{ A}\cdot\text{cm}^{-2}$  (SC  $\approx 38$  %) up to  $\approx 10'000$  hours. It can be noticed that during the durability experiment several incidents of steam starvation have occurred [Rinaldi 2017a], in particular an important water interruption occurred after  $\approx 3'250$  hours causing a drop of the OCV associated to small cracks in the electrolyte. Nevertheless, it has to be pointed out that this incident has not compromised the stack behavior and the experimental characterization has continued. As for *Cell-A3*, a limited voltage increase of  $0.5 \text{ \%}\cdot\text{kh}^{-1}$  is reported during the central part of the test, which corresponds to a degradation rate of  $\approx 6 \text{ mV}\cdot\text{kh}^{-1}$ .

The second type of investigated cell (*Cell-B*) was also aged in electrolysis mode at  $800^\circ\text{C}$  for a total time of 1'000 hours. The durability experiment was performed at a current density of  $-0.5 \text{ A}\cdot\text{cm}^{-2}$  (SC  $\approx 15$  %). The hydrogen electrode was fed with the same gas composition as *Cell-A4* ( $\text{H}_2\text{O}/\text{H}_2 = 90/10$  vol.%) with a total flowrate of  $\approx 24 \text{ Nml}\cdot\text{min}^{-1}\cdot\text{cm}^{-2}$ . Ambient air was sent at the oxygen electrode with a flowrate of  $\approx 112 \text{ Nml}\cdot\text{min}^{-1}\cdot\text{cm}^{-2}$ . The degradation curve and the initial and final performances of the cell are reported in Figure II-12. It can be noticed that a slight steam starvation was observed after  $\approx 150$  hours characterized by the increase in the cell's voltage. Nevertheless, after the incident the behavior of the cell has followed the same curve as before, indicating that the incident did not caused a fatal degradation. In contrast to *Cell-A*, a very high degradation rate of  $\approx 100 \text{ mV}\cdot\text{kh}^{-1}$  was measured in this case.

From the analysis of these long-term tests results, it can be stated that for the same type of cell the measured degradation is significantly higher in electrolysis mode than in fuel cell mode. Indeed,

considering the durability of *Cell-A3* and *Cell-A4*, the long-term test in electrolysis mode is characterized by a degradation rate, which is roughly double with respect to the experiment in fuel cell mode. Moreover, it can be deduced from the comparison of *Cell-A4* and *Cell-B* that, in the same operating mode (SOEC), the severity of the degradation seems to be a function on the type of electrode microstructure.

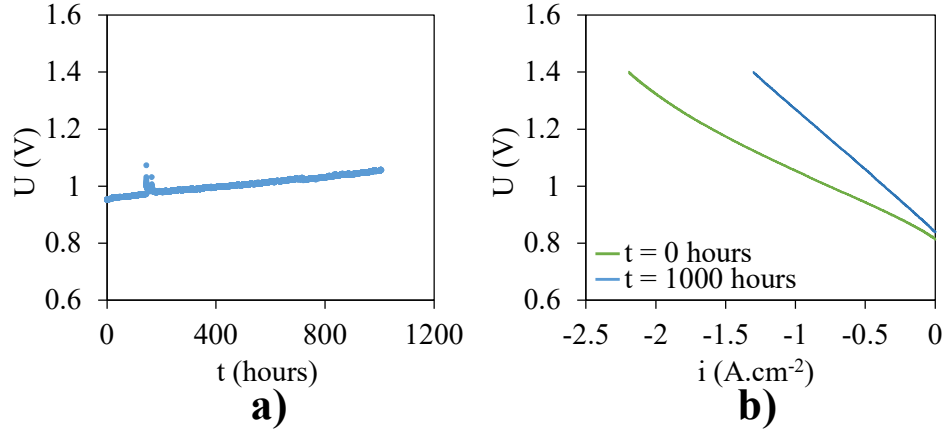


**Figure II-12:** Experimental results for *Cell-B* aged in electrolysis mode for 1'000 hours with  $\text{H}_2\text{O}/\text{H}_2 = 90/10$  vol.% and  $T = 800^\circ\text{C}$  (with  $Q_{\text{air}} = 112 \text{ Nml}\cdot\text{min}^{-1}\cdot\text{cm}^{-2}$  and  $Q_{\text{fuel}} = 24 \text{ Nml}\cdot\text{min}^{-1}\cdot\text{cm}^{-2}$ ): a) Durability curve at  $800^\circ\text{C}$  and  $i_{\text{DC}} = -0.5 \text{ A}\cdot\text{cm}^{-2}$  – b) Comparison of the polarization curves recorded after the reduction and at the end of the experiment.

As mentioned in the introduction chapter, the Ni evolution in the cermet could explain a significant part of the degradation. Moreover, it can be suspected that it could depend on the initial cermet microstructure or the operating mode in SOFC and SOEC. Furthermore, the extent of the Ni evolution in the cermet should slow down with the time for the agglomeration while the migration is expected to continue at the same rate over the entire cell lifetime. Therefore, to study all these possibilities, the cermet of *Cell-A3*, *Cell-A4* and *Cell-B* have been reconstructed by synchrotron X-ray nanoholotomography. The evolutions of the cermet microstructures after operation have been analyzed to better understand the underlying mechanisms involved in the Ni agglomeration and migration and to assess their impact on the electrode and cell response as a function of time, polarization and initial electrode microstructure. The results of this analysis are reported in chapter IV.

## II.3 Physico-Chemical Characterizations and 3D Reconstructions

### II.3.1 Sample Selection

Specimens extracted from the pristine and the aged cells have been characterized at the Paul Scherrer Institute (PSI) and at the European Synchrotron Radiation Facility (ESRF) in order to investigate the

reactivities between the materials at the oxygen electrode side and the microstructural changes in the hydrogen electrode.

Specifically, the physico-chemical evolutions between the electrolyte and the oxygen electrode have been investigated for the samples tested at different temperatures in electrolysis mode (since the destabilization is suspected to be higher for this operating mode as discussed in chapter I). Therefore, samples extracted from *Cell-A1* and *Cell-A2* having classical LSCF-based oxygen electrodes have been analyzed to study the impact of the operating temperature. This study has been complemented with the analysis of *Cell-A3* having the same type of electrode structure but aged in fuel cell mode to confirm the aggravating effects of the electrolysis current (cf. Appendix A). The experiments have been carried out at the microXAS beamline of the Swiss Light Source (SLS) at the PSI with 2D local  $\mu$ XRD/ $\mu$ XRF characterizations. For this purpose, thin lamellae including a part of the electrolyte, the barrier layer and a part of the oxygen electrodes have been prepared according to the protocol given in section II.3.2.1.

In addition, the cermet of specimens taken from *Cell-A3*, *Cell-A4* and *Cell-B* have been reconstructed to analyze the effects of the initial microstructure, the polarization and the aging time on the Ni evolution in the hydrogen electrode. These characterizations have been conducted at the Nano-Imaging beamline (ID16A) of the ESRF by X-ray nano-holotomography. For these experiments, thin pillars with a axial-symmetric shape well adapted for the tomographic experiments have been extracted from the tested cermets according to the procedure detailed in section II.3.2.2.

Therefore, on the one hand the characterization at the microXAS beamline has allowed to study the chemical and crystallographic evolutions of the oxygen electrodes in the aged cells. On the other hand, the nano-holotomography experiment at the ID16A beamline has allows to study the microstructural evolutions in the hydrogen electrode of the aged cells. In this section the different protocols used to extract the two types of specimens are given and the techniques used to characterize the samples taken from the aged and pristine cells are briefly introduced. In addition, the experimental setups at the two beamlines where the analyses have been conducted are shortly described.

### *II.3.2 Sample Preparation*

To perform the characterizations, the samples have been prepared using a plasma-Focused Ion Beam (pFIB) Vion (FEI<sup>TM</sup>), in which Xenon ions are used to mill the material [Munroe 2009, Volkert 2007]. Using  $\text{Xe}^+$ , this technology allows reaching high currents so that the milling rates are about 60 times

faster than classical Gallium ( $\text{Ga}^+$ ) FIB [Hubert 2016]. Thanks to this feature, it is possible to prepare larger samples while keeping a sufficient precision at low currents [Kwakman 2011]. Indeed, with the standard  $\text{Ga}^+$  pFIB, it is difficult to prepare samples with volume exceeding  $\approx 17^3 \mu\text{m}^3$  which could be too small to describe all the heterogeneities in the electrodes [Bleuet 2013, Laurencin 2012]. On the contrary, the  $\text{Xe}^+$  pFIB allows preparing significantly larger samples ( $> 50^3 \mu\text{m}^3$ ) in relatively short amount of time.

### II.3.2.1 Lamellae Preparation for the $\mu\text{XRD}/\mu\text{XRF}$ Experiments

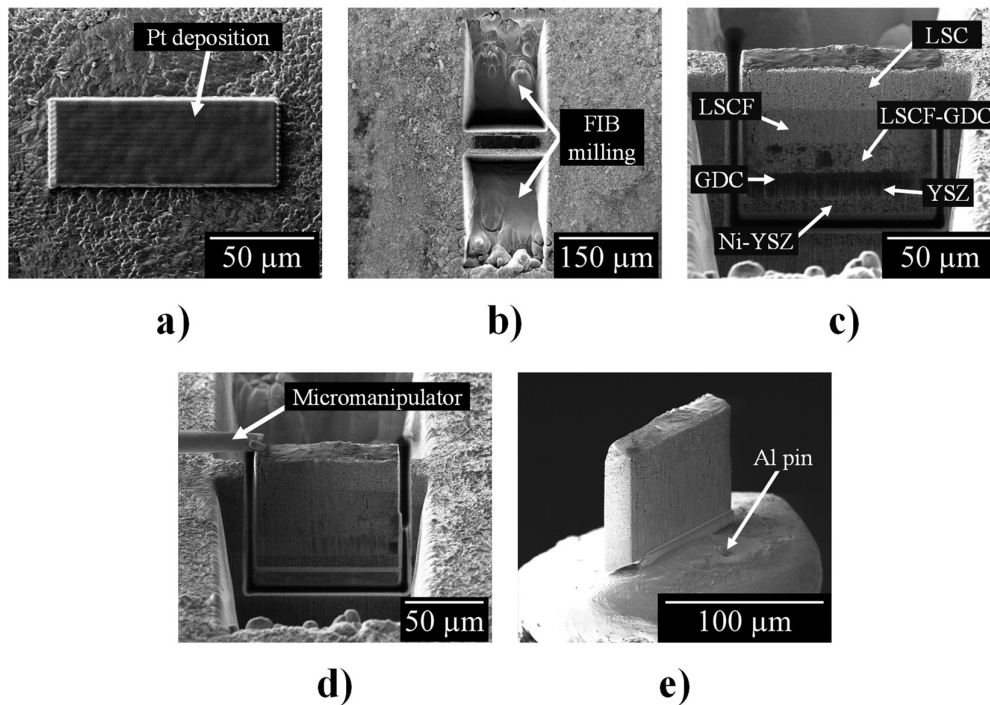


**Figure II-13:** Schematic representation of the lamellae preparation procedure: a) Protective Pt deposition on ROI – b) FIB milling around the ROI – c) Isolated lamella – d) Extraction of the sample from the cell – e) Sample mounted on the Al pin.

To prepare the lamellae, fragments taken from the aged and pristine cells have been positioned in the vacuum chamber of the pFIB machine on a five-axial motorized stage. After the identification of the eucentric height, a rectangular platinum (Pt) layer ( $\approx 3\text{-}4 \mu\text{m}$ ) was deposited on the sample to protect the surface of the Region Of Interest (ROI) (Figure II-13a) [Tao 1990]. This step was carried out using a low current of 59 nA, to ensure the deposition of Pt while preventing any damaging of the specimen surface. Subsequently, the two sides of the ROI were milled to isolate the lamella (Figure II-13b). This step was done at two different currents, 470 nA in the area far from the ROI and at a lower current of 180 nA in the proximity to the ROI to avoid any material damaging in the sample. Once the lamella was isolated (Figure II-13c), a small Pt deposition was used to fix it on a specific

micromanipulator and the sample was detached from the cell using a low ion current of 180 nA (Figure II-13d). Finally, a last Pt deposition was used to glue the lamella to an aluminum (Al) pin (Figure II-13e) and the sample was removed from the vacuum chamber.

It can be pointed out that the final dimensions for all the analyzed specimens are approximately  $100 \times 80 \times 20 \mu\text{m}^3$  for the horizontal dimension (X), the vertical dimension (Y) and the depth (Z), respectively. This geometry allows investigating a representative zone along the interface while the thickness of the sample has been chosen as a tradeoff between the X-ray absorption and the need to probe enough crystallographic grains for the diffraction (cf. the description of the characterization technique in section II.3.3.1).

### II.3.2.2 Micro-Pillars Preparation for the X-Ray Nano-Holotomography Experiments

In order to prepare the micro-pillars for the 3D reconstructions, a similar protocol as the one reported in [Hubert 2018, 2016] has been followed. A circular Pt protective layer was deposited on the surface of the specimens using a current of 59 nA to protect the ROI surface (Figure II-14a).

Subsequently, an elliptic region was milled around the ROI using a high current of 470 nA to isolate the micro-pillar (Figure II-14b). The sample was extracted using the micromanipulator (Figure II-14c) and was fixed on an Al tip. Finally, a last step of shape refining was performed at low current (180 nA) to obtain the desired external diameter (Figure II-14d).

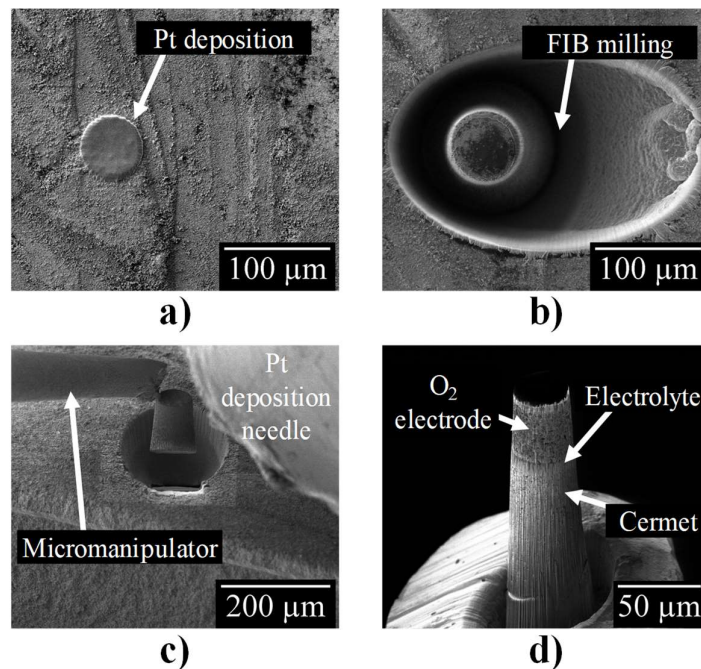


**Figure II-14: Schematic representation of the micro-pillar preparation procedure: a) Protective Pt deposition on ROI – b) Elliptic FIB milling around the ROI – c) Extraction of the sample from the cell – d) Sample mounted on the Al pin with refined shape.**

In this case, all the specimens have a vertical dimension of  $\approx 100\text{-}120\ \mu\text{m}$  and a section of  $\approx 25^2 \times \pi\ \mu\text{m}^2$ . It has been shown that these dimensions represent the best compromise to limit the absorption in the sample while keeping a good resolution and a high field of view for the reconstructions [Hubert 2018].

### II.3.3 Characterization Techniques

#### II.3.3.1 X-Ray $\mu$ -Diffraction and $\mu$ -Fluorescence Experiment

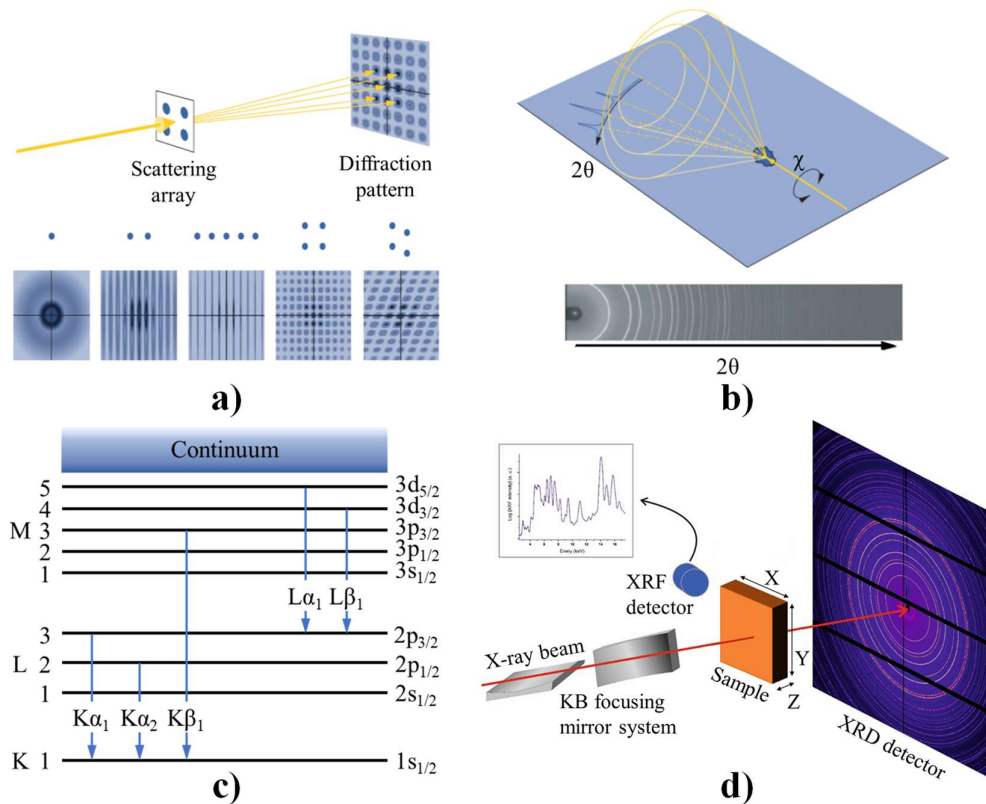


**Figure II-15: Schematic illustration of the  $\mu$ XRD/ $\mu$ XRF experiment: a) Basic principle of scattering in XRD [Willmott 2011] – b) Characteristics of powder XRD [Willmott 2011] – c) Lines of emission for XRF – d) Experimental setup at the microXAS beamline at the PSI.**

*X-ray diffraction (XRD)* – The XRD involves the measurement of the intensity of X-rays scattered from electrons bound to atoms in the crystalline structure of the investigated material. At fixed photon energy, the angle between the incoming X-rays and the diffracted beam is a function of the interplanar spacing of parallel lattice planes (Bragg law) [Dinnebier 2008]. If the analyzed sample has a crystalline structure, it can be shown that diffraction occurs when the scattering vector equals a reciprocal lattice vector. The first one depends on the geometry of the experiment whereas the second one is determined by the orientation and the lattice parameters of the crystalline specimen (Figure II-15a). In powder diffraction techniques, it is possible to take advantage of the different orientations

of the crystals inside the grains of the material to obtain all the possible reflections in the reciprocal space and thus the structure of the material can be investigated (Figure II-15b).

*X-ray fluorescence (XRF)* – The XRF is a technique that allows recognizing the exact chemical composition of a material using the characteristic energies of the photons emitted when the material is illuminated with electrons or X-rays.

In case of X-rays, when a high energy photon interacts with an atom, it transfers its energy to the electrons in the atom (photoelectric effect). The so-called photoelectrons are ejected from the material leaving an electron hole. The fluorescence X-rays result from the transition of an outer-shell electron relaxing to the hole left behind by the emitted photoelectron (radiative relaxation). Each type of electron transition has his specific energy which is a function of the material and the two energy levels involved in the transition. Therefore, measuring the energy of the emitted photons, the identification of the elements present in the sample is possible.

Using the Siegbahn notation, the main types of fluorescence photons for each material correspond to a relaxation to the closest shell to the nucleus (K shell) and to the second-closest shell (L shell). Depending on the energy level from which the relaxing electrons are removed, the fluorescence photons are divided in  $K\alpha$  and  $K\beta$  and  $L\alpha$  and  $L\beta$  (Figure II-15c).

*Experimental setup and beamline description* – The experimental setup at the microXAS beamline is described schematically in Figure II-15d. During the characterization, the specimens have been illuminated with an X-rays beam focused using two Kirkpatrick-Baez (KB) mirrors (photon flux:  $3 \times 10^{12}$  ph·s<sup>-1</sup>). Two photon energies (17.2 keV and 17.99 keV, corresponding to two different beamtimes) have been used for the characterization with a beam size on the sample of around  $1 \times 0.5$   $\mu\text{m}^2$ . Therefore, the vertical spatial resolution (Y, cf. system of coordinates in Figure II-15d) is around 500 nm. The lamellae have been positioned on a motorized holder in the focal point of the X-rays beam and 2D raster scans have been performed on the vertical (Y) and longitudinal (X) directions with a step size of 500 nm all over each sample. A fluorescence detector, positioned at  $\approx 90^\circ$  from the X-ray beam, has been used to detect the fluorescence spectra of the illuminated region of the specimen. In parallel, a 2D diffraction detector (PILATUS 100K) positioned behind the samples has been used to obtain the local XRD, as a cumulated information along the depth of the sample (in the direction of the X-rays). The collection of the diffracted X-rays has been possible thanks to the limited thickness of the specimens along the beam direction (Z) allowing the transmission of X-rays towards the detector. The two detectors allow obtaining at the same time the elemental and crystalline 2D maps of each lamella.

The 2D diffraction rings measured in each point have been azimuthally integrated using the pyFAI Python library [Kieffer 2013] to obtain classical 1D diffraction patterns, whereas the local fluorescence data have been fitted using another Python library, pyMCA [Solé 2007]. The  $\mu$ XRF and  $\mu$ XRD data are subsequently integrated over the horizontal direction to obtain an average elemental composition and XRD pattern for each vertical position in the sample. The Rietveld refinement of these local XRD patterns has been performed using the software XRDUa [De Nolf 2014].

This type of characterization has been carried out on specimens extracted from *Cell-A1*, *Cell-A2* and *Cell-A3* in order to investigate the local chemical and crystalline evolutions at the oxygen electrode/barrier layer/electrolyte interface and along the thickness of the electrode.

### *II.3.3.2 3D Reconstruction via X-ray Nano-Holotomography*

*X-ray nano-holotomography* – In this technique, the sample is illuminated by using a coherent X-ray beam with high brilliance. The refractive index of the materials, which is related to the local electron density in the sample, induces a change in the wavelength resulting in a phase shift at the outlet of the specimen. This phase shift contains the information about the local electron density in the specimen and can be used to obtain the microstructural information of the electrode [Burvall 2011, Cloetens 1999, Paganin 2002]. Indeed, by analyzing the phase modification, it has been shown that the distinction between the pores, the nickel and the YSZ inside the reconstructed cermet is possible [Hubert 2018, 2018b, Villanova 2013].

*Experimental setup and beamline description* – The cermet microstructures have been reconstructed at the Nano-Imaging beamline (ID16A) of the ESRF. The ID16A is located at 185 m from the X-ray source where high coherence of the beam is obtained coupled with high photon flux ( $7 \times 10^{11}$  ph $\cdot$ s $^{-1}$ ) (cf. Figure II-16a). The micro-pillars have been placed on a sample stage consisting in six piezoelectric actuators to precisely control the positioning of the specimens during the experiment. The sample stage is integrated in chamber evacuated down to  $10^{-7}$  mbar. KB mirrors are used to focus the beam before the sample. A Charge Coupled Device (CCD) detector is used to collect the divergent X-rays transmitted across the sample and a magnified 2D projection of the region of interest is obtained. For the classical holotomographic acquisition, 2'000 projections have been collected over 180°. Moreover, the data have been collected at four distances between the focal point and the detector to facilitate the identification of the phase shift from the transmitted photons [Hubert 2018b] (cf. Figure II-16b).

It is worth mentioning that all the procedure including the selection of the photons energy (33.6 keV), the data acquisition and the algorithm of reconstructions have been optimized for the characterization of SOCs materials [Hubert 2018b, Laurencin 2012]. Thanks to these optimizations, 3D images of the electrode microstructure are obtained with a large field of view (reconstructed volume of  $\approx 51.2 \times 25.6^2 \times \pi \mu\text{m}^3$ ) and high spatial resolution ( $\approx 50 \text{ nm}$  with a voxel size of  $25 \text{ nm}$ ) [Hubert 2016]. These features are of critical importance to be representative of the SOCs microstructure as the Representative Volume Element (RVE) for this type of device has been reported to be  $\approx 15^3\text{-}20^3 \mu\text{m}^3$  [Moussaoui 2018]. Moreover, thanks to the large volume of the reconstructions it is possible to observe the long-distance redistribution of nickel in the cermet.

This type of characterization has been carried out to investigate the difference in the microstructural evolutions of the Ni-YSZ cermet for *Cell-A3*, *Cell-A4* and *Cell-B*.

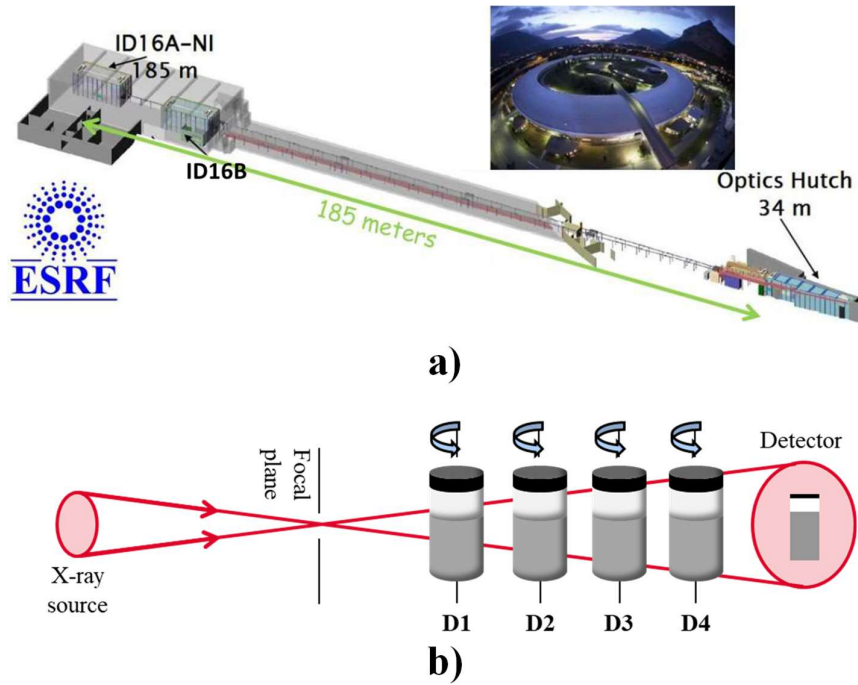


**Figure II-16: Schematic illustration of the X-ray nano-holography experiment: a) ID16A Beamline – b) Experimental setup.**

## II.4 Conclusion of This Chapter

In this chapter, the results of the electrochemical experimental characterizations carried out in the frame of this thesis are described. Using the same type of cell (*Cell-A*), two long-term durability experiments in electrolysis mode have been performed in which all the operating parameters have been kept identical except for the aging temperature. The cell operated at lower temperature has suffered from a significantly higher apparent degradation compared to the cell aged at higher

temperature. Nevertheless, characterizing the two cells in the same conditions at the end of the tests, it has been shown that the ‘intrinsic’ degradation is rather similar in the two cases. Besides, from the analysis of the experimental results it appears that the cell aged at higher temperature has suffered from a higher increase of the Ohmic resistance. In parallel, the experimental results of three long-term tests performed in fuel cell and electrolysis modes on two types of cells (*Cell-A* and *Cell-B*) have been discussed. A limited degradation has been measured for *Cell-A* in both operating modes, whereas the degradation for *Cell-B* has been demonstrated to be significantly higher. Besides, the degradation has been shown to be higher in electrolysis mode than in fuel cell mode.

Finally, taking advantage of these long-term experiments, advanced post-test characterizations have been carried out to investigate the origin of the degradation in the aged cells. In particular,  $\mu$ XRD/ $\mu$ XRF analyses at the oxygen electrode and X-ray nano-holotomography 3D reconstructions of the hydrogen electrode have been performed. These experimental techniques, as well as the procedures for the sample preparation in the two cases, have been briefly introduced. The outcomes of these analyses concerning the stability of the two electrodes will be presented and discussed in chapter V and in chapter IV, respectively. Nevertheless, a deep understanding of the electrode reaction kinetics is needed before addressing the degradation studies. This prerequisite is the goal of the next chapter (chapter III).

In Table II-III, a synthesis of the electrochemical and physico-chemical characterizations performed in the frame of this thesis is given for each one of the analyzed cells.

**Table II-III: Summary of the electrochemical tests results and experimental characterizations**

test conditions and degradation results		$\mu$ XRD	3D $\mu$ XRF volume
<i>Cell-A1</i>	Aging conditions: T = 850°C – SOEC, $i_{DC} = -0.75 \text{ A}\cdot\text{cm}^{-2}$ (SC 50%) – t $\approx 1'800$ h Degradation: $\approx 13.5 \text{ mV}\cdot\text{kh}^{-1}$ (durability curve) – $\approx 14 \text{ mV}\cdot\text{kh}^{-1}$ (i-U curve at 850°C)	X	
<i>Cell-A2</i>	Aging conditions: T = 750°C – SOEC, $i_{DC} = -0.75 \text{ A}\cdot\text{cm}^{-2}$ (SC 50%) – t $\approx 1'800$ h Degradation: $\approx 60 \text{ mV}\cdot\text{kh}^{-1}$ (durability curve) – $\approx 17 \text{ mV}\cdot\text{kh}^{-1}$ (i-U curve at 850°C)	X	
<i>Cell-A3</i>	Aging conditions: T $\approx 780^\circ\text{C}$ – SOFC (FU 40%) and OCV – t $\approx 15'000$ h Degradation: $\approx 3 \text{ mV}\cdot\text{kh}^{-1}$ (from increase in ASR)	X	X
<i>Cell-A4</i>	Aging conditions: T $\approx 720^\circ\text{C}$ – SOEC, $i_{DC} = -0.6$ and $-0.5 \text{ A}\cdot\text{cm}^{-2}$ (SC 45-38%) – t $\approx 10'700$ h Degradation: $\approx 6 \text{ mV}\cdot\text{kh}^{-1}$ (durability curve)		X
<i>Cell-B</i>	Aging conditions: T $\approx 800^\circ\text{C}$ – SOEC, $i_{DC} = -0.5 \text{ A}\cdot\text{cm}^{-2}$ (SC 15%) – t $\approx 1'000$ h Degradation: $\approx 100 \text{ mV}\cdot\text{kh}^{-1}$ (durability curve)		X

# III. Development and Validation of the Multi-Scale Modeling Tools

As discussed in the first chapter of this thesis, the knowledge of the detailed reaction mechanisms occurring within the electrodes is a prerequisite before investigating the underlying causes of the SOCs degradation operated in fuel cell and electrolysis modes. In this objective, electrochemical modeling associated with specific experimental characterizations performed at the electrode and cell levels is an appropriate approach to unravel all the entangled phenomena taking place in the microstructure. In this frame, an existing multiscale tool has been used and complemented with dedicated studies. The available multiscale tool is composed of a macro-scale model describing the complete cell behavior in fuel cell [Laurencin 2008] and electrolysis mode [Bernadet 2017, Laurencin 2011]. It is coupled with two micro-scale electrode models for the hydrogen [Lay-Grindler 2013] and oxygen [Hubert 2016, Laurencin 2015] electrodes, while all the microstructural properties required for the simulations are extracted from synthetic or real electrode reconstructions [Moussaoui 2018, 2020].

Regarding the oxygen electrode, it has been already shown that the initial model is sufficiently detailed for studying the degradation [Laurencin 2017]. However, its validation was clearly insufficient as it was just based on a polarization curve and EIS diagrams taken from literature. Therefore, because of the lack of dedicated and relevant experimental data, a specific effort has been carried out in the frame of this work to propose a full and detailed model validation.

Concerning the hydrogen electrode, the micro-scale model was just based on a single reaction of charge transfer taking place at the TPBs lines within the microstructure. Even if this model was able to reproduce the cell performances [Hubert 2018], a more detailed description of the reaction pathway was missing for the subsequent degradation studies. This limitation has motivated the development and the validation of a model with a full elementary description of the reaction. With this purpose, two micro-scale reaction mechanisms have been investigated to describe the kinetic of the hydrogen oxidation/steam reduction reaction. As detailed in the first chapter of this thesis, the two models are based on the two typical reaction mechanisms proposed for the cermet in literature (i.e. the oxygen spillover and the hydrogen spillover mechanisms). For the two models validation, the same protocol has been used with experimental characterizations obtained on a symmetric cell using a three-electrode configuration. Moreover, a specific attention has been paid to obtain the 3D reconstructions of the studied electrodes to reduce the number of unknown model parameters.

The development and the validation of the micro-scale hydrogen electrode model is reported in the first section of this chapter. The second section is devoted to the presentation of the oxygen electrode model validation. Finally, the integration of the two electrodes models into the numerical tool describing the complete cell behavior is given in the last part of this chapter.

### **III.1 Micro-Scale Models for the Hydrogen Electrode**

In this section, the kinetic models for the hydrogen electrode are described. The models consider the detailed reaction mechanisms occurring at the electrode scale as a function of the microstructure. For this purpose, the microstructural parameters of the cermet have been acquired from a 3D reconstruction obtained *via* synchrotron X-ray nano-holotomography. Furthermore, the models have been validated taking advantage of an experimental campaign carried out on a symmetric cell. This experimental work was done in close collaboration with another PhD student, E. Effori, who took in charge the development, the validation and all the measurements used for the model validation.

#### *III.1.1 Models Description*

Two micro-kinetic models have been developed in parallel: Model I, in which the oxygen spillover mechanism has been implemented [Bieberle 2002, Mizusaki 1994b] and Model II, in which the hydrogen spillover mechanism has been considered [De Boer 1998, Goodwin 2009, Vogler 2009].

In both models, an isothermal slice (1D) of the Ni-YSZ electrode perpendicular to the electrolyte is considered. As shown in Figure III-1a, the simulated domain includes the entire functional layer and a part of the electrolyte ( $0 \leq z \leq \ell_{EL} + \ell_{FL}$ ). The electrode is simulated as a continuous equivalent medium for which the kinetics rates of the reactions and the effective transport properties are scaled on the microstructural parameters deduced from the 3D reconstruction. Mass and charge balances are considered for all the simulated species including source/sink terms related to the reactions rates and a transient term to account for the time-dependent response of the electrode.

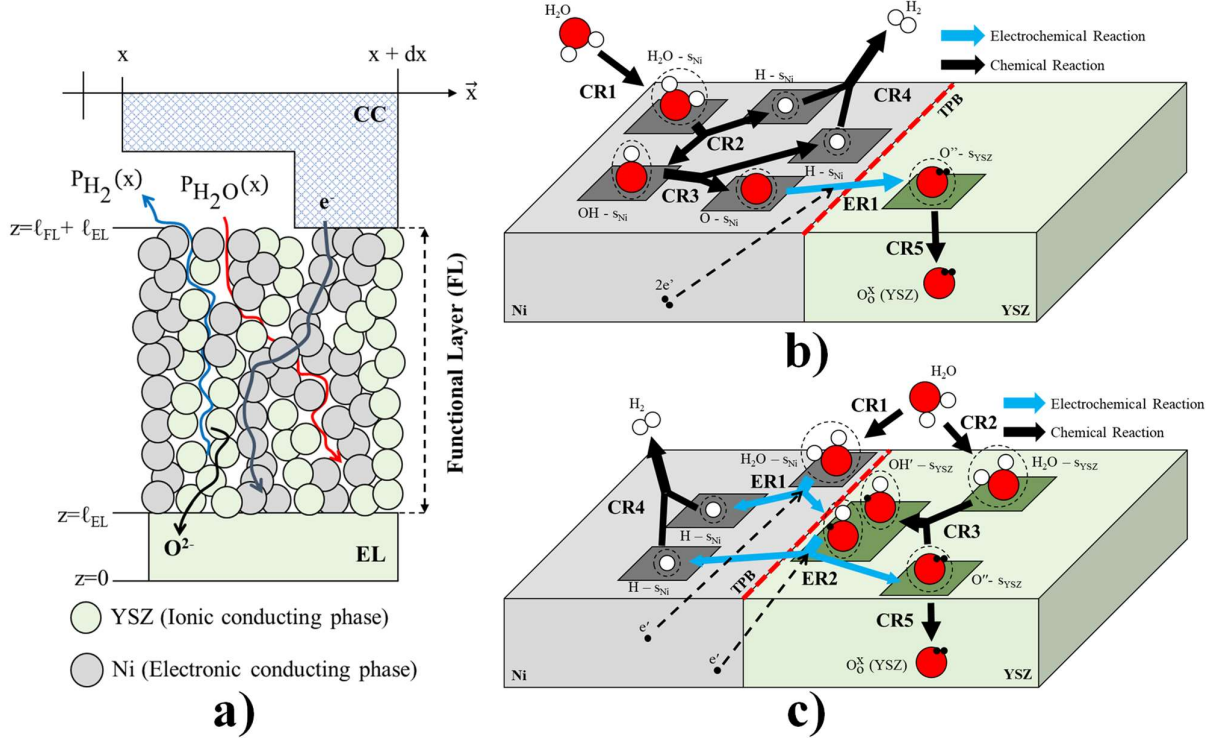
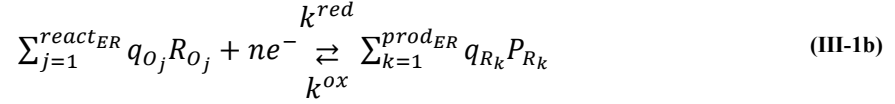


**Figure III-1: Illustration of the Ni-YSZ cermet modeling in electrolysis mode: a) Scheme of the electrode containing part of the electrolyte (EL), the functional layer (FL) and part of the current collector layer (CC) – b) Representation of the oxygen spillover mechanism implemented in Model I – c) Representation of the hydrogen spillover mechanism implemented in Model II.**

### III.1.1.1 General Assumptions and Reaction Mechanisms

The schematic reaction mechanisms implemented in the two models are depicted in Figure III-1b and Figure III-1c for the oxygen (Model I) and hydrogen (Model II) spillover mechanisms, respectively. As a general approach, all the elementary reactions have been expressed using the mass-action kinetic theory [Bard 2001, Kee 2003]. In this frame, the chemical and electrochemical reactions can be written according to eqs. (III-1a) and (III-1b), respectively.

$$\sum_{j=1}^{react_{CR}} q_j R_j \rightleftharpoons \sum_{k=1}^{prod_{CR}} q_k P_k \quad (III-1a)$$



In which  $R/P$  are the reacting/produced species,  $q_{j-k}$  are their respective stoichiometry coefficients,  $n$  is the number of electrons transferred in the reaction and  $k^f$ ,  $k^b$ ,  $k^{red}$ ,  $k^{ox}$  denote the forward, backward, reduction and oxidation kinetic constants, respectively.

For Model I based on the oxygen spillover charge transfer, the expressions of the reactions (III-1a) and (III-1b) are detailed in Table III-I. This reaction pathway was firstly implemented by Bieberle *et al.* [Bieberle 2002] who assumed that the gas species only interact with the Ni. In electrolysis mode (i.e. cathodic polarization), the steam is adsorbed on the Ni surface (**CR1**) before being dissociated into a hydroxyl and a hydrogen adatom (**CR2**). The hydroxyl is further decomposed into an adsorbed oxygen and hydrogen (**CR3**). Finally, the two surface-attached hydrogen atoms are desorbed to produce the dihydrogen gaseous molecule in the electrode porosity (**CR4**). In parallel, the oxygen is electrochemically reduced according to the spillover reaction of charge transfer across the Ni/YSZ at the TPBs lines (**ER1**). Finally, the oxygen ions onto the YSZ surface are incorporated into the lattice by consuming one vacancies (**CR5**). The opposite mechanism occurs in fuel cell mode (i.e. anodic polarization) so that the total reaction mechanism is described by five chemical reactions (**CR**) and one electrochemical reaction (**ER**).

**Table III-I: Reactions for Model I (expressed in electrolysis mode with the abbreviations CR and ER referring to the chemical and electrochemical reactions, respectively)**

<b>CR1</b>	Steam adsorption on the Ni surface	$H_2O(gas) + s_{Ni} \underset{k_{H_2O_{Ni}}^{DES}}{\overset{k_{H_2O_{Ni}}^{ADS}}{\rightleftharpoons}} H_2O_{Ni}$
<b>CR2</b>	H <sub>2</sub> O dissociation on the Ni surface	$H_2O_{Ni} + s_{Ni} \underset{k_{H_2O_{Ni}}^{DISS-}}{\overset{k_{H_2O_{Ni}}^{DISS+}}{\rightleftharpoons}} OH_{Ni} + H_{Ni}$
<b>CR3</b>	Hydroxyl dissociation on Ni surface	$OH_{Ni} + s_{Ni} \underset{k_{OH_{Ni}}^{DISS-}}{\overset{k_{OH_{Ni}}^{DISS+}}{\rightleftharpoons}} O_{Ni} + H_{Ni}$
<b>CR4</b>	Hydrogen desorption from the Ni surface	$2H_{Ni} \underset{k_{H_2_{Ni}}^{ADS}}{\overset{k_{H_2_{Ni}}^{DES}}{\rightleftharpoons}} H_2(gas) + 2s_{Ni}$
<b>ER1</b>	Oxygen spillover from the Ni to the YSZ	$O_{Ni} + s_{YSZ} + 2e^-_{Ni} \underset{k^{ox}}{\overset{k^{red}}{\rightleftharpoons}} O_{YSZ}^{2-} + s_{Ni}$
<b>CR5</b>	Oxygen incorporation in the YSZ lattice	$O_{YSZ}^{2-} + V_{O}^{\bullet\bullet}(YSZ) \underset{k_{O_{YSZ}^{2-}}^{EXC}}{\overset{k_{O_{YSZ}^{2-}}^{INC}}{\rightleftharpoons}} O_{O}^{\times}(YSZ) + s_{YSZ}$

The detail of reactions (III-1a) and (III-1b) for Model II is provided in Table III-II. This mechanism is based on the version of the hydrogen spillover mechanism proposed by Goodwin *et al.* [Goodwin 2009]. In our approach, it is still assumed that hydrogen interacts only with Ni whereas a competitive adsorption/desorption of water is considered for both materials. Considering the cathodic polarization, steam can be adsorbed on Ni and YSZ surface (**CR1** and **CR2**) and two intertwined pathways are possible to produce the hydrogen. On the one hand, the H<sub>2</sub>O attached on Ni can be electrochemically reduced at the TPBs lines to form one hydrogen on the Ni surface and one hydroxyl ion on the YSZ surface (**ER1**). On the other hand, the H<sub>2</sub>O attached on the YSZ can react with an oxygen ion on the surface to produce two hydroxyl ions (**CR3**). These OH<sup>-</sup> species attached on the YSZ surface are subsequently reduced with a second charge transfer according to a hydrogen spillover mechanism, resulting in the formation of a hydrogen adatom on Ni and an oxygen ion on YSZ (**ER2**). Finally, the adsorbed hydrogens on Ni are desorbed in the gas phase (**CR4**) while the oxygen ion is incorporated in the YSZ lattice (**CR5**). As for Model I, the reaction is reversed in anodic polarization so that this mechanism is divided into five **CR** and two **ER**.

**Table III-II: Reactions for Model II (expressed in electrolysis mode with the abbreviation CR and ER referring to the chemical and electrochemical reactions, respectively)**

<b>CR1</b>	Steam adsorption on the Ni surface	$H_2O(gas) + s_{Ni} \xrightleftharpoons[k_{H_2O_{Ni}}^{DES}]{k_{H_2O_{Ni}}^{ADS}} H_2O_{Ni}$
<b>CR2</b>	Steam adsorption on the YSZ surface	$H_2O(gas) + s_{YSZ} \xrightleftharpoons[k_{H_2O_{YSZ}}^{DES}]{k_{H_2O_{YSZ}}^{ADS}} H_2O_{YSZ}$
<b>CR3</b>	H <sub>2</sub> O dissociation on YSZ surface	$H_2O_{YSZ} + O_{YSZ}^{2-} \xrightleftharpoons[k_{H_2O_{YSZ}}^{DISS-}]{k_{H_2O_{YSZ}}^{DISS+}} 2OH_{YSZ}^-$
<b>CR4</b>	Hydrogen desorption from the Ni surface	$2H_{Ni} \xrightleftharpoons[k_{H_2Ni}^{ADS}]{k_{H_2Ni}^{DES}} H_2(gas) + 2s_{Ni}$
<b>ER1</b>	First charge transfer reaction	$H_2O_{Ni} + s_{YSZ} + 1e_{Ni}^- \xrightleftharpoons[k_1^{ox}]{k_1^{red}} OH_{YSZ}^- + H_{Ni}$
<b>ER2</b>	Second charge transfer reaction	$OH_{YSZ}^- + s_{Ni} + 1e_{Ni}^- \xrightleftharpoons[k_2^{ox}]{k_2^{red}} O_{YSZ}^{2-} + H_{Ni}$
<b>CR5</b>	Oxygen incorporation in the YSZ lattice	$O_{YSZ}^{2-} + V_O^{\bullet\bullet}(YSZ) \xrightleftharpoons[k_{O_{YSZ}^{2-}}^{EXC}]{k_{O_{YSZ}^{2-}}^{INC}} O_O^x(YSZ) + s_{YSZ}$

In the next sections, the general set of equations used to express the reaction kinetics rates together with the charge and mass transfer in the electrodes phases are reported. It can be noticed that the

application of these general equations to Model I and Model II are detailed in Appendix B and Appendix C, respectively.

### III.1.1.2 Thermodynamic and Kinetics of the Reactions

Considering the surface elementary steps of the two mechanisms, their kinetic rates can be written according to the general expression (III-2a) for the chemical reactions (III-1a) and using a Butler-Volmer formalism (III-2b) for the electrochemical reactions (III-1b).

$$v^{CR} = Sp_{a-b} \cdot (k^f \cdot \prod_{j=1}^{reactCR} a_j^{q_j} - k^b \cdot \prod_{k=1}^{prodCR} a_k^{q_k}) \quad (\text{III-2a})$$

$$v^{ER} = \xi^{TPBs} \left( k^{red} \cdot \prod_{j=1}^{reactER} a_{O_j}^{q_{O_j}} \exp\left(\frac{-\alpha_{red} n F}{RT} E\right) - k^{ox} \cdot \prod_{k=1}^{prodER} a_{R_k}^{q_{R_k}} \exp\left(\frac{\alpha_{ox} n F}{RT} E\right) \right) \quad (\text{III-2b})$$

In which  $v$  is the kinetic rate ( $\text{mol} \cdot \text{m}^{-3} \cdot \text{s}^{-1}$ ),  $a$  is the activity and  $\alpha_{red/ox}$  are the reduction/oxidation transfer coefficients ( $\alpha_{red} + \alpha_{ox} = 1$ ), which are taken as 0.5 each.  $F$ ,  $R$  and  $T$  are the Faraday's constant ( $\text{C} \cdot \text{mol}^{-1}$ ), the universal gas constant ( $\text{J} \cdot \text{mol}^{-1} \cdot \text{K}^{-1}$ ) and the operating temperature (K), respectively. As already mentioned, the kinetic rates of the reactions are dependent on the electrode microstructural properties. Therefore, the kinetic rates (III-2a) and (III-2b) for the equivalent homogeneous medium are respectively proportional to the Ni/gas or YSZ/gas interfacial specific surface area ( $Sp_{a-b}$ ,  $\text{m}^{-1}$ ) and the density of active TPBs ( $\xi^{TPBs}$ ,  $\text{m}^{-2}$ ). Finally,  $E(z)$  is the local potential in the electrode (V) expressed as the difference between the local electronic potential in the Ni ( $\varphi_{el}$ ) and the local ionic potential in the YSZ ( $\varphi_{io}$ ) (eq. (III-3)).

$$E(z) = \varphi_{el}(z) - \varphi_{io}(z) = -\frac{\tilde{\mu}_{e^-}}{F} + \frac{\tilde{\mu}_{O^{2-}}}{2F} \quad (\text{III-3})$$

Where  $\tilde{\mu}_{e^-}$  and  $\tilde{\mu}_{O^{2-}}$  denote the electrochemical potentials ( $\text{J} \cdot \text{mol}^{-1}$ ) for the electrons in Ni and the oxygen ions in YSZ (considering:  $\tilde{\mu}_{V_O^{\bullet\bullet}} = -\tilde{\mu}_{O^{2-}}$ ).

Ideal solutions for the gas and the surface species have been assumed in the models so that the activities are directly given by the partial pressure  $p_i$  or the surface concentration  $C_i$  through eqs. (III-4a) and (III-4b).

$$a_{gas,i} = \frac{p_{gas,i}}{p_{ref}} \quad (\text{III-4a})$$

$$a_{ads,i} = C_{ads,iS} = \Gamma_S \theta_{ads,iS} \quad (\text{III-4b})$$

Where  $p_{gas,i}$  represent the i-th gas partial pressure (atm),  $p_{ref}$  the reference pressure (1 atm) and  $\Gamma_S$  is the total density of sites available for adsorption on the surface S ( $\text{mol} \cdot \text{m}^{-2}$ ). In eq. (III-4b),  $\theta_{ads,iS}$  represents the surface coverage of i-th species on the surface S. In coherence with the previous

expression of surface activities, a Langmuir isothermal model has been adopted with a monolayer coverage on the Ni or YSZ surface so that  $\sum \theta_{ads,i} + \theta_s = 1$  (where  $\theta_s$  represents the fraction of empty surface sites that are still available for adsorption).

Conversely to the other species that evolve with the position in the electrode and the polarization, the activities of the vacancies  $V_O^{\bullet\bullet}(YSZ)$  and oxygen atoms  $O_O^x(YSZ)$  in the bulk of YSZ have been taken constant. Indeed, YSZ is a good ionic conductor with a high concentration of charge carrier so that [Kawata 2006]:

$$a_{V_O^{\bullet\bullet}} = \frac{C_{V_O^{\bullet\bullet}}}{C_{O_O^x(YSZ)}^{ref}} \approx cte \quad \text{with} \quad C_{V_O^{\bullet\bullet}} = 4 \cdot \frac{\%Y}{UCV \cdot N_a} \quad \text{(III-5a)}$$

$$a_{O_O^x} = \frac{C_{O_O^x}}{C_{O_O^x(YSZ)}^{ref}} \quad \text{with} \quad C_{O_O^x} \approx C_{O_O^x(YSZ)}^{ref} = 4 \cdot \frac{2-\%Y}{UCV \cdot N_a} \quad \text{(III-5b)}$$

Where %Y is the molar percentage of yttrium in the YSZ, UCV is the unit cell volume of the YSZ (m<sup>3</sup>) and N<sub>a</sub> is Avogadro's number (atoms·mol<sup>-1</sup>).

For each reaction *i*, the forward and backward kinetic constants are linked *via* the thermodynamic equilibrium constant ( $K^{eq}$ ). Regarding the chemical reactions, the equilibrium constants are determined from the thermodynamic data using eqs. (III-6a) and (III-6b).

$$K_i^{eq} = \frac{k^{f,i}}{k^{b,i}} = \exp\left(\frac{-\Delta g_i^0(T)}{RT}\right) \quad \text{(III-6a)}$$

$$\Delta g_i^0(T) = \sum_{j=1}^{prod_{CR_i}} [h_j^0(T) - T s_j^0(T)] - \sum_{k=1}^{react_{CR_i}} [h_k^0(T) - T s_k^0(T)] \quad \text{(III-6b)}$$

In which  $\Delta g_i^0$  represents the Gibbs free energy variation (J·mol<sup>-1</sup>) for the *i*-th reaction at standard pressure of reactants and products and  $h_m^0, s_m^0$  represents the standard enthalpy and entropy of formation of the *m*-th species, expressed in (J·mol<sup>-1</sup>) and (J·K<sup>-1</sup>·mol<sup>-1</sup>), respectively. The data for the standard enthalpies and entropies listed in Table III-III for the gas, the adsorbed and the bulk species are taken from the literature [Bessler 2007, Chase 1998] at an operating temperature of 700°C.

Once the equilibrium constants of the chemical reactions are determined, they are used to calculate the surface coverages at equilibrium for the adsorbed species taking advantage of the relation of  $K^{eq}$  with the activities (eq. (III-7)). Finally, the coverages at equilibrium are used to determine the equilibrium constants of the electrochemical reactions according to eq. (III-8).

$$K_{CR_i}^{eq} = \frac{k^{f,i}}{k^{b,i}} = \frac{\prod a_{prod_{CR_i}}^{eq}}{\prod a_{react_{CR_i}}^{eq}} \quad \text{(III-7)}$$

$$K_{ER_i}^{eq} = \frac{k^{red,i}}{k^{ox,i}} = \frac{\prod a_{prod_{ER_i}}^{eq}}{\prod a_{react_{ER_i}}^{eq}} \exp\left(\frac{nF}{RT} E^{eq}\right) \quad (\text{III-8})$$

Where  $E^{eq}$  represents the equilibrium potential (V).

**Table III-III: Thermodynamic data for the species used in the models at 700°C [Bessler 2007, Chase 1998]**

Species	Standard enthalpy (J·mol <sup>-1</sup> )	Standard entropy (J·K <sup>-1</sup> ·mol <sup>-1</sup> )
$H_2(g)$	$19.8 \times 10^3$	231.6
$H_2O(g)$	$-216.9 \times 10^3$	165.4
$H_{Ni}$	$-31.8 \times 10^3$	40.7
$H_2O_{Ni}$	$-273 \times 10^3$	130
$OH_{Ni}$	$-193 \times 10^3$	106
$O_{Ni}$	$-222 \times 10^3$	39
$H_2O_{YSZ}$	$-273 \times 10^3$	98
$OH_{YSZ}^-$	$-282.5 \times 10^3$	67
$O_{YSZ}^{2-}$	$-236.4 \times 10^3$	0
$O_O^x(YSZ)$	$-236.4 \times 10^3$	0
$V_O^{**}(YSZ)$	0	0

### III.1.1.3 Mass and Charge Transport

In the micro-models for the hydrogen electrode, the Fick's law is used to describe the diffusion of gas and surface-attached species, whereas the electronic current in Ni and the ionic current in YSZ are computed considering the classical Ohm's law.

(i) For the gas species, the mass balances and the equations to express the diffusive flux are reported in eqs. (III-9a) and (III-9b).

$$\varepsilon_{pores} \frac{dC_i}{dt} = -\nabla \cdot \vec{N}_i \pm \dot{S}_i \quad (\text{III-9a})$$

$$\vec{N}_i = -D_i^{eff} \nabla C_i \quad (\text{III-9b})$$

In which  $\varepsilon_{pores}$  is the pore volume fraction in the electrode while  $C_i$  and  $\vec{N}_i$  are the molar concentration (mol·m<sup>-3</sup>) and flux (mol·m<sup>-2</sup>·s<sup>-1</sup>) of the i-th species.  $\dot{S}_i$  represents the source/sink term associated to the reactions in which the i-th species is produced/consumed (mol·m<sup>-3</sup>·s<sup>-1</sup>) and  $D_i^{eff}$  represents the effective gas diffusion coefficient for the i-th species (m<sup>2</sup>·s<sup>-1</sup>).

The effective diffusion coefficient in (III-9b) is derived from the Dusty-Gas Model (DGM) by neglecting the permeation flux [Laurencin 2011]. This last approximation is especially relevant for the microstructure of typical Ni-YSZ electrodes for which the mass transfer is fully limited by the gas diffusional process [Bernadet 2017]. In this condition, the effective diffusion coefficient ( $D_i^{eff}$ ) given in eq. (III-10) is a combination of the binary diffusion coefficient ( $D_{i-j}^{eff}$ ) and the Knudsen diffusion coefficient ( $D_{K,i}^{eff}$ ) for a multi-component gas mixture composed of H<sub>2</sub>, H<sub>2</sub>O and a neutral gas used as diluent, such as N<sub>2</sub> [Laurencin 2011].

$$D_i^{eff} = \left( \frac{1}{D_{K,i}^{eff}} + \frac{1}{D_{i-i.g.}^{eff}} + \left( \frac{1}{D_{i-j}^{eff}} - \frac{1}{D_{i-i.g.}^{eff}} \right) \cdot (1 - x_{i.g.}) \right)^{-1} \quad (\text{III-10})$$

Where  $x_{i.g.}$  is the molar fraction of inert gas in the gas flow (e.g. nitrogen). The Knudsen diffusion coefficient is reported in eq. (III-11a) while the binary diffusion coefficient is expressed according to the Fuller's theory and is reported in eq. (III-11b) [Laurencin 2011].

$$D_{K,i}^{eff} = \frac{\varepsilon_{pores}}{\tau_{pores}} \cdot \bar{r}_{pores} \cdot \frac{2}{3} \sqrt{\frac{8000RT}{\pi m_i}} \quad (\text{III-11a})$$

$$D_{i-j}^{eff} = \frac{\varepsilon_{pores}}{\tau_{pores}} \cdot \frac{0.00143}{P_{tot} \cdot (\sqrt[3]{V_i} + \sqrt[3]{V_j})^2} \cdot T^{1.75} \cdot 10^{-4} \cdot \frac{2}{\sqrt{\frac{1}{m_i} + \frac{1}{m_j}}} \quad (\text{III-11b})$$

(ii) The diffusion and mass conservation of surface-attached species on Ni and on YSZ have been modeled using eq. (III-12a) and eq. (III-12b), respectively.

$$\vec{N}_{ads,i} = -S p_{a-b} D_{ads,iS} \nabla C_{ads,iS} \quad (\text{III-12a})$$

$$S p_{a-b} \frac{dC_{ads,iS}}{dt} = -\nabla \cdot \vec{N}_{ads,i} \pm \dot{S}_i \quad (\text{III-12b})$$

In which  $D_{ads,iS}$  represents the surface diffusion coefficient of the i-th specie on Ni or YSZ expressed in m<sup>2</sup>·s<sup>-1</sup>. All the surface diffusion coefficients at 700°C are taken from literature [Vogler 2009]. However, it can be pointed out that a rather large range of uncertainty is expected on these parameters, as the experimental determination of surface diffusion coefficients remains very challenging. Also, despite recent progress in the DFT description of the interaction of water with the YSZ surface, the mechanisms by which the hydroxyls migrate on the YSZ surface remain unclear, as well as their energy barriers, making it difficult to use available DFT results to estimate a diffusion coefficient of water or OH on this surface. Note that the crystallographic orientation of the surface, especially for Ni, obviously impacts the energy barriers for diffusion, and thus the diffusion coefficients of the surface-attached species, contributing to increase the range of uncertainty on these coefficients.

(iii) The electronic and ionic current densities in the electrode are both computed with eq. (III-13), in which the effective conductivities ( $\sigma_{el}^{eff}$  and  $\sigma_{io}^{eff}$ ) are expressed according to eq. (III-14).

$$\vec{i}_{el} = -\sigma_{el}^{eff} \nabla \varphi_{el} \quad \text{and} \quad \vec{i}_{io} = -\sigma_{io}^{eff} \nabla \varphi_{io} \quad (\text{III-13})$$

$$\sigma_{el}^{eff} = \frac{\varepsilon_{el}}{\tau_{el}} \sigma_{el} \quad \text{and} \quad \sigma_{io}^{eff} = \frac{\varepsilon_{io}}{\tau_{io}} \sigma_{io} \quad (\text{III-14})$$

Where  $\sigma_{el}$  and  $\sigma_{io}$  are the bulk electronic and ionic conductivities of Ni and YSZ ( $\text{S}\cdot\text{m}^{-1}$ ), respectively [Lay-Grindler 2013].

The charge conservation equations for the electronic and ionic conductive phases are written in eqs. (III-15a) and (III-15b), respectively.

$$+Sp_{Ni-YSZ}C_{dl} \frac{dE}{dt} = -\nabla \cdot \vec{i}_{el} \pm \dot{S}_{el} \quad (\text{III-15a})$$

$$-Sp_{Ni-YSZ}C_{dl} \frac{dE}{dt} = -\nabla \cdot \vec{i}_{io} \pm \dot{S}_{io} \quad (\text{III-15b})$$

Where  $C_{dl}$  is the capacitance of double layer arising between the Ni and the YSZ ( $\text{F}\cdot\text{m}^{-2}$ ) and  $\dot{S}_{el/io}$  are the source/sink terms for the electronic and ionic charges ( $\text{A}\cdot\text{m}^{-3}$ ), related to the kinetic rates of the reactions in which those are consumed or produced *via* eq. (III-16).

$$\dot{S}_{el/io} = nFv_{el/io} \quad (\text{III-16})$$

It can be noticed that for the electronic and ionic charge conservation equations, a positive flux of charges is associated to a negative current so that, a reaction is considered as a sink if it produces charged species, and vice versa.

Inside the electrolyte, the ionic current is not associated to any reaction and no capacitance effect arises from the accumulation of charges due to the absence of the interface with the electronic conducting material, meaning that eq. (III-15b) becomes:

$$\nabla \cdot \vec{i}_{io} = 0 \quad (\text{III-17})$$

All the diffusivities and conductivities in eqs. (III-9) to (III-17) are expressed as a function of the electrode microstructural properties in order to take into account the effect of the cermet microstructure on the mass/charge transport phenomena. Only the effective ionic conductivity of the YSZ inside the electrolyte has been taken as the property for the dense material (i.e.  $\varepsilon_{io,electrolyte} = \tau_{io,electrolyte} = 1$ ).

The intrinsic diffusion coefficients and conductivities used for the simulations at 700°C are reported in Table III-IV.

**Table III-IV: Diffusion coefficients and conductivities at T=700°C [Lay-Grindler 2013, Todd 2002, Vogler 2009]**

Coefficient	Value	Unit
$D_{H_2(g)-H_2O(g)}$	$7.27 \times 10^{-4}$	$(m^2 \cdot s^{-1})$
$D_{H_2(g)-N_2(g)}$	$6.25 \times 10^{-4}$	$(m^2 \cdot s^{-1})$
$D_{H_2O(g)-N_2(g)}$	$2.07 \times 10^{-4}$	$(m^2 \cdot s^{-1})$
$D_{K,H_2O(g),normalized\ on\ \bar{r}_{pores} = 1\ m}$	$7.13 \times 10^2$	$(m \cdot s^{-1})$
$D_{K,H_2(g),normalized\ on\ \bar{r}_{pores} = 1\ m}$	$2.13 \times 10^3$	$(m \cdot s^{-1})$
$D_{H_{Ni}}$	$7.76 \times 10^{-8}$	$(m^2 \cdot s^{-1})$
$D_{H_2O_{Ni}}$	$1.88 \times 10^{-8}$	$(m^2 \cdot s^{-1})$
$D_{O_{Ni}}$	$3.23 \times 10^{-10}$	$(m^2 \cdot s^{-1})$
$D_{OH_{Ni}}$	$1.38 \times 10^{-8}$	$(m^2 \cdot s^{-1})$
$D_{H_2O_{YSZ}}$	$1.45 \times 10^{-9}$	$(m^2 \cdot s^{-1})$
$D_{OH_{YSZ}^-}$	$1.45 \times 10^{-9}$	$(m^2 \cdot s^{-1})$
$D_{O_{YSZ}^{2-}}$	$8.12 \times 10^{-16}$	$(m^2 \cdot s^{-1})$
$\sigma_{el,Ni,bulk}$	$80 \times 10^3$	$(S \cdot m^{-1})$
$\sigma_{io,3YSZ,bulk}$	0.797	$(S \cdot m^{-1})$
$\sigma_{io,8YSZ,bulk}$	1.713	$(S \cdot m^{-1})$

#### III.1.1.4 Summary of the Main Hypotheses for the Models

Different assumptions have been made to simulate the electrode response and to simplify the determination of the most relevant reaction mechanism for the Ni-YSZ cermet:

- The mixtures for the gaseous molecules and the adsorbed species have been treated as ideal solutions.
- In Model II, the YSZ surface has been simulated considering one single type of adsorption site for all the surface-attached species as in [Luo 2019, Vogler 2009]. In this configuration, the surface attached oxygen ions, hydroxyl ions and molecular water are considered as competitively adsorbed on YSZ.
- To reduce the number of unknown fitting parameters in both models, the reaction of oxygen incorporation/excorporation in the YSZ lattice (**CR5**) has been assumed not limiting (i.e.  $k_{O_{YSZ}^{2-}}^{INC} \gg 0$ ).

- In Model II, since the reaction of H<sub>2</sub>O dissociation on the YSZ surface (**CR3**) is supposed to be very fast [Chaopradith 2015], it has also been considered as not limiting.

Using these assumptions, in each model there are five free fitting parameters:

- For Model I:
  - The kinetic constant of steam adsorption on Ni ( $k_{H_2O_{Ni}}^{ADS}$ );
  - The forward kinetic constant of steam dissociation on Ni ( $k_{H_2O_{Ni}}^{DIS}$ );
  - The forward kinetic constant of hydroxyl dissociation on Ni ( $k_{OH_{Ni}}^{DISS+}$ );
  - The kinetic constant of hydrogen desorption from Ni ( $k_{H_{2N}}^{DES}$ );
  - The reduction kinetic constant of the charge transfer reaction ( $k^{red}$ ).
- For Model II:
  - The kinetic constant of steam adsorption on Ni ( $k_{H_2O_{Ni}}^{ADS}$ );
  - The kinetic constant of steam adsorption on YSZ ( $k_{H_2O_{YSZ}}^{ADS}$ );
  - The kinetic constant of hydrogen desorption from Ni ( $k_{H_{2N}}^{DES}$ );
  - The reduction kinetic constant of the first charge transfer reaction ( $k_1^{red}$ );
  - The reduction kinetic constant of the second charge transfer reaction ( $k_2^{red}$ ).

### III.1.1.5 Numerical Implementation and Boundary Conditions

The equations of charge/mass balances combined with the expressions of fluxes and source terms constitute a set of partial differential equations implemented in the commercial software for finite element computations Comsol Multiphysics<sup>®</sup> and solved in the time domain.

In both models, the overall electrode potential  $E^{tot}$  is taken as the difference between the electronic potential in the Ni ( $\varphi_{el}$ ) at the CC/FL interface and the ionic potential in the YSZ ( $\varphi_{io}$ ) at the FL/EL interface as shown in eq. (III-18).

$$E^{tot} = \varphi_{el}(z = \ell_{FL} + \ell_{EL}) - \varphi_{io}(z = \ell_{EL}) \quad \text{(III-18)}$$

This potential is used to compute the electrode overpotential ( $\eta^{calc}(V)$ ), according to eq. (III-19).

$$\eta^{calc}(V) = E^{tot} - E^{eq} \quad \text{(III-19)}$$

To obtain the steady-state response of the electrode, the ionic potential is fixed in the YSZ (i.e. at  $z = 0$  in Figure III-1a) and the local current densities, the local surface coverages on Ni and YSZ and all the other unknowns are computed.

To simulate the impedance spectra, the procedure reported by Hubert *et al.* [Hubert 2016] has been applied. For each frequency, a sinusoidal perturbation has been imposed to the ionic current in the electrolyte:

$$i_{io,EL}(z = 0, t) = i_{io,DC} + i_{io,AC} \cdot \sin(2\pi ft) \quad (\text{III-20})$$

Ten full cycles of the sinusoid have been simulated and the last two have been analyzed to calculate the impedance of the electrode from the time-dependent current and potential. Using this procedure, the solution has been determined for each point of the diagram keeping the full non-linearity of the system. The models have been run using an amplitude of  $i_{io,AC} = 5 \text{ mA} \cdot \text{cm}^{-2}$  in the frequency range between  $10^{-1}$  and  $10^6$  Hz and seven points per decade have been calculated. In this work, only spectra at OCP have been simulated ( $i_{io,DC} = 0$ ). However, it is worth mentioning that, using this approach, both models are able to simulate the impedance spectra at OCP but also under polarization as detailed by Hubert *et al.* [Hubert 2016].

The imposed boundary conditions are the same in both models and are summarized hereafter:

1) For the *electronic Ni phase*:

$$\varphi_{el}(z = \ell_{EL} + \ell_{FL}) = 0 \quad \text{and} \quad i_{el}(z = \ell_{EL}) = 0$$

2) For the *ionic YSZ phase*:

$$i_{io}(z = \ell_{EL} + \ell_{FL}) = 0 \quad \text{and} \quad \varphi_{io,DC}(z = 0) = \textit{imposed} \text{ for the stationary solution, or} \\ i_{io,EL}(z = 0) = \textit{imposed} \text{ for the time-dependent solution.}$$

3) For the *gas phases*:

$$C_i(z = \ell_{EL} + \ell_{FL}) = \textit{const.} \quad \text{and} \quad \vec{N}_i(z = \ell_{EL}) = 0$$

4) For the *adsorbed phases*:

$$\vec{N}_{ads,i}(z = \ell_{EL} + \ell_{FL}) = 0 \quad \text{and} \quad \vec{N}_{ads,i}(z = \ell_{EL}) = 0$$

### III.1.2 Experimental Characterization

As already mentioned, an experimental campaign has been carried out by another PhD student, E. Effori, to obtain all the data required for the model validation with the purpose to identify the most appropriate mechanism for hydrogen electrode reaction in electrolysis and fuel cell conditions. The tests have been carried out on a symmetric cell in a specific setup developed at CEA. Realistic porous

cermet electrodes composed of Ni and 3 mol.% YSZ have been used (Ni-3YSZ cermet). In this section, the characteristic of the symmetric cell as well as the experimental setup used for the model validation are described. Moreover, the experimental results obtained on the symmetric setup are analyzed to gain more insight about the reaction mechanism of the hydrogen electrode.

### III.1.2.1 Cell Description

In Figure III-2, a schematic representation of the tested cell is shown. It is composed by a thick 8YSZ electrolyte ( $\approx 300 \mu\text{m}$ ) sandwiched between two porous electrodes (thickness  $\approx 25 \mu\text{m}$ ) made of Ni and 3YSZ. It can be noticed that the use of thin electrodes allows limiting the impact of gas diffusion while the reactions are expected to extend in the whole electrode thickness corresponding to the active Functional Layer (FL). Therefore, this configuration is considered at the same time representative of the real SOCs electrodes and adapted to analyze the kinetics of the reaction mechanism.

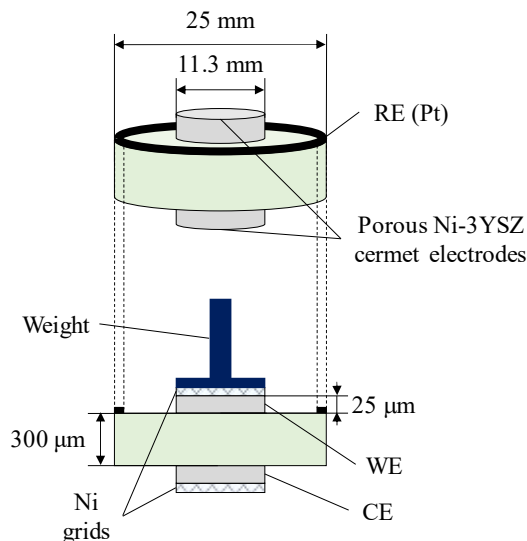


**Figure III-2: Symmetric cell used for the experimental characterization of the hydrogen electrode.**

The Working and Counter Electrodes (WE and CE, respectively) have a circular shape with a diameter of 11.3 mm for an active surface area of  $\approx 1 \text{ cm}^2$ . They have been screen-printed on the two faces of the solid membrane (disk with a diameter of  $\approx 25 \text{ mm}$ ) and then sintered under air. A platinum wire was used as Reference Electrode (RE) and placed at the periphery of the cell on the upper surface of the electrolyte (cf. Figure III-2). A special attention has been paid to position the RE as far as possible from the electrodes. Moreover, the WE and CE were carefully aligned with each other and centered compared to the electrolyte disk. Consequently, the geometrical rules to ensure the reliability of the measurements with a three-electrode configuration have been fulfilled [Jiang 2017]. Finally, two nickel grids having the same dimensions than the electrodes and with a density of  $3600 \text{ mesh}\cdot\text{cm}^{-2}$  have been used as Current Collectors (CCs).

### III.1.2.2 Experimental Setup and Testing Conditions

The test has been conducted in a specific ceramic holder consisting in a single gas chamber supplied by a mixture of H<sub>2</sub> and H<sub>2</sub>O. This experimental setup was placed in a furnace for which the temperature changes were applied using a slow heating rate of 1°C·min<sup>-1</sup> to avoid any mechanical damaging in the cell. It is worth noting that the setup was designed with a total volume for the gas chamber limited to ≈ 50 cm<sup>3</sup> while all the measurements were performed with a high inlet flowrate of reactants (17 – 100 Nml·min<sup>-1</sup>). These conditions were chosen to avoid any gas starvation in the electrodes, and hence, to limit the concentration overpotentials as much as possible. Moreover, a compressive load of 1 kg was applied on the current collectors to minimize the contact resistances between the electrodes and the grids. All these precautions were taken to avoid the pollution of the electrode response with artifacts coming from the experimental setup. A specific attention has been paid to the water management to ensure a constant flowrate without fluctuation up to high steam content, therefore limiting the perturbations in the measurements for a wide range of gas compositions. For this purpose, the vapor was produced using a steam generator, which was kept in saturated conditions and was directly connected to a heated gas flowmeter. A second gas flowmeter was used for the hydrogen, and the two fluxes were mixed in the inlet pipe before entering the chamber. All the tubes were kept at ≈ 130°C to avoid any condensation. Finally, the exhausting gas was sent to a heat exchanger to separate the liquid H<sub>2</sub>O and the H<sub>2</sub>.

Concerning the experimental protocol, two cells were tested to check the reproducibility according to the following procedure. The tested cells were reduced under pure H<sub>2</sub> at 800°C for 24 hours. Subsequently, the cells were operated at 700°C for the whole duration of the test. In the first part of the characterization, the electrodes were swept under three gas compositions: H<sub>2</sub>/H<sub>2</sub>O = 25/75, 50/50 and 75/25 vol.%. For each composition, the i-U polarization curves measured between the electrodes and the reference (WE/CE vs RE = E<sup>meas</sup> (V/ref)) were recorded in potentiostatic mode between +0.2 V and -0.2 V with a step of 2 mV·s<sup>-1</sup>. In addition, the impedance spectra at Open Circuit Potential (OCP) have been measured in galvanostatic mode in the frequency range 10<sup>-1</sup>–10<sup>6</sup> Hz using a sinusoidal perturbation (i<sub>AC</sub>) of +/- 5 mA·cm<sup>-2</sup>. From the EIS data, the Ohmic resistance (R<sub>s</sub>) and the polarization resistance (R<sub>pol</sub>) have been obtained. The overpotential of the WE at each current density (η-i curve) has been determined by subtracting the ohmic contribution (= R<sub>s</sub> · i<sub>DC</sub>) to the overall voltage drop (i-V curve) (i.e.  $\eta(V/Ref) = (E_{WE}^{meas}(V/Ref) - R_s \cdot i_{DC}) - E_{WE}^{eq}(V/Ref)$ ).

In the second part of the test, a large range of gas compositions has been investigated (H<sub>2</sub>/H<sub>2</sub>O = 20/80, 30/70, 40/60, 50/50, 60/40, 70/30 and 80/20 vol.%) and for each condition the EIS at OCP has

been measured to determine the dependency of the polarization resistance on  $p_{H_2}$  and  $p_{H_2O}$ . All the measurements have been performed with an Autolab PGSTAT-302N electrochemical workstation.

### III.1.2.3 Experimental Results and Analyses

In order to check the validity of the measurements with the three-electrode experimental setup, the  $\eta$ - $i$  curves and EIS diagrams vs the RE have been measured at  $H_2/H_2O = 50/50$  vol.% for both electrodes (WE and CE). As shown in Figure III-3a, an almost the two polarization curves of the two electrodes are well superposed, indicating that the symmetrical behavior of the cell is accurately obtained in the setup. Besides, the impedance spectra at OCP for the two electrodes and for the complete symmetric cell are shown in Figure III-3b. It can be noticed that the EIS diagrams of the two electrodes are also well superposed and their sum corresponds to the impedance of the complete cell. These results indicate the absence of misalignment between the electrodes and confirm the validity of the RE positioning. Finally, it can be noticed that the data for the EIS are not perturbed with noise especially in the low frequency range, meaning that the steam supply is stable without any fluctuation. From all these observations, it can be claimed that the experimental setup can be confidently used for the electrochemical characterizations.

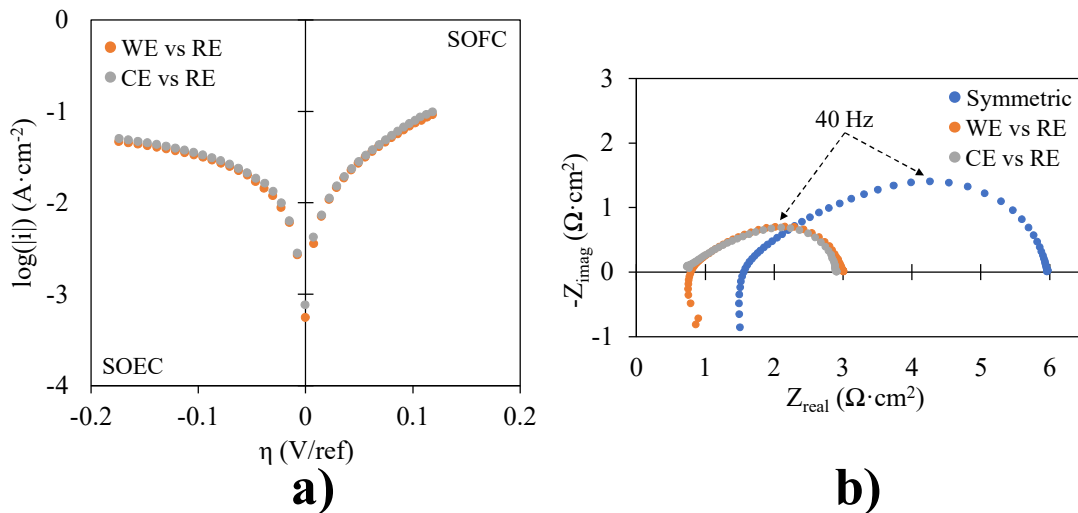


**Figure III-3: Illustration of validity of the measurements for the symmetric cell in the three-electrode setup (with  $H_2/H_2O = 50/50$  vol.% and  $T = 700^\circ\text{C}$ ): a)  $\eta$ - $i$  curves recorded for the WE and the CE vs the RE – b) EIS diagrams at OCP recorded for the two half-cell and the complete cell.**

Once the setup has been validated, the polarization curves at  $H_2/H_2O = 50/50, 25/75$  and  $75/25$  vol.% have been recorded and are provided in Figure III-4a and Figure III-4b (open symbols). A clear dissymmetry can be noticed between the two branches of the  $\eta$ - $i$  curve. The electrode response exhibits a strong potential-activated behavior in anodic polarization (SOFC mode) whereas a rather low limiting current density is observed in cathodic polarization (SOEC mode). This evolution

highlights a modification in the rate co-limiting steps; or it could even indicate a transition in the activated reaction pathway when changing the operating mode from anodic to cathodic polarization. More precisely, the potential-activated behavior under anodic current suggests that the reaction rate could be mainly dominated by the electrochemical reaction of charge transfer, while the presence of a limiting current density under cathodic polarization would reveal a co-limitation with a chemical reaction such as a gas-solid interaction. These statements are in good agreement with the experimental results already reported in literature [Dasari 2013, Grondin 2011, Pan 2016] for a Ni-8YSZ cermet electrode. Therefore, the co-limitation in electrolysis mode seems to appear irrespectively of the level of Zirconia doping from 3% to 8% moles of Ytria. This last remark might constitute a ‘weak’ clue suggesting that the co-limitation in SOEC mode would be more related to an interaction of gas with Ni.

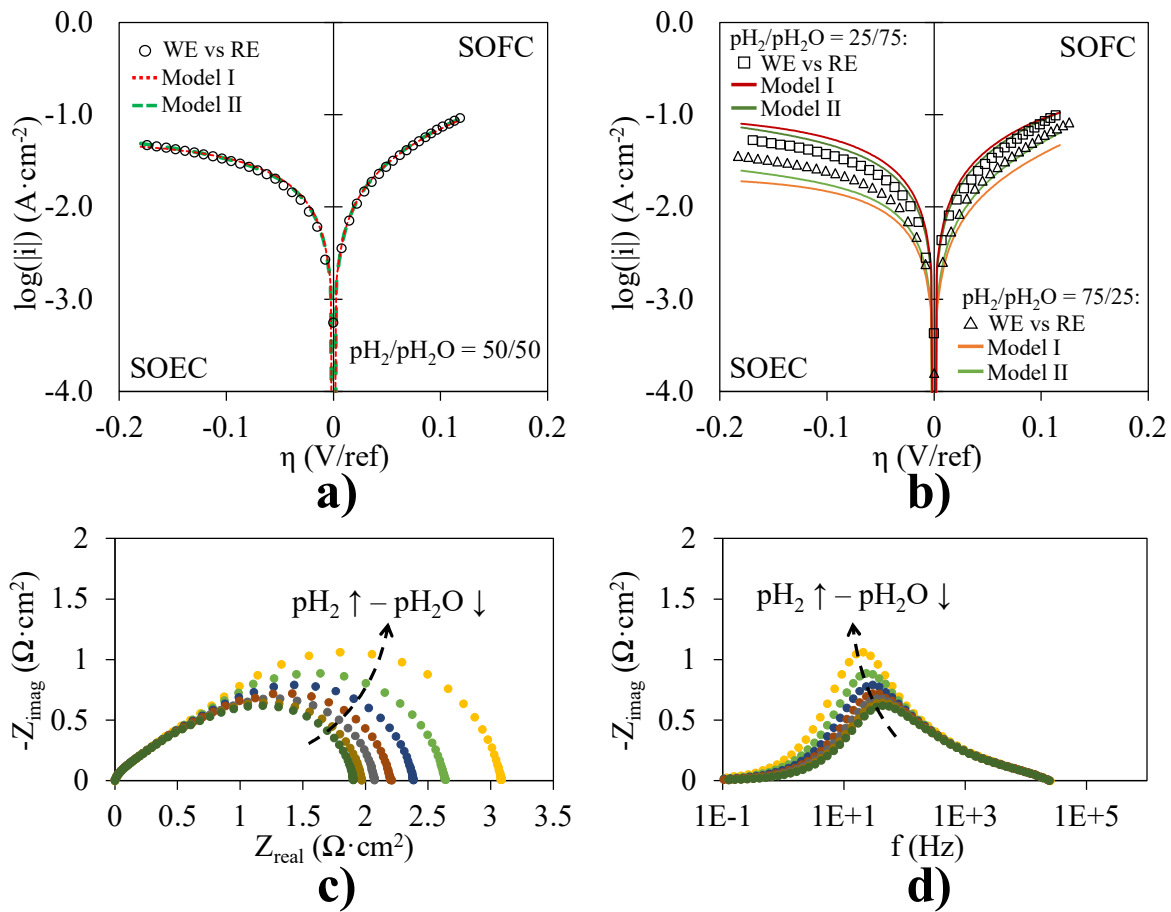


**Figure III-4: Experimental and simulation results at 700°C: a) Experimental and simulated  $\eta$ - $i$  curves with  $\text{H}_2/\text{H}_2\text{O} = 50/50$  vol.%– b) Experimental and simulated  $\eta$ - $i$  curves with  $\text{H}_2/\text{H}_2\text{O} = 25/75$  vol.% and  $\text{H}_2/\text{H}_2\text{O} = 75/25$  vol.%– Experimental Nyquist plot (c) and partial Bode plot (d) of the EIS diagrams at OCP measured at different  $\text{H}_2/\text{H}_2\text{O}$  ratios (20/80, 30/70, 40/60, 50/50, 60/40, 70/30, 80/20 vol.%).**

From Figure III-4b, it can be seen that the electrode response in both polarizations is improved when the partial pressure of steam is increased. Conversely, increasing the partial pressure of hydrogen

appears less impacting (so that the dominant effect is a worsening of the performances due to the decrease of  $p_{H_2O}$ ). Moreover, it can be noticed in Figure III-4b that the dependency of the electrode performance with  $p_{H_2O}$  is more pronounced in cathodic polarization, suggesting that the co-limiting step observed in electrolysis mode could be associated to an interaction of steam with the electrode surface.

To go further in the analysis, the impedance spectra have been acquired at OCP for a large range of gas compositions (Figure III-4c and Figure III-4d). As a first comment, it can be seen that the Nyquist plots of the diagrams (Figure III-4c) exhibit a global shape that tends toward a kind of Finite-Length Gerischer (FLG) impedance. This global shape of the EIS diagrams must be explained by the transport of oxygen vacancies in the 3YSZ backbone taking place in parallel to the electrochemical and chemical reactions in the electrode. In other words, the contributions with a line at around  $45^\circ$  from real axis in the Nyquist plot must be ascribed to a contribution of the oxygen vacancies migration in the depth of the electrode. Moreover, the FLG type impedance behavior would suggest that the reaction could extend over a large distance in the depth of the electrode compared the whole Ni-YSZ thickness [Nielsen 2011]. It is worth noting that this shape of the EIS spectra is in good agreement with the one published by Boukamp *et al.* [Boukamp 2006] for porous Ni/Ti-doped YSZ electrodes. When changing the steam content in the gas flow, they have reported a ‘minor dispersive contribution in the high frequency region and a dominating dispersion down to 0.01 Hz’. This global trend is also coherent with the EIS evolutions as a function of the  $p_{H_2}/p_{H_2O}$  ratio as displayed in Figure III-4c and Figure III-4d, even if a difference in the characteristic frequencies is detected.

The EIS data have been used to determine the dependency of the overall reaction rate at OCP on the partial pressure of hydrogen and steam. In this objective, the electrode polarization resistance has been classically expressed according to eq. (III-21) [Luo 2017].

$$R_{pol}^{OCP} = const \cdot p_{H_2}^{-\alpha} \cdot p_{H_2O}^{-\beta} \quad (III-21)$$

In which *const* is a proportionality factor and the exponents  $\alpha$  and  $\beta$  are the reaction orders at OCP with respect to  $H_2$  and  $H_2O$  respectively. A least-square algorithm has been used to fit the exponents  $\alpha$  and  $\beta$  for all the tested compositions (i.e.  $H_2/H_2O = 20/80, 30/70, 40/60, 50/50, 60/40, 70/30, 80/20$  vol.%). A single solution for the two exponents has been found for all the experimental data in the investigated range of gas compositions. This result means that the reaction is controlled by one single mechanism at OCP whatever the steam content in the gas mixture. The fitted values for the two exponents are given in Table III-V. A very low value has been obtained for the hydrogen ( $\alpha=0.035$ ) while the exponent on the steam partial pressure is much higher ( $\beta=0.38$ ). Therefore, the global

reaction rate of the electrode at OCP is almost independent of  $p_{H_2}$  whereas a clear influence of  $p_{H_2O}$  is found. This dependency confirms the behavior suggested by the  $\eta$ - $i$  curves. Moreover, as already mentioned, changing the steam content affects mainly the diagrams in the medium and low frequency range while they remain almost unchanged at high frequencies (Figure III-4d). Therefore, even at OCP, the electrode reaction rate is co-limited by the charge transfer (expected to appear at high frequencies in the diagram), the oxygen vacancies migration in 3YSZ (at intermediate frequencies) and a pure chemical surface process sensitive to the steam partial pressure (expected to arise at low frequencies in the diagram). According to the literature [Atangulov 1993, Boukamp 2006], this impact of steam on a FLG-type element for the cermet could be attributed to a slow steam adsorption/desorption coupled with surface diffusion up to the TPBs.

**Table III-V: Determination of the reaction order for  $H_2$  and  $H_2O$  at OCP from the experimental and simulated EIS with  $H_2/H_2O = 20/80, 30/70, 40/60, 50/50, 60/40, 70/30, 80/20$  vol.% and  $T = 700^\circ C$**

	Reaction order for $H_2$ ( $\alpha$ )	Reaction order for $H_2O$ ( $\beta$ )
Experimental results	0.035	0.38
Model I (standard version calibrated on $\eta$ - $i$ curves)	0.043	1.08
Model II (standard version calibrated on $\eta$ - $i$ curves)	0.066	0.81
Model II – limited by CR5 kinetics	0.119	0.55
Model II – limited by CR3 kinetics	0.024	0.86
Model II – limited by surface diffusion	0.046	0.77

To conclude, it can be stated from the experimental results that the overall reaction rate for the porous Ni-3YSZ cermet electrode is co-limited at OCP by the charge transfer at the TPBs, the oxygen solid-state diffusion in the electrode thickness and a surface process, which is sensitive to the steam partial pressure. This surface process could be associated to a steam-solid phase interaction potentially followed by a surface diffusional transfer. Finally, the strong dissymmetry of the electrode polarization curve suggests that the contribution of this surface process on the overall reaction rate appears to be more and more pronounced when changing the operating mode from anodic to cathodic polarization. It could even indicate a change in the reaction pathway between the two operating modes.

For a deeper analysis of the experimental data and to gain more insight about the nature of the co-limitations for the porous Ni-3YSZ electrode, the two elementary micro-kinetic models (Model I and Model II) implemented for the porous electrode have been used in order to discriminate between the two mechanisms for the Ni-3YSZ electrode and to check the validity of the assertions deduced from the experiments.

### III.1.3 Models Validation and Discussion

In order to verify which reaction mechanism is the most appropriate to describe the hydrogen oxidation/steam reduction reactions in a porous Ni-YSZ cermet the two models have been compared to the experimental data obtained in the symmetric setup. To limit the number of the unknown parameters, a 3D reconstruction of the cermet obtained by synchrotron X-ray nano-holotomography has been used to obtain the real microstructural data of the tested cermet that have been implemented in the micro-scale modes. In this section, the microstructural parameters from the 3D reconstruction are given and the comparison between the simulation results and the experimental data is analyzed.

#### III.1.3.1 Microstructural Parameters from the 3D Reconstruction

A Region Of Interest (ROI) containing the cermet has been extracted from the whole reconstruction obtained by synchrotron X-ray holotomography of the micro-pillar shown in Figure III-5a.

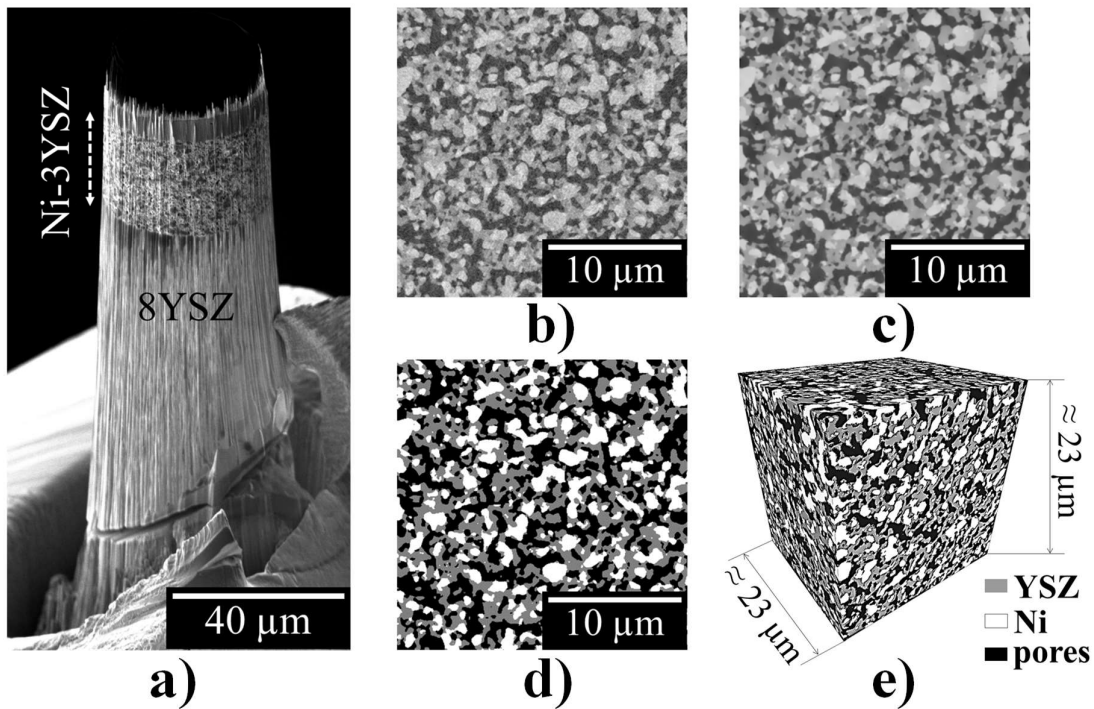


**Figure III-5: Determination of the cermet microstructural parameters: a) Pillar extracted from the reduced cell containing the electrode – b) 2D cross-section extracted from the raw reconstruction – c) 2D cross-section taken from the filtered reconstruction – d) Segmented cross-section – e) Rendering of the segmented 3D volume.**

A volume size of  $\approx 23 \times 23 \times 23 \mu\text{m}^3$  has been taken for the ROI, which is large enough to be well representative of the heterogeneous Ni-YSZ microstructure. Indeed, it has been already shown that the Representative Volume Elements (RVEs) for the functional layer microstructures of typical cermet electrodes are ranging from around  $15^3 \mu\text{m}^3$  to  $20^3 \mu\text{m}^3$  [Moussaoui 2018]. In Figure III-5b, a

2D slice of ROI extracted from the raw reconstruction is shown. As it can be seen, the three phases of the cermet can be identified by their corresponding grey-levels in the micrograph (darker: pores, grey: 3YSZ, clearer: Ni). Before computing the electrode microstructural properties, the 3D image has been segmented by labelling the Ni, YSZ and pore phases. To facilitate this image processing, the volume has been previously filtered using in-house codes to increase the contrast between the different phases and separate the peaks on the histogram (Figure III-5c). The filtering is based on the Malik-Perona method [Perona 1990] and the procedure followed in this work is reported in the work by Villanova *et al.* [Villanova 2013]. Subsequently, the volume has been segmented following the Otsu approach [Otsu 1979] and each of the three phases in the electrode has been labeled univocally (Figure III-5d). A rendering of the segmented 3D volume is given in Figure III-5e.

**Table III-VI: Microstructural properties of the Ni-3YSZ cermet electrode extracted from the 3D reconstruction**

Property	Value	Unit
Pores volume fraction ( $\varepsilon_{pores}$ )	39.85	(%)
Nickel volume fraction ( $\varepsilon_{Ni}$ )	21.57	(%)
3YSZ volume fraction ( $\varepsilon_{YSZ}$ )	36.36	(%)
Specific surface area between 3YSZ and pores ( $Sp_{YSZ-pores}$ )	2.09	( $\mu\text{m}^{-1}$ )
Specific surface area between pores and Ni ( $Sp_{pores-Ni}$ )	0.48	( $\mu\text{m}^{-1}$ )
Specific surface area between Ni and 3YSZ ( $Sp_{Ni-YSZ}$ )	0.97	( $\mu\text{m}^{-1}$ )
Mean pores radius ( $\bar{r}_{pores}$ )	0.26	( $\mu\text{m}$ )
Mean Ni particle radius ( $\bar{r}_{Ni}$ )	0.29	( $\mu\text{m}$ )
Mean 3YSZ particle radius ( $\bar{r}_{YSZ}$ )	0.19	( $\mu\text{m}$ )
Triple phase boundary length density ( $\xi^{TPBs}$ )	4.329	( $\mu\text{m}^{-2}$ )
Pores tortuosity factor ( $\tau_{pores}$ )	2.66	(-)
Ni tortuosity factor ( $\tau_{Ni}$ )	17.01	(-)
3YSZ tortuosity factor ( $\tau_{YSZ}$ )	2.75	(-)

Finally, the isolated voxels have been identified and excluded from the volumes used for the computation. In this way, only the percolated networks of each phase have been considered to evaluate the microstructural parameters. All the properties extracted from the volume are given in Table III-VI. The volume fractions ( $\varepsilon_a$ ), the interfacial specific surface areas between the phases ( $Sp_{a-b}$ ), the mean radii ( $\bar{r}_a$ ) and the density of the active TPBs lengths ( $\xi^{TPBs}$ ) have been measured using the methods reported by Moussaoui *et al.* [Moussaoui 2018]. In addition, the apparent tortuosity

factors ( $\tau_a$ ) of each phase has also been computed by homogenization following the procedure reported in the manuscript by Laurencin *et al.* [Laurencin 2012].

### III.1.3.2 Model calibration and elements of validation

For the simulations with each model, the thermodynamic data and the diffusion coefficients have been taken from literature, whereas all the microstructural parameters characterizing the cermet morphology have been deduced from the 3D reconstruction (cf. data listed in Table III-III, Table III-IV, Table III-VI, respectively). The other parameters including the forward kinetic constants of the reactions are given in Table III-VII for both models.

**Table III-VII: Parameters used in the simulations at 700°C**

Parameters used in both models	Value	Unit	
Density of available sites on Ni surface ( $\Gamma_{Ni}$ )	$1.7 \times 10^{-5}$	(mol·m <sup>-2</sup> )	[Hanna 2014]
Density of available sites on YSZ surface ( $\Gamma_{YSZ}$ )	$2.5 \times 10^{-5}$	(mol·m <sup>-2</sup> )	[Hanna 2014]
Double layer capacitance at the Ni/YSZ interface ( $C_{dl}$ )	1.3	(F·m <sup>-2</sup> )	[Hendriks 2002b]
Volume of the unit-cell for the 3YSZ ( $UCV$ )	134.47	(Å <sup>3</sup> )	[Ingel 1986]
<b>Forward kinetic constants (Model I)</b>			
Steam adsorption on Ni ( $k_{H_2O_{Ni}}^{ADS}$ )	$2.5 \times 10^2$	(s <sup>-1</sup> )	Fitted
Steam dissociation on Ni ( $k_{H_2O_{Ni}}^{DISS+}$ )	$1 \times 10^{10}$	(m <sup>2</sup> ·s <sup>-1</sup> ·mol <sup>-1</sup> )	Fitted
Hydroxyl dissociation on Ni ( $k_{OH_{Ni}}^{DISS+}$ )	$7.5 \times 10^{10}$	(m <sup>2</sup> ·s <sup>-1</sup> ·mol <sup>-1</sup> )	Fitted
Hydrogen desorption from Ni ( $k_{H_{2Ni}}^{DES}$ )	$1.6 \times 10^7$	(m <sup>2</sup> ·s <sup>-1</sup> ·mol <sup>-1</sup> )	Fitted
Charge transfer reaction in the reduction direction ( $k^{red}$ )	$2 \times 10^3$	(m <sup>3</sup> ·s <sup>-1</sup> ·mol <sup>-1</sup> )	Fitted
Oxygen incorporation in the YSZ ( $k_{O_{YSZ}^{INC}}/C_{O_0^{ref}}(YSZ)$ )	$1 \times 10^5$	(m <sup>3</sup> ·s <sup>-1</sup> ·mol <sup>-1</sup> )	Assumed as not limiting
<b>Forward kinetic constants (Model II)</b>			
Steam adsorption on Ni ( $k_{H_2O_{Ni}}^{ADS}$ )	$1.25 \times 10^2$	(s <sup>-1</sup> )	Fitted
Steam adsorption on YSZ ( $k_{H_2O_{YSZ}}^{ADS}$ )	$1 \times 10^2$	(s <sup>-1</sup> )	Fitted
Steam dissociation on YSZ ( $k_{H_2O_{YSZ}}^{DISS+}$ )	$2.5 \times 10^{13}$	(m <sup>2</sup> ·s <sup>-1</sup> ·mol <sup>-1</sup> )	Assumed as not limiting
Hydrogen desorption from Ni ( $k_{H_{2Ni}}^{DES}$ )	$8.1 \times 10^7$	(m <sup>2</sup> ·s <sup>-1</sup> ·mol <sup>-1</sup> )	Fitted
First charge transfer reaction in the reduction direction ( $k_1^{red}$ )	$1 \times 10^3$	(m <sup>3</sup> ·s <sup>-1</sup> ·mol <sup>-1</sup> )	Fitted
Second charge transfer reaction in the reduction direction ( $k_2^{red}$ )	$7.5 \times 10^2$	(m <sup>3</sup> ·s <sup>-1</sup> ·mol <sup>-1</sup> )	Fitted
Oxygen incorporation in the YSZ ( $k_{O_{YSZ}^{INC}}/C_{O_0^{ref}}(YSZ)$ )	$1 \times 10^5$	(m <sup>3</sup> ·s <sup>-1</sup> ·mol <sup>-1</sup> )	Assumed as not limiting

As first step of the validation, the two models have been calibrated fitting the simulated  $\eta$ - $i$  curves on the experimental one at  $H_2/H_2O = 50/50$  vol.%. The objective on these preliminary simulations was to identify the numerical values of the unknown kinetic parameters for the two studied models. The results of the fitting procedure are shown in Figure III-4a. It is worth noting that the error minimization between the experimental data and the simulated curves has led to determine a single set of solutions for the missing parameters of the two models. In this condition, it was found that both models are able to mimic accurately the  $\eta$ - $i$  curves. Indeed, the asymmetric behavior between the cathodic and the anodic branches is accurately reproduced by the oxygen spillover mechanism (Model I) as well as the hydrogen spillover mechanism (Model II).

Once calibrated on the  $\eta$ - $i$  curve at  $H_2/H_2O = 50/50$  vol.%, the EIS diagram at OCP measured in the same conditions has been simulated with the two models (Figure III-6a and Figure III-6b). It can be noticed that this validation step has carried out without any further adjustments of the input models parameters. In this condition, it has been found that both models are able to predict with a good level of confidence the impedance diagram in terms of shape (Figure III-6a) but also in terms of frequency distribution (Figure III-6b). Based on these results, both reaction pathways appear to be suitable to predict the electrode response. At this stage, it is thus not possible to discriminate between the two elementary models for the porous Ni-3YSZ electrode.

To gain more insight about the most relevant mechanism, the  $\eta$ - $i$  curves at different partial pressures have been simulated using the two calibrated models. As shown in Figure III-4b, a slight difference is found between the simulated curves and the experimental results. Indeed, both models overestimate the effect of the steam partial pressure on the electrode response. This statement is also confirmed by the impedance spectra simulated at different  $p_{H_2}/p_{H_2O}$  (Figure III-6). Although the two models are able to mimic the electrode behavior in terms of frequency distribution, the decrease of the simulated polarization resistance with increasing the  $H_2O$  partial pressure is higher than the experimental one (Figure III-6c and Figure III-6d). In contrast, the opposite behavior is observed when increasing the partial pressure of hydrogen (Figure III-6e and Figure III-6f). Nevertheless, it can be noticed that the simulated curves obtained with Model II are significantly closer to the measured data suggesting that the mechanism based on the hydrogen spillover could be more relevant for a Ni-3YSZ cermet electrode. To support this claim, the exponents on the  $H_2$  and  $H_2O$  partial pressures involved in the expression of the electrode polarization resistance at OCP (eq. (III-21)) have been evaluated by computing the electrode response over the same range of gas compositions than the one used for the experiments. The results obtained with the calibrated models are given and compared to the

experimental exponents in Table III-V. Although the effect of  $\text{pH}_2\text{O}$  is slightly overestimated on both cases, it is worth noting that the two models are able to retrieve the very low dependency of  $R_{\text{pol}}$  on the hydrogen partial pressure. Regarding the exponent for  $\text{pH}_2\text{O}$ , it appears that the prediction given by Model II is more accurate than Model I even if the discrepancy between the experimental exponent and the calculated one remains noticeable. Therefore, the comparison between the reaction orders obtained for Model I and Model II reinforces the statement that the reaction mechanism based on the hydrogen spillover charge transfer appears to be the most suitable to describe the electrode response.

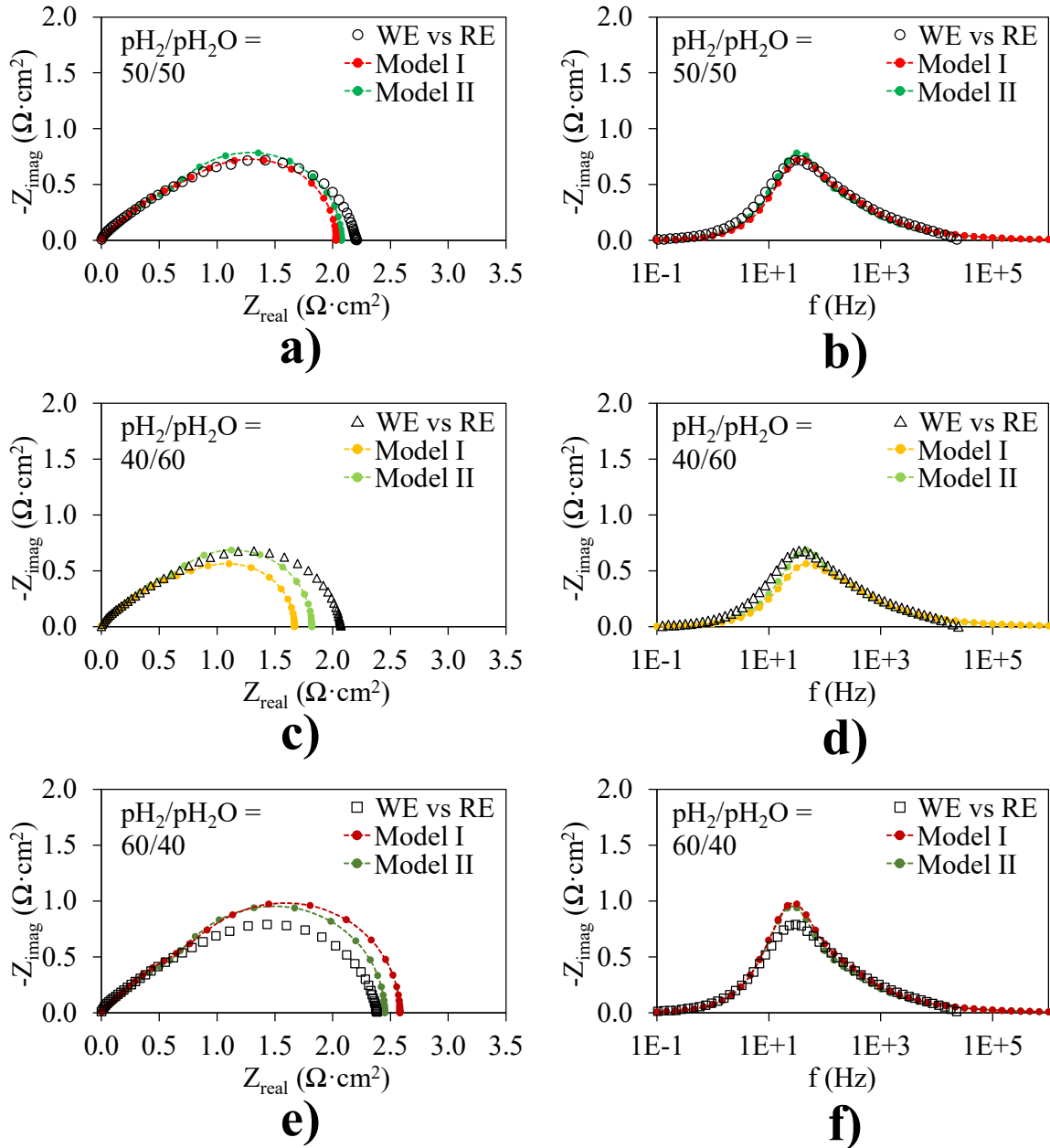


**Figure III-6: Experimental and simulated impedance spectra at OCP with different  $\text{pH}_2/\text{pH}_2\text{O}$ : Nyquist (a) and partial Bode (b) plots with  $\text{H}_2/\text{H}_2\text{O} = 50/50$  vol.%– Nyquist (c) and partial Bode (d) plots with  $\text{H}_2/\text{H}_2\text{O} = 40/60$  vol.% – Nyquist (e) and partial Bode (f) plots with  $\text{H}_2/\text{H}_2\text{O} = 60/40$  vol.%.**

To conclude, the model based on the hydrogen spillover mechanism is found to capture the global electrode behavior in an acceptable way, even if its predictability must be still improved. Therefore, it seems that the mechanism proposed for the Ni-8YSZ cermet is still valid for the porous Ni-3YSZ electrode. Consequently, Model II could be used to analyze the nature of the limiting reactions for the Ni-3YSZ electrode.

### *III.1.3.3 Discussion*

*Reaction mechanism and electrode co-limiting steps with Model II* – Simulations have been conducted with the most likely reaction mechanism (Model II) in order to identify the dominant pathway and the main limiting steps in the electrode global process for the porous Ni-3YSZ cermet.

First, a sensitivity analysis has been performed by changing the tortuosity factor of the 3YSZ affecting its ionic conductivity. As expected, it was found that the polarization curve is dependent on this parameter meaning that the electrode efficiency is partially limited by the oxygen vacancies transfer from the electrolyte into the depth of the electrode. The EIS simulations have also confirmed that this limitation is related to the contribution, at high and intermediate frequencies, related to the line at around  $45^\circ$  in the impedance spectra. This statement strengthens the interpretation of the experimental EIS diagrams as a kind of (finite-length) Gerischer element, which can be seen as a transmission line model [Shin 2016] for which the local resistance induced by the transport of vacancies is in parallel with a resistance and a capacitor associated to the reaction process. In addition, a sensitivity analysis on the diffusion coefficients has revealed that the electrode response appears to be slightly dependent on the diffusion of YSZ-attached hydroxyl ions, suggesting that this species could play a key role on the electrode response. Moreover, changing the density of active TPBs has also shown that the overall kinetic rate is affected by this parameter controlling the reactions of charge transfer. It was also confirmed that the contribution of the electrochemical reactions appears at high frequencies in the impedance spectra. Finally, the skewed semi-circle at low frequencies, which is sensitive the global electrode specific surface area, is clearly ascribed to a chemical process taking place at the solid-gas interface.

In order to identify the suspected co-limiting step due to the gas-solid interaction associated to the semi-circle at low frequencies in the EIS diagram, the local kinetic rates for the steam adsorption on Ni (**CR1**) and YSZ (**CR2**) have been plotted in the electrode thickness (at  $H_2/H_2O = 50/50$  vol.% for an electrode overpotential of -0.06 V and +0.06 V) (Figure III-7a and Figure III-7b). In the simulated conditions, it is found that both reactions extend in the whole electrode thickness suggesting that the

entire functional layer contributes to the electrode response. This modeling result is fully consistent with the global shape of the experimental electrode impedance related to a type of finite-length Gerischer element (cf. Figure III-4c and Figure III-4d).

Moreover, it can be noticed in Figure III-7a and Figure III-7b that the kinetics of the two reactions of adsorptions (**CR1** and **CR2**) are activated in both polarizations, indicating that steam interacts with both Ni and YSZ surfaces.

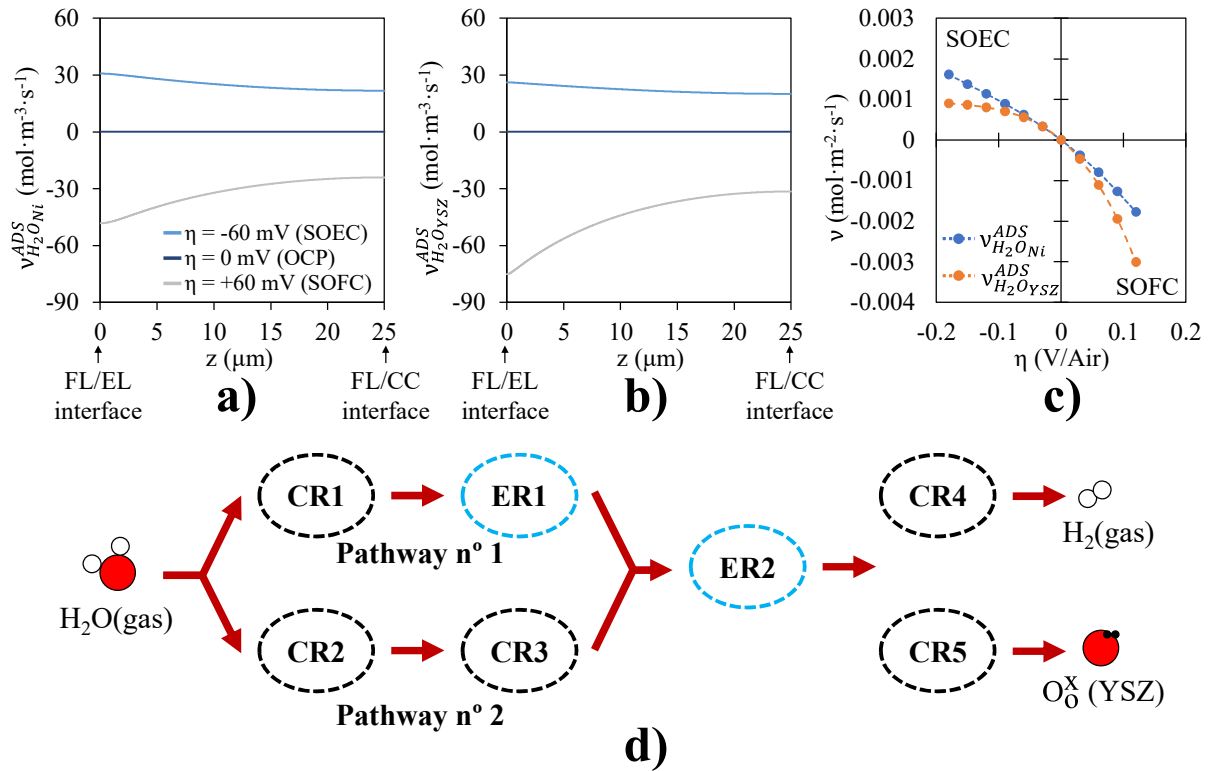


**Figure III-7: Results of the simulation with Model II on the steam interaction with Ni and YSZ surfaces with H<sub>2</sub>/H<sub>2</sub>O = 50/50 vol.%. a) Local kinetic rate of H<sub>2</sub>O adsorption/desorption on Ni surface (**CR1**) – b) Local kinetic rate of H<sub>2</sub>O adsorption/desorption on YSZ surface (**CR3**) – c) Kinetic rate of steam adsorption/desorption on Ni and YSZ integrated over the electrode thickness as a function of the overpotential – d) Schematic representation of the two parallel pathways for the electrode reaction with Model II (given in electrolysis mode).**

In electrolysis mode, the gaseous H<sub>2</sub>O is partially adsorbed on the Ni surface (Figure III-7a). In this case, the adsorbed molecules are reduced directly at the TPBs by the first charge transfer reaction (**ER1**) according to the pathway n°1 defined as **CR1** followed by **ER1** (cf. schematic representation in Figure III-7d). In parallel, it can be seen in Figure III-7b that the gaseous H<sub>2</sub>O molecules are also adsorbed on the YSZ surface where they dissociate in two hydroxyl ions according to the pathway n°2 defined as the **CR2** followed by the **CR3** (Figure III-7d). In both cases, the hydroxyl ions, which are produced by the two pathways, are commonly consumed by the second charge transfer (**ER2**).

In fuel cell mode, the opposite directions for the two pathways are found with part of the steam produced *via* the oxidation at the TPBs (**Reverse-ER1** and **Reverse-CR1**) (pathway n°1) and part of the H<sub>2</sub>O formed directly on the YSZ surface through the reverse reaction of the water dissociation (**Reverse-CR3** and **Reverse-CR2**) (pathway n°2).

Therefore, this simulation results show that two pathways are activated in parallel for the two operating mode as shown in Figure III-7d (i.e. pathway n°1: **CR1** followed by **ER1**, pathway n°2: **CR2** followed by **CR3**, while the common reactions belonging to the two pathways corresponds to the second charge transfer (**ER2**), the oxygen incorporation in YSZ (**CR5**) and the hydrogen desorption from Ni (**CR4**)).

In order to determine the contribution of each pathway to the total electrode response, the local kinetic rates integrated over the electrode thickness are plotted as a function of the overpotential in Figure III-7c. Interestingly, a modification in the dominant pathway is highlighted. In fuel cell mode, most of the steam is produced by the water desorption from the YSZ surface according to the pathway n°2, whereas in electrolysis mode, the reaction mechanism is dominated by the pathway n°1. Indeed, in this case, the contribution of the H<sub>2</sub>O adsorbed on Ni is higher compared to the reaction of adsorption on YSZ. Therefore, these modeling results suggest that the nature of the co-limitation due to the gas-solid interaction would change with the electrode polarization. Under anodic current (fuel cell mode), the reaction would be mainly controlled by the pathway n°2, which is co-limited by the steam interaction with YSZ (cf. Figure III-7d). On the contrary, the pathway n°1, which is co-limited by the interaction of steam with Ni, would be activated under electrolysis current (cf. Figure III-7d) (knowing that the rate of steam adsorption on YSZ becomes negligible for this polarization). This global behavior allows identifying the nature of the gas-solid interaction, which was highlighted experimentally, but also explain the dissymmetry of the electrode polarization curves in the two operating modes.

To deepen the analysis and clarify the details of the mechanism, the local kinetic rates of the two charge transfer reactions (**ER1** and **ER2**) are given in Figure III-8 at H<sub>2</sub>/H<sub>2</sub>O = 50/50 vol.% and -0.06 V / +0.06 V. Whatever the electrode polarization, it can be seen that the rate of the second charge transfer reaction (**ER2**) is always higher with respect to the first one (**ER1**) (Figure III-8). In addition, the charge transfer reaction **ER2** is strongly promoted at the FL/EL interface whereas **ER1** takes place more homogeneously along the electrode thickness. This difference in the distribution of the two reaction rates is associated to the reacting species involved in the second charge transfer. Indeed, it is reminded that **ER2** involves as product (or reactant in the fuel cell mode) the oxygen ions coming

from the electrolyte. Because of the very fast kinetic rate of the oxygen exchange from the surface into the bulk of YSZ, this reaction **ER2** is thus strongly promoted in a region close to the electrolyte interface. In order to investigate the impact of these electrochemical reactions on the two reaction pathways, the surface coverages of hydroxyl ions and water attached on the YSZ as well as water attached on the Ni are given in Figure III-9.

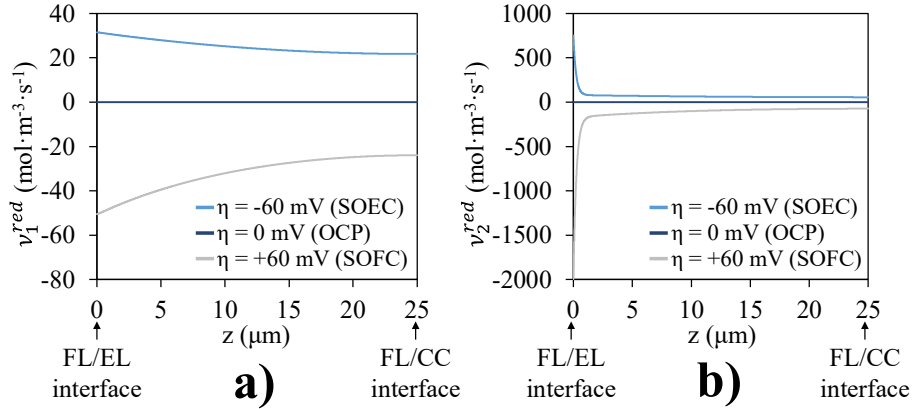


**Figure III-8: Kinetic rate of the charge transfer reactions at different polarizations with  $\text{H}_2/\text{H}_2\text{O} = 50/50$  vol.%: a) Local kinetic rate of the first charge transfer reaction (ER1) – b) Local kinetic rate of the second charge transfer reaction (ER2).**

In fuel cell mode for which the pathway  $n^{\circ}2$  is activated, the fast charge transfer **ER2** corresponds to an increase of surface attached hydroxyl ions (Figure III-9a). This increase favors both (i) the reverse reaction of water dissociation (**Reverse-CR3**) and (ii) the first charge transfer reaction (**Reverse-ER1**), leading to produce  $\text{H}_2\text{O}$  on both the YSZ surface (Figure III-9b) and the Ni surface (Figure III-9c), respectively. Nevertheless, due to the fast kinetic of the reverse dissociation, a significant part of  $\text{H}_2\text{O}$  is formed directly on the YSZ surface where the coverage of water is increased by almost one order of magnitude with respect to the equilibrium conditions. This increase promotes the direct desorption of water from the YSZ surface. All these evolutions provide an insight in the underlying mechanism explaining why the pathway  $n^{\circ}2$  dominates the reaction mechanism under anodic polarization (fuel cell mode). It can be noticed that the direct formation of  $\text{H}_2\text{O}$  on the YSZ surface *via* the reverse reaction of dissociation is not considered in the reaction scheme proposed in other works [Luo 2019] for which only the charge transfer reaction (**ER1**) is taken into account. However, based on our modeling results, it appears that the direct formation of water on the YSZ surface would also contribute to the electrode response. This possibility has been suggested by Goodwin *et al.* [Goodwin 2009] even if it was finally not included in their modeling scheme.

In electrolysis mode where the pathway  $n^{\circ}1$  is dominant, the fast kinetic of **ER2** triggers an important consumption of  $\text{OH}_{\text{YSZ}}^-$  (Figure III-9a) which promotes the steam dissociation reaction on the YSZ

surface (**CR3**) and the H<sub>2</sub>O reduction at the TPBs (**ER1**). The very fast dissociation reaction consumes the H<sub>2</sub>O on the YSZ surface causing a drop in the water surface coverage (Figure III-9b). This decrease of water attached on the YSZ surface is not balanced by the adsorption reaction (**CR2**) blocking the pathway n°2, so that the reduction of Ni-attached H<sub>2</sub>O at the TPBs (**ER1**) becomes the main source of hydroxyl ions on the YSZ surface (resulting in the activation of the pathway n°1).

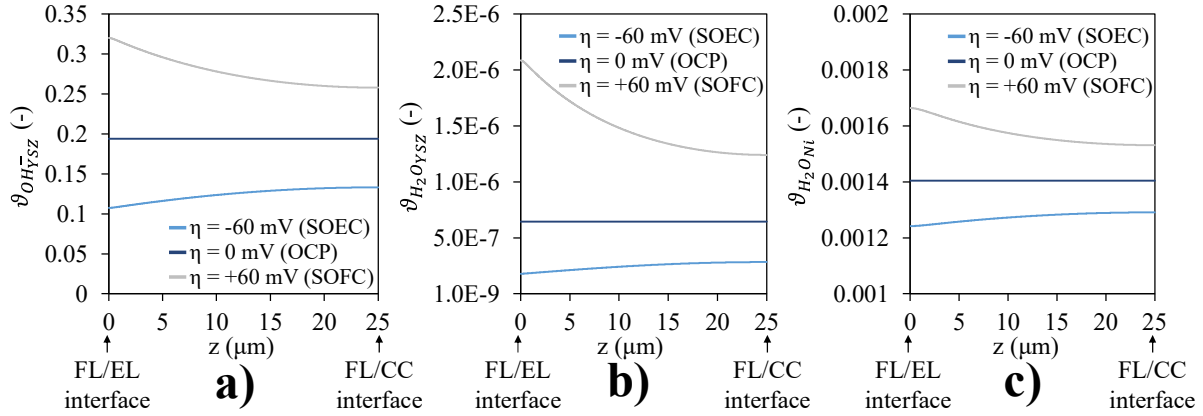


**Figure III-9: Local surface coverages at different polarizations with H<sub>2</sub>/H<sub>2</sub>O = 50/50 vol.%: a) hydroxyl ions on the YSZ surface – b) H<sub>2</sub>O on the YSZ surface – c) H<sub>2</sub>O on the Ni surface.**

To summarize, the global reaction rate is dominated in fuel cell mode (i.e. anodic polarization) by the pathway n°2. In this case, most of the steam is produced on the YSZ surface and the reaction rate is mostly controlled by the charge transfer reaction (**ER2**) and the water desorption from the YSZ (reverse of **CR2**). In electrolysis mode (i.e. cathodic polarization), the pathway n°1 becomes predominant. Indeed, the adsorption rate of H<sub>2</sub>O on the YSZ (**CR2**) becomes very slow yielding to activate the contribution of the first charge transfer reaction (**ER1**) and the steam adsorption on Ni (**CR1**). As this last reaction is not kinetically favored, it explains the appearance of a relatively low limiting current density in electrolysis mode.

As a general comment, it can be inferred from this numerical analysis that the second charge transfer at the TPBs (**ER2**) and the variation in concentration for the YSZ-attached hydroxyl ions play a key role on the electrode response in both polarizations. This strong effect of YSZ-attached hydroxyl ions has been ascribed to their production/consumption and is consistent with the influence of the  $OH_{YSZ}^-$  surface diffusivity on the electrode response.

*Sensitivity analysis on Model II parameters* – A complementary sensitivity analysis has been performed aiming to improve the Model II predictability regarding the dependence of the electrode response with p<sub>H<sub>2</sub>O</sub>. This study has been realized with the purpose to check the validity of the assumptions concerning the non-limiting nature of the oxygen ions incorporation into YSZ and the

water dissociation reactions on the YSZ surface (**CR5** and **CR3**, respectively). In addition, according to the simulation results, the surface coverage of  $OH_{YSZ}^-$  and its surface diffusion are expected to have an impact on the electrode response. However, as already stated, a large uncertainty exists on the diffusion coefficients, especially for the surface-attached species. This means that the contribution of the surface diffusion could have been slightly underestimated [Vogler 2009]. For this reason, a third sensitivity analysis has been carried out to investigate the impact on the reaction of the hydroxyl ions surface diffusivity.

The analysis have been carried out by lowering the value of the examined parameter in order to make the electrode response dependent on it (or to increase the dependency in case of the  $OH_{YSZ}^-$  diffusivity). Afterwards, the forward kinetic constants of the other reactions have been re-fitted on the experimental  $\eta$ -i curve at  $H_2/H_2O = 50/50$  vol.% and the EIS at OCP have been simulated without any further adjustment. In addition, the reaction orders with respect to  $H_2$  and  $H_2O$  have been evaluated and compared to the results obtained experimentally. The values of the hydroxyl diffusion coefficient and of the forward kinetic constants used in the sensitivity analysis are reported in Table III-VIII while the results are given in Figure III-10 and Table III-V.

**Table III-VIII: Parameters in the sensitivity analysis for Model II**

	Limited by CR5 kinetic	Limited by CR3 kinetic	Limited by $OH_{YSZ}^-$ diffusion	Unit
YSZ-attached hydroxyl ions diffusion coefficient ( $D_{OH_{YSZ}^-}$ )	$1.45 \times 10^{-9}$	$1.45 \times 10^{-9}$	$1.45 \times 10^{-11}$	$(m^2 \cdot s^{-1})$
Steam adsorption on Ni ( $k_{H_2O_{Ni}}^{ADS}$ )	$5 \times 10^2$	$7.5 \times 10^1$	$1.25 \times 10^2$	$(s^{-1})$
Steam adsorption on YSZ ( $k_{H_2O_{YSZ}}^{ADS}$ )	$5 \times 10^2$	$1.5 \times 10^2$	$1.25 \times 10^2$	$(s^{-1})$
Steam dissociation on YSZ ( $k_{H_2O_{YSZ}}^{DISS+}$ )	$1 \times 10^{11}$	$1 \times 10^8$	$2.5 \times 10^{11}$	$(m^2 \cdot s^{-1} \cdot mol^{-1})$
Hydrogen desorption from Ni ( $k_{H_2Ni}^{DES}$ )	$4 \times 10^{12}$	$8.1 \times 10^7$	$8.1 \times 10^8$	$(m^2 \cdot s^{-1} \cdot mol^{-1})$
First charge transfer reaction in the reduction direction ( $k_1^{red}$ )	$2 \times 10^3$	$3 \times 10^3$	$1 \times 10^3$	$(m^3 \cdot s^{-1} \cdot mol^{-1})$
Second charge transfer reaction in the reduction direction ( $k_2^{red}$ )	$1 \times 10^3$	$1 \times 10^2$	$5 \times 10^3$	$(m^3 \cdot s^{-1} \cdot mol^{-1})$
Oxygen incorporation in the YSZ ( $k_{O_{YSZ}}^{INC}/C_{O_0}^{ref}(YSZ)$ )	$5 \times 10^{-3}$	$1 \times 10^5$	$1 \times 10^5$	$(m^3 \cdot s^{-1} \cdot mol^{-1})$

As shown in Figure III-10a-c, it is possible to obtain a satisfactory fitting of the electrode  $\eta$ -i curve at  $H_2/H_2O = 50/50$  vol.% in all the three analyzed cases. Nevertheless, the EIS diagram calculated at OCP with the model limited by the oxygen ions incorporation/excorporation reaction (**CR5**) presents a different shape from the experimental spectrum (Figure III-10d). Indeed, in this case, the impedance arc at  $\approx 40$  Hz appears to be similar to a pure semicircle with a more ideal capacitive behavior

compared to the experimental one. Besides, the simulated characteristic frequency is clearly shifted towards higher values and does not match anymore the experimental data. For these reasons, it can be stated that the hypothesis on the not-limiting nature of the reaction **CR5** is well confirmed.

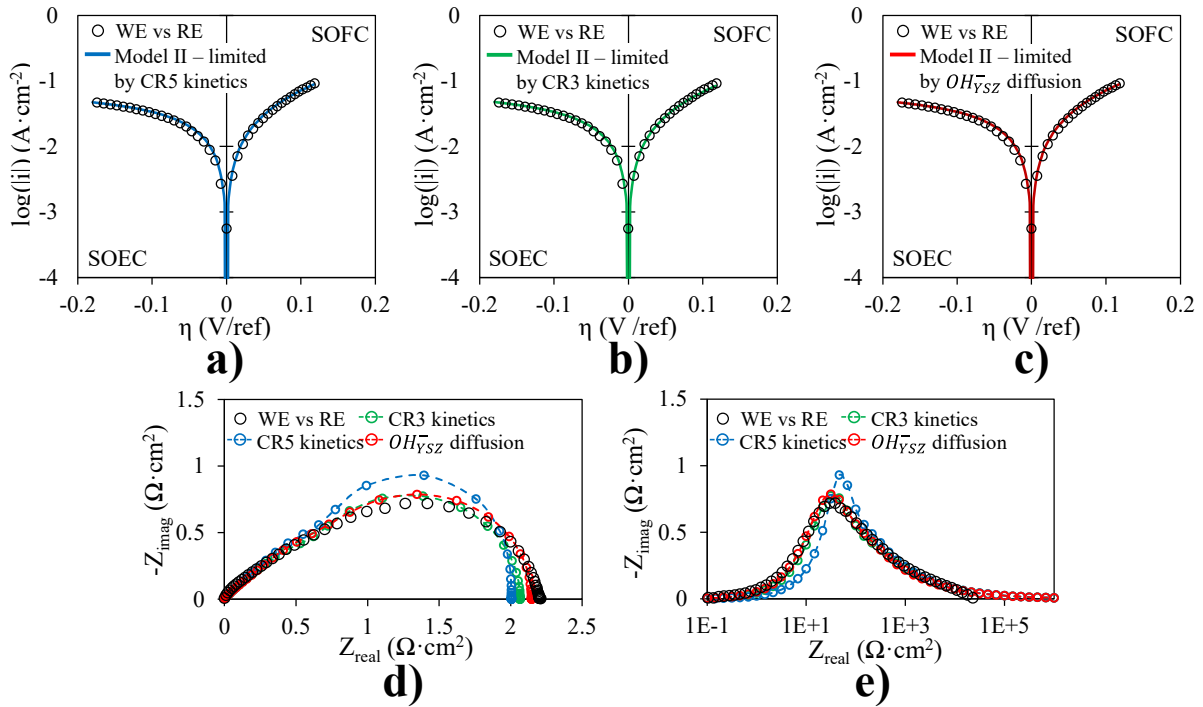


**Figure III-10: Results of the sensitivity analysis on the parameters of Model II at 700°C: a)  $\eta$ - $i$  curve at  $\text{H}_2/\text{H}_2\text{O} = 50/50$  vol.% for the model limited by the incorporation/excorporation of oxygen ions in the YSZ (CR5) – b)  $\eta$ - $i$  curve at  $\text{H}_2/\text{H}_2\text{O} = 50/50$  vol.% for the model limited by the dissociation of water adsorbed on the YSZ (CR3) – c)  $\eta$ - $i$  curve at  $\text{H}_2/\text{H}_2\text{O} = 50/50$  vol.% for the model limited by the surface diffusion of hydroxyl ions on the YSZ – Nyquist (d) and partial Bode (e) plots of the EIS diagrams at OCP at  $\text{H}_2/\text{H}_2\text{O} = 50/50$  vol.%.**

When using the model limited by the kinetics of water dissociation (**CR3**), it is also possible to reproduce accurately the  $\eta$ - $i$  curves and the EIS diagrams (Figure III-10 Figure III-10e). Nevertheless, the reaction orders for  $\text{H}_2$  and  $\text{H}_2\text{O}$  become less consistent in this case (cf. Table III-V). In particular, the exponent for the steam partial pressure is increased with respect to the reference parameters of Model II, obtaining a value that is even less comparable to the experimental data. Therefore, the hypothesis of fast water dissociation on the YSZ surface is also confirmed.

Finally, the decrease of the hydroxyl ions diffusivity on the YSZ surface has been studied. From Figure III-10, it can be seen that, increasing the limitation by  $\text{OH}^-_{\text{YSZ}}$  diffusion, the polarization curves as well as the EIS diagrams at OCP are well captured by the model. Moreover, it can be seen in Table III-V that the orders of reaction for hydrogen and water obtained with this model are more similar to the experimental data with respect to the ones calculated with the standard version of Model II. This result indicates that the impact of the surface diffusion of  $\text{OH}^-_{\text{YSZ}}$  on the electrode response could be

higher than in the standard case. From this point of view, the surface diffusivity of the hydroxyl ions appears to be key property that would require a precise determination for a better prediction of the electrode behavior.

### *III.1.4 Concluding Remarks and Model Adaptation for the Degradation Studies*

#### *III.1.4.1 Conclusion on the Model Relevance to Predict the Electrode Performances*

To investigate the nature of the hydrogen electrode reactions in the two polarizations, two micro-kinetic elementary models, based on the oxygen and hydrogen spillover mechanisms, have been developed.

To discriminate which reaction mechanism is the most appropriate to describe the electrode response, experimental characterizations have been carried out at 700°C with symmetric cells having porous electrodes made of Ni-3YSZ over a large range of gas compositions. Analyzing the experimental results, the  $\eta$ - $i$  curves have shown that electrode response is activated by the electrode potential in anodic polarization while a strong co-limitation is found under cathodic current. The electrode performances were found to be significantly dependent on variations of steam partial pressure whereas modifying the partial pressure of hydrogen had a substantially lower impact. Impedance spectra have been also measured at OCP with a shape exhibiting a type of finite-length Gerischer element. The skewed semi-circle at low frequencies was also found to be strongly sensitive to the steam content in the gas phase. Thanks to all these observations, it has been suggested that the co-limitation especially under electrolysis current is related to an interaction of steam with the one of the electrode solid phases.

The models have been validated on the experimental results considering the real microstructural properties of the tested cermet which have been deduced from a 3D electrode reconstruction obtained by synchrotron X-ray nano-holotomography. It has been shown that the model based on the hydrogen spillover mechanism is the most appropriate to predict in an acceptable way the electrode response in terms of impedance spectra and polarization curves obtained at different gas compositions.

Once validated, the model based on the hydrogen spillover mechanism has been used in order to clarify the reaction pathway for the Ni-3YSZ electrode. The analysis of the simulated impedance diagrams at OCP has confirmed that the electrode reaction rate is co-limited by the charge transfer at TPBs (contribution arising at high frequencies in the diagram), the oxygen vacancies migration in 3YSZ network and a pure chemical surface process (contribution arising at low frequencies).

Moreover, the simulations under polarizations have highlighted a change of reaction pathway from cathodic to anodic polarizations. In fuel cell mode, the charge transfer would be mainly controlled by the electrochemical reduction of the hydroxyl ions and by the water desorption from the YSZ surface. In electrolysis mode, the adsorption rate of H<sub>2</sub>O on the YSZ would become very slow leading to activate a reaction pathway controlled by the steam adsorption on Ni. This change of mechanism explains the strong dissymmetry of the electrode polarization curve. Moreover, it has been clearly shown that the attached hydroxyl ions on the YSZ surface play a key role of this electrode mechanism.

In addition, a sensitivity analysis on the main model assumptions has been carried out to improve the accuracy of the simulations. On the one hand, it has been confirmed that the hypotheses based on the non-limiting nature of the water dissociation on the YSZ surface as well as the incorporation of oxygen ions in the YSZ lattice are correct. On the other hand, it has been found that decreasing the surface diffusivity of the hydroxyl ions could improve the global quality of the model predictions. Knowing the uncertainty on this key parameter, it can be reasonably supposed that electrode response is also co-controlled by surface diffusion.

#### *III.1.4.2 Model II Adaptation for the Degradation Studies*

Thanks to these analyses, the hydrogen spillover mechanism has been confirmed to be the most appropriate model to describe the hydrogen electrode reaction. Therefore, this mechanism has been selected in chapter IV to compute the Ni-YSZ electrode response in order to investigate the effects of the microstructural evolutions after aging. Beforehand, the model has been slightly adapted for the degradation studies. Indeed, it could be suspected that all the possible Ni-attached species and their evolutions in operation could play a crucial role on the cermet degradation. Therefore, Model II has been complemented by adding all the species suspected to be involved in the degradation mechanism. For this purpose, the chemical reactions, which have been taken into account on the Ni surface for Model I, has been also considered for the second version of Model II as shown in Figure III-11. They correspond to the water molecule dissociation into one hydrogen and one hydroxyl adsorbate (**CR6**). Then, the hydroxyls are further decomposed into hydrogen and oxygen attaches species (**CR7**). These reactions are summarized in Table III-IX where the forward kinetic constants are also given for both reactions.

It can be noticed that these reactions have been introduced by considering a fast kinetics to keep them at equilibrium. Nevertheless, it has been found that the coverage rates of the active species on Ni surface are not significantly affected by the new adsorbed species introduced in the model. Indeed, from the thermodynamic data reported in Table III-III a very low numerical value for the oxygen and

hydroxyl coverages on Ni at equilibrium is obtained. Therefore, the introduction of the water and hydroxyl dissociations on the Ni surface does not change the electrode response. Consequently, the mechanism remains based on the hydrogen spillover charge transfers. In addition, since the oxygen spillover was not considered in the second version of Model II, the newly introduced species are not involved in the electrochemical charge transfers and thus cannot limit the overall electrode kinetics. For all these reasons, it has been found that the electrode response for the pristine electrode remains unchanged, and hence, all the model conclusions drawn using the standard version of Model II remain valid. The choice to use a simplified version for the validation step was initially motivated to limit the number of unknown model parameters as much as possible.

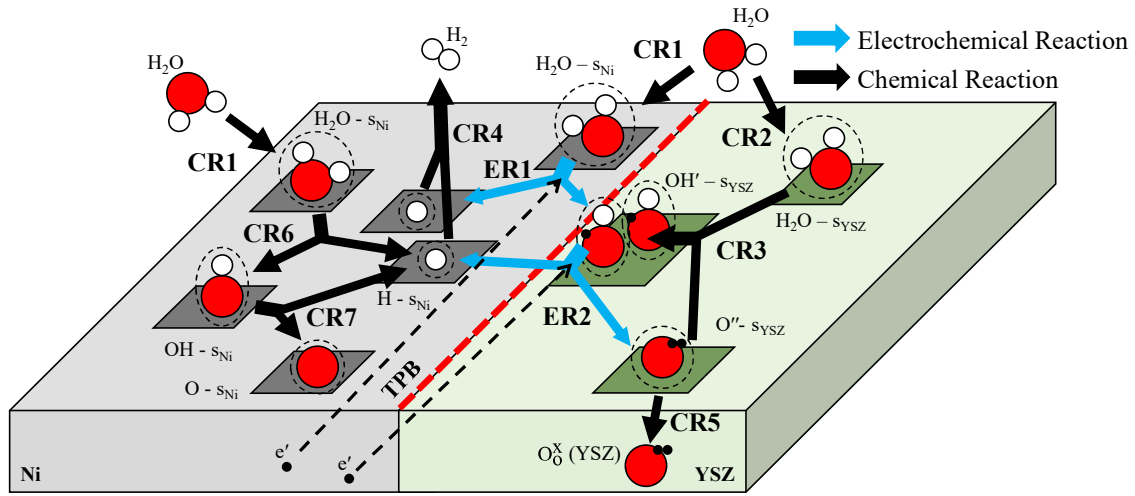


**Figure III-11: Adaptation of Model II to study the degradation considering water and hydroxyl dissociation on the surface of Ni.**

**Table III-IX: Reactions on Ni surface added in the hydrogen spillover micro-scale model to study the degradation**

CR6	H <sub>2</sub> O dissociation on the Ni surface	$H_2O_{Ni} + s_{Ni} \xrightleftharpoons[k_{H_2O_{Ni}}^{DISS-}]{k_{H_2O_{Ni}}^{DISS+}} OH_{Ni} + H_{Ni}$	$k_{H_2O_{Ni}}^{DISS+} = 1 \times 10^{12} \text{ (m}^2 \cdot \text{s}^{-1} \cdot \text{mol}^{-1}\text{)}$
CR7	Hydroxyl dissociation on Ni surface	$OH_{Ni} + s_{Ni} \xrightleftharpoons[k_{OH_{Ni}}^{DISS-}]{k_{OH_{Ni}}^{DISS+}} O_{Ni} + H_{Ni}$	$k_{OH_{Ni}}^{DISS+} = 1 \times 10^{12} \text{ (m}^2 \cdot \text{s}^{-1} \cdot \text{mol}^{-1}\text{)}$

### III.2 Micro-Scale Model for the Oxygen Electrode

As introduced in the first chapter of this thesis, a stationary and dynamic model for porous LSCF and LSCF-GDC composite electrodes has been developed in the frame of a previous PhD thesis [Hubert 2018]. This model allowed the simulation of polarization curves [Laurencin 2015] as well as EIS at OCP and under polarization [Hubert 2016]. A special attention was paid to take into account the

influence of the electrode microstructure on the transport and electrochemical processes. The model considers two parallel reaction pathways combining the oxygen exchange at the LSCF/gas interface (i.e. “bulk path”) and the direct oxidation/reduction at the TPBs (i.e. “surface path”). As expected for the porous LSCF electrode, the simulations have shown that the reaction pathway is dominated by the bulk path under cathodic polarization and at OCP. Nonetheless, the simulations have highlighted a transition from the bulk to the surface path occurring in anodic polarization. The presence of a polarization threshold that depends on the temperature in electrolysis mode is thus proposed but still needs to be fully validated [Laurencin 2015].

In the frame of this thesis, the reaction mechanism for the porous LSCF electrodes in anodic polarization has been validated. For this purpose, experiments have been conducted at different temperatures on two symmetric cells (denoted Cell I and Cell II thereafter) exhibiting different microstructures prepared and tested in two independent ways. For one of the two cells, the polarization curves and the impedance spectra at OCP and under anodic polarization have been simulated with the model considering the electrode microstructural properties taken from a 3D reconstruction. For the other cell, electrochemical tests have been performed in order to obtain two sets of independent experimental data to validate the electrode behavior. The presence of a threshold related to the transition from the bulk to the surface path has been verified, confirming the modification of the reaction pathway in anodic polarization for the porous LSCF electrode. Subsequently, the impact of temperature on the reaction pathway has been investigated and the value of the LSCF/GDC double layer capacitance has been discussed.

### *III.2.1 Experimental Characterization*

In this section, the experimental campaigns carried out to validate the reaction mechanism for the pure LSCF electrode are described. The first cell (Cell I) was characterized by a post-doctoral student, Dr. Sergii Pylypko, at CEA. The second cell (Cell II) was manufactured and tested by another PhD student, Vladyslav Tezyk, in the frame of a collaboration with LEPMI/CNRS.

The tested cells and the experimental setups are described hereafter. Moreover, the experimental results are analyzed.

#### *III.2.1.1 Cells Description*

Two different symmetric button cells (Cell I and Cell II) were fabricated with the same  $\text{La}_{0.6}\text{Sr}_{0.4}\text{Co}_{0.2}\text{Fe}_{0.8}\text{O}_{3-\delta}$  material. The manufacturing conditions were not the same for the two cells in

order to obtain different electrode microstructures. The main characteristics and conditions of cell fabrication are detailed hereafter:

- For the first cell (Cell I), a  $\text{La}_{0.6}\text{Sr}_{0.4}\text{Co}_{0.2}\text{Fe}_{0.8}\text{O}_{3-\delta}$  commercial powder provided by Fuel Cell Materials was used ( $d_{50} = 0.6 \mu\text{m}$ ). Porous LSCF electrodes with a thickness of  $\approx 35 \mu\text{m}$  and a surface area of  $1 \text{ cm}^2$  were deposited symmetrically by screen printing on both sides of a dense 8YSZ electrolyte (diameter: 25 mm, thickness: 260  $\mu\text{m}$ , provider: Kerafol). A  $\text{Ce}_{0.8}\text{Gd}_{0.2}\text{O}_{2-\delta}$  barrier layer of 2  $\mu\text{m}$  was deposited by screen printing to limit the formation of insulating phases ( $\text{SrZrO}_3$  and  $\text{La}_2\text{Zr}_2\text{O}_7$ ) between LSCF and YSZ (Figure III-12a). GDC powder was provided by Fuel Cell Materials. LSCF and GDC inks were made up by mixing LSCF or GDC powders (nearly 50 wt%) with a mixture of terpineol (Sigma Aldrich) as solvent and PVb (Polyvinyl butyral) as binder. GDC was sintered at 1300 °C for 1 hour and LSCF at 1000°C for 1 hour.

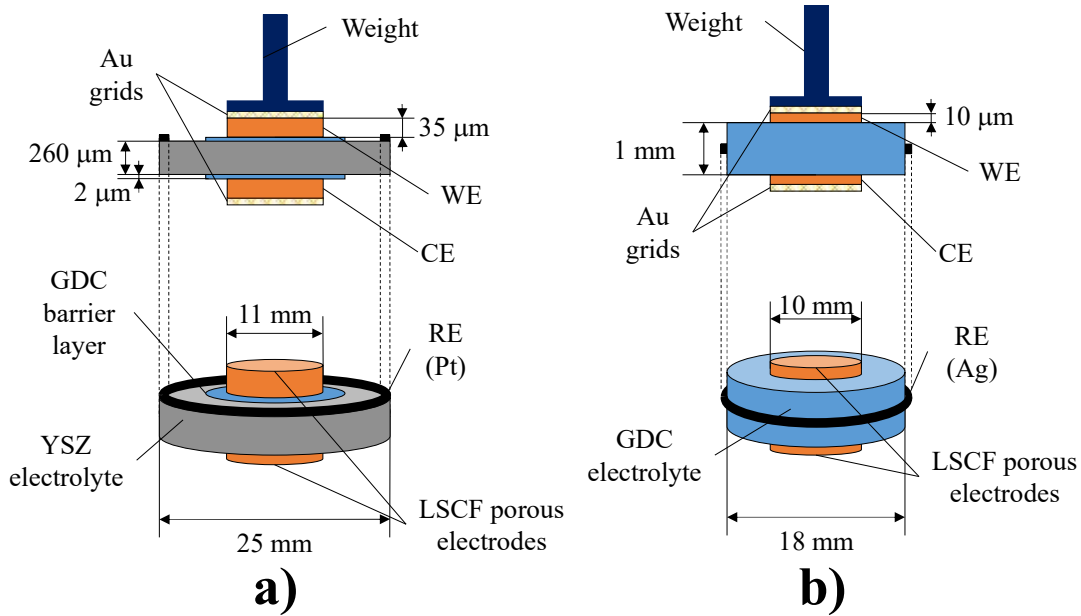


**Figure III-12: Cell dimensions and experimental setups: a) Cell I – b) Cell II.**

- For the second cell (Cell II), a  $\text{La}_{0.6}\text{Sr}_{0.4}\text{Co}_{0.2}\text{Fe}_{0.8}\text{O}_{3-\delta}$  commercial powder provided by Marion Technologies ( $d_{50} = 0.27 \mu\text{m}$ ) was used. X-Ray Diffraction showed that it contained a small amount of  $\text{SrCO}_3$  impurity. Porous LSCF electrodes with a thickness of  $\approx 10 \mu\text{m}$  and a surface area of  $0.79 \text{ cm}^2$  were deposited symmetrically by screen printing on both sides of a dense  $\text{Ce}_{0.9}\text{Gd}_{0.1}\text{O}_{2-\delta}$  electrolyte (Figure III-12b). The GDC substrate (1 mm thick and 18 mm in diameter) was prepared by isostatic pressing of powder (Praxair, 99.9 %,  $20.5 \text{ m}^2 \cdot \text{g}^{-1}$ ) at 300 MPa, followed by sintering at 1200°C for 2 h in air. Afterwards, the substrate was grinded in order to obtain a flat and uniform surface with good adhesion. The LSCF ink was made up by mixing

LSCF powder with a commercial solvent “Product KD2921” (ZSCHIMMER & SCHWARZ) 50/50 wt% and 2% total weight polymer PVb (Polyvinyl butyral) as binder. A printing screen with a very fine mesh was used. The screen-printed sample was pre-annealed at 450°C (heating rate 1°C·min<sup>-1</sup>) in order to burn out binders and ink solvents. Then, it was fired at 900°C for 2 hours in air (heating rate 2°C·min<sup>-1</sup>). Observation of electrode polished cross-sections with a SEM has revealed a rather fine LSCF microstructure.

It is worth noting that, also in these cases, a special attention has been paid to center the WE and the CE on the two faces of the electrolyte in order to avoid any perturbation on the EIS measurements [Adler 2000].

### *III.2.1.2 Experimental Setups and Testing Conditions*

Both cells have been characterized using a three-electrode configuration, as presented in Figure III-12. For Cell I, the RE consists in a Pt wire applied on the upper surface of the electrolyte on the periphery of the membrane as far as possible from the electrode (i.e. the diameter of the Pt wire ring is  $\approx 25$  mm as illustrated in Figure III-12a). For Cell II, on the other hand, an Ag wire is positioned on the edge of the GDC pellet in the middle of the electrolyte thickness and is used as reference electrode (Figure III-12b). It can be noticed that, for both configurations, the rules for positioning of RE have been fulfilled [Jiang 2017]. Moreover, gold grids with equal surface to the LSCF electrodes are used as current collectors. To ensure the electrical contact between the grids and the electrodes, a load of  $\approx 0.7$  kg is applied on the setups.

The electrochemical responses of Cell I and Cell II were characterized in two independent test rigs. Before the study, the consistency of the two benches has been checked and calibrated by testing a same type of cell in the two setups. The protocols of cells characterization are detailed hereafter:

- Cell I has been analyzed at three temperatures (700°C, 750°C and 800°C) with a high air flowrate (67 Nml·min<sup>-1</sup>) to ensure homogenized gas supply in the test rig. All temperature changes have been performed with an heating rate of 1 °C·min<sup>-1</sup>. At each temperature, electrode polarization curves have been recorded in galvanostatic mode with a current step of 1 mA·s<sup>-1</sup>. EIS measurements were carried out in galvanostatic mode at OCP and under anodic polarization for different steady-state current densities,  $i_{DC}$ . The diagrams were acquired in the frequency range of 10<sup>-2</sup> Hz – 10<sup>4</sup> Hz with a sinusoidal perturbation,  $i_{AC}$ , of +/- 10 mA·cm<sup>-2</sup>. All electrochemical

measurements have been conducted using an Autolab potentiostat/impedance frequency analyzer (PGSTAT302N).

- For Cell II, the electrochemical characterizations have been conducted at 700°C with an air flowrate of  $\approx 50 \text{ Nml} \cdot \text{min}^{-1}$ . The polarization curves have been measured in potentiostatic mode with an applied potential ranging from 0.3 V to -0.7 V (potential step of 50 mV) and an equilibration time equal to 600 s. Impedance spectra have been acquired in potentiostatic mode at OCP and under anodic polarization in the frequency range of  $2 \times 10^3 \text{ Hz}$  to  $5 \times 10^{-1} \text{ Hz}$  with an amplitude of  $\pm 50 \text{ mV}$ . Prior to the electrochemical tests at 700°C, impedance spectra at OCP were also measured as a function of the temperature from 400°C to 700°C. All the measurements have been performed with a Solartron SI 1280B electrochemical workstation.

For both experiments, the amplitude of the sinusoidal perturbation for the impedance measurements was chosen to remain in the linear regime of the cell polarization curve response. Furthermore, diagrams measured on the half-cells (i.e. between the WE/CE and the RE) are roughly the same at OCP, and their sum is equal to the EIS of the complete cell (i.e. between the WE and CE) confirming the reliability of the measurements.

### III.2.1.3 Experimental Results

*Results for Cell I* – The experimental electrode polarization curves  $\eta$ - $i$  at 700°C, 750°C and 800°C of the WE of Cell I are presented in Figure III-13a, while the corresponding electrode polarization resistances are plotted in Figure III-13b.

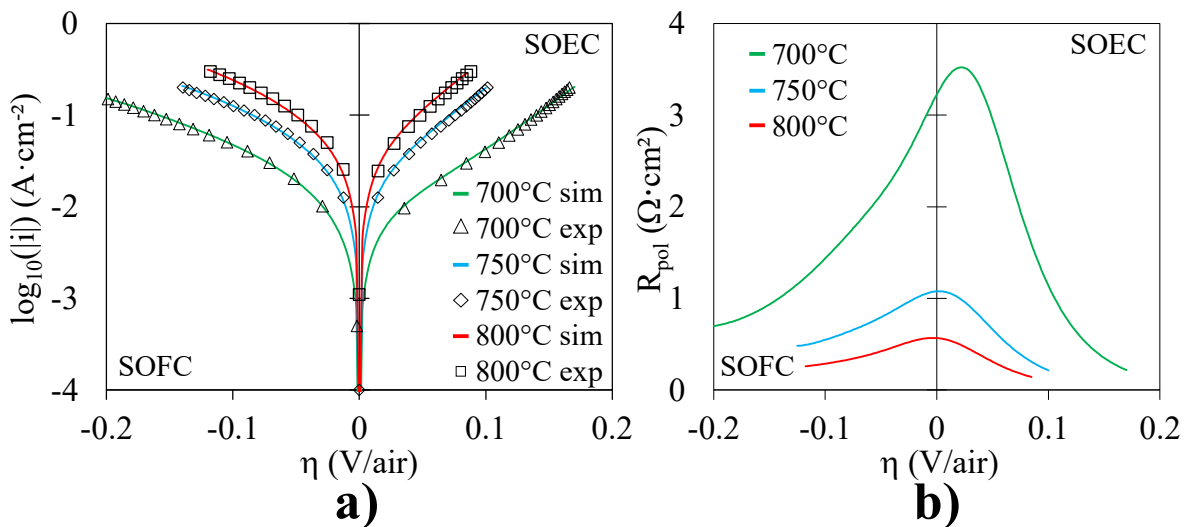


**Figure III-13: Results for the WE of Cell I at 700°C, 750°C and 800°C in air atmosphere ( $p_{\text{O}_2} = 0.21 \text{ atm}$ ): a) Experimental and simulated  $\eta$ - $i$  curves – b) Electrode polarization resistance.**

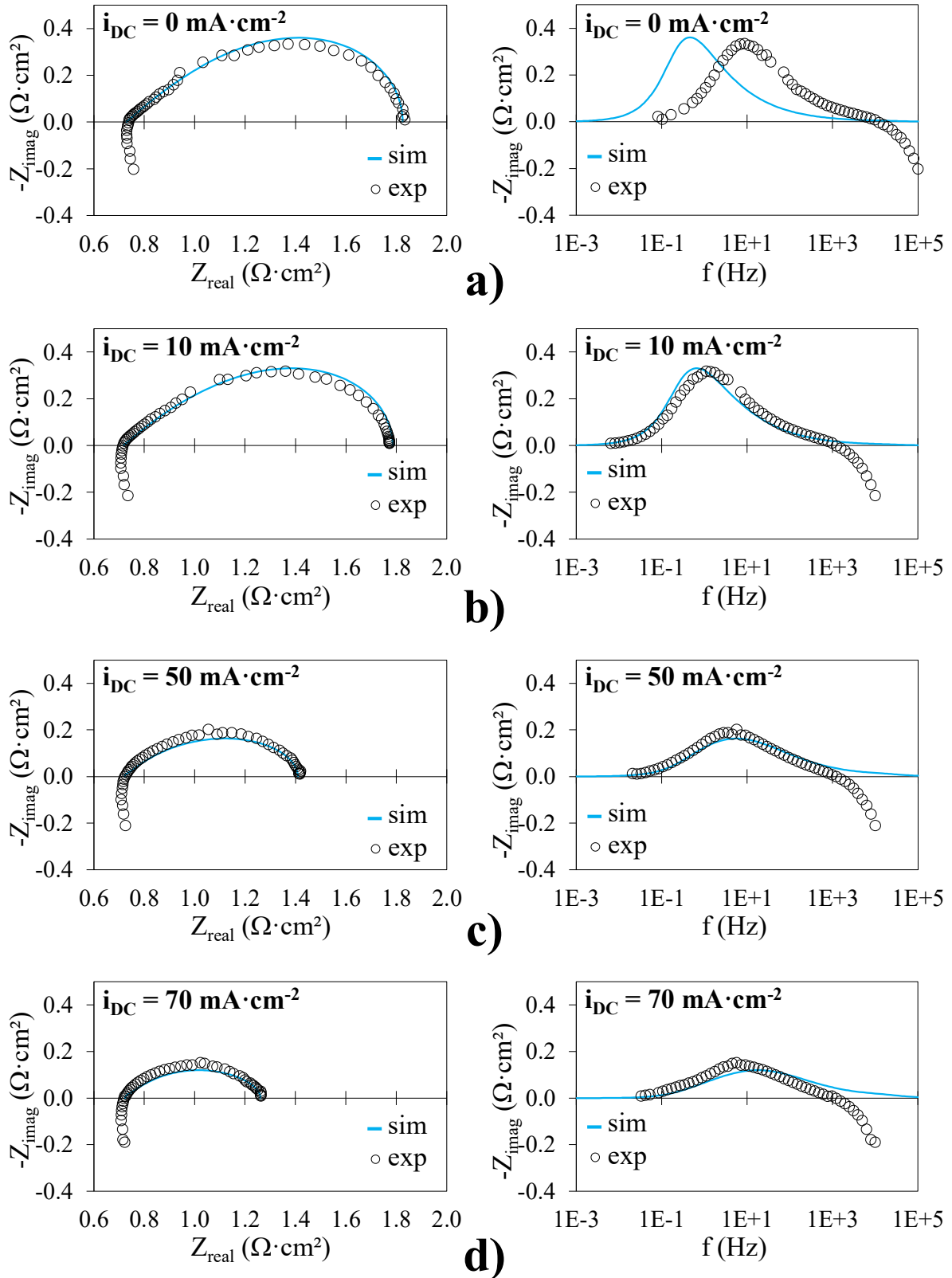


**Figure III-14: Impedance spectra for Cell I at 750°C recorded at different current densities, Nyquist plot (left) and partial Bode plot (right): a)  $i_{DC} = 0 \text{ mA} \cdot \text{cm}^{-2}$  – b)  $i_{DC} = 10 \text{ mA} \cdot \text{cm}^{-2}$  – c)  $i_{DC} = 50 \text{ mA} \cdot \text{cm}^{-2}$  – d)  $i_{DC} = 70 \text{ mA} \cdot \text{cm}^{-2}$  (line=simulation, open symbols=experimental,  $i_{AC} = \pm 10 \text{ mA} \cdot \text{cm}^{-2}$ ).**

The electrode polarization curves exhibit a non-symmetrical shape with respect to the OCP (Figure III-13a). Indeed, the  $\eta$ - $i$  curves present a strong potential-dependent activation in anodic polarization, while in cathodic polarization, the curves show a more linear behavior. This evolution could be related to a modification of the reaction mechanism depending on the cathodic or anodic polarization. This statement is confirmed by the evolution of  $R_{pol}$  plotted as a function of the electrode overpotential (Figure III-13b). Indeed, the curves exhibit a dissymmetry with a steeper decrease in anodic polarization indicating a strong potential-dependent activation. In addition, it can be seen at 700°C that the change in the slope of  $R_{pol}=f(\eta)$  occurs for a slight anodic overpotential. It means that the change in reaction mechanism is triggered when the anodic polarization exceeds a specific threshold estimated to  $\approx 0.02$  V/air at 700°C. As shown in Figure III-13b, this threshold is found to be shifted toward the OCP when the temperature is increased.

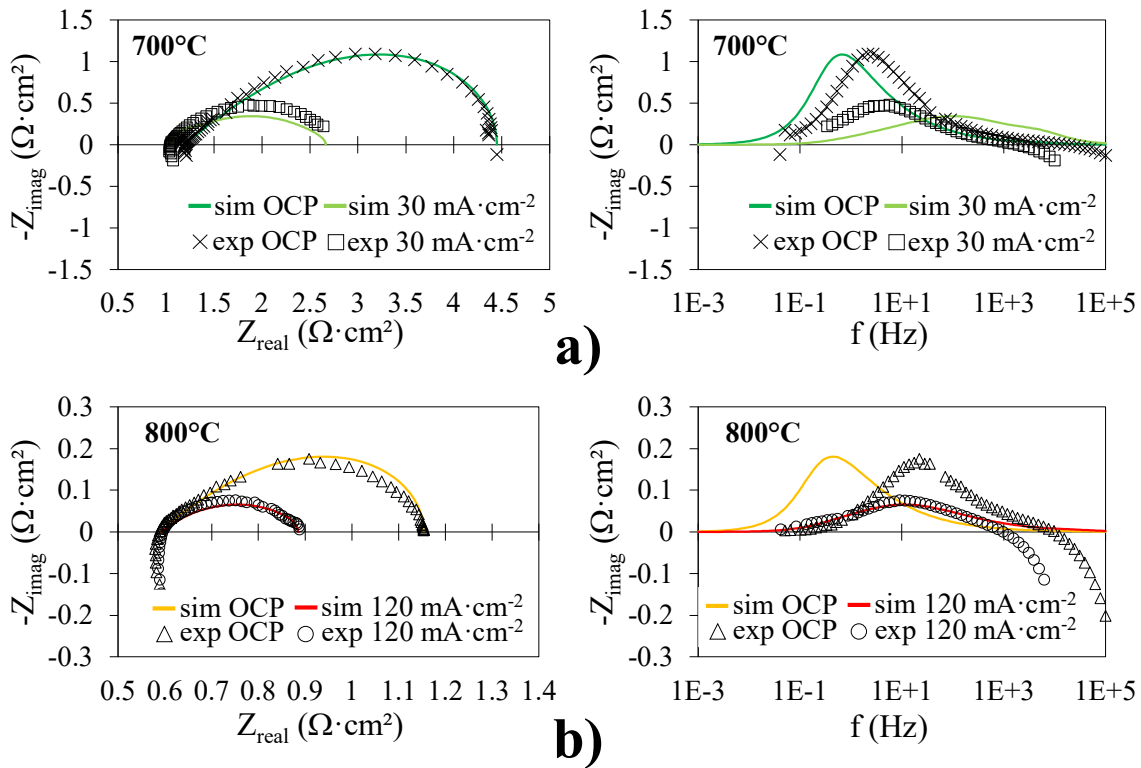


**Figure III-15: Impedance spectra for Cell I recorded at OCP and under anodic polarization at different temperatures, Nyquist plot (left) and partial Bode plot (right): a) 700°C – b) 800°C (lines= simulation, open symbols=experimental,  $i_{AC} = \pm 10 \text{ mA} \cdot \text{cm}^{-2}$ ).**

To go further in the analysis, impedance spectra have been acquired at OCP and for different anodic DC currents. The evolution of the EIS with anodic polarization is given in Figure III-14 at 750°C. As expected at OCP [Adler 1996, Grunbaum 2006], the diagram corresponds to a classical Gerischer-type element. However, the shape of the spectra is affected by the anodic polarization. Indeed, increasing the DC current results in a modification from the Gerischer-type element towards more

flattened and convoluted diagrams. This observation is consistent with the change in electrode reaction mechanism under anodic polarization that was deduced from the  $\eta$ -i curves. Moreover, the same trend is observed at 700°C and 800°C as shown in Figure III-15. Interestingly, the modification of the EIS shape happens at lower overpotential for higher temperature. These results also reinforce the claim of a temperature-dependent threshold for the change in reaction mechanism.

*Results for Cell II* – The results for Cell II are shown in Figure III-16 where the current density and polarization resistance deduced from the EIS are plotted as a function of the electrode overpotential at 700°C. Even if the two cells differ in terms of preparation techniques and microstructures, it can be noticed that they present similar performances in cathodic polarization. However, the performances of Cell II appear to be significantly higher under anodic polarization. This result is consistent with its finer electrode microstructure due to its lower sintering temperature and also to its smaller nominal grain size of the powder [Hubert 2016].

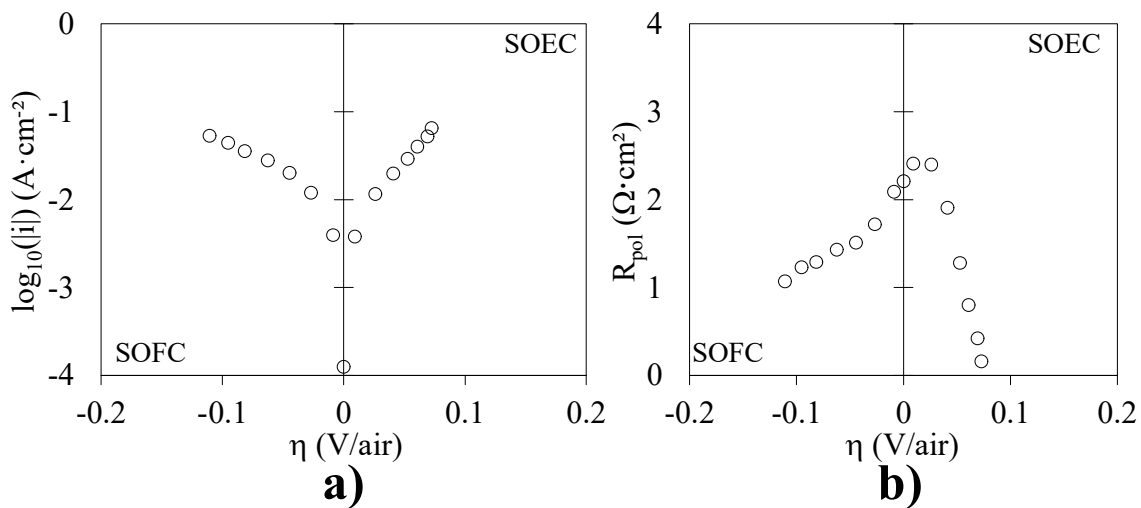


**Figure III-16: Results for Cell II at 700°C in air atmosphere ( $pO_2 = 0.21$  atm): a) Experimental and simulated  $\eta$ -i curves – b) Electrode polarization resistance.**

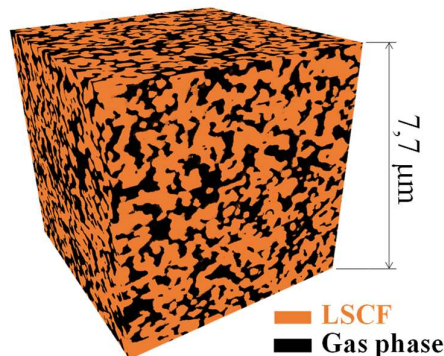
It is worth mentioning that the electrode response for Cell II presents the same behavior of Cell I with a clear non-symmetrical shape and a strong electrode potential-dependent activation in anodic polarization. An “asymmetry in performance under cathodic and anodic polarization” was also observed by Marina *et al.* [Marina 2007] for a  $La_{0.6}Sr_{0.4}Co_{0.2}Fe_{0.8}O_{3-\delta}$  electrode deposited on a Samaria-doped Ceria barrier layer. Nevertheless, in their case, the losses were found to be lower in cathodic than anodic polarization. This apparent discrepancy with these results could be also explained by the dependence of electrode response with the microstructure as discussed in Hubert *et al.* [Hubert 2016].

Figure III-16b shows the evolution of the electrode polarization resistance for Cell II. The overpotential for which  $R_{pol}$  decreases abruptly at 700°C is detected at  $\approx 0.015$  V/air. Therefore, a similar threshold is found for Cell I and Cell II despite different test rigs and electrode microstructures. As for the cell performances, the slight difference in the threshold could be also due to the finer electrode microstructure of Cell II that could facilitate the change of the reaction mechanism in anodic polarization.

The good agreement between the two independent experimental results confirms a change in the reaction mechanism for a porous  $\text{La}_{0.6}\text{Sr}_{0.4}\text{Co}_{0.2}\text{Fe}_{0.8}\text{O}_{3-\delta}$  electrode arising at low anodic polarization. According to the previous modeling studies [Hubert 2016, Laurencin 2015], this electrode behavior in terms of  $\eta$ -i and EIS could be interpreted as the transition from a bulk path in cathodic and low anodic polarizations to a surface path for higher anodic polarization. In order to fully validate this claim and analyze the underlying electrode operating mechanisms for LSCF, the model capability to reproduce the polarization curves as well as EIS at OCP and under polarization has been investigated for Cell I.

### III.2.2 Microstructural Reconstruction for Cell I

To simulate the electrode behavior, it is required to determine the electrode microstructural properties in order to reduce the number of unknown model parameters. For this reason, the electrode microstructure of Cell I has been reconstructed with a FIB-SEM FEI Versa 3D. The FIB-SEM tomographic method consists in collecting a stack of electrode cross-sectional images, each cross-section being successively milled by an ions beam of  $\text{Ga}^+$  [Vivet 2011].



**Figure III-17: Three-dimensional rendering volume for the LSCF electrode of Cell I.**

The detailed protocol for data acquisition and the procedure for the electrode reconstruction can be found in [Lay-Grindler 2013, Vivet 2011]. As shown in Figure III-17, the 3D image presents a volume of  $7.7 \times 7.7 \times 7.7 \mu\text{m}^3$  with a voxel size of 17 nm. The electrode microstructural properties, which are

listed in Table III-X, have been measured by image analysis on the 3D volume as reported in [Laurencin 2012, Moussaoui 2018]. It can be noticed that the parameters are in the range of classical LSCF electrodes [Bertei 2013, Virkar 2000].

**Table III-X: Microstructural parameters of Cell I reconstructed *via* FIB-SEM**

Parameter	Value	Units
Density of TPBs at the LSCF/GDC at the interface ( $\xi_{TPBs}$ )	2.56	( $\mu\text{m}^{-1}$ )
Specific surface area of LSCF/GDC at the interface ( $Sp_{GDC-LSCF}$ )	0.55	(-)
Specific surface area of LSCF/gas interface ( $Sp_{pores-LSCF}$ )	6.67	( $\mu\text{m}^{-1}$ )
Average pore radius ( $\bar{r}_{pores}$ )	0.109	( $\mu\text{m}$ )
Porosity of the electrode ( $\varepsilon_{gas}$ )	41.4	(%)
Volume fraction of LSCF ( $\varepsilon_{LSCF}$ )	58.6	(%)
Tortuosity factor of LSCF ( $\tau_{LSCF}$ )	1.885	(-)
Tortuosity factor of gas phase ( $\tau_{gas}$ )	2.088	(-)

### III.2.3 Description of the Modeling Tools

All the results obtained on Cell I have been analyzed in the light of the physically-based model proposed in [Hubert 2016, Laurencin 2015] In parallel, the impedance spectra of Cell II have been fitted by means of an electrical Equivalent Circuit Model (ECM). A brief description of the in-house model used to simulate the behavior of porous LSCF electrode in anodic and cathodic polarization is reported in this section. For more details, the reader is invited to read references [Hubert 2016, Laurencin 2015]. Furthermore, the ECM used to analyze the experimental data of Cell II is given and described.

#### III.2.3.1 Physically-based Model Description

The micro-scale model considers an isothermal slice (1D) of electrode in which transport properties and reaction kinetics are scaled on the microstructural parameters in a continuum approach (cf. Figure III-18). A transient term is introduced in the mass and charge conservation equations in order to model the time-dependent response of the electrode. The set of equations are solved in the time domain keeping the full non-linearity of the system. Thanks to this procedure, the model is able to simulate the impedance spectra at OCP but also under polarization. Two possible reaction pathways for oxygen reduction/oxidation are considered in the model. As depicted in Figure III-18 in electrolysis mode, the ‘bulk path’ is characterized by oxygen ion migration in the GDC (**T1**) followed by the oxygen transfer across the LSCF/GDC interface (**R1**). After diffusion in the bulk of LSCF (**T2**), oxygen is

excorporated from the lattice to produce oxygen adsorbates on the surface (**R2**). In parallel, the ‘surface path’ considers the direct production of adsorbed oxygen atoms by oxidation at TPBs (**R3**). Subsequently, oxygen adsorbates can diffuse on the surface of the LSCF particles (**T3**) before being desorbed under gaseous molecules in the pores of the electrode (**R4**). Finally, the gaseous oxygen is removed from the electrode by molecular and Knudsen diffusion (**T4**). For both reaction pathways, holes migration in LSCF (**T5**) is also accounted in the model.

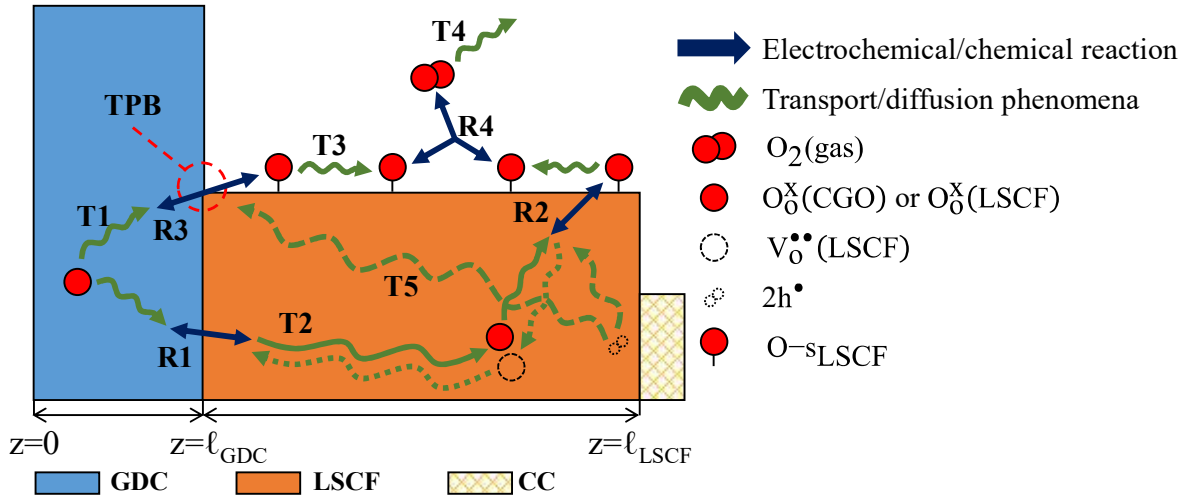


**Figure III-18: Illustration of the reaction pathways for the oxygen electrode (shown in electrolysis mode): *Bulk path*: oxygen ion migration in GDC (**T1**) – oxygen transfer across the LSCF/GDC interface (**R1**) – oxygen ion/vacancy diffusion in LSCF (**T2**) – oxygen excorporation from the bulk to the surface of LSCF (**R2**) – oxygen adsorbate diffusion on the surface of the LSCF (**T3**) – associative desorption of oxygen (**R4**) – gas diffusion (**T4**) – hole migration in the LSCF (**T5**). *Surface path*: oxygen ion migration in the GDC (**T1**) – direct oxidation at the TPBs (**R3**) – oxygen adsorbate diffusion on the surface of the LSCF (**T3**) – associative desorption of oxygen (**R4**) – gas diffusion (**T4**) – hole migration in the LSCF (**T5**).**

All the equations for the reactions (**R1** to **R4**), for the mass and charge transport (**T1** to **T5**) and for the conditions at the LSCF/GDC interface are listed in Table III-XI. A classical Ohm’s law is used to compute the ionic current in GDC as well as the electronic current in LSCF. The diffusion of oxygen adsorbates on the surface of electrode particles and oxygen vacancies in LSCF is modeled using a Fick’s law whereas the oxygen transport in the pores is computed in the frame of the DGM. It can be noticed that in the latter, the Knudsen diffusion coefficient is expressed as a function of the mean pore radius ( $D_{K,O_2} = \bar{r}_{pores} \cdot 2/3 \cdot \sqrt{8000RT/(m_{O_2}\pi)}$ , cf. [Krishna 1997]). Moreover, all the effective transport parameters (such as effective conductivities and diffusivities) are expressed as a function of their intrinsic values and the electrode microstructural parameters given in Table III-X. For instance, the effective electronic conductivity of LSCF is given by  $\sigma_{h_{LSCF}}^{eff} = \varepsilon_{LSCF}/\tau_{LSCF} \sigma_{h_{LSCF}}$  (so that  $\vec{i}_e = -\varepsilon_{LSCF}/\tau_{LSCF} \sigma_{h_{LSCF}} \nabla \phi_{LSCF}$ , cf. **T5** in Table III-XI). This is a typical approach for homogeneous media as also reported in [Kanit 2003, Laurencin 2012]. The chemical and

electrochemical reactions are written using the ‘Kröger-Vink’ notation and the corresponding kinetic rates are also expressed as a function of the electrode morphological properties. It can be noticed that the forward and backward kinetic constants for each reaction are linked in the model through the thermodynamic equilibrium constants [Laurencin 2015].

For each species (holes, oxygen vacancies in LSCF, adsorbates, etc.), the conservation equations are expressed with the chemical/electrochemical reactions as sources/sinks. Finally, a dynamic contribution is also introduced in the mass/charge balances to consider the time-dependent response of the electrode. The set of equations given in Table III-XI has been implemented in the mathematical toolbox of COMSOL Multiphysics<sup>®</sup> software using the external boundary conditions detailed in [Hubert 2016, Laurencin 2015]. Taking advantage of (i) the microstructural properties taken from the 3D reconstruction, (ii) the thermodynamic data and (iii) the transport properties known from literature as a function of temperature and oxygen partial pressure [Hubert 2016, Laurencin 2015], it is possible to reduce the unknown parameters of the model. Under the assumption of a fast ionic transfer at the LSCF/GDC interface [Deseure 2005], only the kinetic constants for the reactions **R2**, **R3** and **R4**, the adsorbates surface diffusivity and the capacitance of the LSCF/GDC double layer have to be fitted on the experimental data as a function of the operating temperature.

### III.2.3.2 Equivalent Electrical Circuit Model

The impedance diagrams of Cell II have been fitted with an equivalent electrical circuit using the EC-Lab<sup>®</sup> software (V11.01). As depicted in Figure III-19, the whole circuit is composed of one element related to the electrolyte ohmic resistance,  $R_s$ , in series with the electrode circuit. The latter is constituted by the combination a fractal Gerischer element,  $GE(f)$  [Diard 2017], taking into account the non-faradaic processes (diffusion and surface reactions) in series with the resistance,  $R_{int}$ , associated to the charge transfer at the LSCF/GDC interface (oxidation/reduction at TPBs and ionic transfer). The capacitance of the LSCF/GDC double layer,  $C_{dl}$ , is introduced in parallel to the elements  $R_{int}$  and  $GE(f)$  as reported in [Baumann 2006, Jamnik 1999, Prestat 2007]. Fitting the experimental data with the equivalent circuit allowed to determine the electrode polarization resistance,  $R_{pol}$ , as well as the value of the double layer capacitance of the LSCF/GDC interface.

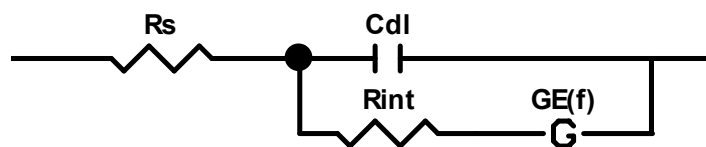


Figure III-19: Equivalent circuit used to fit the EIS of Cell II.

**Table III-XI: Equations of the physically-based model of the oxygen electrode made of porous LSCF (cf. List of symbols)**

Reactions		Kinetic rates	
R1	$2O_o^x(GDC) + 2V_o^{**}(LSCF) \xrightleftharpoons[k_-]{k_+} 2O_o^x(LSCF) + 2V_o^{**}(GDC)$	$v_{(R1)} = Sp_{GDC-LSCF} \left( k_+ \left( 1 - \frac{C_{O_o^x}}{C_{O_o^x}^{max}} \right)^2 \exp\left(\frac{4\alpha_{(R1)}^{ox} F}{RT} E\right) - k_- \left( \frac{C_{O_o^x}}{C_{O_o^x}^{max}} \right)^2 \exp\left(\frac{-4\alpha_{(R1)}^{red} F}{RT} E\right) \right)$	
R2	$2O_o^x(LSCF) + 4h^* + 2s_{LSCF} \xrightleftharpoons[k_{red}]{k_{ox}^{LSCF/gas}} 2V_o^{**}(LSCF) + 2O - s_{LSCF}$	$v_{(R2)} = Sp_{pores-LSCF} \Gamma_{LSCF}^2 \left( k_{ox}^{LSCF/gas} (1 - \theta_{O_{LSCF}})^2 C_{O_o^x}^2 - k_{red}^{LSCF/gas} \theta_{O_{LSCF}}^2 (C_{O_o^x}^{max} - C_{O_o^x})^2 \right)$	
R3	$2O_o^x(GDC) + 4h^* + 2s_{LSCF} \xrightleftharpoons[k_{red}^{TPB}]{k_{ox}^{TPB}} 2O - s_{LSCF} + 2V_o^{**}(GDC)$	$v_{(R3)} = \xi_{TPBs} \Gamma_{LSCF}^2 \left( k_{ox}^{TPB} (1 - \theta_{O_{LSCF}})^2 \exp\left(\frac{4\alpha_{(R3)}^{ox} F}{RT} E\right) - k_{red}^{TPB} (\theta_{O_{LSCF}})^2 \exp\left(\frac{-4\alpha_{(R3)}^{red} F}{RT} E\right) \right)$	
R4	$2O - s_{LSCF} \xrightleftharpoons[k_{ads}]{k_{des}} O_2(gas) + 2s_{LSCF}$	$v_{(R4)} = Sp_{pores-LSCF} \Gamma^2 \left( k_{des} \theta_{O_{LSCF}}^2 - k_{ads} p_{O_2} (1 - \theta_{O_{LSCF}})^2 \right)$	
Transport phenomena	Conservation equations	Conditions at the LSCF/GDC interface	
T1	$\vec{i}_{io} = -\sigma_{io,GDC} \nabla \varphi_{GDC}$	$\nabla \cdot \vec{i}_{io} = 0$	$\vec{i}_{io,local} = 4F(v_{(R1)} + v_{(R3)}) - Sp_{GDC-LSCF} C_{dl} \frac{\partial(\varphi_{LSCF} - \varphi_{GDC})}{\partial t}$
T2	$\vec{N}_{V_o^{**}} = -\frac{\varepsilon_{LSCF}}{\tau_{LSCF}} \tilde{D}_{chem} \nabla C_{V_o^{**}}$	$\nabla \cdot \vec{N}_{V_o^{**}} = +2v_{(R2)} - \varepsilon_{LSCF} \frac{dC_{V_o^{**}}}{dt}$	$\vec{N}_{V_o^{**},local} = -2v_{(R1)}$
T3	$\vec{N}_{O_{LSCF}} = -S_p^{LSCF/gas} \Gamma_{LSCF} D_{O_{LSCF}} \nabla \theta_{O_{LSCF}}$	$\nabla \cdot \vec{N}_{O_{LSCF}} = 2(v_{(R2)} - v_{(R4)}) - Sp_{pores-LSCF} \Gamma \frac{d\theta_{O_{LSCF}}}{dt}$	$\vec{N}_{O_{LSCF},local} = 2v_{(R3)}$
T4	$\nabla y_{O_2} = -\frac{RT}{P_t} \left( \frac{N_{O_2}}{\frac{\varepsilon_{pores}}{\tau_{pores}} D_{K,O_2}} + \frac{N_{O_2} y_{N_2}}{\frac{\varepsilon_{pores}}{\tau_{pores}} D_{O_2-N_2}} \right)$	$\nabla \cdot \vec{N}_{O_2} = v_{(R4)} - \frac{\varepsilon_{pores}}{RT} P_{tot} \frac{dx_{O_2}}{dt}$	$\vec{N}_{O_2,local} = 0$
T5	$\vec{i}_{e^-} = -\frac{\varepsilon_{LSCF}}{\tau_{LSCF}} \sigma_{h_{LSCF}} \nabla \varphi_{LSCF}$	$\nabla \cdot \vec{i}_{e^-} = -4Fv_{(R2)}$	$\vec{i}_{e^-,local} = -4Fv_{(R3)} + Sp_{GDC-LSCF} C_{dl} \frac{d(\varphi_{LSCF} - \varphi_{GDC})}{dt}$

### III.2.4 Model Validation and Discussion

The physically-based model for the porous LSCF electrode has been validated on the experimental data of Cell I taking advantage of the microstructural parameters coming from the 3D reconstruction. In this section, the procedure followed for the model validation is described and the model results are discussed. Furthermore, the extension of the model to composite LSCF/GDC electrodes is introduced.

#### III.2.4.1 Input parameters and procedure for model validation

Thanks to the 3D electrode reconstruction, all the microstructural properties required for the simulations of Cell I are known (Table III-X). Regarding the transport properties for the mass and charge transfers, the Knudsen and molecular gas diffusivities are calculated as a function of the temperature using the classical relations given by Suwanwarangkul *et al.* [Suwanwarangkul 2003]. Except for the oxygen surface diffusivity, all the transport properties in LSCF are taken from published works at 800°C as a function of oxygen partial pressure. The temperature dependence of the oxygen bulk diffusion in LSCF is also taken into account through an Arrhenius law. Therefore, only the surface diffusivity for the oxygen adsorbates has been adjusted on the experimental curves at the three temperatures, whereas the activation energy for the LSCF chemical diffusivity has been estimated with the data at 700°C and 750°C.

For the thermodynamic computation, all the data at equilibrium including the oxygen coverage rate and the oxygen under-stoichiometry in LSCF are taken from literature [Bishop 2009, Deseure 2005]. The oxygen under-stoichiometry (or concentration at equilibrium) is given as a function of temperature and partial pressure. In accordance with the bibliography data on LSCF [Deseure 2005, Gong 2012, Svensson 1998], a very low numerical value for the oxygen coverage rate at equilibrium is taken for the simulations ( $\theta_{O_{LSCF}}^{eq} \ll 1$ , cf. Table III-XII). Since its thermal evolution between 700°C and 800°C remains in the same range of such low values, its modification does not affect deeply the reaction thermodynamic constants and hence the electrode response. Therefore, its temperature dependence has been neglected in the simulations. Regarding the kinetic parameters, it is assumed that the ionic transfer (**R1**) is non-limiting [Laurencin 2015] so that only the forward kinetic constants for excorporation/incorporation (**R2**), charge transfer at TPBs (**R3**), and desorption/adsorption (**R4**) are unknown.

Finally, because of a large scattering of values reported in the publications for the LSCF/GDC double layer capacitance [Baumann 2006, Prestat 2007], it has been chosen to include the assessment of this parameter in the study.

In the first step of the modeling procedure, the oxygen surface diffusivity, and the three missing kinetics constants have been fitted on the polarization curve at each temperature while the activation energy for LSCF bulk diffusivity has been evaluated with the curves at 700°C and 750°C. Once these parameters have been determined, the EIS at OCP and under polarization have been simulated using the protocol detailed by Hubert *et al.* [Hubert 2016]. For this purpose, a sinusoidal perturbation on the ionic current,  $i_{io}$ , is applied in the electrolyte and the time-dependent response of the electrode is computed. Ten cycles of current are calculated for each frequency and only the last two are used to determine the electrode impedance. In the simulations 89 frequencies are computed, logarithmically spaced between  $10^{-3}$  Hz and  $10^5$  Hz.

#### III.2.4.2 Model calibration on the $\eta$ - $i$ curves and validation with EIS

The polarization curves computed with the input parameters reported in Table III-XII are compared to the experimental data in Figure III-13a. Thanks to the dissymmetry of the  $\eta$ - $i$  curves, only a set of consistent solutions has been found for the unknown parameters of the model (cf. fitted parameters in Table III-XII). It can be noticed that the activation energy for the LSCF chemical diffusion coefficient is estimated to  $\approx 153$  kJ·mol<sup>-1</sup> using the data reported in Table III-XII. It is worth mentioning that dedicated methods, such as conductivity relaxation technique, must be used for an accurate and precise determination of the oxygen chemical diffusivity. For example, Bouwmeester *et al.* [Bouwmeester 2004] have measured the chemical diffusion constants of La<sub>0.6</sub>Sr<sub>0.4</sub>Co<sub>0.2</sub>Fe<sub>0.8</sub>O<sub>3- $\delta$</sub>  leading to an activation energy of  $\approx 145$  kJ·mol<sup>-1</sup> (with pO<sub>2</sub> = 0.1 atm), while Yashiro *et al.* [Yashiro 2011] have determined for the same material and in the same conditions an activation energy of  $\approx 116$  kJ·mol<sup>-1</sup>. Moreover, Sogaard *et al.* [Sogaard 2006] have reported a value of  $\approx 132$  kJ·mol<sup>-1</sup> for the same LSCF composition. Therefore, our estimation of  $\approx 153$  kJ·mol<sup>-1</sup> is in the same order of magnitude of the values which have been specifically measured on the same kind of LSCF compound. Moreover, the reaction kinetic constants estimated at 800°C are also found to be in good agreement with the values determined at the same temperature on another La<sub>0.6</sub>Sr<sub>0.4</sub>Co<sub>0.2</sub>Fe<sub>0.8</sub>O<sub>3- $\delta$</sub>  electrode microstructure [Laurencin 2015]. As a general comment, it is worth mentioning that an excellent agreement is achieved between the simulations and the experiments for each temperature (Figure III-13a). Therefore, since the simulations are able to reproduce the transition in the polarization curve at different temperatures, the model can be considered roughly validated.

Nevertheless, to fully confirm the model strength, the same set of parameters has been used to compute the EIS. At 750°C, the model is able to predict with a high level of confidence the gradual transition from a Gerischer-type element at OCP and at low anodic polarization (Figure III-14a and

Figure III-14b) towards flattened and convoluted diagrams at higher polarization (Figure III-14c and Figure III-14d). Besides, the same evolution of the spectra changing from OCP to higher anodic polarization is also well reproduced by the model at 700°C and 800°C (Figure III-15a and Figure III-15b). Therefore, a good consistency in the global shapes of the simulated and experimental EIS is observed whatever the polarization and the operating temperature. Only a slight shift in frequency distribution is detected between the simulations and experimental results at OCP which tends to disappear under polarization.

All the simulations in the time domain have been performed with a capacitance for the LSCF/GDC double layer estimated to  $10 \mu\text{F}\cdot\text{cm}^{-2}$ . This value allows minimizing the error between the modeled and the experimental spectra in the high frequency region ( $f > 1000\text{Hz}$ ). Nevertheless, it is worth underlining that the main part of the EIS ranging from low to medium frequencies ( $f < 1000\text{Hz}$ ) remains unaffected by the choice of the  $C_{dl}$ .

**Table III-XII: Parameters used in the model to fit the experimental data (fitted values in italic)**

Parameter	Value			Units
Electrode Thickness ( $\ell_{LSCF}$ )	35			( $\mu\text{m}$ )
Maximum oxygen concentration in the LSCF ( $C_{O_2}^{max}$ )	83'108			( $\text{mol}\cdot\text{m}^{-3}$ )
Electronic conductivity of LSCF ( $\sigma_{h,LSCF}$ )	33'739			( $\text{S}\cdot\text{m}^{-1}$ )
Oxygen coverage rate at equilibrium ( $\theta_{O_{LSCF}}^{eq}$ )	$4.6 \times 10^{-5}$			(-)
Maximum density of adsorption sites ( $\Gamma_{LSCF}$ )	$10^{-5}$			( $\text{mol}\cdot\text{m}^{-2}$ )
Kinetic constant for the ionic transfer (R1) ( $k_+$ )	$10^6$			( $\text{mol}\cdot\text{m}^{-2}\cdot\text{s}^{-1}$ )
Oxygen partial pressure ( $p_{O_2}$ )	0.21			(bar)
Double layer capacitance (for EIS modeling) ( $C_{dl}$ )	0.1			( $\text{F}\cdot\text{m}^{-2}$ )
	<b>700°C</b>	<b>750°C</b>	<b>800°C</b>	
Oxygen Knudsen diffusion coefficient ( $D_{K,O_2}$ )	$5.83 \times 10^{-5}$	$5.98 \times 10^{-5}$	$6.12 \times 10^{-5}$	( $\text{m}^2\cdot\text{s}^{-1}$ )
Ionic conductivity of GDC ( $\sigma_{io,GDC}$ )	2.87	4.05	5.52	( $\text{S}\cdot\text{m}^{-1}$ )
Oxygen binary diffusion coefficient ( $D_{O_2-N_2}$ )	$1.51 \cdot 10^{-4}$	$1.8 \cdot 10^{-4}$	$1.96 \cdot 10^{-4}$	( $\text{m}^2\cdot\text{s}^{-1}$ )
Oxygen concentration in the LSCF at equilibrium ( $C_{O_2}^{eq}$ )	82'887	82'666	82'444	( $\text{mol}\cdot\text{m}^{-3}$ )
Oxygen chemical diffusion coefficient in LSCF ( $\tilde{D}_{chem}$ )	$1.51 \times 10^{-11}$	$5.1 \times 10^{-11}$	$0.9 \times 10^{-10}$	( $\text{m}^2\cdot\text{s}^{-1}$ )
Oxygen adsorbates diffusion coefficient ( $D_{O_{LSCF}}$ )	$2.52 \times 10^{-7}$	$7.7 \cdot 10^{-7}$	$2 \times 10^{-6}$	( $\text{m}^2\cdot\text{s}^{-1}$ )
Kinetic constant for adsorption (R4) ( $k_{ads}$ )	$1.25 \times 10^6$	$1.6 \times 10^6$	$2.8 \times 10^6$	( $\text{m}^2\cdot\text{mol}^{-1}\cdot\text{atm}^{-1}\cdot\text{s}^{-1}$ )
Kinetic constant for oxygen exorporation (R2) ( $k_{ox}^{LSCF/gas}$ )	$2.17 \times 10^{-5}$	$2.8 \times 10^{-5}$	$3 \times 10^{-5}$	( $\text{m}^8\cdot\text{mol}^{-3}\cdot\text{s}^{-1}$ )
Kinetic constant for oxidation at TPBs (R3) ( $k_{ox}^{TPB}$ )	0.354	2.61	7	( $\text{m}^3\cdot\text{mol}^{-1}\cdot\text{s}^{-1}$ )

Aside from the double layer capacitance, it is worth reminding that the EIS simulations have been performed without adjusting any input parameter of the model (which have been determined only on the polarization curves). Without any additional fitting, the model is able to reproduce accurately the

shape of the impedance whatever the temperature or the polarization. As a consequence, the overall comparison between the simulated and experimental EIS confirms the model relevance to predict the LSCF behavior so that it can be considered fully validated.

Even if the present work allows justifying the proposed reaction pathway for the porous electrode, the use of the  $\eta$ -i curves and impedance spectra is not enough to avoid a slight uncertainty on the determination of the kinetic constants and surface diffusivity. From this point of view, other experimental studies are still needed to improve the precision for the determination of the model parameters. In this frame, the modeling of experimental cyclic voltammetry [Kournoutis 2011, Tezyk 2019] and nonlinear impedance spectroscopy [Geary 2016] could be especially relevant. Nevertheless, the model validity allows claiming that the experimental transition observed on the polarization resistance and impedance spectra can be related to the passage from the bulk path to the surface path as discussed hereafter.

### III.2.4.3 Discussion

*Influence of polarization on the reaction pathway* – As proposed in Laurencin *et al.* [Laurencin 2015], the relative proportion of the surface to the bulk paths can be expressed through the indicator  $\xi$  defined as the ratio between the kinetic rates of direct oxidation/reduction at TPBs (**R3**) and oxygen incorporation/excorporation from LSCF (**R2**) (eq. (III-22)).

$$\xi = \frac{v_{R3}}{\int_{z=\ell_{GDC}}^{z=\ell_{LSCF}} v_{R2} dz} \quad \text{(III-22)}$$

It is reminded that the reaction at the TPBs occurs only at the LSCF/GDC interface ( $z = \ell_{GDC}$ ), while the incorporation/excorporation reaction is liable to occur all over the electrode thickness ( $\ell_{GDC} < z < \ell_{LSCF}$ ). For this reason, the ratio between the two reaction rates has to be calculated integrating the velocity of **R2** on the whole electrode thickness. A value of  $\xi$  lower than one corresponds to a reaction mechanism dominated by the ‘bulk path’ while a ratio higher than one indicates a mechanism controlled by the ‘surface path’.

Once the model has been validated, the ratio has been computed as a function of the current density (Figure III-20a). For example, at 750°C, it can be seen that the ratio becomes higher than the unity at low anodic current ( $i_{DC} \approx 15 \text{ mA} \cdot \text{cm}^{-2}$ ) corresponding to an overpotential of 0.016 V/air. This result confirms that the change observed in the experimental polarization curves at low anodic overpotential (Figure III-13) is explained by the transition from the bulk to the surface path. Moreover, at the same temperature, the modification of the EIS shape from the Gerischer-type element to a flattened semi-

circle is detected experimentally between  $i_{DC} = 10 \text{ mA}\cdot\text{cm}^{-2}$  and  $i_{DC} = 50 \text{ mA}\cdot\text{cm}^{-2}$  (Figure III-14b and Figure III-14c, respectively). This range of current for which the shape of the EIS changes is thus fully consistent with the computed current of  $\approx 15 \text{ mA}\cdot\text{cm}^{-2}$  for which the dominant reaction mechanism is changed from the bulk to the surface path.

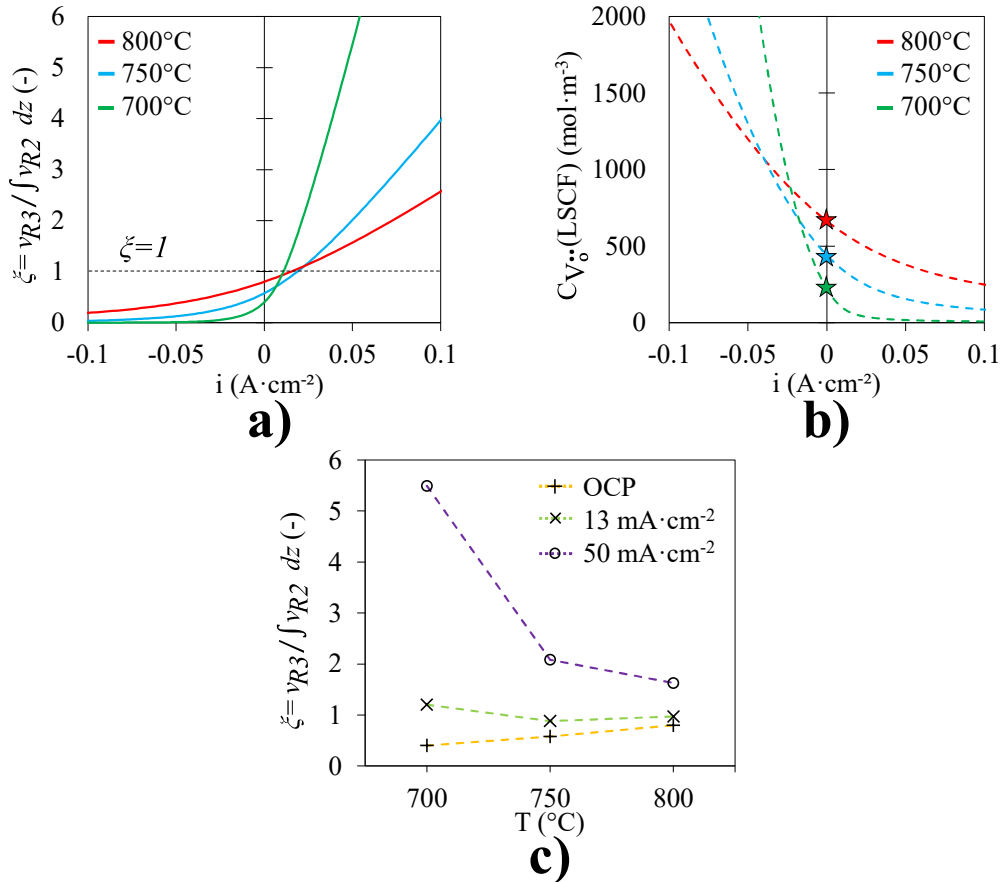


**Figure III-20: Results of the simulations: a) Ratio calculated with the model between the kinetic rate of R3 and R2 – b) Oxygen vacancies concentration in the LSCF lattice,  $\star$  = equilibrium concentration – c) Comparison of the ratio at OCP and under anodic polarization at different temperatures**

The transition from the bulk to the surface path in anodic polarization can be explained with the evolution of the oxygen vacancies content in LSCF [Laurencin 2015]. To highlight this dependency, the concentration of oxygen vacancies in the LSCF at the interface with the GDC has been plotted as a function of the current density in Figure III-20b. A strong decrease in oxygen vacancies concentration is found increasing the anodic overpotential. Indeed, under anodic polarization, a depletion of oxygen vacancies in the LSCF lattice is expected ( $C_{V_o} \ll C_{V_o}^{eq}$ ), due to the slower kinetic of oxygen excorporation (**R2**) with respect to ionic transfer (**R1**) ( $v_{R2} \ll v_{R1}$ ). When the vacancy concentration tends to zero, the ionic transfer and the overall bulk path are limited all together in such a way that the surface path with the oxidation at TPBs becomes predominant.

*Influence of temperature on the reaction mechanism* – The influence of temperature on the ratio of the surface to the bulk path is illustrated in Figure III-20a at 700°C, 750°C and 800°C. Over this range of temperature at OCP, the ratio is found to be lower than the unity meaning that the reaction mechanism remains controlled by the bulk path. Conversely, when the anodic current density is increased, the contribution of the surface path becomes progressively more important until becoming predominant ( $\xi > 1$ ). To study the electrode thermal behavior when the bulk or the surface path is activated, the ratio has been plotted in Figure III-20c for different dc current densities from OCP ( $\xi < 1$ ) to +50 mA·cm<sup>-2</sup> ( $\xi \gg 1$ ).

It can be seen in Figure III-20c that the ratio at OCP increases with the temperature. Therefore, even if the bulk path remains predominant, this evolution points out that the contribution of the oxidation at TPBs in the global reaction mechanism is enhanced with increasing the operating temperature. Since the oxygen surface and bulk diffusivities evolve roughly similarly with the temperature (cf. Table III-XII), the electrode behavior at OCP is basically explained by the characteristics of the thermally-activated reaction kinetics. Indeed, as shown in Table III-XII, the temperature dependence of the kinetic constant for the oxidation at TPBs is found to be higher than the one for oxygen excoorporation/incorporation. In this condition, the relative weight of the surface path at OCP is enhanced with increasing the temperature. This statement is consistent with the plot of the experimental polarization resistance in Figure III-13b. Indeed, at 700°C, the maximum of the polarization resistance, which is linked to the transition in the reaction mechanism, is reached under anodic polarization, while, at 800°C, it is found very close to the OCP. Furthermore, this result is also confirmed by the impedance spectra acquired at OCP. At 700°C, a well-defined Gerischer-type diagram is observed (Figure III-15a) which indicates a bulk path dominated mechanism ( $\xi_{OCP} = 0.4$ , cf. Figure III-20c) as deeply discussed in Adler *et al.* [Adler 1998, 1996]. Conversely, at 800°C, the experimental diagram (Figure III-15b) becomes to be slightly flattened and convoluted indicating a non-negligible contribution of the oxidation/reduction at TPBs ( $\xi_{OCP} = 0.8$ , cf. Figure III-20c). This evolution of the impedance spectra with the temperature is in good agreement with the experimental results reported in Kournoutis *et al.* [Kournoutis 2009]. Moreover, this statement is also consistent with the studies of Liu *et al.* [Liu 1998a, 1998b] who have proposed a likely contribution of TPBs even at OCP.

It can be noticed that the error on the frequency distribution at OCP between the simulations and the experiments discussed in section III.2.4.2 increases with increasing the temperature (Figure III-14 and Figure III-15). This discrepancy seems to be correlated to a more depressed impedance spectrum

in the Nyquist representation at 800°C (cf. Figure III-15b). From this point of view, it could be possible that a higher contribution of the charge transfer at TPBs would improve the agreement between the model results and the experiments at 800°C. This remark means that, in the present simulations, the role of TPBs at OCP could even be slightly underestimated at high temperature.

In contrast to the evolution at OCP, as illustrated in Figure III-20c for  $i_{DC} = +50 \text{ mA}\cdot\text{cm}^{-2}$ , the ratio at ‘high’ anodic current density increases steeply by decreasing the temperature. This behavior is explained since the oxygen under-stoichiometry at equilibrium for the LSCF material is strongly decreased when the temperature is lowered [Bishop 2009, Hartley 2000]. Therefore, as the concentration of oxygen vacancies at equilibrium is decreased ( $T \downarrow \Rightarrow C_{V_o}^{eq} \downarrow$ ), the oxygen vacancies depletion within the LSCF lattice under anodic current ( $C_{V_o} \rightarrow 0$ ) is reached more rapidly at lower temperature. As a consequence, the bulk path is more easily blocked under current when the temperature is decreased. In this condition, despite the thermal effect on the kinetics, the potential-activated charge transfer at TPBs is favored so that the surface path is promoted at low temperature under anodic polarization (at 700°C,  $\xi_{i_{DC}=50 \text{ mA}\cdot\text{cm}^{-2}} = 5.5$  and at 800°C,  $\xi_{i_{DC}=50 \text{ mA}\cdot\text{cm}^{-2}} = 1.6$ , cf. Figure III-20c). This explanation is consistent with the variation of the experimental polarization resistance in anodic polarization (Figure III-13b). Indeed, at 700°C, the curve exhibits a steep potential-dependent decrease in anodic polarization while at 800°C, the curve is more symmetric indicating a smoother transition.

Finally, at low anodic current between OCP and  $i_{DC} = +50 \text{ mA}\cdot\text{cm}^{-2}$ , the impacts of temperature on the kinetics and on the oxygen vacancies concentration counteract each other leading to a roughly constant value for the ratio. It can be noticed in Figure III-20c that, at low anodic current for  $i_{DC} = +13 \text{ mA}\cdot\text{cm}^{-2}$ , the ratio  $\xi$  is roughly equal to one independently of the temperature. This remark means that the transition from the bulk to the surface path occurs approximatively at the same current density whatever is the temperature between 700°C and 800°C. However, it is reminded that the polarization curve is strongly activated by the temperature (Figure III-13a) so that the threshold ( $\xi=1$ ) for a given current density appears at different electrode overpotential. Therefore, the transition happens at higher anodic overpotential decreasing the temperature ( $\eta_{\xi \approx 1}^{800^\circ\text{C}} < \eta_{\xi \approx 1}^{750^\circ\text{C}} < \eta_{\xi \approx 1}^{700^\circ\text{C}}$ ), in agreement with the experimental results previously discussed in section III.2.1.3.

*Value of the LSCF/GDC double layer capacitance* – As reported in section III.2.4.2 for Cell I, the LSCF/GDC interfacial capacitance has been evaluated to be  $\approx 10 \mu\text{F}\cdot\text{cm}^{-2}$  by fitting the experimental EIS with the physically-based model. This result is consistent with the value estimated for Cell II at

OCP on both electrodes. Indeed, in this case, a capacitance comprised between 1 and 100  $\mu\text{F}\cdot\text{cm}^{-2}$  has been obtained by fitting the experimental data with the equivalent electrical circuit described in Figure III-19 in the temperature range 400°C – 700°C. For both cells, the double layer capacitance is found to be roughly independent of temperature. This range of values (10 – 100  $\mu\text{F}\cdot\text{cm}^{-2}$ ) corresponds to a classical capacitance due to the electrostatic double layer for a metal-solid electrolyte interface [Armstrong 1997, Mitterdorfer 1999]. This behavior for the LSCF/GDC system is expected considering the LSCF as a good electronic conductor and the GDC as a good ionic conductor. Nevertheless, some authors [Baumann 2006, Marinha 2012] have reported higher values for the LSCF/GDC interfacial double layer capacitance ranging from 100 to 1000  $\mu\text{F}\cdot\text{cm}^{-2}$ . From this point of view, further studies are needed to better analyze the nature of the LSCF/GDC interface.

### *III.2.5 LSCF-GDC Composite Electrodes*

In this work, it can be noticed that a micro-kinetic model for LSCF-GDC composite electrode has been also used for the simulation of *Cell-A* (cf. chapter II and section III.3). The model was initially developed in [Hubert 2016, Laurencin 2015] while its validations is done in the frame of the thesis of E. Effori [Effori 2019]. In this model, the porous LSCF oxygen electrode was extended to be able to simulate the behavior of a composite LSCF-GDC electrode. This step has been done modifying the mass and charge conservation equations considering the GDC in the entire electrode. In this case, the surface path can occur in the whole electrode thickness. Because of this property, the charge transfer at the TPBs was found to dominate the reaction mechanism independently of the polarization [Effori 2019].

### *III.2.6 Concluding Remarks*

In order to validate the reaction mechanism of the classical porous LSCF electrode, a set of experiments has been conducted on two symmetric cells with different microstructures. The cells, tested in two separate setups, have been found to exhibit consistent electrochemical behaviors. In both cases, the  $\eta$ - $i$  curves present a clear dissymmetry between anodic and cathodic polarizations. The transition occurs at a low anodic overpotential threshold that decreases with increasing the operating temperature. This electrode behavior is confirmed by a modification of the electrochemical impedance spectra from a classical Gerischer-type element at OCP to a flattened semicircle under anodic DC current. All these results indicate a change in electrode reaction mechanism occurring at low anodic polarization.

In order to interpret the experimental results, a micro-scale physically-based electrode model has been used. This model includes two parallel multi-step reaction pathways with an oxygen incorporation/excorporation at the gas/LSCF interface (bulk path) and a direct oxidation/reduction at TPBs (surface path). For one of the two studied cells, a 3D electrode reconstruction has been obtained to determine all the microstructural properties required for the simulations. With a reduced number of unknown parameters, the model has been found to reproduce the dissymmetry of the electrode polarization curves at different temperatures. Furthermore, the model simulates accurately the impedance spectra reproducing the evolution of the diagrams from OCP to anodic polarization. The good agreement between the simulated curves and experimental data allows validating the main model assumptions. The analyses of the computed electrode kinetic rates have shown that the transition detected at low anodic polarization is due to a change of dominant reaction pathway passing from the bulk to the surface path.

Once validated, the model has been used to unravel the complex electrode operating mechanisms. The analysis of the local quantities in the electrode has revealed that the change in electrode reaction pathways is driven by a depletion of oxygen vacancies in LSCF under anodic polarization. Moreover, the relative contribution of the bulk and the surface paths has been investigated as a function of temperature. The simulations at OCP have shown that the weight of the surface path is reinforced increasing the temperature even if the bulk path remains dominant. Conversely, under ‘high’ anodic current, the surface path is always prevalent and its contribution is enhanced when the temperature is lowered. In between, the surface and the bulk paths are equally activated at a ‘low’ anodic current corresponding to different overpotentials depending on the temperature. This thermal behavior at OCP and under current is explained by the combination of two opposite effects of temperature on the global reaction mechanism: the temperature-dependent evolution of the oxygen under-stoichiometry in LSCF at equilibrium and the thermal activation of reaction kinetics.

Subsequently, the LSCF/GDC double layer capacitance fitted on the impedance spectra at high frequency has been found to be consistent with an electrostatic double layer capacitance for a metal-solid electrolyte interface.

To conclude, this micro-kinetic model for the LSCF and the composite LSCF-GDC oxygen electrodes can be considered validated. Therefore, it can be used to investigate the origins of the degradation in LSCF-based oxygen electrodes after aging (cf. chapter V).

### III.3 Macro-Scale Model at the Cell level and Multi-Scale Integration

As already presented in [Hubert 2018, Laurencin 2017], the two micro-scale models are coupled with a macro-scale model that has been developed at CEA to describe the cell behavior in SOFC [Laurencin 2008] and SOEC modes [Aicart 2014, Bernadet 2015, Laurencin 2011]. The macro-scale model allows the simulation of the overall response of the cell taking into account the macroscopic operating parameters such as the operating temperature, the current density, the overpotentials and the gas compositions [Godula-Jopek 2015].

In this section, the macro-scale model is shortly described, and the methodology used to link the micro-scale models to the macro-scale model is introduced. Finally, the multi-scale model calibration specifically obtained for this study is given based on the experimental data at the complete cell level reported in chapter II.

#### III.3.1 Macro-Scale Model Description

The macro-scale model allows the simulation of the cell performances starting from the nominal operating conditions in terms of temperature, pressure and gas compositions. It can be noticed that the knowledge of the microstructure properties for the current collecting layers is also essential to reduce the number of unknown model parameters. As illustrated in Figure III-21 (left), a 2D radial approach is adopted describing the geometry of the entire button cell and the interconnect, taking into account the radial co-flow configuration of the experimental setup (cf. chapter II).

In the model version used for this study, the gas flows in the anodic and cathodic channels are taken into account by using local mass balances performed of each species. Moreover, the mass transport in the porous electrode is also considered using the DGM and taking into account the molecular and Knudsen diffusional processes. In this frame, the source terms for the reactants and products at the two electrodes are linked to the faradaic current originating from the electrochemical reactions that are supposed to take place in the vicinity of the electrodes/electrolyte interfaces. In other words, the functional layers are reduced to the electrode/electrolyte interfaces in this macroscopic approach. Finally, all the Ohmic resistances are taken into account considering the ionic conductivity of the electrolyte, the electronic conductivity in the two electrodes and the contact resistances at the two electrode/current collector interfaces.

Using the Nernst equation, the OCV is determined in the macro-scale model starting from the gas compositions and the operating temperature. From the OCV, the model can be used to compute all

the contributions to the cell overpotentials. In particular, the Ohmic losses are directly derived from the various contributions to the Ohmic resistances and the local current densities evolving along the cell radius. In addition, the local concentration overpotentials for the two electrodes are obtained by considering the evolutions of the gas compositions between the gas channel and the functional layers at OCV and under operation. Finally, the local activation overpotentials are also calculated all along the electrode/electrolyte interfaces. For this purpose, a global Butler-Volmer formalism is used through local ‘apparent’ exchange current densities ( $i_0$ ) for each electrode. These exchange current densities depend on the local gas partial pressure taken at the electrode/electrolyte interface. Using this phenomenological approach, the activation overpotentials at the cell level include all the microscopic processes occurring in the active layers (reaction kinetics, gaseous and adsorbate diffusion, charge migration).

### III.3.2 Multi-Scale Integration

The connection between the micro-scale and the macro-scale simulations is done by imposing the same activation overpotential for each electrode at the two levels. With this objective, the micro-scale models are used to evaluate the overpotentials associated to the reaction mechanisms in the electrodes as a function of the local gas composition, and these are used to determine the local activation overpotentials at the cell level as depicted in Figure III-21.

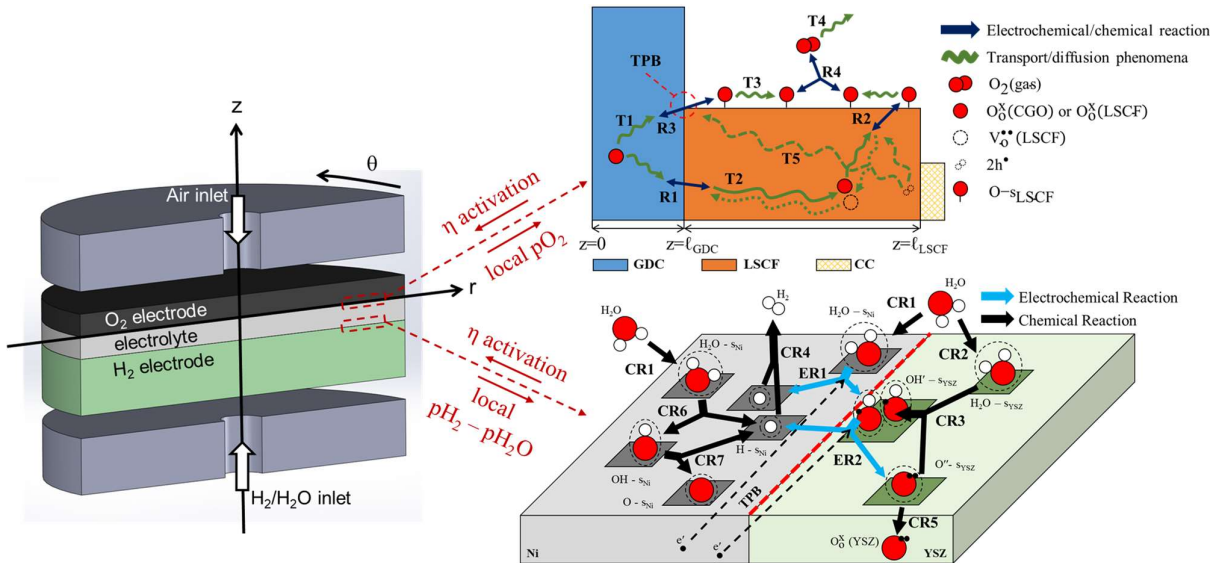


**Figure III-21: Illustration of the procedure to integrate the micro-scale models for the fuel and oxygen electrodes in the macro-scale model at the cell level.**

In other words, a classical multiscale approach is used to connect the cell and electrodes models. Indeed, the activation overpotentials used at the cell levels are calculated along the cell radius thanks

to the micro-scale electrode models. For these computations, the gas partial pressures are taken from the macroscopic model and they are used as boundary conditions for the micro-scale simulations. With this purpose, the exchange current densities in the macro-scale model are expressed according to eqs. (III-23a) and (III-23b) for the fuel and the oxygen electrodes, respectively.

$$i_0^{H_2} = i_{00}^{H_2} \cdot x_{H_2}^\gamma \cdot x_{H_2O}^\chi \cdot \exp\left(-\frac{E_{act}^{H_2}}{RT}\right) \quad \text{(III-23a)}$$

$$i_0^{O_2} = i_{00}^{O_2} \cdot x_{O_2}^\lambda \cdot \exp\left(-\frac{E_{act}^{O_2}}{RT}\right) \quad \text{(III-23b)}$$

In these expressions, the exchange current densities depend on the operating temperature and the molar fractions of products and reactants ( $x_i$ ) in the vicinity of the active sites (i.e. at the electrode/electrolyte interfaces for the macroscopic model and at the top of the active layer for the microscopic ones). The terms  $E_{act}^i$  represent the activation energies for the two electrodes, expressed in  $\text{kJ}\cdot\text{mol}^{-1}$ , whereas the exponents  $\gamma$ ,  $\chi$  and  $\lambda$  are used to express the dependency of the exchange current densities on the gas compositions. These exponents have been determined using a large dataset of partial pressures in the two micro-scale models for the hydrogen and oxygen electrodes and a least-square algorithm has been used to obtain the values for fuel cell or electrolysis operation [Hubert 2018].

All the fitted values are reported in Table III-XIII and it can be noticed that they are in good agreement with published data for the both electrodes [Aicart 2015, Costamagna 1998, Kanno 2011, Nagata 2001, Yonekura 2011] as discussed in the thesis of M. Hubert [Hubert 2018].

**Table III-XIII: Parameters for the computation of the exchange current densities for the fuel and oxygen electrodes fitted on the micro-scale models [Hubert 2018]**

	Fitted parameter	SOFC polarization	SOEC polarization	Unit
<b>Hydrogen electrode</b>	$\gamma$	0.0871	0.073	(-)
	$\chi$	0.57	0.61	(-)
	$E_{act}^{H_2}$		117	( $\text{kJ}\cdot\text{mol}^{-1}$ )
<b>Oxygen electrode</b>	$\lambda$	0.34	0.15	(-)
	$E_{act}^{O_2}$		120	( $\text{kJ}\cdot\text{mol}^{-1}$ )

### III.3.3 Multi-Scale Model Validation

The multi-scale modeling framework has been validated considering the experimental results reported in chapter II for *Cell-A1* and *Cell-A2*. In order to simulate the overall cell response, it is necessary to take into account the microstructural data of the two electrodes. With this objective, the microstructural data for the Ni-YSZ electrode have been obtained from a 3D reconstruction of a

pristine cell of type *A* (as will be discussed in chapter IV). The data for the microstructure of the LSCF-GDC//LSCF electrode bilayer have been taken from FIB-SEM reconstructions [Effori 2019] for the micro-scale model, whereas the microstructure of the LSCF//LSC obtained by X-ray nanohotomography has been used for the macro-scale model. With these microstructural parameters the multi-scale model has been validated on the initial performances for the two cells in both operating conditions simulating the polarization curves without any additional fitting.

The results of the model validation in SOFC and SOEC modes are given in Figure III-22. As can be seen, the experimental results and simulated polarization curves are well superposed with only a slight difference at high current densities ( $\approx 5 - 8\%$ ) that does not invalidate the model results. Therefore, the overall modeling scheme can be considered validated for the investigation of the degradation mechanisms.

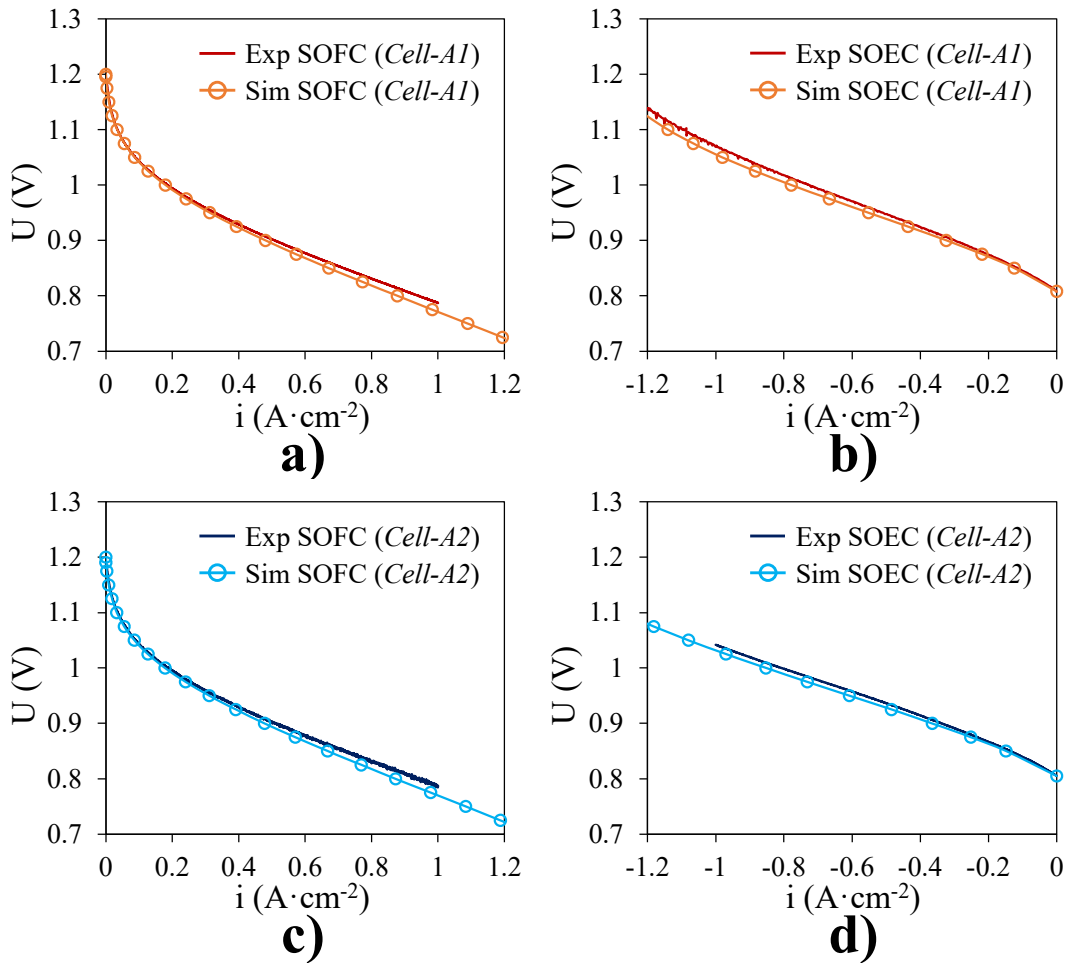


**Figure III-22: Validation of the multi-scale modeling scheme on the initial performances of *Cell-A1* and *Cell-A2* (SOFC fuel composition:  $H_2/H_2O = 100/0$  vol.%, SOEC fuel composition:  $H_2/H_2O = 10/90$  vol.%): a) SOFC performances of *Cell-A1* at  $800^\circ C$  – b) SOEC performances of *Cell-A1* at  $850^\circ C$  – c) SOFC performances of *Cell-A2* at  $800^\circ C$  – d) SOEC performances of *Cell-A2* at  $850^\circ C$ .**

### III.4 Conclusion of This Chapter

In this chapter, the improvements of an existing multi-scale modeling scheme have been detailed. A specific focus has been dedicated to the development and the validation of a detailed micro-kinetic model for the hydrogen electrode, i.e. Ni-YSZ cermet, while an existing oxygen electrode model has been carefully validated for LSCF and LSCF-GDC.

For the hydrogen electrode, it has been shown that the reaction process can be successfully simulated considering a double hydrogen spillover mechanism for the charge transfer. This mechanism has been validated taking advantage of the experimental characterization of a symmetric cell consisting in a Ni-3YSZ cermet. Based on the simulation results, the reaction mechanism appears to be co-limited by the charge transfer, the vacancies migration in the ionic conductive material and an interaction between the steam and the solid phases. Furthermore, it has been found that the limiting interaction is strongly related to the operating conditions. Indeed, the simulations suggest that the interaction with the YSZ could be co-limiting in SOFC mode, whereas the interaction with the Ni would become the co-rate determining step in SOEC conditions.

In parallel, a micro-kinetic model for a porous LSCF oxygen electrode has been completely validated. The model consists in two reaction pathways, named the ‘bulk path’ and the ‘surface path’. In cathodic polarization and at the OCP, it has been shown that the electrode response is controlled by the ‘bulk path’, whereas in anodic polarization the surface paths is the main reaction pathway. The transition between the two reaction pathways would be related to the depletion of oxygen vacancies in the LSCF material occurring in anodic polarization.

Finally, the two micro-scale models are coupled to a macro-scale model that allows simulating the behavior of a complete button cell based in the operating conditions. The multi-scale modeling scheme has been validated on experimental data of two different button cells demonstrating the large flexibility of the modeling tool. Therefore, it can be used to investigate the degradation mechanisms of the SOCs operated in the fuel cell and electrolysis mode, taking into account the evolutions at the electrodes level and the overall cell response.

# **IV. Hydrogen Electrode Degradation: Impact of Polarization and Initial Microstructure on the Ni Evolution**

As introduced in chapter II, two types of cells with different Ni-YSZ cermets (*Cell-A* and *Cell-B*), which were aged by partners, have been thoroughly analyzed in the frame of this thesis with advanced post-test characterizations and modeling. These cells were aged in fuel cell and electrolysis modes for operating times ranging from 1'000 hours to 15'000 hours. Thanks to the careful inspection of the experimental data, it was clearly confirmed and reported in chapter II that the degradation rate measured in electrolysis mode is higher than in fuel cell mode (for the same type of cell). Moreover, it has been shown that the degradation for *Cell-B* is significantly higher than for *Cell-A*. According to the literature, it is known that a significant part of the degradation could come from the Ni evolution in operation (cf. chapter I). Therefore, it could be suggested that the difference in the degradation rate between the two types of cells could be related to the difference in the initial Ni-YSZ cermets microstructures. To go further in the interpretation, the microstructures for the pristine and aged cermets (for the two types of cells) have been carefully characterized by 3D reconstructions obtained *via* X-ray nano-holotomography.

In a second step, the microstructural data extracted from the 3D volumes have been implemented in the multi-scale modeling tool to quantify the impact of Ni evolution on the cell performances.

Concerning the Ni coarsening in the bulk, the phenomenological law for the Ni agglomeration proposed in the thesis of M. Hubert has been used [Hubert 2018, 2018a] in order to evaluate the impact on the performances for very long operating times. In addition, the extent of Ni depletion at the electrolyte interface has been quantified and its effect on the electrode and cell response has been evaluated. Thanks to the simulations, a mechanism to account for the higher nickel migration observed after an operation in electrolysis mode has been proposed and discussed.

The first section of this chapter is dedicated to the presentation of the cermet reconstruction with the data acquisition and the 3D image processing for microstructural computations. The second section is devoted to the presentation and the analyses of the evolutions of the microstructural properties before and after ageing. The assessment by electrochemical modeling of the impact of both the Ni coarsening and migration on cell performances is reported in the third section of the chapter. Finally, the presentation of an alternative mechanism for the Ni depletion is detailed in the last part of this chapter.

## **IV.1 3D Reconstructions and Image Processing Techniques for Microstructural Computations**

To investigate the microstructural evolutions occurring in the Ni-YSZ cermet after operation, 3D reconstructions have been obtained *via* X-ray nano-holotomography. The volumes have been analyzed using in-house codes to determine the overall modifications in the microstructural properties in the bulk of the cermets. In addition, a specific attention has been given to obtain the local evolutions of the microstructural parameters in the vicinity of the electrode/electrolyte interface.

In this section the samples extracted from each cell are described as well as the procedure followed to measure the evolutions of the microstructural parameters.

### *IV.1.1 Samples Extracted from Cell-A and Cell-B*

Eight micro-pillars have been analyzed in this work. The samples have been prepared for the nano holotomography experiment using the pFIB and following the procedure reported in section II.3.2.2. As an illustration, one of prepared pillars is shown in Figure IV-1a.

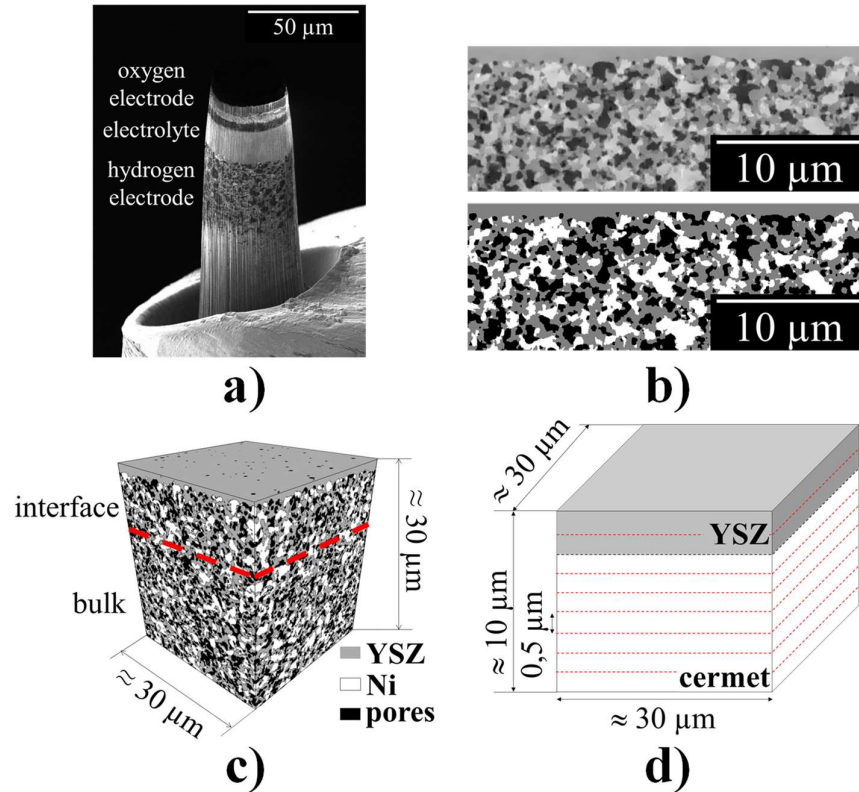


**Figure IV-1: Procedure for the sample preparation, reconstruction and analysis: a) Micro-pillar of *Cell-B Reference* prepared with the pFIB – b) Comparison of a 2D slice before and after the segmentation – c) 3D segmented volume – d) Illustration of the slice-by-slice approach for the computation of the local microstructural properties at the electrode/electrolyte interface.**

For *Cell-A3*, three samples have been extracted from the inlet, the center and the outlet segments as reported in Figure II-10b (named *Cell-A3 Inlet*, *Cell-A3 Center* and *Cell-A3 Outlet*, respectively). For *Cell-A4*, one sample coming from the inlet of the fifth RU has been analyzed (*Cell-A4 Inlet*). Moreover, two samples taken from *Cell-B* have been studied (Figure IV-2).

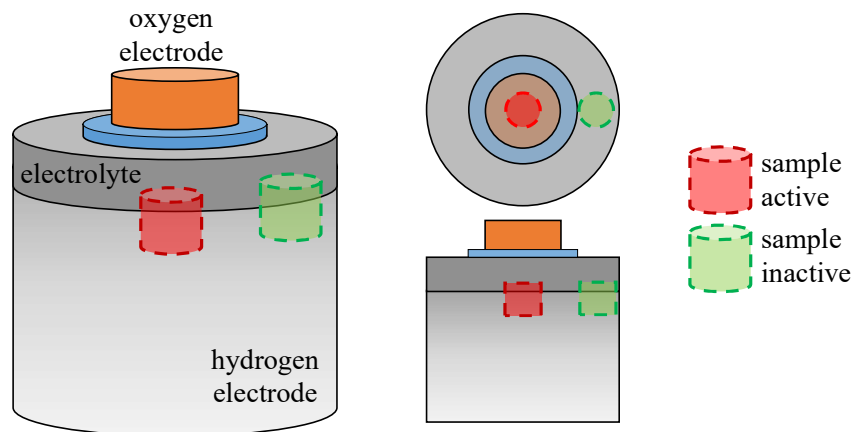


**Figure IV-2: Illustration of the two samples taken from the aged cell of type *B* corresponding to *Cell-B Active* and *Cell-B Inactive*.**

One of these two samples has been extracted from the center of the cell, in the electrochemically active region (*Cell-B Active*). The other one has been taken from the periphery of the cell, from a region in which no electrochemistry occurs (*Cell-B Inactive*). Finally, for both types of cells, a representative reference sample coming from a pristine cell just after the cermet reduction has also been prepared and reconstructed (*Cell-A Reference* and *Cell-B Reference*).

#### IV.1.2 Methodology for the Determination of the Microstructural Parameters

The 3D reconstructions of each sample have been obtained *via* X-ray nano-holotomography as described in section II.3. Once the microstructure had been reconstructed, a region containing part of the hydrogen electrode and the electrode/electrolyte interface has been identified. For each sample, a sub-volume of  $\approx 30 \times 30 \times 30 \mu\text{m}^3$  has been selected. These dimensions allow to be representative for the classical Ni-YSZ cermet being larger than the typical Representative Volume Element (RVE) of  $\approx 17^3 \mu\text{m}^3$  [Moussaoui 2018]. The raw images have been processed by using in-house codes in order to identify the percolated phases (Ni, pores and YSZ) [Quey 2013, Usseglio-Viretta 2014, Villanova 2013]. For this purpose, the raw data in grey levels have been filtered following the approach proposed by [Perona 1990] to enhance the contrast between the different phases. Afterwards, the filtered 3D images have been segmented using the criterion proposed by [Otsu 1979], and a specific value has been assigned to each phase. A visual comparison between a 2D cross-section taken from the raw 3D image and the corresponding 2D slice coming from the segmented reconstruction is shown in Figure IV-1b. A good accordance can be noticed between the two images proving the reliability of the filtering and segmentation procedures. A 3D rendering volume containing a part of the Ni-YSZ cermet and a part of the electrolyte is also given in Figure IV-1c as an illustration. As a last step, the connected paths for each phase have been identified in the reconstructions [Usseglio-Viretta 2014] so that the microstructural properties are computed on the percolated and disconnected phases.

The density of active TPBs ( $\xi_{TPBs}$ ), the volume fraction of each phase ( $V_f$ ), the specific surface areas ( $Sp_{i-j}$ ) and the mean phase diameters ( $\bar{D}_m$ ) have been measured on the volumes using an in-house algorithm [Moussaoui 2018]. Moreover, the M-factors (eq. (IV-1)), defined as the ratio between the effective conductivity (or diffusivity) and the intrinsic value for the solid (or gas) phase, have been computed by solving the Laplace equation on the microstructures [Laurencin 2012].

$$M_i = \frac{\sigma_i^{eff}}{\sigma_i^{bulk}} \quad (\text{IV-1})$$

Where  $\sigma_i^{eff}$  and  $\sigma_i^{bulk}$  represent the effective and the intrinsic conductivity/diffusivity of phase  $i$  expressed in  $\text{S} \cdot \text{m}^{-1}$ .

All these microstructural parameters have been computed in two ways: (i) to evaluate the global microstructural evolution in the bulk and (ii) to take into account the potential gradients arising in the neighborhood of the electrode/electrolyte interface. For this purpose, the microstructural properties in the bulk of the electrodes have been calculated for each reconstruction on a sub-volume taken  $\approx 10 \mu\text{m}$  away from the electrode/electrolyte interface ( $\approx 30 \times 30 \times 20 \mu\text{m}^3$ ) (Figure IV-1c). In order to evaluate the gradients, the first  $10 \mu\text{m}$  of each Ni-YSZ electrode reconstruction have been divided in twenty slices of  $30 \times 30 \times 0.5 \mu\text{m}^3$  (Figure IV-1d) and the local microstructural parameters have been calculated with a slice-by-slice approach.

## IV.2 Results of the Microstructural Analysis

The microstructural parameters extracted from the bulk of the pristine and aged samples have been measured. In addition, the gradients and the electrode/electrolyte interfaces have also been computed and compared between the different samples. In this way it has been possible to investigate the evolutions of each cell as a function of the initial microstructures and operating conditions. In this section, the comparison between the two pristine cells is analyzed as well as the changes occurring in *Cell-A* and *Cell-B* after aging as a function of the operating modes. It can be noticed that the occurrence of incidents during the long-term test does not seem to have significantly influenced the morphological evolution in the cermets of the aged cells, so that the analysis of the Ni evolution after aging can be considered as reliable.

### IV.2.1 Microstructural Properties of the Reference Cells

As a first analysis, the reconstructions coming from the two reference samples (*Cell-A Reference* and *Cell-B Reference*) have been studied to investigate the differences in the initial microstructures between the two types of Ni-YSZ electrodes.

The comparison between the two rendering volumes taken in the bulk of the two pristine cermets is shown in Figure IV-3a and Figure IV-3b. It can be seen that the two initial microstructures differ significantly between each other. On the one hand, *Cell-A Reference* presents a fine microstructure with a rather homogenous distribution of Ni particles (Figure IV-3a). On the other hand, *Cell-B Reference* presents a much coarser microstructure, with large agglomerates of Ni even before aging (Figure IV-3b). This difference in the initial microstructures is also revealed by the inspection of the nickel Particle Size Distribution (PSD) plotted for the two electrodes (Figure IV-3c). The coarser

microstructure for *Cell-B Reference* is reflected in a broader distribution for the Ni phase compared to the narrow peak computed for *Cell-A Reference*. As a result, the Ni mean particle diameter of *Cell-B Reference* is more than twice the one for *Cell-A* (1.14  $\mu\text{m}$  vs 0.46  $\mu\text{m}$ : cf. Table IV-I). From this observation, an important difference in the other microstructural parameters for the two samples can be expected. Indeed, a finer microstructure must lead to a higher number of active TPBs and higher specific surface areas between the phases [Moussaoui 2019]. This dependence is well confirmed by the microstructural properties provided in Table IV-I for the two types of cermet (as an example, the density of TPBs for *Cell-A Reference* is four time larger than for *Cell-B Reference*).

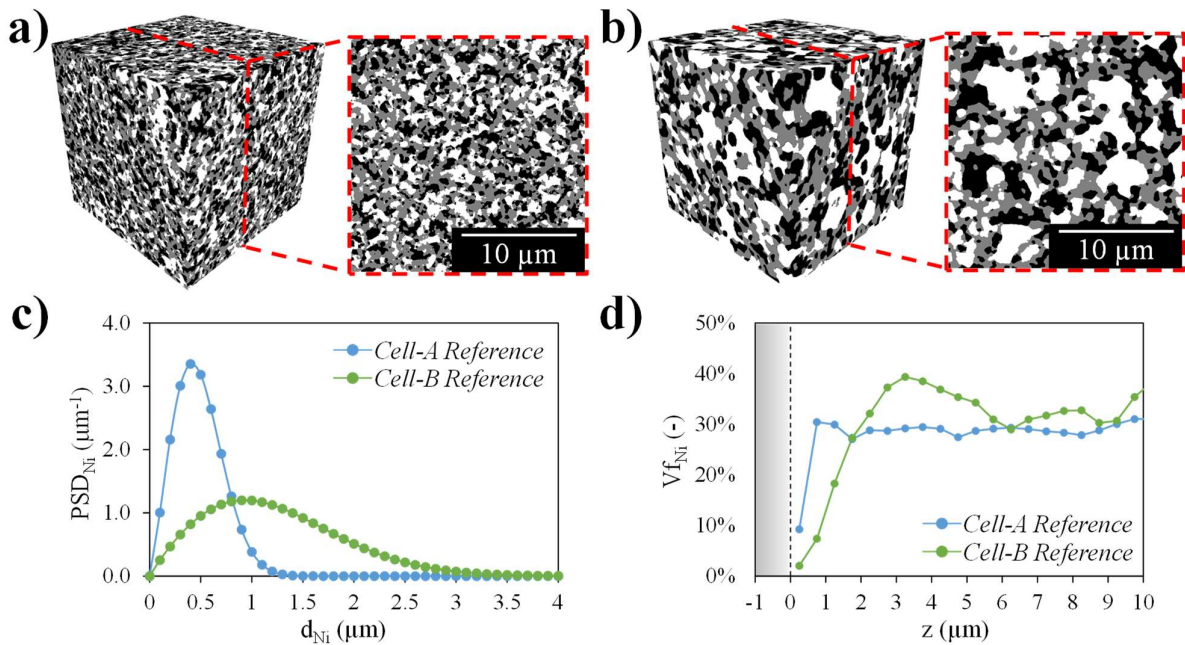


**Figure IV-3: Comparison of the microstructural properties between the two types of reference cells: 3D rendering and 2D cross-section of a) *Cell-A Reference* and b) *Cell-B Reference* (White: Ni, Grey: YSZ, Black: Pores) – c) Nickel particle size distribution for the two types of reference cells – d) Evolution of the Ni volume fraction for the two cells at the electrode/electrolyte interface.**

Finally, the local Ni volume fractions for the two pristine cells are plotted in Figure IV-3d as a function of the position in the depth of the cermet starting from the electrolyte interface (i.e.  $z=0$ ). In both cases, gradients with a quite sharp increase of the Ni volume fraction are detected. Because of its coarser microstructure, the transition for *Cell-B* is smoother and more extended before reaching the Ni volume fraction in the bulk. These gradients, which are observed even for the pristine cermet, can probably be explained by the manufacturing process based on the co-sintering of the electrolyte and the cermet. To investigate the morphological evolution of Ni after operation for the two types of cell, the reconstructions coming from the aged samples have been analyzed.

**Table IV-I: Connected bulk properties of the Ni-YSZ extracted away from the electrode/electrolyte interface for the eight samples (*Cell-A3*: aged SOFC – *Cell-A4* and *Cell-B Active*: aged SOEC)**

Sample	$\xi_{TPBs}$ ( $\mu\text{m}^{-2}$ )	$Vf_p$ (%)	$Vf_{YSZ}$ (%)	$Vf_{Ni}$ (%)	$Sp_{p-YSZ}$ ( $\mu\text{m}^{-1}$ )	$Sp_{p-Ni}$ ( $\mu\text{m}^{-1}$ )	$Sp_{YSZ-Ni}$ ( $\mu\text{m}^{-1}$ )	$\bar{D}_{m,p}$ ( $\mu\text{m}$ )	$\bar{D}_{m,YSZ}$ ( $\mu\text{m}$ )	$\bar{D}_{m,Ni}$ ( $\mu\text{m}$ )	$M_{pores}$ (-)	$M_{YSZ}$ (-)	$M_{Ni}$ (-)
<i>Cell-A Reference</i>	6.03	29.0	42.3	28.7	1.99	0.67	1.71	0.41	0.37	0.46	0.027	0.173	0.044
<i>Cell-B Reference</i>	1.55	29.1	36.8	34.1	1.21	0.28	0.90	0.72	0.59	1.14	0.036	0.150	0.065
<i>Cell-A3 Inlet</i>	4.26	26.9	42.7	30.4	1.89	0.41	1.55	0.44	0.39	0.62	0.034	0.186	0.038
<i>Cell-A3 Center</i>	4.42	27.5	42.4	30.1	1.89	0.43	1.54	0.44	0.39	0.61	0.037	0.180	0.039
<i>Cell-A3 Outlet</i>	4.11	27.7	42.5	29.8	1.87	0.41	1.47	0.45	0.40	0.63	0.038	0.184	0.037
<i>Cell-A4 Inlet</i>	4.40	25.3	44.9	29.8	1.90	0.45	1.52	0.40	0.41	0.61	0.024	0.207	0.039
<i>Cell-B Active</i>	1.11	28.3	32.3	39.4	1.07	0.18	0.76	0.80	0.59	1.81	0.061	0.124	0.073
<i>Cell-B Inactive</i>	1.14	32.1	30.6	37.2	1.07	0.26	0.60	0.84	0.63	1.93	0.079	0.103	0.055

## IV.2.2 Microstructural Evolution of the Aged Cells

### IV.2.2.1 Evolution in the Bulk

Figure IV-4 displays the 3D rendering volumes as well as the 2D images extracted from the bulk of the aged samples. For *Cell-A3*, only the reconstruction coming from the outlet (*Cell-A3 Outlet*) is shown as an illustration of the overall microstructural evolution for this cell. The visual comparison between Figure IV-3 and Figure IV-4 shows without any ambiguity that all cermets are subjected to an agglomeration of nickel after aging. Nevertheless, it is clear that the morphological evolution is more pronounced for *Cell-B* than for *Cell-A* whatever the considered operating mode.

To deepen the analysis, all the microstructural parameters measured on the 3D volumes after operation have been computed and are given in Table IV-I. The evolution of the properties between the fresh and the aged cells confirms the Ni agglomeration arising upon operation. Indeed, an increase of the mean Ni diameter is found in all the reconstructions taken from the operated cells. As expected, the Ni particle coarsening is accompanied by a loss of TPBs densities and by a decrease in the specific surface area of Ni (Table IV-I).

It can be noticed that, for the aged specimens of *Cell-A*, the Ni volume fractions remain almost constant after aging. This behavior confirms that the agglomeration in the bulk can be described by a local particle sintering without significant redistribution of Ni at long-distance. Furthermore, the Ni particle growth is not severely influenced either by the polarization or the gas composition, in good

agreement with the thermally activated process related to Ni coarsening proposed by Hubert *et al.* [Hubert 2018a]. This behavior is in accordance with the experimental results reported by [Khan 2018].

Conversely, for *Cell-B*, a noticeable enrichment of Ni is measured in the bulk of the cermet after operation. This behavior is more pronounced in the sample taken from the electrochemically active region (*Cell-B Active*) than in the sample extracted from the periphery of the cell (*Cell-B Inactive*). This type of evolution could be explained by a combination of Ni agglomeration based on local sintering and Ni volatilization/re-deposition process [Lee 2014].

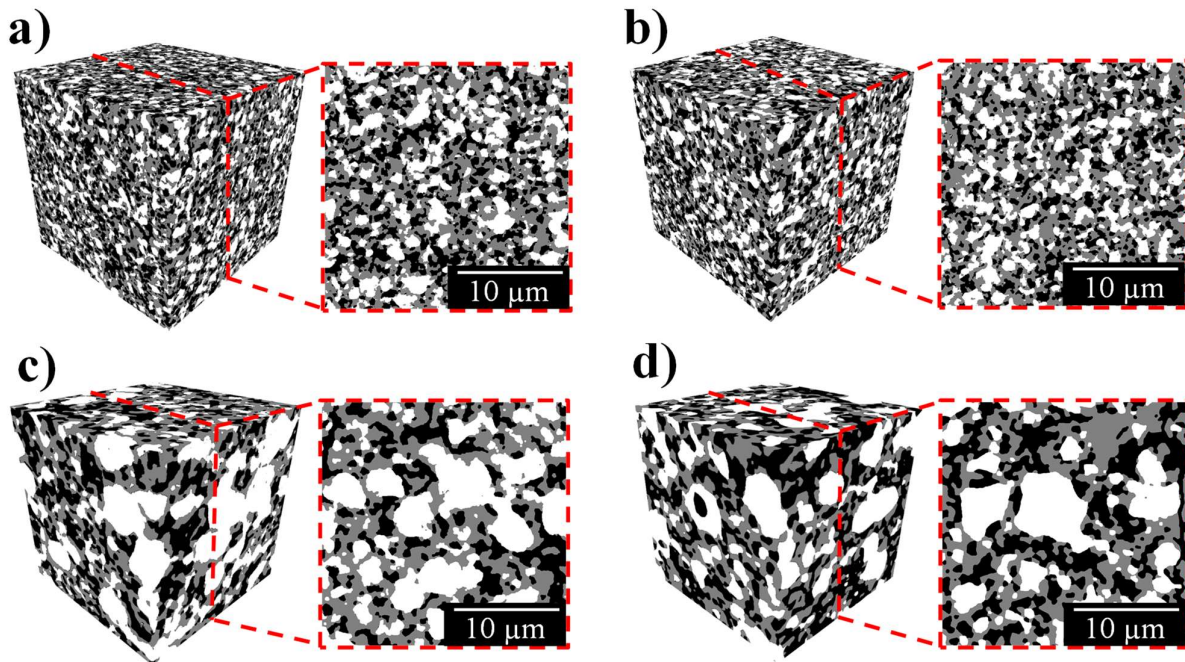


**Figure IV-4:** 3D segmented rendering and 2D cross-sections extracted for the bulk reconstructions of the aged samples: a) *Cell-A3 Outlet* – b) *Cell-A4 Inlet* – c) *Cell-B Active* – d) *Cell-B Inactive* (White: Ni, Grey: YSZ, Black: Pores).

To investigate the Ni evolution at the electrode/electrolyte interface the local microstructural properties of the aged cells have been calculated using the slice-by-slice approach.

#### *IV.2.2.2 Evolution at the Electrode/Electrolyte Interface*

In Figure IV-5, a zoom on the cermet microstructure at the electrode/electrolyte interface for each reconstruction is shown. To better visualize the microstructural evolutions, 2D images coming from the whole reconstructions are shown with slices taken perpendicular and parallel to the interface with the electrolyte. Once again, for *Cell-A3* only the outlet reconstruction (*Cell-A3 Outlet*) is reported as an illustration.

As shown in Figure IV-5a–c for *Cell-A*, nickel is present at the electrode/electrolyte interface for the reference cell as well as for all the aged samples. Nevertheless, it can be noticed that the sample operated for 10'700 hours in electrolysis mode (*Cell-A4 Inlet*, Figure IV-5c) presents a slight depletion of Ni at the interface that is not observed in the sample aged for 15'000 hours in fuel cell mode even at high steam partial pressure (*Cell-A3 Outlet*, Figure IV-5b).

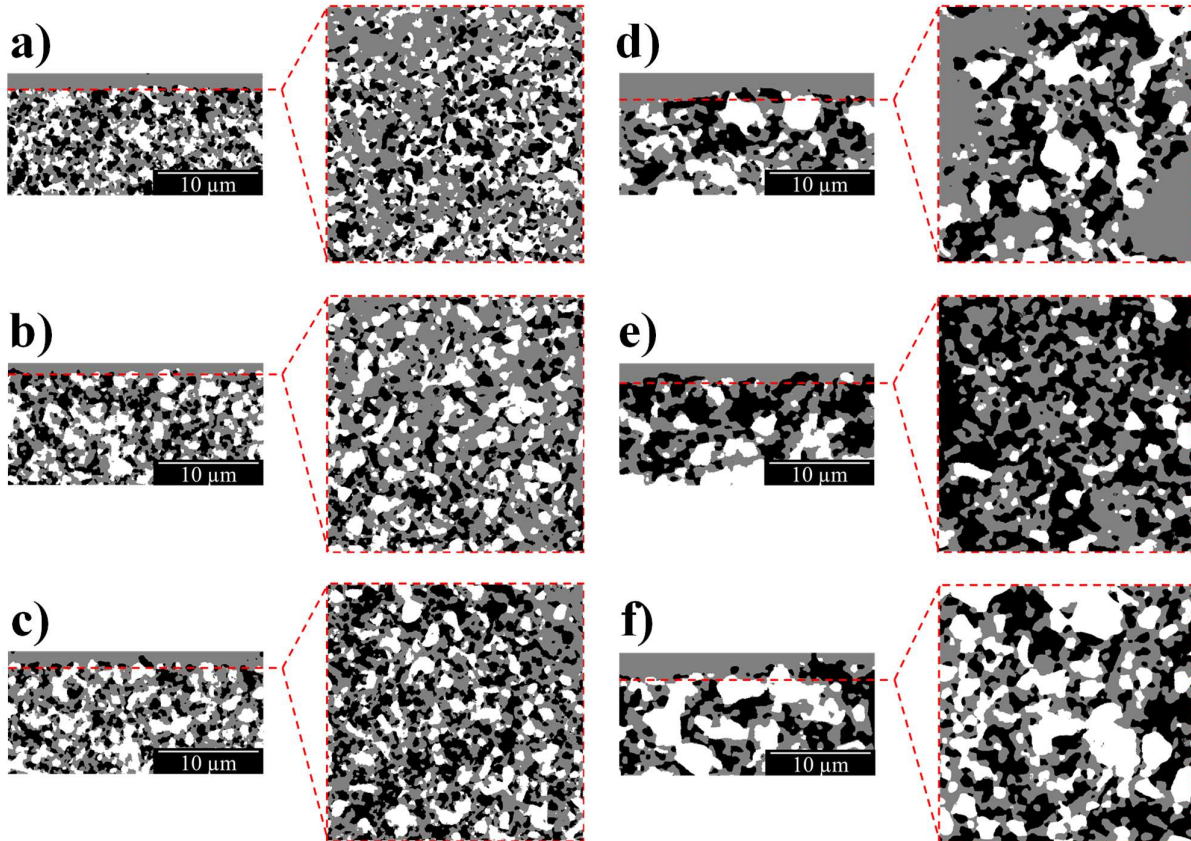


**Figure IV-5:** 2D images from the segmented volumes extracted parallel and perpendicular to the electrode/electrolyte interface: a) *Cell-A Reference* – b) *Cell-A3 Outlet* – c) *Cell-A4 Inlet* – d) *Cell-B Reference* – e) *Cell-B Active* – f) *Cell-B Inactive* (White: Ni, Grey: YSZ, Black: Pores).

On the contrary, the local evolutions for *Cell-B* are quite different as can be seen in Figure IV-5d–f. In this case, after only 1'000 hours in electrolysis mode, a severe Ni depletion is observed at the electrode/electrolyte interface for the sample coming from the electrochemically active region (*Cell-B Active*, Figure IV-5e). This evolution is in good agreement with the enrichment that has been measured in the bulk of the sample. However, it is worth noting that a larger amount of Ni is still present at the interface for the sample extracted from the periphery of the aged cell (*Cell-B Inactive*, Figure IV-5f). These results reveal that an important loss of nickel from the electrode/electrolyte interface occurs for this type of cell, specifically in the electrochemically active region.

To confirm these evolutions, the gradients in the local microstructural parameters have been evaluated at the electrode/electrolyte interface using the slice-by-slice approach (Figure IV-6).

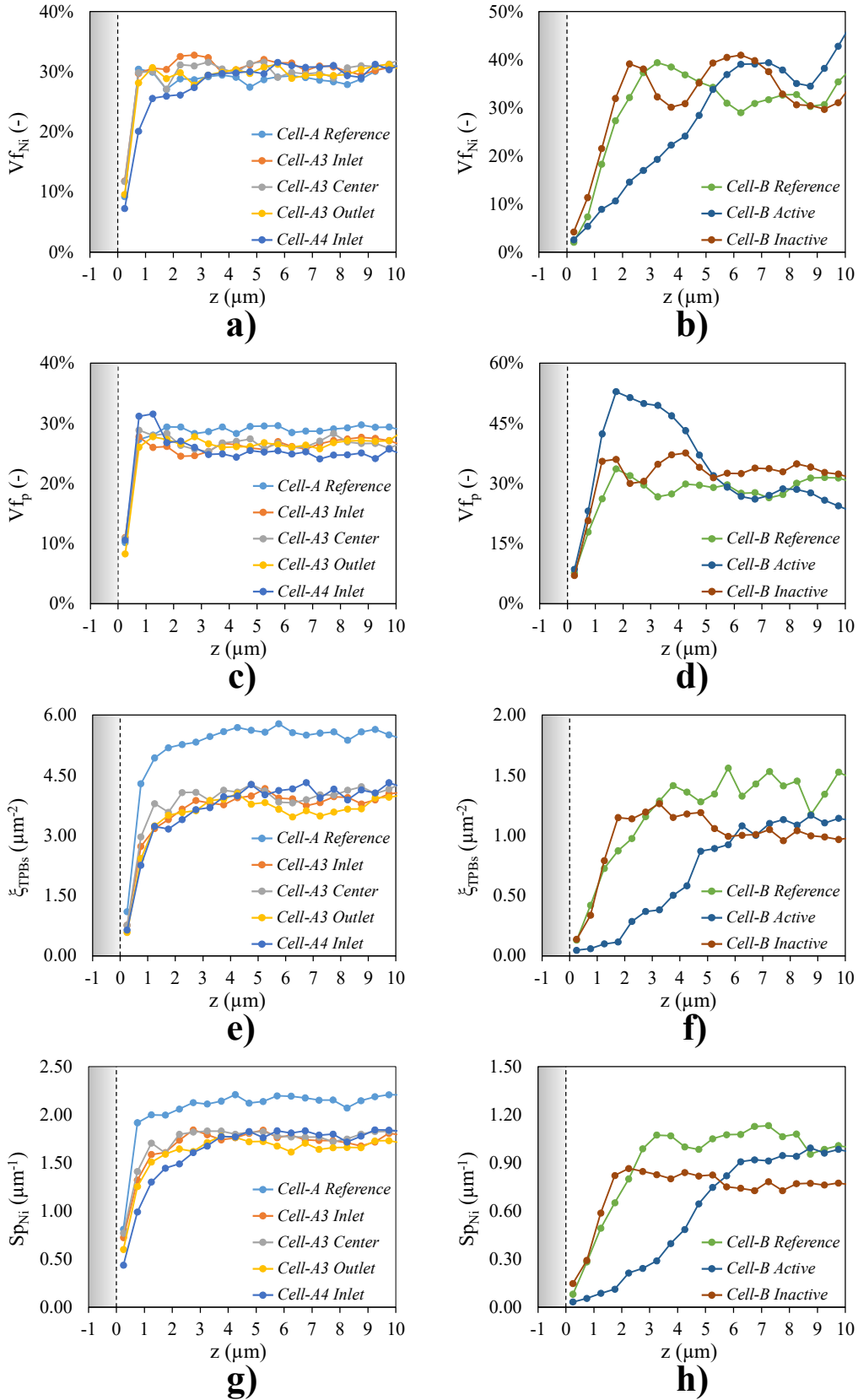


**Figure IV-6: Local microstructural parameters at the electrode/electrolyte interface for *Cell-A* and *Cell-B*: (a, b) Nickel volume fraction – (c, d) Pores volume fraction – (e, f) TPBs density – (g, h) Ni specific surface area.**

For *Cell-A3*, the gradients for the inlet, center and outlet reconstructions are almost superimposed with only a minor decrease of Ni volume fraction for the outlet segment (Figure IV-6a). This slight evolution could be associated to the higher steam partial pressure at the outlet of this cell operated in SOFC mode. However, it is worth mentioning that the difference is very limited even after 15'000 hours, indicating an overall similar evolution between the three segments.

Conversely, a more-pronounced decrease of Ni volume fraction is found for *Cell-A4*, which is concomitant with an increase of the pore volume fraction (Figure IV-6c). This slight Ni depletion extends from the electrolyte interface in the first two micrometers within the cermet. It can be noticed that this extension is in good agreement with the observations reported by Rinaldi *et al.* [Rinaldi 2017a], where cells coming from the same stack have been characterized. This Ni depletion induces a moderate loss of TPBs and Ni specific surface area as shown in (Figure IV-6e and Figure IV-6g). From this analysis of *Cell-A*, it can be stated that the Ni depletion is favored under cathodic polarization (i.e. electrolysis mode) although it is worth mentioning that this phenomenon is rather limited for both cells (*Cell-A3* and *Cell-A4*).

In contrast to *Cell-A*, the severe Ni depletion at the electrode/electrolyte interface for *Cell-B Active* is confirmed by the local quantifications of the Ni volume fractions. Indeed, an important loss of Ni is measured at the electrolyte interface, which spreads in the first  $\approx 5-6 \mu\text{m}$  of the electrode (Figure IV-6b). This local decrease of Ni volume fraction is accompanied by a simultaneous increase of the porosity (Figure IV-6d). Therefore, an almost full depletion of Ni is measured nearby the electrolyte interface in good agreement with the 2D slice given in Figure IV-5e. Consequently, a huge decrease of  $\xi_{TPBs}$  and  $Sp_{Ni}$  is measured at the interface (Figure IV-6f and Figure IV-6h) for this sample. On the contrary, the local evolutions for *Cell-B Inactive* are more similar to the pristine cermet, reinforcing the observation that no severe migration of nickel is detected in this sample. This statement is in good agreement with the experimental observation reported in [Hoerlein 2018, Mogensen 2017], indicating the key impact of the electrochemical activity on the Ni depletion.

Finally, from the comparison between the behavior of *Cell-A* and *Cell-B*, it can be pointed out that the initial microstructure of the electrode and the nature of the materials of the Ni-YSZ cermet play a central role on the severity of the loss of Ni from the electrode/electrolyte interface.

### IV.3 Impact of Ni Evolution on the Cell Performances

After the identification of the microstructural modifications for the aged cells, the multi-scale model has been used to evaluate the impact of Ni agglomeration and depletion on the electrode and cell

performances. Concerning the Ni agglomeration, the phenomenological law for the particle coarsening proposed in the thesis of M. Hubert [Hubert 2018] has been used to predict the increase of the Ni mean particle diameter. This evolution has been coupled with the microstructural correlations developed in the thesis of H. Moussaoui [Moussaoui 2019a] to express the corresponding evolution on the TPBs and thus, the effects on the overall cell response. In order to investigate the effect of the Ni depletion at the electrolyte interface, the micro-scale model has been adapted to take into account the gradients in microstructural properties measured with the slice-by-slice approach. In this section, the impacts on the electrode and cell performances of the two phenomena associated to the Ni phase modification in the cermet are presented and analyzed.

#### *IV.3.1 Preliminary Remark: Adaptation of the H<sub>2</sub> Electrode Model*

For this analysis, the second version of Model II for the hydrogen electrode, which was specifically developed for the durability studies, has been employed (cf. chapter III section III.1.4.2, for reminding, this model is based on the hydrogen spillover mechanism by considering all the expected species on Ni surface). It is worth noting that this model was slightly adapted here to take into account the gradients in microstructural properties measured on the 3D volumes. For this purpose, the kinetic rates, the gas diffusivities and the electronic/ionic conductivities have been scaled with the local microstructural properties evolving from the electrolyte interface into the electrode thickness. In other words, each microstructural property implemented in the model is not a single value as used in chapter III but depends on its position in the electrode thickness. Using this approach, it is possible to evaluate the impact of Ni agglomeration/redistribution on the electrode and cell response.

#### *IV.3.2 Role of Ni Agglomeration on Degradation*

To investigate the impact of Ni agglomeration, our dataset for *Cell-A* has been merged with the one analyzed in [Hubert 2018, 2018a] for the same type of cell. In Figure IV-7a, the evolutions at different temperatures of the Ni mean particle diameters are plotted as a function of the operating time. It can be noticed that the data for *Cell-A3* (aged in SOFC mode) and *Cell-A4* (aged in SOEC mode) are roughly aligned with those of the sample aged at 750°C for 9'000 hours in fuel cell mode taken from [Hubert 2018a]. For this reason, these data have been fitted approximating the aging temperature at 750°C and using the phenomenological agglomeration law given in eq. (IV-2) based on an Ostwald ripening process that has been proposed by Hubert *et al.* [Hubert 2018a].

$$[\bar{D}_m(t)^n - \bar{D}_m(t=0)^n] = k_{pow} \cdot t \quad \text{with} \quad k_{pow} = k_{00} \cdot \exp(-\Delta H/RT) \quad (\text{IV-2})$$

Where  $t$ ,  $n$  and  $\Delta H$  represent the time, the process related exponent and the activation energy.

As it can be seen from Figure IV-7a, the data are accurately fitted using  $n = 8$  and an activation energy of  $\approx 210 \text{ kJ} \cdot \text{mol}^{-1}$ . This high exponent confirms the inhibiting effect of the YSZ backbone that limits the rate of Ni agglomeration in the cermet [Faes 2009, Hubert 2018a, Jiang 2003]. This statement is also highlighted by the relative stability of  $Sp_{YSZ-Ni}$  with respect to the  $Sp_{p-Ni}$ , as reported in Table IV-I for the aged cells of type *A*. Conversely, the evolutions of the specific surface areas are quite different for *Cell-B* with a higher modification of  $Sp_{YSZ-Ni}$  under operation (Table IV-I). This difference between the two types of cells is in good agreement with the more severe Ni coarsening of *Cell-B* and reveals the crucial role of the Ni/YSZ interfacial adhesion on the electrode microstructure stability.

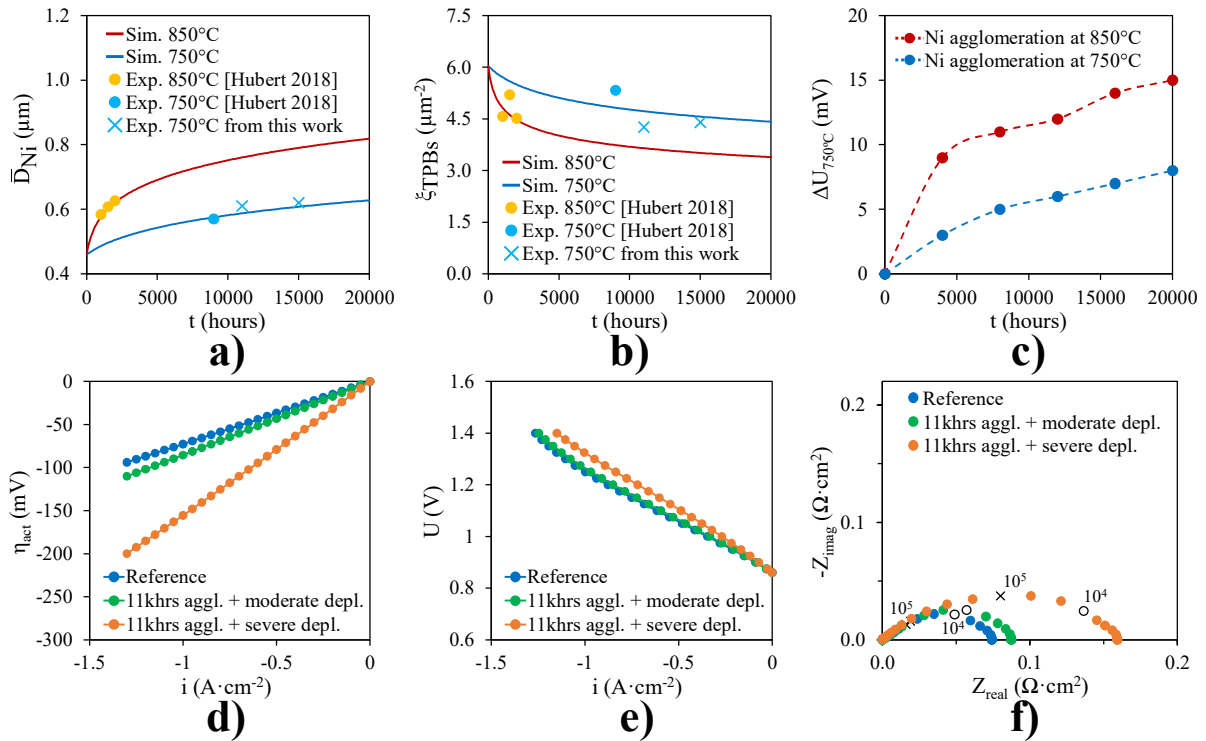


**Figure IV-7: Effects of the hydrogen electrode microstructural evolution on the H<sub>2</sub> electrode and cell performances: a) Increase of the Ni mean particle diameter associated to the Ni agglomeration – b) Effect of the Ni agglomeration on the density of TPBs – c) Simulated voltage drop at 750°C and  $-0.5 \text{ A} \cdot \text{cm}^{-2}$  caused by Ni agglomeration at 750°C and 850°C – Effect of the Ni depletion on the hydrogen electrode activation overpotential (d) and on the cell performances (e) – f) Evolution of the EIS associated to the Ni depletion.**

To determine the decrease of TPBs density associated to the Ni agglomeration as a function of the aging time, eq. (IV-2) has been combined with the microstructural correlation given in [Moussaoui

2019, 2019a]. As shown in Figure IV-7b, a satisfactory approximation of the TPBs decrease at 850°C and 750°C is found without any additional fitting.

The TPBs evolutions at the two temperatures have been implemented in the multi-scale model to quantify the impact of Ni agglomeration on the cell degradation. For the different values of  $\zeta_{TPBs}$ , the cell response has been evaluated at 750°C and  $-0.5 \text{ A}\cdot\text{cm}^{-2}$ . The gas compositions used for the simulations were  $\text{H}_2\text{O}/\text{H}_2 = 90/10 \text{ vol.}\%$  at the hydrogen electrode (total flowrate of  $12 \text{ Nml}\cdot\text{min}^{-1}\cdot\text{cm}^{-2}$ ) and air at the oxygen electrode (flowrate of  $62 \text{ Nml}\cdot\text{min}^{-1}\cdot\text{cm}^{-2}$ ). Taking advantage of the model calibration over long operating times, the voltage increase has been calculated up to 20'000 hours. It is shown in Figure IV-7c that the voltage drop due to Ni agglomeration is higher when the cell is operated at higher temperature and tends to stabilize for very long-term operation. For instance, at 750°C, the voltage degradation associated to the Ni coarsening evolves from  $\approx 5 \text{ mV}$  at 8'000 hours to  $\approx 8 \text{ mV}$  at 20'000 hours in electrolysis mode. Extrapolating this evolution for the requested lifetime of  $\approx 40'000$  hours, a voltage increase of  $\approx 10 \text{ mV}$  is found. Therefore, even if there is not a full asymptotic behavior for the Ni agglomeration, its impact on the performance does not diverge and should not compromise the overall cell durability.

### IV.3.3 Role of Ni Depletion on Degradation

In addition to the agglomeration, the depletion of Ni from the electrolyte interface is also expected to decrease the cell performance. Although a general physically-based model describing the Ni migration is still missing, the gradients measured after electrolysis operation for the two types of studied cells (*Cell-A4 Inlet* and *Cell-B Active*) can be used as lower and upper bounds to evaluate the impact of the loss of nickel. To quantify the cell degradation in these two limiting cases, the corresponding microstructural evolutions at the electrode/electrolyte interface have been implemented in the model. The hydrogen electrode activation overpotential and the cell performances have been simulated after 11'000 hours at 750°C (Figure IV-7d and Figure IV-7e). In case of moderate depletion, it is found that the effects on the electrode and cell responses are quite limited. Indeed, in this case a voltage loss of  $\approx 6.5 \text{ mV}$  can be assessed for the complete cell after 11'000 hours at  $-0.5 \text{ A}\cdot\text{cm}^{-2}$ .

This value is slightly above to the degradation computed by considering only the agglomeration for the same aging conditions ( $\approx 5.9 \text{ mV}$ ). This result indicates that, in this case, the degradation in cell performances due to the microstructure change in the hydrogen electrode is mainly controlled by the Ni agglomeration while the impact of Ni migration is noticeable but not dominant. On the contrary, when a severe loss of Ni from the electrode/electrolyte interface is introduced in the model (with the

gradients for *Cell-B Active*), the effects on the electrode and cell response are much more pronounced (Figure IV-7d and Figure IV-7e). In this case, the increase of the absolute value for the electrode overpotential is much higher than if only the agglomeration is taken into account. This huge electrode degradation yields to a significant cell voltage loss of  $\approx 50$  mV calculated at  $-0.5 \text{ A}\cdot\text{cm}^{-2}$ . A sensitivity analysis has been conducted with the model to identify the most impacting microstructural parameters. It has been found that the important cell degradation is mostly related to the substantial loss in the local density of TPBs at the electrolyte interface that directly controls the rate of the charge transfer reactions. At the same time, the effect of the other microstructural changes has been found to be less impacting. More specifically, it has been found that the decrease of the Ni/gas interfacial surface area has a much smaller influence on the electrode/cell performances compared to the drop of TPBs lengths. Moreover, even with the significant decrease of the Ni volume fraction, the local effective Ni conductivity in the active layer remains sufficiently high to not induce too large Ohmic losses.

This high impact of the Ni depletion on the charge transfer reactions is also confirmed by the EIS spectra computed at OCV for the hydrogen electrode in the two limiting situations of Ni migration (Figure IV-7f). In case of moderate loss of Ni from the electrode/electrolyte interface, an overall limited increase in the polarization resistance is obtained for the aged electrode, while the characteristic frequencies remain comparable to the reference. Instead, when a severe depletion is considered, an important increase of the polarization resistance is calculated. This higher resistance is accompanied by an increase of the contribution of the high frequency phenomenon, which is classically associated with the charge transfer at the TPBs [Nechache 2016]. In our case, it is worth noting that Ni is still percolating up to the interface with the electrolyte even considering the severe gradients taken for *Cell-B Active*. In this condition, the serial resistance determined from the EIS diagrams is not shifted due to an additional Ohmic resistance induced by a fully depleted layer in Ni.

From these numerical analyses, it appears that the impact of the Ni depletion on the cell performances can be very important depending on the initial cermet microstructure. This statement must explain a large part of the higher experimental degradation rates measured for the *Cell B* compared to *Cell A*. Moreover, it is worth reminding that the destabilization of the oxygen electrode material accelerated under electrolysis current must also contribute to the overall cell degradation [Frey 2018, Laurencin 2017] as discussed in chapter V.

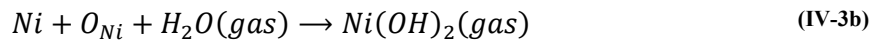
Finally, the comparison between the two studied cermet microstructures of *Cell-A* and *Cell-B* shows that the mitigation of the Ni depletion should be possible by microstructural optimization.

Nevertheless, in this objective, it is still required to clarify the underlying mechanisms driving the migration.

#### IV.4 Suggested Mechanism of Ni Depletion

Based on our experimental results, it can be stated that the Ni migration causes a loss of nickel at the electrolyte interface. This Ni depletion takes place within the cermet active layer where the electrochemical reactions take place. Indeed, a clear influence of the electrochemistry on the severity of the Ni depletion has been detected. Moreover, it appears that this phenomenon is strongly favored in cathodic polarization (i.e. SOEC mode) whereas the analyses of the samples aged in fuel cell mode indicate that the impact of the steam partial pressure remains less pronounced. Finally, the comparison between *Cell-A* and *Cell-B* highlights the strong impact on the Ni redistribution of the initial characteristics of the electrode (in terms of microstructure and materials). Indeed, it has been clearly shown that the Ni migration is favored in case of coarser initial microstructures. Moreover, as for the Ni agglomeration, it can be suspected that the nature of the Ni/YSZ interface could play a central role in the Ni depletion (i.e. interfacial adhesion between Ni and YSZ).

Even if the precise mechanism for the Ni depletion is not completely understood, it has been proposed that the Ni migration occurs in the gas phase with the formation of volatile hydroxyl species according to eqs. (IV-3a) and (IV-3b) [Chen 2016, Jiao 2011].



Based on these reactions, an influence of the steam partial pressure and the activities of the oxygen and hydroxyl species attached on the Ni surface could be expected.

To verify these dependencies, the micro-model for the hydrogen electrode has been used to simulate the electrode behavior at +/- 0.5 A·cm<sup>-2</sup>, with a gas composition of H<sub>2</sub>O/H<sub>2</sub> = 50/50 vol.% at 750°C. The evolution of the steam partial pressure and the coverages of species attached on the surface of Ni are presented in Figure IV-8 as a function of the position in the electrode. It can be seen that surface concentrations of oxygen and hydroxyl adsorbates are increased in fuel cell mode and decreased in electrolysis mode (Figure IV-8b and Figure IV-8c). According to the gas interaction with Ni (cf. chapter III), these evolutions are consistent with the higher steam partial pressure at the electrolyte interface in fuel cell compared to electrolysis mode (Figure IV-8a). Regarding the reactions of Ni evaporation (eqs. (IV-3a) and (IV-3b)), these simulations suggest that the Ni(OH)<sub>x</sub> formation should

be promoted under fuel cell current in the electrode active layer. In other words, if the rate-limiting step is the Ni evaporation, the global process should be accelerated in fuel cell mode. However, the analysis of the experimental results has clearly revealed that the depletion of Ni from the electrode/electrolyte interface is favored in electrolysis mode, while it remains almost negligible in SOFC mode, even at high  $p_{H_2O}$ . This contradictory result indicates that the Ni evaporation cannot be the limiting step for the Ni depletion. This means that even if the Ni migration occurs *via* volatile species, there must be another physical phenomenon triggering the nickel instability.

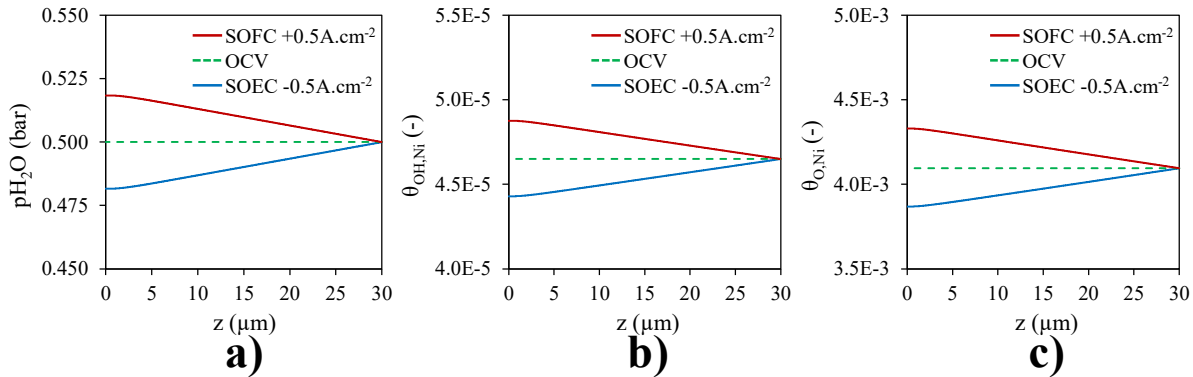


**Figure IV-8: Simulation results for the hydrogen electrode at  $H_2O/H_2 = 50/50$  vol.% and  $750^\circ C$ : a) Steam partial pressure, b) hydroxyl Ni surface coverage and c) oxygen Ni surface coverage as a function of the position in the electrode at  $\pm 0.5 A \cdot cm^{-2}$ .**

In this context, it has been proposed that the electrode polarization could be involved in the mechanism of Ni depletion [Mogensen 2017]. To check this possibility, the local electrode overpotentials have been plotted in the depth of the electrode for a current density of  $\pm 0.5 A \cdot cm^{-2}$  (Figure IV-9a). In contrast to the coverages and steam partial pressures, sharp evolutions of the electrode overpotential are simulated. These evolutions spread from the electrolyte interface over  $\approx 5 \mu m$  micrometers within the cermet. Interestingly, this penetration depth of the charge transfer reactions is in the same range as the one for which the Ni depletion has been observed in Figure IV-6b. Therefore, the large overpotential difference in anodic and cathodic polarization could be associated to the process of Ni depletion triggered in electrolysis mode.

In this frame, it has been recently proposed that the driving force for the Ni transport could be a gradient in Ni wettability across the active layer as a function of the electrode overpotential [Nakajo 2020, Rinaldi 2019, Trini 2020]. Alternatively, it has been suggested that the reductive potential could induce the detachment of Ni from YSZ [Chen 2013, Mogensen 2017]. Once detached, the Ni particles would no longer be stabilized by the YSZ backbone. These highly unstable particles could evaporate and increase the local partial pressure of hydroxyl species that would diffuse toward the bulk. Besides,

the detachment of the Ni from the YSZ would modify the local electrochemical activity, inverting the local steam partial pressure gradients. In this condition, the isolated Ni particles could also evaporate and migrate in the gas phase to agglomerate in the upper layer of the electrode [Hoerlein 2018, Mogensen 2017]. It is worth mentioning that a mechanism of Ni depletion controlled by the delamination between Ni and YSZ is in good agreement with the experimental observation. Indeed, it allows taking into account the influence of the Ni/YSZ interfacial stability highlighted by the comparison between *Cell-A* and *Cell-B*. As already discussed, this stability could be related to the adhesion of Ni on the YSZ which is strongly dependent on contaminants in YSZ [Kishimoto 2012a, Skarmoutsos 2000, Tsoga 1996b]. It could be also related to the microstructural difference between the two cermets. Indeed, the fine microstructure of *Cell-A* with a high density of TPBs allows limiting the overpotential for a given current density and could therefore mitigate the process of Ni migration. To illustrate this possibility, the model has been used and it has been shown that the passage from the coarse to the fine microstructure of *Cell-B* and *Cell-A* allows reducing significantly the absolute value of the overpotential at the electrolyte interface. For example, at a current of  $-0.5 \text{ A} \cdot \text{cm}^{-2}$ , a decrease of  $\approx 35 \text{ mV}$  for the absolute value of the overpotential has been calculated at the electrolyte interface ( $750^\circ\text{C}$  and gas composition  $\text{H}_2\text{O}/\text{H}_2 = 50/50 \text{ vol.}\%$ ). This quantification is in good agreement with the analysis reported by [Hauch 2016] suggesting that a fine Ni particle distribution would reduce the depletion of Ni. In addition, it can be noticed that increasing the temperature from  $700^\circ\text{C}$  to  $800^\circ\text{C}$  also induces a significant decrease of the electrode overpotential. From this point of view, a higher operating temperature should alleviate the rate of Ni depletion.

In spite of all these results, the exact microscopic process at the origin of the nickel instability at the electrode/electrolyte interface remains unclear. As an explanation, it could be proposed that the high cathodic overpotential could modify the structure of the double layer leading to the deterioration of the Ni/YSZ interface. In other words, the polarization could affect the Ni/YSZ interfacial adhesion through the accumulation of charges in the double layer. Indeed, the atomic interaction between the Ni and YSZ is characterized by a large number of Ni-O bonds at the interface [Christensen 2001, Sasaki 2004]. From this statement, it was suggested by Sasaki *et al.* [Sasaki 2004] that ‘the number of on-top Ni-O bonds is one of the critical factors that can determine the stability of the metal/oxide interface’. Therefore, the replacement of O atoms by vacancies (due to a modification of the double layer structure in electrolysis mode) is expected to reduce the number of Ni-O bonds, and hence, to weaken the Ni-YSZ adhesion.

To assess the relevance of this suggestion, the concentration of oxygen vacancies in the vicinity of the electrolyte interface has been evaluated as a function the electrode polarization. In the bulk of the

solid phases, that is to say far away from the TPBs lines, the Ni/YSZ interface can be seen as a blocking electrode. In this case, the oxygen vacancies concentration could be modeled considering a classical Boltzmann distribution, with a maximal concentration depending on the material [Hendriks 2002a], as reported in eq. (IV-4).

$$C_{V_{O}^{\bullet\bullet}}^{int} = \frac{C_{V_{O}^{\bullet\bullet}}^{MAX} C_{V_{O}^{\bullet\bullet}}^{bulk} \exp\left(\frac{-2F}{RT}\eta\right)}{C_{V_{O}^{\bullet\bullet}}^{MAX} + C_{V_{O}^{\bullet\bullet}}^{bulk} \left(\exp\left(\frac{-2F}{RT}(\eta)\right) - 1\right)} \quad (IV-4)$$

Where  $\eta$  is the electrode overpotential,  $C_{V_{O}^{\bullet\bullet}}^{int}$  is the oxygen vacancies concentration taken at the Ni/YSZ interface and  $C_{V_{O}^{\bullet\bullet}}^{MAX}$  is the maximum concentration of vacancies in YSZ. The term  $C_{V_{O}^{\bullet\bullet}}^{bulk}$  denotes the bulk concentration of vacancies. By coupling eq. (IV-4) with the electrochemical model, the evolution of the oxygen vacancies at the electrolyte interface has been plotted as a function of the current density. In Figure IV-9b, a sharp increase of oxygen vacancies can be observed at the electrolyte interface with increasing cathodic current in SOEC mode. It can be noticed that this evolution is steeper for a coarser microstructure due to the higher negative overpotential for a given current density. Conversely, the decrease of vacancies is less pronounced under anodic polarization in SOFC mode. The strong accumulation of vacancies in the double layer associated to a depletion of oxygen could thus trigger the destabilization of the interface leading to the Ni/YSZ delamination (Figure IV-9c). Interestingly, interfacial cracks between Ni and YSZ have been observed in the active layer after aging in electrolysis mode [Chen 2013, Hauch 2016].

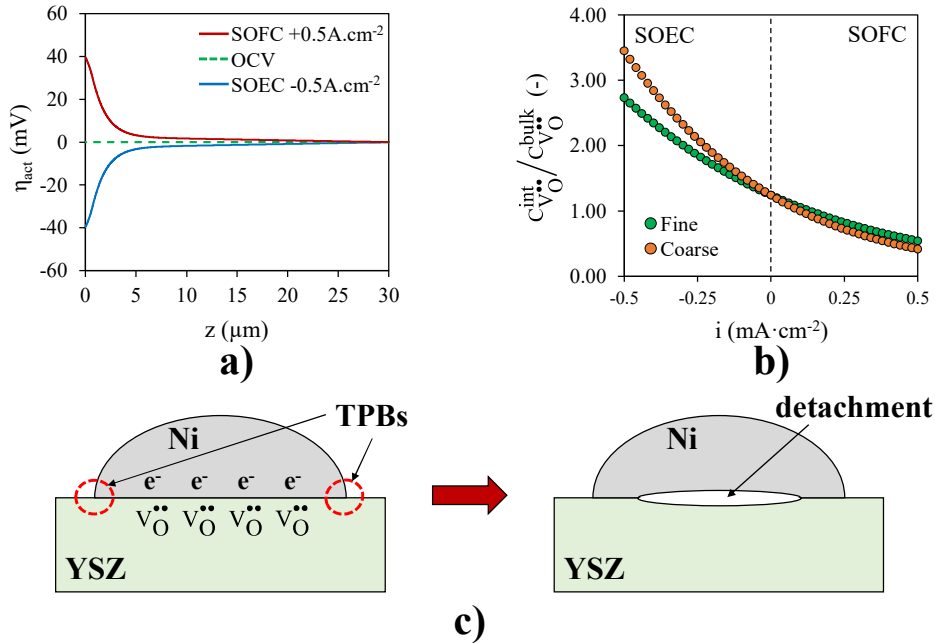


**Figure IV-9: Mechanism for Ni depletion: a) Electrode overpotential as a function of the position in the electrode at +/- 0.5 A·cm<sup>-2</sup> – b) Normalized oxygen vacancies concentration in the YSZ at the electrode/electrolyte interface as a function of the applied current density – c) Proposed mechanism for the weakening of the Ni/YSZ interface.**

Finally, it can be noticed that the weakening of the Ni/YSZ interface due the accumulation of oxygen vacancies could lead to the detachment of Ni and trigger the migration of the highly unstable isolated particles *via* volatile species. Moreover, the decrease of the Ni-YSZ interfacial energy will increase the Ni wettability in the vicinity of the electrolyte interface. This evolution has been measured by Rinaldi *et al.* [Nakajo 2020, Rinaldi 2019] after aging in electrolysis mode and could also be involved in the process of Ni migration. From this point of view, increasing the interfacial adhesion between Ni and YSZ could represent the main challenge to mitigate the Ni depletion in electrolysis mode. Nevertheless, further investigations are still required for a full validation of this proposition.

## IV.5 Conclusion of This Chapter

Two classical solid oxide cells with different Ni-YSZ microstructures have been aged in fuel cell and electrolysis modes for operating times ranging from 1'000 hours to 15'000 hours. In electrolysis mode, it has been found that the degradation is much higher for the cell that presents a coarser Ni-YSZ microstructure (cf. chapter II). To analyze this result, the hydrogen electrodes of the pristine and aged cells have been reconstructed by synchrotron X-ray nano-holotomography. Thanks to the large volume of the 3D images, the Ni-YSZ microstructural evolutions have been investigated in the bulk and at the electrode/electrolyte interface.

The quantification of the microstructural properties in the bulk has revealed a Ni particle growth for all the operated samples. This phenomenon of agglomeration is independent of the polarization and it can be ascribed to a local sintering process. The comparison between the two cells has confirmed the crucial role of the Ni/YSZ interfacial adhesion on this mechanism.

The microstructural evolutions have been introduced in the multi-scale model described in chapter III to quantify the impact of the Ni agglomeration on the electrode and cell performances. Thanks to the data extracted from the longest experimental dataset, the effects of the Ni agglomeration have been extrapolated up to 20'000 hours with a good level of confidence. As expected, the contribution of the agglomeration on the cell degradation is significant but tends to slow down for very long-term operation. From this point of view, it should not compromise the cell durability on its overall requested lifetime for fuel cell or electrolysis operation.

The analyses of the 3D electrode reconstructions have also revealed a Ni migration toward the bulk of the electrodes resulting in Ni depletion at the electrode/electrolyte interfaces. It has been found that this Ni migration is favored in electrolysis mode and much less pronounced in fuel cell operation.

Moreover, the phenomenon has been observed to occur only in the electrochemically active region of the hydrogen electrode. The microstructural characterization of the two cells has highlighted the strong impact of the initial characteristics of the electrode. Indeed, it has been clearly stated that the Ni depletion is favored in case of coarser initial microstructure.

As for the agglomeration, the gradients in microstructure parameters due to the loss of Ni at the electrode/electrolyte interface have been implemented in the model. In electrolysis mode, the impact of the moderate Ni depletion observed for the fine electrode microstructure is limited in such a way that the electrode degradation remains dominated by the agglomeration. Conversely, for the coarse cermet microstructure, the severe depletion induces a strong decrease of the cell and electrode performances. This behavior must explain a large part of the difference in the experimental degradation rates measured for the two types of cells. A sensitivity analysis performed with the model has shown that the important loss of active TPBs at the electrolyte interface is the main cause of the degradation whereas the evolutions of the other parameters are less impacting. The effect of the Ni depletion on the impedance spectra has been also computed and discussed.

Finally, the underlying mechanism at the origin of the Ni migration has been discussed taking advantage of the model. The simulations at the electrode scale have shown that the reaction of Ni evaporation cannot be the limiting step in the depletion process. Instead, the computation of the local overpotential at the electrode/electrolyte interface has revealed a large difference between the two operating modes. In this frame, the high cathodic overpotential under electrolysis current could be involved in the rate of Ni depletion. In order to unravel the role of the overpotential on Ni redistribution, the concentration of oxygen vacancies in the double layer has been estimated at the electrolyte interface in both operating modes. A strong accumulation of vacancies at high cathodic overpotential has been found. It has been proposed that this accumulation could deteriorate the Ni/YSZ interface leading to detach the Ni particles and favor the loss of nickel from the electrode/electrolyte interface. This mechanism allows taking into account the effect of the operating mode as well as the role of the Ni/YSZ adhesion and the cermet microstructure.



# V. Oxygen Electrode Degradation: LSCF Demixing and Interdiffusion at the GDC/8YSZ Interface

As discussed in chapter II, two in-house long-term tests ( $\approx 1'800$  hours) in electrolysis mode have been carried out in the frame of this thesis to investigate the influence of the operating temperature on the degradation (*Cell-A1* and *Cell-A2*). The electrochemical characterizations of the two cells have revealed similar increases of the overall area specific resistance, whereas a larger increase of the Ohmic resistance has been found for the cell aged at higher operating temperature. As indicated in chapter II, this increase in the Ohmic resistance may be partially associated to a modification of the inter-diffusional layer (IDL) between the GDC and the 8YSZ under operation [Matsui 2019, Tsoga 1999a].

In addition, a third cell (*Cell-A3*), presenting the exact same materials in terms of compositions and microstructures, has been operated by partners in fuel cell mode for 15'000 hours with an overall limited degradation, suggesting that the physico-chemical evolutions at the oxygen electrode would be less severe in this case.

To verify these statements and analyze the destabilization of the LSCF and the IDL evolution as a function of the operating conditions, specimens extracted from the three aged cells have been

characterized *via* micro X-ray diffraction ( $\mu$ XRD) and micro X-ray fluorescence ( $\mu$ XRF). These analyses have been complemented by the characterization of a pristine oxygen electrode to assess the initial state after sintering. In particular, the formation of strontium zirconate ( $\text{SrZrO}_3$ ) at the electrolyte interface, which is associated to the Sr release from LSCF due to its decomposition, has been investigated. Moreover, a specific attention has been paid to highlight an expected modification of the IDL after operation in electrolysis mode. All the physico-chemical evolutions occurring during the long-term tests have been then qualitatively explained in the frame of the degradation mechanism proposed by Laurencin *et al.* [Laurencin 2017].

The first section of this chapter is dedicated to the results corresponding to the characterization of the fresh oxygen electrode just after manufacturing. The second section is devoted to the analysis of the operated samples and it is sub-divided in three parts: Firstly, the degradation mechanism detailed in the manuscript of Laurencin *et al.* [Laurencin 2017] is recalled. Secondly, the effects of the operating conditions on the LSCF demixing are analyzed. Finally, the evolution of the IDL after operation in electrolysis mode is discussed as a possible cause to explain the increase of the cells' Ohmic resistances reported in chapter II.

## V.1 Characterization of the Pristine Cell

As a first step of the characterizations, the pristine cell has been analyzed in order to investigate the precipitation of strontium zirconates and the formation of an IDL at the interface between the barrier layer and the electrolyte during the cell manufacturing. For this purpose, a lamella extracted from a fresh cell of type *A* (*Cell-A Reference*) has been prepared and the  $\mu$ XRD/ $\mu$ XRF 2D maps have been acquired and analyzed.

### V.1.1 Detection of $\text{SrZrO}_3$ After Sintering

In Figure V-1a, 2D maps showing the normalized elemental distribution in the active layer of Strontium (Sr), Cerium (Ce), Gadolinium (Gd) and Yttrium (Y) are given for the pristine cell. According to the XRF signal, small amounts of Sr are detected at the interface between the barrier layer in GDC and the 8YSZ electrolyte. The diffusion of Sr is also revealed in Figure V-1b in which the XRF intensities integrated along the horizontal direction are given for each vertical position. This indicates that during the LSCF electrode sintering the Sr diffuses through the GDC and reacts at the barrier layer/electrolyte interface.

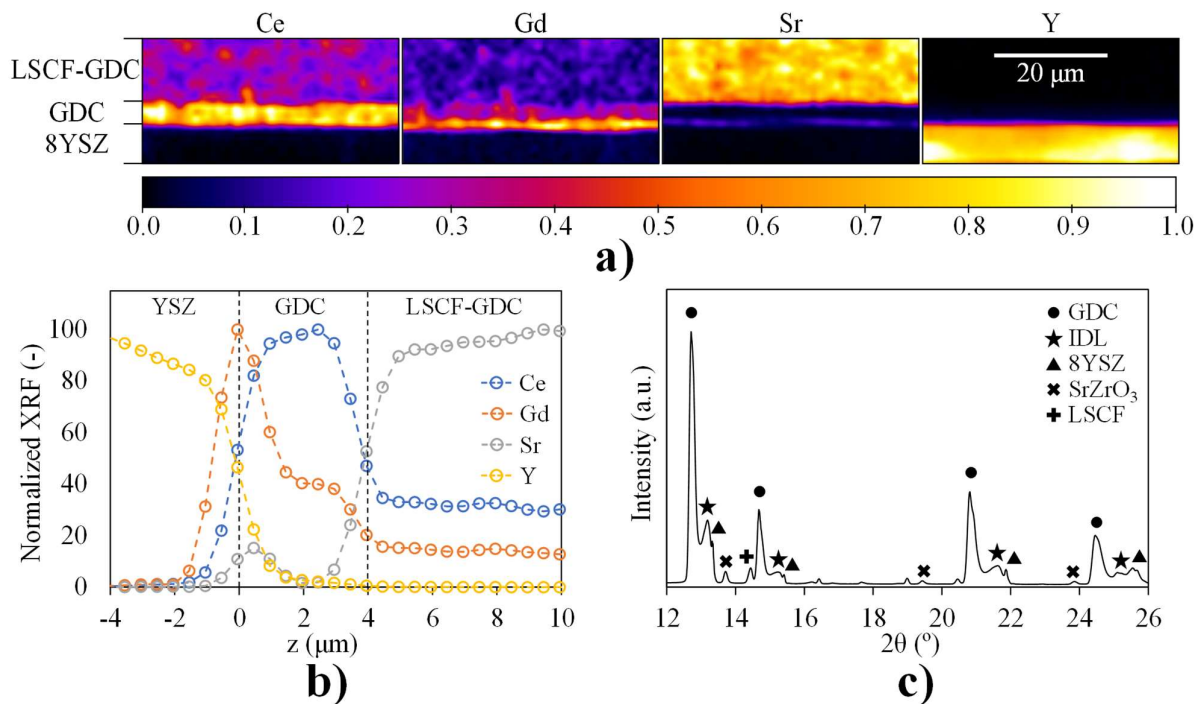


**Figure V-1: Analysis of the pristine oxygen electrode: a) 2D element distribution obtained from the XRF signal at the electrode/barrier layer/electrolyte interface – b) Local XRF intensity integrated over the horizontal direction – c) XRD pattern at the GDC/8YSZ interface.**

To verify the crystalline phase of the Sr-based compound, the average XRD pattern obtained at the interface is plotted in Figure V-1c. As can be seen, three peaks at  $13.66^\circ$ ,  $19.38^\circ$  and  $23.78^\circ$  are detected corresponding to the (011), (020) and (121) reflections of the perovskite structure of  $\text{SrZrO}_3$ . Therefore, it is confirmed that during the sintering Sr diffuses through the barrier layer and forms  $\text{SrZrO}_3$  at the interface between GDC and the 8YSZ as already observed by several authors [Ferreira-Sanchez 2017, Morales 2017, Villanova 2019].

### V.1.2 Inter-Diffusional Layer Between the GDC and the YSZ

From the XRF data given in Figure V-1a and Figure V-1b, it can be also seen that the distribution of gadolinium is significantly different with respect to the cerium with an accumulation of Gd in the region close to the GDC/8YSZ interface. It could be suspected that this high Gd concentration could be due to its dissolution in the YSZ resulting in the formation of the thin IDL at the barrier layer/electrolyte interface. This claim is consistent with the results reported in literature [Morales 2017, Szász 2018, Uhlenbruck 2009, Villanova 2019, Wilde 2015], in which a thin layer containing a relatively high concentration of Gd was also observed at the electrolyte interface after sintering.

The XRD pattern collected at the electrolyte interface (Figure V-2a) can also be used to contribute at the fine characterization of this inter-diffusional layer. Indeed, the inspection of the XRD pattern has allowed identifying a crystalline phase whose main peaks are detected at  $13.15^\circ$ ,  $15.20^\circ$ ,  $21.56^\circ$  and  $25.33^\circ$ . Interestingly, it can be noticed that all these peaks are close and slightly shifted with respect to the peaks of the 8YSZ (found at  $13.33^\circ$ ,  $15.41^\circ$ ,  $21.86^\circ$  and  $25.69^\circ$  for the (111), (020), (022) and (131) reflections, respectively). This simple shift indicates that the IDL presents the same cubic structure than the fluorite 8YSZ but with a different lattice cell volume. This observation was confirmed by the estimation of the lattice parameter obtained by Rietveld refinement. Indeed, it has been found that the lattice parameter in the region close to the interface is slightly higher than one measured in the bulk of the electrolyte ( $\approx 5.20 \text{ \AA}$  vs  $5.14 \text{ \AA}$ ). Moreover, it can be mentioned that the peaks at the interface are significantly larger than the ones in the bulk.

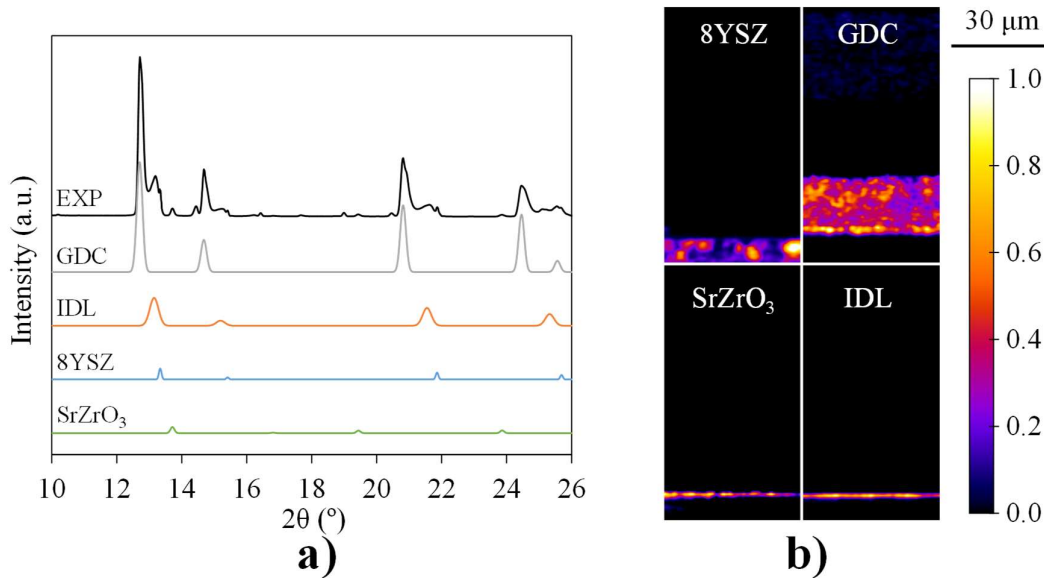


**Figure V-2: Analysis of the XRD pattern at the interface for *Cell-A Reference*: a) Main crystalline phases identified at the barrier layer/electrolyte interface – b) 2D maps of the XRD showing the distribution of the crystalline phases.**

All the aforementioned characterizations by  $\mu$ XRF and  $\mu$ XRD are fully consistent with the Gd diffusion in YSZ resulting in a solid solution corresponding to the IDL formation during sintering. Indeed, the insertion of Gd in the  $\text{Y}_2\text{O}_3$ -doped  $\text{ZrO}_2$  has been reported to favor the crystallization of nanoscale-grains [Leib 2016], which is consistent with the broad peaks measured experimentally for the IDL. Moreover, the bigger ionic radius of Gd with respect to Y would also be consistent with the larger lattice parameter [Katamura 1995, Rebollo 2003].

Therefore, it can be reasonably stated that the crystalline phase ascribed to the IDL must correspond to a  $\text{Gd}_2\text{O}_3$ - $\text{Y}_2\text{O}_3$ - $\text{ZrO}_2$  solid solution exhibiting nano-grains and cubic fluorite-type crystal similar to the ones reported in [Basu 2012, Lee 2009, Vaisakhan Thampi 2015, Yamamura 2003]. It can be

pointed out that this type of IDL originating from the reactivity between the GDC and the 8YSZ is expected to cause a drop in the ionic conductivity in the region [Matsui 2019, Tsoga 1999b, Xu 2019, Yamamura 2003].

### *V.1.3 Crystalline Phases Distribution Across the Electrolyte and Barrier Layer*

To confirm the localization of the inter-diffusional-layer, the spatial distribution of the crystalline phases has been deduced from the XRD maps by identifying the peaks corresponding to the GDC, the 8YSZ, the IDL and the SrZrO<sub>3</sub>. These distributions are shown in Figure V-2b across the barrier layer including part of the electrolyte and the electrode. Firstly, the barrier layer and the electrolyte can be clearly distinguished as they are ascribed to the GDC and 8YSZ, respectively. Secondly, the zirconate corresponds to the line at the interface between the GDC and 8YSZ. Finally, the close examination of the maps shows that the IDL is a fine layer of less than 1 μm (thickness ≈ 500 nm) located just below the zirconates. This confirms the formation of the solid solution in the electrolyte just at the interface with the barrier layer. Besides, this observation means that, in our case, the inter-diffusion between the GDC and the 8YSZ does not prevent the formation of SrZrO<sub>3</sub> as it has been reported for different types of IDL forming at different sintering temperature [Szász 2018, Wankmüller 2017, Wilde 2018]. Therefore, for this type of cells, the appearance of this IDL after sintering presents mainly negative effects on the cell performances as it causes a decrease in the ionic conductivity without preventing the reactivity between the Sr and the Zr from the electrolyte.

## **V.2 Characterization of the Aged Cells**

Once the pristine cell has been characterized, the evolutions occurring in the oxygen electrode and at the barrier layer/electrolyte interface after operation have been investigated. This analysis has been based on the degradation mechanism proposed by Laurencin *et al.* [Laurencin 2017] in which it is suggested that the decrease in performances would be primarily associated to the LSCF destabilization favored by the operation in electrolysis mode.

Therefore, specimen extracted from the aged cells have been analyzed to investigate the impact of the operating conditions on the LSCF destabilization and SrZrO<sub>3</sub> formation. In particular, the evolutions in *Cell-A1* and *Cell-A2* (aged in electrolysis mode for ≈ 1'800 hours at 850°C and 750°C, respectively) have been studied to understand the impact of the operating temperature. Moreover,

*Cell-A3* (aged in fuel cell mode at  $\approx 780^\circ\text{C}$  for  $\approx 15'000$  hours) has been also characterized to confirm the aggravating effects of the anodic polarization.

Finally, the evolution of the IDL after operation in electrolysis mode as a function of the operating temperature has been investigated by comparing the diffraction patterns at the barrier layer/electrolyte interface of *Cell-A1* and *Cell-A2* with the pristine cell.

### V.2.1 Preliminary Remark: Proposed Mechanism for the LSCF Destabilization

Thanks to the cells aged in the frame of M. Hubert's thesis [Hubert 2018], which were complemented with post-test characterizations and modeling, a mechanism for the LSCF destabilization has been suggested by Laurencin *et al.* [Laurencin 2017]. In this previous work, it has been proposed that the degradation of the oxygen electrode should be accelerated in anodic polarization due to the nature of the activated reaction mechanism for the LSCF and the LSCF-GDC composite electrodes. Indeed, as discussed in chapter III, it is reminded that a passage from the 'bulk path' to the 'surface path' occurs at low anodic polarization. This transition in the reaction pathway is associated with the evolution of the oxygen vacancies content in LSCF that are depleted under electrolysis current. As a result, the bulk path is blocked while, in the same time, the evolution of oxygen surface species on the LSCF leads to promote the surface path (cf. chapter III section III.2.4.3). As an illustration of this behavior, the concentration of oxygen atoms in the LSCF lattice along the electrode thickness is plotted as a function of the overpotential in Figure V-3.

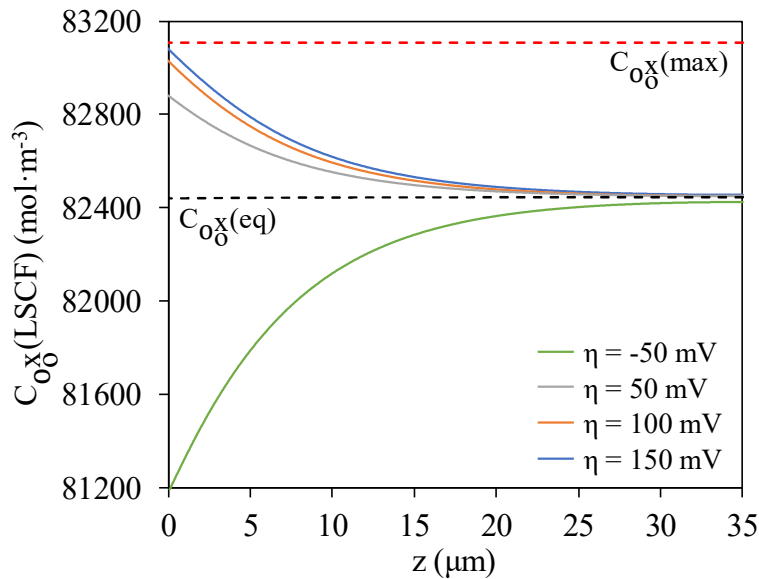


**Figure V-3:** Evolution of the oxygen atom concentration in the LSCF along the electrode thickness as a function of the overpotential (illustrated for a pure LSCF electrode operated at  $800^\circ\text{C}$ ).

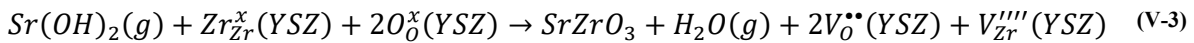
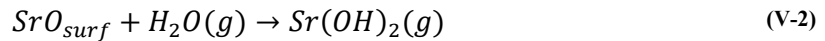
Operating the cell in electrolysis mode ( $\eta > 0$  V) an accumulation of incorporated oxygen atoms in LSCF is found, especially in the vicinity of the electrolyte. This oxygen content is increased up to reach an almost complete saturation of the material meaning that the understoichiometry in the compound tends to zero ( $\delta \rightarrow 0$ ).

Based on this observation, Laurencin *et al.* [Laurencin 2017] have proposed that the accumulation of the oxygen in LSCF would be the main driving force for the electrode demixing associated with the Sr exorporation from the perovskite structure. This proposition is illustrated with the following reaction leading to the precipitation of strontium oxide (SrO) on the LSCF surface (eq. (V-1)).



It is worth noting that the strontium oxide is a passivation film that will block the electrochemical reactions, while the loss of Sr will decrease the LSCF ionic conductivity (i.e. its chemical diffusivity). The two phenomena will obviously degrade the electrode performances by increasing the electrode polarization resistance [Baque 2017]. Therefore, the LSCF demixing, which is clearly accelerated under anodic current, could partially explain the higher degradation rates measured in SOEC mode.

It can be noticed that the strontium oxide could subsequently react with trace of steam present in the air flow to form volatile strontium hydroxide (eq. (V-2)) which would then diffuse in the porosities of the electrode and the barrier layer. Then, the hydroxide would react with the zirconium coming from the electrolyte and form strontium zirconate in the porosity of the barrier layer (eq. (V-3)).



This mechanism allows explaining the much higher amount of zirconates after an electrolysis operation, which were observed in the porosity of the GDC at the electrolyte interface [Laurencin 2017]. Moreover, the precipitation of vacancies in the electrolyte could explain the concomitant formation of a continuous line of nano-porosities in the electrolyte [The 2015].

Finally, it can be proposed that the depletion of Zr in the electrolyte could affect the inter-diffusional layer that would evolve under electrolysis operation. The precipitation of zirconates in the porosities of the barrier layer should not affect the cell performances. However, the Zr depletion in the IDL is expected to decrease its ionic conductivity [Butz 2009]. This behavior could thus explain the increase of the Ohmic resistances, which were clearly observed for *Cell-A1* and *Cell-A2* (knowing that the Ni depletion is very limited for this type of cells, cf. chapter IV).

On the one hand, to better validate the mechanism of LSCF demixing, the oxygen electrode crystallographic structure for the operated cells has been studied and related to the SrZrO<sub>3</sub> formation as a function of temperature and polarization. On the other hand, in order to check the assertion on a possible evolution of the IDL upon electrolysis operation, an attempt to its characterization by  $\mu$ XRD and  $\mu$ XRF is discussed.

### V.2.2 LSCF Destabilization: Sr Release from the Material as a Function of Temperature and Polarization

It has been reported by several authors that the loss of Sr in the LSCF structure is expected to cause an increase in the unit cell volume (UCV) [Hardy 2012, Mineshige 2005, Świerczek 2009]. Therefore, this parameter could be a relevant indicator to highlight the LSCF demixing. For this reason, the evolution of the UCV for the tetragonal perovskite structure of the LSCF along the electrode thickness has been estimated by Rietveld refinement to investigate the destabilization of the oxygen electrode (Figure V-4).

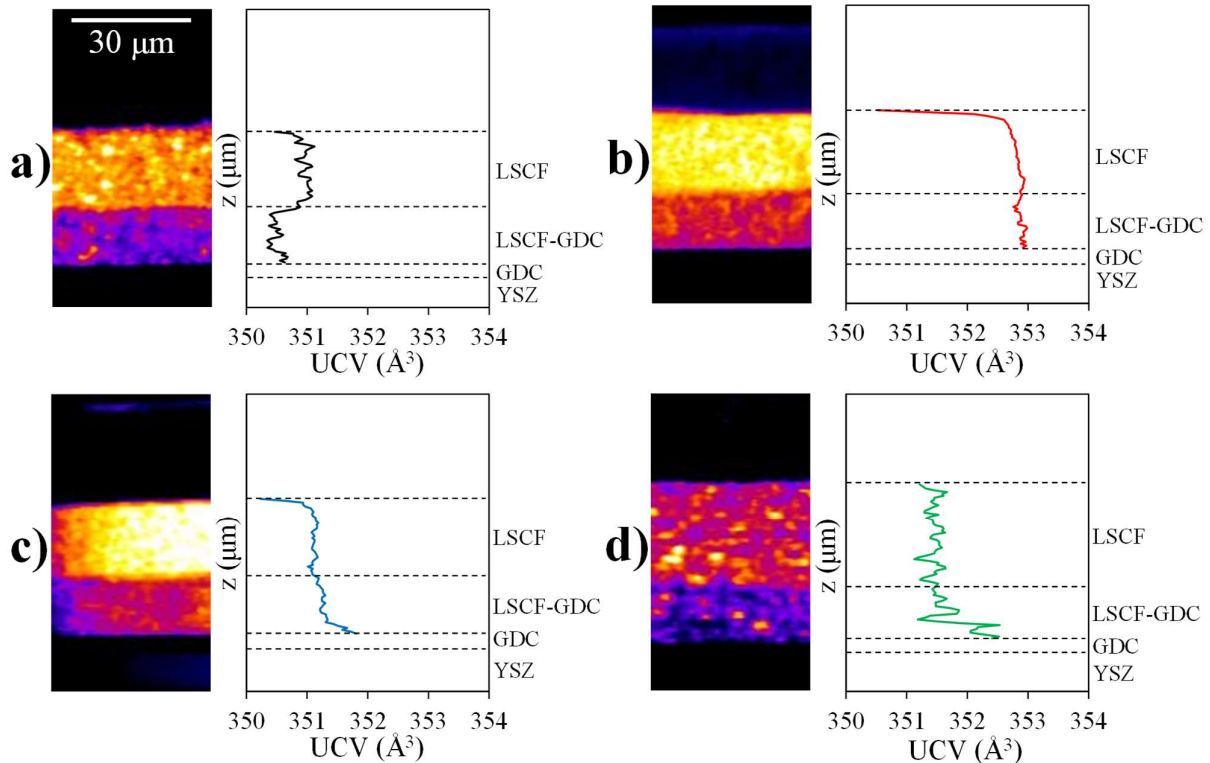


**Figure V-4: 2D XRD maps of the LSCF phase and evolution of the LSCF Unit Cell Volume along the oxygen electrode thickness for the four samples analyzed: a) *Cell-A Reference* – b) *Cell-A1* – c) *Cell-A2* – d) *Cell-A3*.**

These analyses have been carried out for the reference cell, for *Cell-A1* and *Cell-A2*, aged in electrolysis mode for 1'800 hours at 850°C and 750°C, respectively, and for *Cell-A3* aged in fuel cell mode for 15'000 hours at 780°C (cf. Appendix A). It is worth noting that the uncertainty of the LSCF unit cell volume measured remains quite high, especially for the LSCF-GDC composite layer. Therefore, the results reported hereafter must be considered as a preliminary study, with the main purpose to demonstrate the relevance of the method.

Comparing the pristine cell to *Cell-A1* (Figure V-4a and Figure V-4b, respectively), an overall increase of the UCV is found across the active layer (LSCF-GDC) and the pure LSCF layer ( $UCV_{\max} \approx 353 \text{ \AA}^3$  for *Cell-A1* and  $\approx 351 \text{ \AA}^3$  for the pristine cell). On the other hand, *Cell-A2* presents an increase of UCV that appears to be less significant as can be seen in Figure V-4c ( $UCV_{\max} \approx 352 \text{ \AA}^3$ ). In addition, in this case the increase of UCV is found to be limited to the composite layer in the vicinity of the GDC whereas in the pure LSCF layer the UCV remains similar to the one of *Cell-A Reference*. These observations would, thus, suggest that a significant destabilization of the LSCF extended beyond the active functional layer of the electrode would occur in electrolysis mode when the cell is operated at high temperature (*Cell-A1*, 850°C). In contrast, a limited degree of Sr excorporation, which seems to be restricted to the electrochemical active region close to the GDC barrier layer, is observed for *Cell-A2* aged at lower temperature (750°C). Finally, the electrode destabilization of *Cell-A3* aged in fuel cell mode for a very long time of 15'000 hours at 780°C is roughly the same than the one found for *Cell-A2* aged at around the same temperature for a shorter time (1'800 hours). Therefore, it could be concluded that the destabilization is favored under electrolysis current as expected. Moreover, it would be aggravated at high temperature.

These preliminary results show that the electrode demixing can be characterized by local XRD by determining the evolution of the lattice parameter after operation. However, to analyze the destabilization in the electrode thickness, the resolution is still insufficient here and must be improved for further studies by using characterization techniques at the nanoscale.

To verify the diffusion of Sr towards the electrolyte, the normalized XRF signals from the electrode/barrier layer/electrolyte area have been considered for the same samples (i.e. *Cell-A1*, *Cell-A2* and *Cell-A3*). The 2D maps for the Ce, Gd, Sr and Y chemical-elements are shown in Figure V-5a. The XRF maps show a clear signal of Sr, detected at the interface between the GDC and the 8YSZ for all the samples (Figure V-5a).

To quantify the amount of Sr at the barrier layer/electrolyte interface, the XRF signal has been integrated over the longitudinal dimension along the direction parallel to the electrolyte interface. The integrated data are plotted as a function of the position across the LSCF-GDC electrode, the barrier layer and a part of the electrolyte in Figure V-5b. A clear evolution of Sr content can be detected as a function of the operating conditions. Indeed, after aging in electrolysis mode at 850°C (*Cell-A1*), the accumulation of Sr at the GDC/8YSZ interface is more than double with respect to the pristine cell, consistently with the higher excorporation of Sr from the LSCF detected *via* the UCV evolution. In addition, it can be seen that the amount of Sr at the interface in the two cells aged in electrolysis mode at 750°C (*Cell-A2*) and in fuel cell mode at 780°C (*Cell-A3*) is quite similar and only slightly higher than *Cell-A Reference*. Once again, this observation is consistent with the limited destabilization of the LSCF highlighted by the UCV estimations for these two samples.

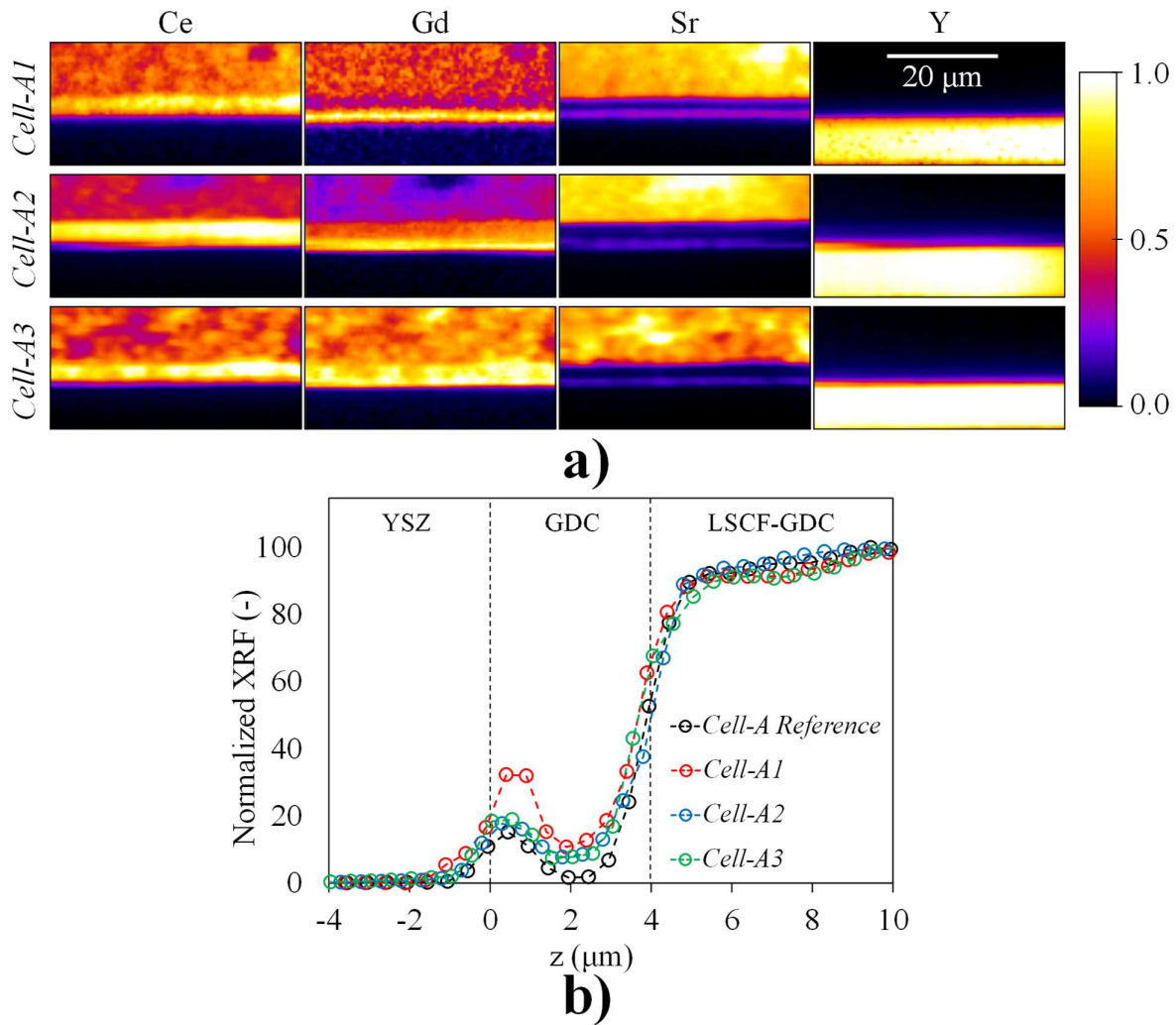


**Figure V-5: Analysis of the operated cells: a) 2D element distribution obtained from the XRF signal at the electrode/barrier layer/electrolyte interface for *Cell-A1*, *Cell-A2* and *Cell-A3* – b) Comparison of the integrated XRF signal of Sr between the pristine cell and the aged samples.**

This observation (i.e.  $\text{Sr}_{\text{Cell-A2}} \approx \text{Sr}_{\text{Cell-A3}}$  at the interface) confirms that the process of LSCF destabilization and the following formation of  $\text{SrZrO}_3$  is favored in electrolysis mode as proposed by Laurencin *et al.* [Laurencin 2017]. Indeed, these two cells (*Cell-A2* and *Cell-A3*) present similar evolutions but the operating times are significantly different indicating that roughly the same extent of LSCF destabilization and  $\text{SrZrO}_3$  formation have occurred after 1'800 hours in electrolysis mode at 750°C and 15'000 hours in fuel cell mode at 780°C.

Furthermore, it can be pointed out that the important changes in UCV and the large XRF signal for Sr found at the barrier layer/electrolyte interface for the operated at high temperature (*Cell-A1*) mean that the process of LSCF destabilization associated with the formation of zirconates is promoted with the temperature. These results suggest that the kinetic rate of reaction for the Sr excorporation (eq. (V-1)) would be strongly thermally activated, so that operating the cell at high temperature would favor the destabilization. It can be noticed that this consideration is well consistent with the higher degradation observed for the LSCF electrode at higher temperature by [Mai 2006, Oh 2012].

Based on these results it can be concluded that the Sr release from the LSCF appear to be favored by the anodic polarization, confirming the results already discussed in the work of Laurencin *et al.* [Laurencin 2017]. Moreover, it appears that the degradation would be significantly thermally activated resulting in an acceleration of the LSCF demixing and Sr accumulation at the barrier layer/electrolyte interface at higher operating temperature.

### *V.2.3 Evolution of the IDL After Aging in Electrolysis Mode: Preliminary Characterizations and Discussion*

#### *V.2.3.1 XRF Maps and Profile for the Gadolinium*

As already mentioned, the loss of Zr in the electrolyte due to the formation zirconates is liable to change the composition of the IDL. In this frame, it can be noticed in Figure V-5a that the distribution of gadolinium is not uniform for the operated cells with a clear increase at the interface with the electrolyte. It can also be observed that the accumulation of Gd would be the highest for *Cell-A1* operated at high temperature in electrolysis mode. Therefore, a combined effect between the loss of Zr due the  $\text{SrZrO}_3$  precipitation and the diffusion of Gd could be suspected for the IDL. Indeed, it could be proposed that the loss of zirconium from the 8YSZ associated to the formation  $\text{SrZrO}_3$  (eq. (V-3)) could trigger the dissolution of gadolinium in the electrolyte *via*  $\text{Zr}^{4+}$  substitution [Bekale 2008]. To discuss this hypothesis, the XRD patterns at the barrier layer/electrolyte interface have been analyzed for the cells operated in electrolysis mode and compared to the pristine cell.

### V.2.3.2 Structural Analysis of the IDL After Electrolysis Operation

As a first step, the spatial distributions of the different crystalline phases for the 8YSZ, the GDC, the SrZrO<sub>3</sub> and the IDL are plotted for *Cell-A1* and *Cell-A2* in Figure V-6.

The maps for the 8YSZ and GDC allow identifying without ambiguity the electrolyte and the barrier layer, respectively. Moreover, the inhomogeneity in the signal for the 8YSZ is simply explained by the quite coarse crystallographic grains in the electrolyte. In comparison with the maps of the pristine cell given in Figure V-2b, it can be noticed that the overall thickness of the IDL is roughly the same after operation and remains in the order of a few hundreds of nanometers (500 nm). It is worth noting that this dimension corresponds to the vertical resolution of the microXAS beamline. Therefore, a precise analysis of this suspected evolution of the IDL upon electrolysis operation is not possible here. This statement clearly indicates the need of post-test characterizations performed at the nanoscale. Nevertheless, despite this limitation, a preliminary qualitative analysis has been conducted for discussion.

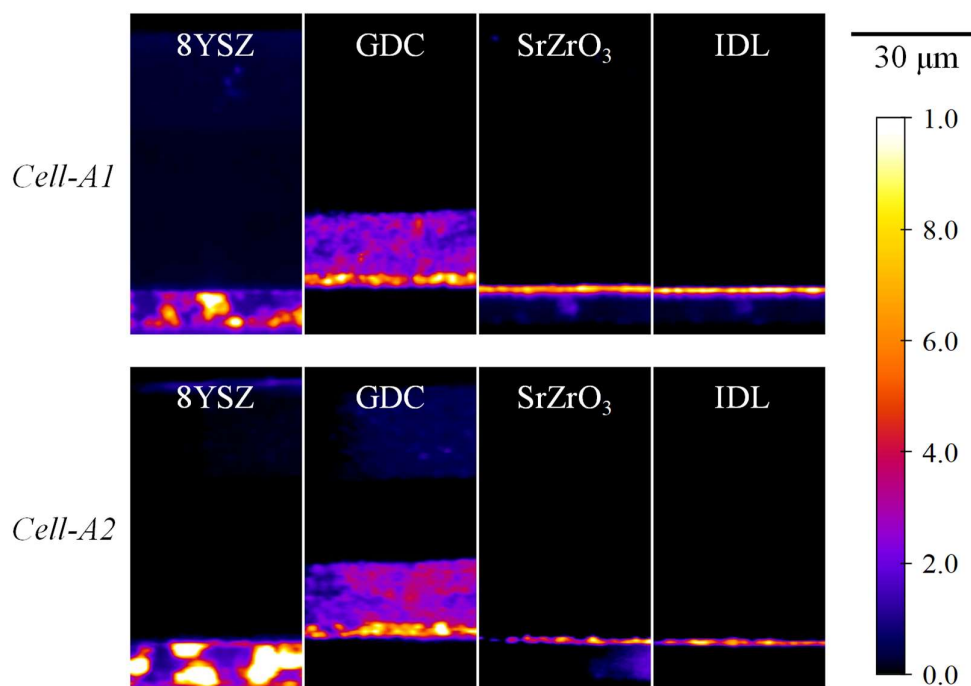


**Figure V-6: XRD maps exhibiting the crystalline phases at the interface between the barrier layer and the electrolyte in the cells aged in electrolysis mode.**

With this purpose, the diffraction patterns obtained at the interface between the barrier layer and the electrolyte for *Cell-A1* and *Cell-A2* are compared with the XRD of the pristine cell in Figure V-7. All the peaks associated to the SrZrO<sub>3</sub> are increased after aging at high temperature (*Cell-A1* at 850°C, Figure V-7a), whereas they remain similar to the pristine sample for the cell aged at lower temperature (*Cell-A2* at 750°C, Figure V-7b). These evolutions are consistent with the analysis of the XRF signal

obtained for the two cells confirming the aggravating effect of the high operating temperature on the formation of strontium zirconate associated with the accumulation of Sr.

Interestingly, an evolution of the intensity of the IDL peaks is also detected. For *Cell-A1*, all the peaks associated to the inter-diffusional layer are slightly increased in intensity. This evolution would suggest a modification of the IDL with an increase in the amount of the solid solution. For *Cell-A2*, instead, the peaks associated to the IDL are essentially superposed with the XRD pattern of the reference cell (except the (111) reflection). This observation may suggest that in this case only a limited augmentation of the IDL at the interface is detected.

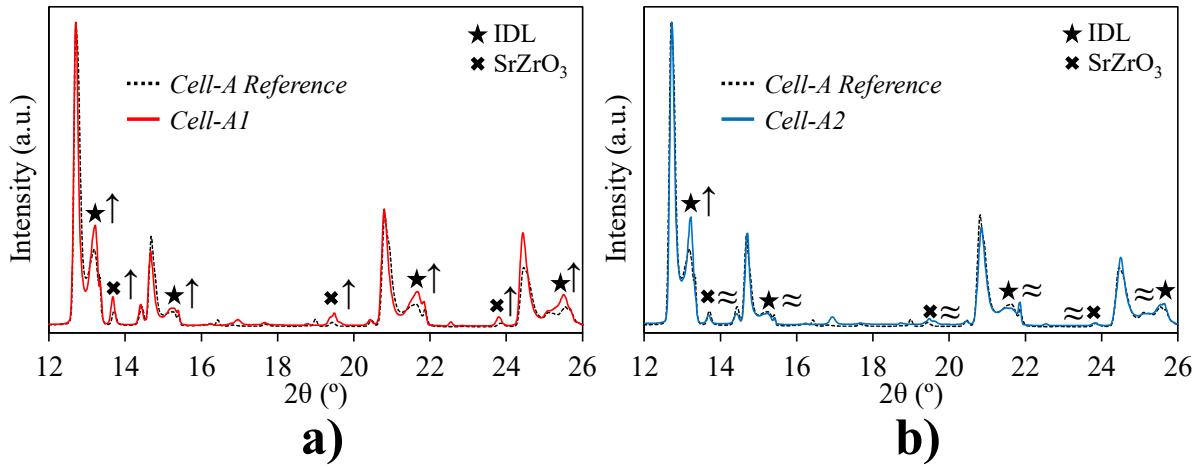


**Figure V-7: Evolution of the XRD pattern at the interface for the cells aged in electrolysis mode as a function of the operating temperature: a) *Cell-A1* (aged at 850°C) vs *Cell-A Reference* – b) *Cell-A2* (aged at 750°C) vs *Cell-A Reference*.**

Based on these observations, it could be suspected that the IDL would evolve after operation especially at high temperature when the LSCF destabilization (eq. (V-1)) and the SrZrO<sub>3</sub> formation (eq. (V-3)) are also aggravated. Therefore, this could represent a clue that the increase of the IDL at the interface would be promoted by the loss of Zr from the electrolyte favoring the inter-diffusion of gadolinium. It is worth noting that this proposition is quite in good agreement with the recent study of Matsui *et al.* [Matsui 2019] who have observed an evolution of the IDL after aging by EDX analysis. Moreover, Villanova *et al.* have used nanoscale X-ray fluorescence to investigate the chemical evolutions after aging of a hydrogen electrode supported cell ( $i_{DC} = -0.75 \text{ A}\cdot\text{cm}^{-2}$ ,  $T \approx 780^\circ\text{C}$ ,  $t \approx 6'100$  hours) and an electrolyte supported cell ( $i_{DC} = -0.9 \text{ A}\cdot\text{cm}^{-2}$ ,  $T \approx 840^\circ\text{C}$ ,  $t \approx 23'000$  hours) [Villanova 2019]. In their study, they have found no significant modification of gadolinium distribution at the GDC/8YSZ interface for the cell aged at lower temperature while an accumulation of Gd has been observed at the interface for the cell aged at higher temperature (although in this case the electrolyte was made of 6/1 mol.% scandia/ceria-doped zirconia (6Sc1CeSZ)). Their findings

highlight the relevance of the operating conditions as well as the cell manufacturing protocol (sintering that controls the IDL for the pristine cell). Nevertheless, it appears that further studies are still needed to fully validate this mechanism.

Finally, it is reminded that the loss of Zr and the enrichment in Gd reduce the conduction of oxygen ions in the IDL as measured by Matsui *et al.* [Matsui 2019]. Indeed, these authors have synthesized several compounds, based on the local atomic compositions obtained by EDX, and have shown that the interdiffusional process of Gd and Zr corresponds to an overall decrease of the ionic conductivity. Therefore, it can be reasonably proposed that the increase in Ohmic resistances measured experimentally for *Cell-A1* and *Cell-A2* (cf. chapter II section II.1) could be ascribed to an evolution of the IDL. In this frame, the higher increase in the serial resistance of *Cell-A1* with respect to *Cell-A2* would be consistent with a higher evolution of the IDL for this cell.

This discussion shows that more characterizations at the nanoscale are still needed to understand the suspected physico-chemical evolution in the oxygen electrode/barrier layer/electrolyte region.

### **V.3 Conclusion of This Chapter**

In this chapter the physico-chemical reactivity at the oxygen electrode/barrier layer/electrolyte interface has been analyzed *via* coupled micro X-ray diffraction/micro X-ray fluorescence 2D maps. The characterization of the specimen extracted from the pristine electrode has confirmed that the reactivity between Sr released from the LSCF and Zr coming from the 8YSZ occurs already during the sintering of the electrode. Moreover, the presence of a Gd-rich inter-diffusional layer has been identified at the interface between the barrier layer and the electrolyte. The analysis of the XRD at the interface has suggested that the IDL could cause a decrease in the local ionic conductivity of the material.

The analysis of the aged cells has pointed out that the destabilization of the LSCF could be identified by an increase of the UCV associated for the excorporation of strontium. This evolution has been shown to be strongly dependent on the operating conditions. Indeed, it has been confirmed that the LSCF destabilization is favored in electrolysis mode, whereas the evolution is significantly less severe under fuel cell operation. Furthermore, it has been demonstrated that the Sr release is favored at high operating temperature. The analysis of the Sr diffusion towards the electrolyte, has been found completely consistent with the LSCF destabilization, with a larger formation of strontium zirconate at the GDC/8YSZ interface after an operation in anodic polarization and at higher temperature. All

these results bring supplementary evidence for the validation of the LSCF destabilization mechanism driven by the depletion of oxygen vacancies in the anodic polarization (associated with the transition in the reaction pathway described in chapter III).

Finally, a preliminary study has been conducted to investigate the IDL evolution upon operation at high temperature. It has been proposed that the loss of  $Zr^{4+}$  from the electrolyte associated to the  $SrZrO_3$  formation could facilitate the inter-diffusion of Gd increasing the inter-diffusional layer and reducing the local ionic conductivity. This type of behavior could explain the increase in the Ohmic resistances observed for the cells operated in electrolysis mode and especially at high temperature. However, the study has shown that further post-test characterizations at the nanoscale are required to finely investigate the IDL and its evolution.



# VI. Conclusions and Perspectives

This last chapter is dedicated to outline the main results of this PhD thesis and propose different perspective for forthcoming investigations. In the first part, the main findings of this work are summarized and analyzed whereas in the second part some outlooks for future work are discussed.

## VI.1 General Conclusions

This work has been dedicated to the investigation of the intrinsic causes of the degradation occurring in SOCs during operation. Long-term durability tests have been performed and the pristine and operated cells have been characterized to highlight the modifications occurring during the aging. In particular, the microstructural evolutions at the hydrogen electrode and the physico-chemical reactivity between the oxygen electrode and the electrolyte have been studied. A specific focus has been paid to the modeling of the detailed reaction mechanisms at the two electrodes. These modeling tools have been used to propose a better understanding of the underlying causes for the degradation as a function of the operating conditions. For the hydrogen electrode, the kinetic model has been also used to evaluate the impact of degradation on the electrode and cell performances.

Five long-term tests have been analyzed in this study. The electrochemical tests have shown that a specific attention must be given when comparing different experimental results. Indeed, two long-term tests on the same type of cell performed in electrolysis mode at different operating temperatures

have shown that the measured degradation rate is strongly dependent on the aging conditions. The cell aged at lower temperature exhibited a significantly higher degradation rate with respect to the cell aged at higher temperature. Nevertheless, when comparing the behavior of the two cells at the end of the tests in the same conditions, similar performances have been found indicating that the ‘intrinsic’ degradation would remain similar in this temperature range and for this test duration. These results highlight the importance of standardized conditions for the assessment of the degradation, to avoid contradictory results. In addition, it has been shown that operating the cell at higher temperature may be associated with a higher increase of the Ohmic resistance.

In parallel, very long-term tests on two cells having the same cermet microstructure have been performed by partners in SOFC mode and in SOEC mode. The durability results obtained have clearly indicated that for this type of cell the degradation is higher in electrolysis mode with respect to fuel cell operation. Moreover, the experimental results obtained for another cell with coarser initial cermet microstructure in SOEC mode have demonstrated that the nature and the microstructure of the Ni-YSZ electrode also plays a significant role on the degradation under electrolysis current.

Specimens extracted from the aged and pristine cells have been characterized *via* synchrotron X-ray nano-holotomography and synchrotron X-ray micro-diffraction/micro-fluorescence techniques to investigate the microstructural and physico-chemical evolutions after aging.

In particular, the holotomography experiments allowed obtaining 3D reconstructions of the Ni-YSZ cermet with a large field of view to draw good statistics on the microstructural properties. In this frame, the effects on Ni evolution of the initial electrode microstructure and electrode polarization in SOFC and SOEC modes have been studied. In the bulk of the electrodes, it has been observed that a Ni agglomeration occurs during operation for all the aged cells causing a decrease in the density of triple phase boundary lengths. It has been confirmed that this nickel particle coarsening is purely thermally activated, whereas no significant effect of the polarization has been found. Contrary to nickel agglomeration, the analyses of the local microstructural evolutions at the hydrogen electrode/electrolyte interface have shown that a depletion on Ni is found specifically in the electrochemically active area after aging in cathodic polarization (SOEC mode). On the contrary, in SOFC mode, no Ni redistribution in the cermet has been detected. Moreover, the comparison between the two different types of cells has highlighted a clear impact of the initial electrode microstructure on the Ni depletion. Indeed, a severe redistribution of nickel has been observed for the coarser initial cermet microstructure whereas this phenomenon was moderate in the cell presenting the finer Ni distribution. These results highlight the importance of the electrode microstructure during the

manufacturing process. Moreover, as the results have been obtained on two different cells, it can be speculated that the physical properties of nickel and YSZ interface could also play a key role on Ni migration in electrolysis mode.

The X-ray micro-diffraction/micro-fluorescence characterizations have been performed to study the reactivity between the LSCF-based oxygen electrode and the 8YSZ electrolyte. 2D maps giving the elemental and crystallographic distributions in the electrode at the sub-micron scale have been obtained for a pristine electrode and after aging. The impact of polarization and operating temperature has been assessed by comparing the evolutions for cells tested in SOEC mode at two temperatures and in SOFC mode. The analysis of the pristine cell has confirmed that the reactivity between the electrode and the electrolyte occurs already during the sintering forming strontium zirconates at the interface between the GDC barrier layer and the electrolyte. In addition, the formation of a Gd-rich inter-diffusional layer has been found in the electrolyte just below the zirconates. It has been proposed that this inter-diffusional layer could correspond to a Gd-doped YSZ exhibiting a similar crystal structure but lower ionic conductivity. The investigation of the LSCF destabilization after aging has been carried out by analyzing the evolution of its unit cell volume which is a function of the strontium content. It has been confirmed that the Sr release should be favored in electrolysis conditions and this phenomenon has been found to be strongly thermally activated. A consistent correlation has been found between the destabilization of the LSCF and the accumulation of strontium zirconate at the barrier layer/electrolyte interface. Moreover, a possible evolution of the inter-diffusional layer associated to the reactivity of Zr coming from the electrolyte with the Sr coming from the electrode material has been suggested based on preliminary observations.

To investigate the intrinsic causes and quantify the impact of these degradation phenomena at the scale of the two electrodes it is necessary to have detailed models able to describe the reaction mechanisms occurring therein. Therefore, an important part of this thesis was dedicated to the development and the preliminary validation of an elementary kinetic model for the reaction mechanism of the hydrogen electrode. Furthermore, an existing model for the LSCF-based oxygen electrode has been fully validated for the operation under air studying the effects of the operating temperature on the electrode response. Both models are able to simulate the stationary and dynamic behavior of the electrodes in the time domain and without linearization. Therefore, they can be used to model polarization curves but also electrochemical impedance spectra at open circuit and under polarization. In addition, it can be noticed that they could also be employed to simulate the response

of the electrodes to non-linear perturbations, such as cyclic voltammetry and non-linear impedance spectroscopy, even if this application is beyond the scope of this work.

The preliminary validation of the elementary kinetic model for the hydrogen electrode has indicated that the most suitable reaction mechanism occurring therein would be based on the hydrogen spillover charge transfer. The analysis of the experimental data on a Ni-3YSZ cermet has shown that the electrode response appears to be co-limited by the charge transfer at the triple phase boundaries, the migration of oxygen ions in the depth of the electrode and a steam-solid interaction coupled with diffusional processes of surface-attached species. Thanks to the modeling scheme, it has been proposed that the steam-solid interaction could change as a function of the polarization. Under anodic current (SOFC mode) the steam interaction with the YSZ would be the rate co-determining step, whereas in cathodic polarization (SOEC mode) the adsorption of H<sub>2</sub>O on nickel would become limiting.

For the LSCF-based oxygen electrode, the validation of the model has shown that the reaction mechanism based on two parallel pathways is able to reproduce the response of the electrode at different temperatures under air. The two reaction pathways consist in the ‘bulk path’, in which the ionic transfer at the LSCF/GDC interface and the surface reactions are considered, and in the ‘surface path’, in which the oxidation/reduction at the triple phase boundaries is taken into account. For a pure LSCF electrode, the simulations have shown that at open circuit and under cathodic polarization (SOFC mode) the reaction mechanism is dominated by the ‘bulk path’, whereas in anodic polarization (SOEC mode) the ‘surface path’ becomes the main reaction pathway. This modification of the main reaction mechanism allows explaining the changes of the impedance spectra measured from open circuit to anodic DC current. The activation of the ‘surface path’ is associated to the evolution of the surface coverage and to the depletion of oxygen vacancies in the LSCF in the vicinity of the electrolyte. This latter phenomenon is dependent on the current (or polarization), the thermal activation of the reaction and the evolution of the oxygen vacancies concentration at equilibrium as a function of the operating temperature.

Finally, these two micro-scale models have been coupled with a macro-scale model to simulate the response of the complete cell and investigate the effects of the degradation phenomena on the overall performances.

This overall modeling scheme has been implemented to quantify the impact of Ni agglomeration and Ni depletion from the hydrogen electrode/electrolyte interface.

Regarding the agglomeration in the bulk, the Ni coarsening has been simulated using a classical power-law model. The decrease of the triple phase boundary lengths associated to the agglomeration has been mimicked combining the power-law and microstructural correlations. Thanks to the very long experimental data, it has been possible to simulate the nickel particle growth and the decrease of triple phase boundaries up to  $\approx 20'000$  hours with a good level of confidence. It has been confirmed that the agglomeration tends to decelerate over time thanks to the stabilizing effect of the YSZ scaffold. As a consequence it has been found that the Ni coarsening causes a significant drop in the overall cell performances even if the inhibiting role of the YSZ backbone on the nickel agglomeration allows limiting its impact on the cell performances for very long operating times ( $> 20'000$  hours). For the Ni migration over large distance, the gradients obtained for the severe and moderate Ni depletion have been implemented in the micro-scale model to quantify the effects on the electrode and cell performances. The simulations have shown that the loss of nickel from the interface becomes a dominant contribution on the cell degradation in electrolysis mode and for coarse initial microstructures. Therefore, it appears that the Ni depletion must explain a part of the higher degradation rates measured in SOEC mode compared to SOFC operation.

The model has been also used to analyze the causes of Ni detachment from the YSZ. It has been found that the reaction of Ni volatilization cannot explain the severity of the phenomenon in electrolysis condition whereas an impact of the cathodic overpotential has been highlighted. To justify this effect, it has been proposed that the accumulation of oxygen vacancies in the double layer between the nickel and YSZ in electrolysis mode could reduce the interfacial adhesion. The deterioration of the interface could thus trigger the Ni detachment. Subsequently, as they are not stabilized anymore by YSZ, the nickel particles, could evaporate, diffuse and re-condense in the upper part of the electrode (where the electrochemical reaction can still occur). Besides, the modification of the interfacial adhesion modifies the wettability properties and could generate gradients in curvatures between Ni and YSZ that could represent a second driving force for nickel migration.

In parallel, the results of the characterizations of the oxygen electrode have been analyzed in the frame of a degradation mechanism that was previously proposed (on the basis of the detailed model for the LSCF electrode). In this mechanism, the depletion of oxygen vacancies in the LSCF structure taking place in electrolysis mode would trigger the destabilization of the material and the excorporation of strontium. The evolutions observed for the aged cells are consistent with this mechanism suggesting that the performance loss for the LSCF electrode in electrolysis mode could be controlled by this degradation phenomenon. As the LSCF decomposition has a direct impact on

the performances, it can be concluded that the demixing of the oxygen electrode material must also explain in part the higher degradation rate under SOEC condition.

Finally, it has been proposed that the formation of strontium zirconates associated to the destabilization of the LSCF, could contribute to the evolution of the inter-diffusion layer. Indeed, the loss of Zr from the electrolyte material could favor the interdiffusion of gadolinium in the electrolyte. This hypothesis could contribute to explain the increase in the Ohmic resistance measured after aging in electrolysis mode, even if more characterizations at the nanoscale are needed to fully prove this claim.

In summary, this work has brought new insights on the causes and impacts of the Ni evolution in the hydrogen electrode, and on the physico-chemical reactivity at the oxygen electrode/electrolyte interface. Based on the results presented in this work, it can be confirmed that the degradation of SOCs is significantly larger in electrolysis mode with respect to fuel cell operation. This difference can be ascribed to two main phenomena: On the one hand, the effect of the cathodic overpotential on the Ni instability at the interface with the electrolyte and, on the other hand, the high-temperature destabilization of the LSCF in the oxygen electrode favored by the anodic current.

## **VI.2 Perspectives**

To investigate the effects of the operating conditions on the degradation, it has been necessary to analyze the results of long-term tests which are by nature severely time consuming. In order to speed-up the analysis of the degradation in SOCs, while keeping a good representativeness of the real durability, the implementation of standardized accelerated tests could be proposed. In this context, the development of aggravated but representative testing protocols could represent an important achievement to facilitate the study of the degradation mechanisms in SOCs under fuel cell and electrolysis operation. As an example, durability tests could be performed adding steam in the air flow for the oxygen electrode to facilitate the decomposition of the LSCF and the formation of strontium zirconates. Indeed, this type of test is expected to increase the kinetics of the destabilization reaction but would not modify its nature.

For the degradation of hydrogen electrode, the addition of specific pollutants in the fuel flow, such as hydrogen sulfide, could be used to block the active sites and accelerate the degradation. Alternatively, durability experiments at low temperature and high current density could be envisaged to exacerbate the overpotential in the hydrogen electrode and investigate its effects on the Ni

migration. In this context, degradation tests on symmetric cells having Ni-YSZ cermet electrodes could help discriminate even more decisively the effect of the electrode polarization.

Aside from the tests duration, this study has highlighted the importance of the precise determination of the reaction mechanisms at the two electrodes as a tool to investigate the intrinsic causes of the degradation and its effects on the cell performances. The validation of the two micro-kinetic models has allowed to employ a reliable modeling scheme to analyze the electrodes and cell response. Nevertheless, some improvements to both models are still needed. In particular, the predictability of the hydrogen electrode micro-kinetic model can still be improved. This could be achieved by a better understanding of the interaction between hydrogen, steam and the Ni-YSZ cermet. For example, it has been pointed out that a more precise determination of the thermodynamic and transport properties for the surface-attached species is requested. With this objective the use of numerical tools, such as density functional theory or molecular dynamics, could help obtaining more trustworthy input data for the kinetic modeling.

For the LSCF-based oxygen electrodes, in order to catch the evolutions of the electrode response at different operating pressure it could be envisaged to enrich the model by implementing a full-elementary approach taking into account the double layer arising at the LSCF/gas interface. This improvement is currently being addressed in the frame of the PhD thesis of E. Effori.

The analysis of Ni agglomeration and redistribution in the hydrogen electrode has highlighted that the coarsening of nickel should remain an important issue but should not compromise the long-term durability of SOCs. Indeed, the stabilization of the microstructure provided by the YSZ backbone should allow to slow down the degradation for very long operating times. In contrast, the Ni depletion from the interface appears to be intrinsically triggered by the operation in electrolysis mode. The origin of the Ni migration remains unclear and more investigations are needed to completely understand the cause of the nickel detachment. Based on the coupled experimental and modeling approach, it has been proposed in this work that the modification of the double layer at the Ni/YSZ interface could be the triggering phenomenon leading to the Ni instability. In other words, the accumulation of oxygen vacancies at the interface between the Ni and the YSZ could weaken the interfacial adhesion between the two causing the nickel detachment. However, other groups have recently suggested that the driving force for Ni migration could be the evolution of the Ni/YSZ interfacial energy with the polarization [Trini 2020]. The two hypotheses are both relevant although they appear to be contradictory. At this stage, there are not enough experimental evidences to conclude on the most likely mechanism. Therefore, further experimental and modeling investigations

are needed to bring additional information on the underlying causes of Ni migration in electrolysis mode.

From a practical point of view, in this work it has been shown that this phenomenon could be dominating for coarser electrodes microstructures. Therefore, it should be possible to mitigate or at least limit the Ni depletion by microstructural optimization. In addition, it has been proposed that the Ni/YSZ adhesion must play a crucial role on the Ni stability. Consequently, methods to anchor Ni onto the YSZ backbone should stabilize the microstructure for both Ni agglomeration and migration. For example, addition of impurities in YSZ such as titanium could be envisaged as a potential solution to increase Ni/YSZ adhesion. Indeed, it has been shown that this element could enhance the Ni/YSZ interfacial adhesion [Skarmoutsos 2000, Tsoga 1996a]. Alternatively, in order to reduce the overpotential that triggers the Ni detachment, it could be possible to operate the cells at higher temperature. This last option could, theoretically, contribute to reduce the severity of Ni depletion, but it is expected to increase the impact of other thermally activated degradation phenomena. Finally, it can be pointed out that the modification of the electrode materials could be also a solution in the stabilization of the microstructure in electrolysis operation. In this context, the use of Ni-GDC electrodes could represent a more stable alternative to classical Ni-YSZ cermets.

Concerning the degradation of the LSCF-based oxygen electrode, an impact of the anodic current on the material destabilization has been highlighted. Furthermore, a clear effect of the temperature has been observed indicating that the phenomenon of strontium release could be alleviated by operating the cell at lower temperature. It has been shown that the formation of secondary phases at the barrier layer/electrolyte interface is ascribed to the LSCF destabilization. In this frame, it has been suggested that the inter-diffusion layer in the electrolyte could evolve under electrolysis current. However, this phenomenon could be strongly dependent on the cell and operating conditions. To validate this proposition, new characterizations at the nanoscale level will be necessary. The results reported in this thesis have indicated that the adopted approach remains valid. Therefore, the same type of characterizations, performed at the nanoscale, could be envisaged to analyze the oxygen electrode degradation coupling chemical and crystallographic data. Alternatively, Transmission Electron Microscopy (TEM), could be used to obtain the localized crystallographic information, whereas Secondary-Ions Mass Spectrometry (SIMS) could be used to investigate the chemical composition.

In addition to the precise determination of the underlying causes for the LSCF destabilization, the quantification of its impact on the performances could be envisioned. With this objective, the multi-

scale kinetic modeling scheme represents a powerful tool. Indeed, the passivation associated to the LSCF demixing could be implemented in the validated micro-scale model to directly evaluate the evolution of the electrode and cell response as a function of time. In addition, this approach could be coupled with computational thermodynamic data to identify a suitable law describing the demixing and the passivation during the aging.

For the application, it is clear that classical MIEC electrodes exhibits intrinsic material destabilization arising under anodic current. To find a mitigation solution by keeping the same material, it would be necessary to optimize the microstructure to spread and thus limit the strong depletion of vacancies in the electrode occurring in electrolysis mode. Moreover, it could be proposed to replace LSCF by alternative materials with a higher stability for SOEC operation. For example, rare-earth nickelates ( $\text{Ln}_2\text{NiO}_{4+\delta}$  with  $\text{Ln} = \text{La, Pr, Nd}$ ) have recently shown promising results in terms of durability for an operation in electrolysis mode [Khamidy 2020].

To conclude, several challenges arise when operating a solid oxide cell in electrolysis mode and to face them it is necessary to deeply understand their origins. In this context, the threefold methodology applied in this work by coupling (i) electrochemical characterizations (ii) advanced post-test analyses and (iii) multi-scale modeling, appears as a suitable procedure to investigate the intrinsic causes of the cell degradation. Based on this study, it can be stated that some compromise may be needed to improve the durability of SOCs in electrolysis and reversible mode and thus ensure their commercial attractiveness.



# Appendix A

## Cells Description and Experimental Conditions

		Material			Test		Characterization	
Type of cell	Hydrogen Electrode	Electrolyte	Oxygen Electrode	Test Conditions	Degradation Results	3D Volume	$\mu$ XRD	$\mu$ XRF
<b>Cell-A1</b>	Button cell Ni-YSZ fine microstructure ( $\approx 260 \mu\text{m}$ )	8YSZ ( $\approx 8 \mu\text{m}$ )	Multilayer (GDC $\approx 4 \mu\text{m}$ // LSCF-GDC $\approx 16 \mu\text{m}$ // LSCF $\approx 20 \mu\text{m}$ // LSC $\approx 25 \mu\text{m}$ )	SOEC T = 850°C $i_{\text{oc}} = -0.75 \text{ A}\cdot\text{cm}^{-2}$ (SC 50%) t $\approx 1'800 \text{ h}$	From durability curve: $\approx 13.5 \text{ mV}\cdot\text{kh}^{-1}$ From i-U curve at 850°C: $\approx 14 \text{ mV}\cdot\text{kh}^{-1}$		X	
<b>Cell-A2</b>	Button cell Ni-YSZ fine microstructure ( $\approx 260 \mu\text{m}$ )	8YSZ ( $\approx 8 \mu\text{m}$ )	Multilayer (GDC $\approx 4 \mu\text{m}$ // LSCF-GDC $\approx 16 \mu\text{m}$ // LSCF $\approx 20 \mu\text{m}$ // LSC $\approx 25 \mu\text{m}$ )	SOEC T = 750°C $i_{\text{oc}} = -0.75 \text{ A}\cdot\text{cm}^{-2}$ (SC 50%) t $\approx 1'800 \text{ h}$	From durability curve: $\approx 60 \text{ mV}\cdot\text{kh}^{-1}$ From i-U curve at 850°C: $\approx 17 \text{ mV}\cdot\text{kh}^{-1}$		X	
<b>Cell-A3</b>	Segmented cell Ni-YSZ fine microstructure ( $\approx 260 \mu\text{m}$ )	8YSZ ( $\approx 8 \mu\text{m}$ )	Multilayer (GDC $\approx 4 \mu\text{m}$ // LSCF-GDC $\approx 16 \mu\text{m}$ // LSCF $\approx 20 \mu\text{m}$ // LSC $\approx 25 \mu\text{m}$ )	SOFC T = 780°C $i_{\text{oc}} = 0.25 \text{ A}\cdot\text{cm}^{-2}$ (FC 40%) t $\approx 15'000 \text{ h}$	From increase in ASR at 0.25 A $\cdot\text{cm}^{-2}$ : $\approx 3 \text{ mV}\cdot\text{kh}^{-1}$	X		X
<b>Cell-A4</b>	Cell from short-stack Ni-YSZ fine microstructure ( $\approx 260 \mu\text{m}$ )	8YSZ ( $\approx 8 \mu\text{m}$ )	GDC ( $\approx 4 \mu\text{m}$ ) // LSC ( $\approx 75 \mu\text{m}$ )	SOEC T = 720°C $i_{\text{oc}} = -0.6$ and $-0.5 \text{ A}\cdot\text{cm}^{-2}$ (SC 45-38%) t $\approx 10'700 \text{ h}$	From durability curve: $\approx 6 \text{ mV}\cdot\text{kh}^{-1}$	X		
<b>Cell-B</b>	Button cell Ni-YSZ coarse microstructure ( $\approx 350 \mu\text{m}$ )	8YSZ ( $\approx 10 \mu\text{m}$ )	GDC ( $\approx 5 \mu\text{m}$ ) // LSCF ( $\approx 50 \mu\text{m}$ )	SOEC T = 800°C $i_{\text{oc}} = -0.5 \text{ A}\cdot\text{cm}^{-2}$ (SC 15%) t $\approx 1'000 \text{ h}$	From durability curve: $\approx 100 \text{ mV}\cdot\text{kh}^{-1}$	X		



# Appendix B

## Development of the Micro-Kinetic Model for the Hydrogen Electrode Reaction Mechanism: Model I Based on the Oxygen Spillover Mechanism

As explained in chapter III section III.1, the oxygen spillover mechanism implemented in Model I is described by five chemical reactions and one electrochemical charge transfer reaction.

These reactions are accompanied by the surface diffusion of the adsorbed species ( $H_{Ni}$ ,  $H_2O_{Ni}$ ,  $OH_{Ni}$ ,  $O_{Ni}$  and  $O_{YSZ}^{2-}$ ), the ionic conduction in the YSZ, the electronic conduction in the nickel phase and gas diffusion in the pores of the electrode ( $H_2$  and  $H_2O$ ).

For each reaction, the kinetic rate is expressed according to eqs. (III-2a) and (III-2b).

$$v_{H_2O_{Ni}}^{ADS} = Sp_{pores-Ni} \cdot \Gamma_{Ni} \cdot \left( k_{H_2O_{Ni}}^{ADS} \cdot \frac{p_{H_2O}}{p_{ref}} \cdot \theta_{Ni} - k_{H_2O_{Ni}}^{DES} \cdot \theta_{H_2O_{Ni}} \right) \quad (B.1)$$

$$v_{H_2O_{Ni}}^{DISS} = Sp_{pores-Ni} \cdot \Gamma_{Ni}^2 \cdot \left( k_{H_2O_{Ni}}^{DISS+} \cdot \theta_{H_2O_{Ni}} \cdot \theta_{Ni} - k_{H_2O_{Ni}}^{DISS-} \cdot \theta_{OH_{Ni}} \cdot \theta_{H_{Ni}} \right) \quad (B.2)$$

$$v_{OH_{Ni}}^{DISS} = Sp_{pores-Ni} \cdot \Gamma_{Ni}^2 \cdot \left( k_{OH_{Ni}}^{DISS+} \cdot \theta_{OH_{Ni}} \cdot \theta_{Ni} - k_{OH_{Ni}}^{DISS-} \cdot \theta_{O_{Ni}} \cdot \theta_{H_{Ni}} \right) \quad (B.3)$$

$$v_{H_2_{Ni}}^{DES} = Sp_{pores-Ni} \cdot \Gamma_{Ni}^2 \cdot \left( k_{H_2_{Ni}}^{DES} \cdot \theta_{H_{Ni}}^2 - k_{H_2_{Ni}}^{ADS} \cdot \frac{p_{H_2}}{p_{ref}} \cdot \theta_{Ni}^2 \right) \quad (B.4)$$

$$v_{RED}^{ct} = \xi^{TPBIs} \cdot \Gamma_{Ni} \cdot \Gamma_{YSZ} \cdot \left( k^{red} \cdot \theta_{O_{Ni}} \cdot \theta_{YSZ} \cdot \exp\left(\frac{-2 \cdot \alpha_{ct}^{red} \cdot F}{RT} E\right) - k^{ox} \cdot \theta_{Ni} \cdot \theta_{O_{YSZ}^{2-}} \cdot \exp\left(\frac{2 \cdot \alpha_{ct}^{ox} \cdot F}{RT} E\right) \right) \quad (B.5)$$

$$v_{O_{YSZ}^{2-}}^{INC} = Sp_{YSZ-pores} \cdot \Gamma_{YSZ} \cdot \left( k_{O_{YSZ}^{2-}}^{INC} \cdot \theta_{O_{YSZ}^{2-}} \cdot \frac{c_{V_{O_{YSZ}^{2-}}}(YSZ)}{c_{O_{YSZ}^{2-}}^{ref}} - k_{O_{YSZ}^{2-}}^{EXC} \cdot \theta_{YSZ} \cdot \frac{c_{O_{O_{YSZ}^{2-}}}(YSZ)}{c_{O_{O_{YSZ}^{2-}}}^{ref}} \right) \quad (B.6)$$

The thermodynamic equilibrium constants for the five chemical reactions (**CR1-CR5**) are evaluated using eqs. (III-6a) and (III-6b).

$$K_{ADS,H_2O_{Ni}}^{eq} = \frac{k_{H_2O_{Ni}}^{ADS}}{k_{H_2O_{Ni}}^{DES}} = \exp\left(\frac{-\left[\left(h_{H_2O_{Ni}}^0(T) - Ts_{H_2O_{Ni}}^0(T)\right) - \left(h_{H_2O(g)}^0(T) + h_{s_{Ni}}^0(T) - T\left(s_{H_2O(g)}^0(T) + s_{s_{Ni}}^0(T)\right)\right)\right]}{RT}\right) \quad (B.7)$$

$$K_{DISS,H_2O_{Ni}}^{eq} = \frac{k_{H_2O_{Ni}}^{DISS+}}{k_{H_2O_{Ni}}^{DISS-}} = \exp\left(\frac{-\left[h_{OH_{Ni}}^0(T) + h_{H_{Ni}}^0(T) - T\left(s_{OH_{Ni}}^0(T) + s_{H_{Ni}}^0(T)\right) - \left(h_{H_2O_{Ni}}^0(T) + h_{s_{Ni}}^0(T) - T\left(s_{H_2O_{Ni}}^0(T) + s_{s_{Ni}}^0(T)\right)\right)\right]}{RT}\right) \quad (B.8)$$

$$K_{DISS,OH_{Ni}}^{eq} = \frac{k_{OH_{Ni}}^{DISS+}}{k_{OH_{Ni}}^{DISS-}} = \exp\left(\frac{-\left[h_{O_{Ni}}^0(T) + h_{H_{Ni}}^0(T) - T\left(s_{O_{Ni}}^0(T) + s_{H_{Ni}}^0(T)\right) - \left(h_{OH_{Ni}}^0(T) + h_{s_{Ni}}^0(T) - T\left(s_{OH_{Ni}}^0(T) + s_{s_{Ni}}^0(T)\right)\right)\right]}{RT}\right) \quad (B.9)$$

$$K_{DES,H_2Ni}^{eq} = \frac{k_{H_2Ni}^{DES}}{k_{H_2Ni}^{ADS}} = \exp\left(\frac{-\left[\left(h_{H_2(g)}^0(T) - Ts_{H_2(g)}^0(T) + 2\left(h_{s_{Ni}}^0(T) - Ts_{s_{Ni}}^0(T)\right)\right) - 2\left(h_{H_{Ni}}^0(T) - Ts_{H_{Ni}}^0(T)\right)\right]}{RT}\right) \quad (B.10)$$

$$K_{INC,O_{YSZ}^{2-}}^{eq} = \frac{k_{O_{YSZ}^{2-}}^{INC}}{k_{O_{YSZ}^{2-}}^{EXC}} = \exp\left(\frac{-\left[h_{O_O^x}^0(T) + h_{s_{YSZ}}^0(T) - T\left(s_{O_O^x}^0(T) + s_{s_{YSZ}}^0(T)\right) - \left(h_{O_{V_O}^{2-}}^0(T) + h_{V_O^{2-}}^0(T) - T\left(s_{O_{V_O}^{2-}}^0(T) + s_{V_O^{2-}}^0(T)\right)\right)\right]}{RT}\right) \quad (B.11)$$

The thermodynamic data used for the calculations are reported in Table III-III.

Once the equilibrium constants have been determined, these have been used to evaluate the surface coverages at equilibrium on Ni and YSZ with eq. (III-7).

For the equilibrium on Ni surface:

$$K_{ADS,H_2O_{Ni}}^{eq} = \frac{\theta_{H_2O_{Ni}}^{eq}}{\frac{p_{H_2O}^{eq}}{p_{ref}} \cdot \theta_{Ni}^{eq}} = \theta_{H_2O_{Ni}}^{eq} = K_{ADS,H_2O_{Ni}}^{eq} \cdot \frac{p_{H_2O}^{eq}}{p_{ref}} \cdot \theta_{Ni}^{eq} \quad (B.12)$$

$$K_{DES,H_2Ni}^{eq} = \frac{\frac{p_{H_2}^{eq}}{p_{ref}} \cdot \theta_{Ni}^{eq^2}}{\theta_{H_{Ni}}^{eq^2}} = \theta_{H_{Ni}}^{eq} = \sqrt{\frac{1}{K_{DES,H_2Ni}^{eq}} \cdot \frac{p_{H_2}^{eq}}{p_{ref}}} \cdot \theta_{Ni}^{eq} \quad (B.13)$$

$$K_{DISS,H_2O_{Ni}}^{eq} = \frac{\theta_{OH_{Ni}}^{eq} \cdot \theta_{H_{Ni}}^{eq}}{\theta_{H_2O_{Ni}}^{eq} \cdot \theta_{Ni}^{eq}} = \theta_{OH_{Ni}}^{eq} = K_{DISS,H_2O_{Ni}}^{eq} \cdot K_{ADS,H_2O_{Ni}}^{eq} \cdot \frac{p_{H_2O}^{eq}}{p_{ref}} \cdot \left(\sqrt{\frac{1}{K_{DES,H_2Ni}^{eq}} \cdot \frac{p_{H_2}^{eq}}{p_{ref}}}\right)^{-1} \cdot \theta_{Ni}^{eq} \quad (B.14)$$

$$K_{DISS,OH_{Ni}}^{eq} = \frac{\theta_{O_{Ni}}^{eq} \cdot \theta_{H_{Ni}}^{eq}}{\theta_{OH_{Ni}}^{eq} \cdot \theta_{Ni}^{eq}} = \theta_{O_{Ni}}^{eq} = K_{DISS,OH_{Ni}}^{eq} \cdot K_{DISS,H_2O_{Ni}}^{eq} \cdot K_{ADS,H_2O_{Ni}}^{eq} \cdot K_{DES,H_2Ni}^{eq} \cdot \frac{p_{H_2O}^{eq}}{p_{H_2}^{eq}} \cdot \theta_{Ni}^{eq} \quad (B.15)$$

$$\Sigma \theta = 1 \Rightarrow \theta_{Ni}^{eq} = \left(1 + K_{ADS,H_2O_{Ni}}^{eq} \cdot \frac{p_{H_2O}^{eq}}{p_{ref}} + \sqrt{\frac{1}{K_{DES,H_2Ni}^{eq}} \cdot \frac{p_{H_2}^{eq}}{p_{ref}}} + K_{DISS,H_2O_{Ni}}^{eq} \cdot K_{ADS,H_2O_{Ni}}^{eq} \cdot \frac{p_{H_2O}^{eq}}{p_{ref}} \cdot \left(\sqrt{\frac{1}{K_{DES,H_2Ni}^{eq}} \cdot \frac{p_{H_2}^{eq}}{p_{ref}}}\right)^{-1} + K_{DISS,OH_{Ni}}^{eq} \cdot K_{DISS,H_2O_{Ni}}^{eq} \cdot K_{ADS,H_2O_{Ni}}^{eq} \cdot K_{DES,H_2Ni}^{eq} \cdot \frac{p_{H_2O}^{eq}}{p_{H_2}^{eq}} \cdot \left(\sqrt{\frac{1}{K_{DES,H_2Ni}^{eq}} \cdot \frac{p_{H_2}^{eq}}{p_{ref}}}\right)^{-1}\right)^{-1} \quad (B.16)$$

Whereas on the YSZ surface:

$$K_{INC,O_{YSZ}^{2-}}^{eq} = \frac{c_{O_O^x} \cdot \theta_{YSZ}^{eq}}{c_{V_O^{2-}} \cdot \theta_{O_{YSZ}^{2-}}^{eq}} = \theta_{O_{YSZ}^{2-}}^{eq} = \frac{1}{K_{INC,O_{YSZ}^{2-}}^{eq}} \cdot \frac{c_{O_O^x}}{c_{V_O^{2-}}} \cdot \theta_{YSZ}^{eq} \quad (B.17)$$

$$\Sigma \theta = 1 \Rightarrow \theta_{YSZ}^{eq} = \left(1 + \frac{1}{K_{INC,O_{YSZ}^{2-}}^{eq}} \cdot \frac{c_{O_O^x}}{c_{V_O^{2-}}}\right)^{-1} \quad (B.18)$$

Subsequently the surface coverages at equilibrium have been used to evaluate the equilibrium constant for the electrochemical charge transfer reaction **ER1** as reported in Eq. (III-8).

$$K_{ct-RED}^{eq} = \frac{\theta_{Ni}^{eq} \cdot \theta_{O_{Y\bar{S}Z}}^{eq}}{\theta_{O_{Ni}}^{eq} \cdot \theta_{Y\bar{S}Z}^{eq}} \exp\left(\frac{2F}{RT} E^{eq}\right) \quad (B.19)$$

The diffusion of all the species involved in the reaction mechanism has been modeled according to eqs. (III-9) to (III-15) and using the diffusion coefficients reported in Table III-IV.

$$\varepsilon_{pores} \frac{dC_{H_2}}{dt} + \nabla \cdot (-D_{H_2}^{eff} \nabla C_{H_2}) = +v_{H_2Ni}^{DES} \quad (B.20)$$

$$\varepsilon_{pores} \frac{dC_{H_2O}}{dt} + \nabla \cdot (-D_{H_2O}^{eff} \nabla C_{H_2O}) = -v_{H_2ONi}^{ADS} \quad (B.21)$$

$$Sp_{Ni-Y\bar{S}Z} C_{dl} \frac{dE}{dt} = -\nabla \cdot (-\sigma_{el}^{eff} \nabla \varphi_{el}) + 2Fv_{RED}^{ct} \quad (B.22)$$

$$-Sp_{Ni-Y\bar{S}Z} C_{dl} \frac{dE}{dt} = -\nabla \cdot (-\sigma_{io}^{eff} \nabla \varphi_{io}) - 2Fv_{O_{Y\bar{S}Z}}^{INC} \quad (B.23)$$

$$Sp_{pores-Ni} \Gamma_{Ni} \frac{d\theta_{H_{Ni}}}{dt} + \nabla \cdot (-Sp_{pores-Ni} \Gamma_{Ni} D_{H_{Ni}} \nabla \theta_{H_{Ni}}) = -2v_{H_2Ni}^{DES} + v_{H_2ONi}^{DISS} + v_{OH_{Ni}}^{DISS} \quad (B.24)$$

$$Sp_{pores-Ni} \Gamma_{Ni} \frac{d\theta_{H_2ONi}}{dt} + \nabla \cdot (-Sp_{pores-Ni} \Gamma_{Ni} D_{H_2ONi} \nabla \theta_{H_2ONi}) = +v_{H_2ONi}^{ADS} - v_{H_2ONi}^{DISS} \quad (B.25)$$

$$Sp_{pores-Ni} \Gamma_{Ni} \frac{d\theta_{OH_{Ni}}}{dt} + \nabla \cdot (-Sp_{pores-Ni} \Gamma_{Ni} D_{OH_{Ni}} \nabla \theta_{OH_{Ni}}) = +v_{H_2ONi}^{DISS} - v_{OH_{Ni}}^{DISS} \quad (B.26)$$

$$Sp_{pores-Ni} \Gamma_{Ni} \frac{d\theta_{ONi}}{dt} + \nabla \cdot (-Sp_{pores-Ni} \Gamma_{Ni} D_{ONi} \nabla \theta_{ONi}) = +v_{OH_{Ni}}^{DISS} - v_{RED}^{ct} \quad (B.27)$$

$$Sp_{Y\bar{S}Z-pores} \Gamma_{Y\bar{S}Z} \frac{d\theta_{O_{Y\bar{S}Z}}}{dt} + \nabla \cdot (-Sp_{Y\bar{S}Z-pores} \Gamma_{Y\bar{S}Z} D_{O_{Y\bar{S}Z}} \nabla \theta_{O_{Y\bar{S}Z}}) = +v_{RED}^{ct} - v_{O_{Y\bar{S}Z}}^{INC} \quad (B.28)$$

Solving this set of partial differential equations with the boundary conditions reported in chapter III section III.1.1.5, the model is used to simulate the  $\eta$ -i curves and the impedance spectra.



# Appendix C

## Development of the Micro-Kinetic Model for the Hydrogen Electrode Reaction Mechanism: Model II Based on the Hydrogen Spillover Mechanism

The H spillover mechanism implemented in Model II is described by five chemical reactions and two electrochemical reactions.

These reaction steps are accompanied by the surface diffusion of the adsorbed species ( $H_{Ni}$ ,  $H_2O_{Ni}$ ,  $H_2O_{YSZ}$ ,  $OH_{YSZ}^-$  and  $O_{YSZ}^{2-}$ ), the ionic conduction in the YSZ, the electronic conduction in the nickel and gas diffusion in the pores of the electrode ( $H_2$  and  $H_2O$ ).

For each one of the electrode reactions, the kinetic rate is expressed according to eqs. (III-2a) and (III-2b).

$$v_{H_2O_{Ni}}^{ADS} = Sp_{pores-Ni} \cdot \Gamma_{Ni} \cdot \left( k_{H_2O_{Ni}}^{ADS} \cdot \frac{p_{H_2O}}{p_{ref}} \cdot \theta_{Ni} - k_{H_2O_{Ni}}^{DES} \cdot \theta_{H_2O_{Ni}} \right) \quad (C.1)$$

$$v_{H_2O_{YSZ}}^{ADS} = Sp_{YSZ-pores} \cdot \Gamma_{YSZ} \cdot \left( k_{H_2O_{YSZ}}^{ADS} \cdot \frac{p_{H_2O}}{p_{ref}} \cdot \theta_{YSZ} - k_{H_2O_{YSZ}}^{DES} \cdot \theta_{H_2O_{YSZ}} \right) \quad (C.2)$$

$$v_{H_2O_{YSZ}}^{DISS} = Sp_{YSZ-pores} \cdot \Gamma_{YSZ}^2 \cdot \left( k_{H_2O_{Ni}}^{DISS+} \cdot \theta_{H_2O_{YSZ}} \cdot \theta_{O_{YSZ}^{2-}} - k_{H_2O_{YSZ}}^{DISS-} \cdot \theta_{OH_{YSZ}^-}^2 \right) \quad (C.3)$$

$$v_{H_2Ni}^{DES} = Sp_{pores-Ni} \cdot \Gamma_{Ni}^2 \cdot \left( k_{H_2Ni}^{DES} \cdot \theta_{H_{Ni}}^2 - k_{H_2Ni}^{ADS} \cdot \frac{p_{H_2}}{p_{ref}} \cdot \theta_{Ni}^2 \right) \quad (C.4)$$

$$v_{RED}^{ct,1} = \xi^{TPBlS} \cdot \Gamma_{Ni} \cdot \Gamma_{YSZ} \cdot \left( k_1^{red} \cdot \theta_{H_2O_{Ni}} \cdot \theta_{YSZ} \cdot \exp\left(\frac{-\alpha_{ct,1}^{red} \cdot F}{RT} E\right) - k_1^{ox} \cdot \theta_{OH_{YSZ}^-} \cdot \theta_{H_{Ni}} \cdot \exp\left(\frac{\alpha_{ct,1}^{ox} \cdot F}{RT} E\right) \right) \quad (C.5)$$

$$v_{RED}^{ct,2} = \xi^{TPBlS} \cdot \Gamma_{Ni} \cdot \Gamma_{YSZ} \cdot \left( k_2^{red} \cdot \theta_{OH_{YSZ}^-} \cdot \theta_{Ni} \cdot \exp\left(\frac{-\alpha_{ct,2}^{red} \cdot F}{RT} E\right) - k_2^{ox} \cdot \theta_{O_{YSZ}^{2-}} \cdot \theta_{H_{Ni}} \cdot \exp\left(\frac{\alpha_{ct,2}^{ox} \cdot F}{RT} E\right) \right) \quad (C.6)$$

$$v_{O_{Y\bar{S}Z}^{INC}} = Sp_{Y\bar{S}Z-pores} \cdot \Gamma_{Y\bar{S}Z} \cdot \left( k_{O_{Y\bar{S}Z}^{INC}} \cdot \theta_{O_{Y\bar{S}Z}^{2-}} \cdot \frac{C_{V_O^{**}(Y\bar{S}Z)}}{C_{O_O^{2-}(Y\bar{S}Z)}^{ref}} - k_{O_{Y\bar{S}Z}^{EXC}} \cdot \theta_{Y\bar{S}Z} \cdot \frac{C_{O_O^x(Y\bar{S}Z)}}{C_{O_O^{2-}(Y\bar{S}Z)}^{ref}} \right) \quad (C.7)$$

The thermodynamic equilibrium constants of the five chemical reactions (**CR1-CR5**) are obtained using eqs. (III-6a) and (III-6b) and the thermodynamic data reported in Table III-III.

$$K_{ADS,H_2O_{Ni}}^{eq} = \frac{k_{H_2O_{Ni}}^{ADS}}{k_{H_2O_{Ni}}^{DES}} = \exp \left( \frac{- \left[ \left( h_{H_2O_{Ni}}^0(T) - T s_{H_2O_{Ni}}^0(T) \right) - \left( h_{H_2O(g)}^0(T) + h_{s_{Ni}}^0(T) - T \left( s_{H_2O(g)}^0(T) + s_{s_{Ni}}^0(T) \right) \right) \right]}{RT} \right) \quad (C.8)$$

$$K_{ADS,H_2O_{YSZ}}^{eq} = \frac{k_{H_2O_{YSZ}}^{ADS}}{k_{H_2O_{YSZ}}^{DES}} = \exp \left( \frac{- \left[ \left( h_{H_2O_{YSZ}}^0(T) - T s_{H_2O_{YSZ}}^0(T) \right) - \left( h_{H_2O(g)}^0(T) + h_{s_{YSZ}}^0(T) - T \left( s_{H_2O(g)}^0(T) + s_{s_{YSZ}}^0(T) \right) \right) \right]}{RT} \right) \quad (C.9)$$

$$K_{DISS,H_2O_{YSZ}}^{eq} = \frac{k_{H_2O_{YSZ}}^{DISS+}}{k_{H_2O_{YSZ}}^{DISS-}} = \exp \left( \frac{- \left[ 2 \left( h_{OH_{YSZ}^-}^0(T) - T s_{OH_{YSZ}^-}^0(T) \right) - \left( h_{H_2O_{YSZ}}^0(T) + h_{O_{Y\bar{S}Z}^{2-}}^0(T) - T \left( s_{H_2O_{YSZ}}^0(T) + s_{O_{Y\bar{S}Z}^{2-}}^0(T) \right) \right) \right]}{RT} \right) \quad (C.10)$$

$$K_{DES,H_2Ni}^{eq} = \frac{k_{H_2Ni}^{DES}}{k_{H_2Ni}^{ADS}} = \exp \left( \frac{- \left[ \left( h_{H_2(g)}^0(T) - T s_{H_2(g)}^0(T) + 2 \left( h_{s_{Ni}}^0(T) - T s_{s_{Ni}}^0(T) \right) \right) - 2 \left( h_{H_{Ni}}^0(T) - T s_{H_{Ni}}^0(T) \right) \right]}{RT} \right) \quad (C.11)$$

$$K_{INC,O_{Y\bar{S}Z}^{2-}}^{eq} = \frac{k_{O_{Y\bar{S}Z}^{2-}}^{INC}}{k_{O_{Y\bar{S}Z}^{2-}}^{EXC}} = \exp \left( \frac{- \left[ h_{O_O^x}^0(T) + h_{s_{YSZ}}^0(T) - T \left( s_{O_O^x}^0(T) + s_{s_{YSZ}}^0(T) \right) - \left( h_{O_{Y\bar{S}Z}^{2-}}^0(T) + h_{V_O^{**}}^0(T) - T \left( s_{O_{Y\bar{S}Z}^{2-}}^0(T) + s_{V_O^{**}}^0(T) \right) \right) \right]}{RT} \right) \quad (C.12)$$

Once the equilibrium constants have been determined, these have been used to calculate the Ni and YSZ surface coverages at equilibrium with eq. (III-7) and subsequently the equilibrium constants for the electrochemical reactions as reported in eq. (III-8).

For the Ni surface, the coverages at equilibrium are:

$$K_{ADS,H_2O_{Ni}}^{eq} = \frac{\theta_{H_2O_{Ni}}^{eq}}{\frac{p_{H_2O}^{eq}}{p_{ref}} \theta_{Ni}^{eq}} \Rightarrow \theta_{H_2O_{Ni}}^{eq} = K_{ADS,H_2O_{Ni}}^{eq} \cdot \frac{p_{H_2O}^{eq}}{p_{ref}} \cdot \theta_{Ni}^{eq} \quad (C.13)$$

$$K_{DES,H_2Ni}^{eq} = \frac{\frac{p_{H_2}^{eq}}{p_{ref}} \theta_{Ni}^{eq^2}}{\theta_{H_{Ni}}^{eq^2}} \Rightarrow \theta_{H_{Ni}}^{eq} = \sqrt{\frac{1}{K_{DES,H_2Ni}^{eq}} \cdot \frac{p_{H_2}^{eq}}{p_{ref}} \cdot \theta_{Ni}^{eq}} \quad (C.14)$$

$$\sum \theta = 1 \Rightarrow \theta_{Ni}^{eq} = \left( 1 + K_{ADS,H_2O_{Ni}}^{eq} \cdot \frac{p_{H_2O}^{eq}}{p_{ref}} + \sqrt{\frac{1}{K_{DES,H_2Ni}^{eq}} \cdot \frac{p_{H_2}^{eq}}{p_{ref}}} \right)^{-1} \quad (C.15)$$

While for the YSZ surface:

$$K_{ADS,H_2O_{YSZ}}^{eq} = \frac{\theta_{H_2O_{YSZ}}^{eq}}{\frac{p_{H_2O}^{eq}}{p_{ref}} \theta_{YSZ}^{eq}} \Rightarrow \theta_{H_2O_{YSZ}}^{eq} = K_{ADS,H_2O_{YSZ}}^{eq} \cdot \frac{p_{H_2O}^{eq}}{p_{ref}} \cdot \theta_{YSZ}^{eq} \quad (C.16)$$

$$K_{INC,O_{Y\bar{S}Z}^{2-}}^{eq} = \frac{C_{O_O^x} \cdot \theta_{YSZ}^{eq}}{C_{V_O^{**}} \cdot \theta_{O_{Y\bar{S}Z}^{2-}}^{eq}} \Rightarrow \theta_{O_{Y\bar{S}Z}^{2-}}^{eq} = \frac{1}{K_{INC,O_{Y\bar{S}Z}^{2-}}^{eq}} \cdot \frac{C_{O_O^x}}{C_{V_O^{**}}} \cdot \theta_{YSZ}^{eq} \quad (C.17)$$

$$K_{DISS,H_2O_{YSZ}}^{eq} = \frac{\theta_{OH_{YSZ}^-}^{eq^2}}{\theta_{H_2O_{YSZ}}^{eq} \cdot \theta_{O_{Y\bar{S}Z}^{2-}}^{eq}} \Rightarrow \theta_{OH_{YSZ}^-}^{eq} = \sqrt{K_{DISS,H_2O_{YSZ}}^{eq} \cdot K_{ADS,H_2O_{YSZ}}^{eq} \cdot \frac{p_{H_2O}^{eq}}{p_{ref}} \cdot \frac{1}{K_{INC,O_{Y\bar{S}Z}^{2-}}^{eq}} \cdot \frac{C_{O_O^x}}{C_{V_O^{**}}} \cdot \theta_{YSZ}^{eq}} \quad (C.18)$$

$$\Sigma \theta = 1 \Rightarrow \theta_{Y\bar{S}Z}^{eq} = \left( 1 + K_{ADS,H_2O_{Y\bar{S}Z}}^{eq} \cdot \frac{p_{H_2O}^{eq}}{p_{ref}} + \sqrt{K_{DISS,H_2O_{Y\bar{S}Z}}^{eq} \cdot K_{ADS,H_2O_{Y\bar{S}Z}}^{eq} \cdot \frac{p_{H_2O}^{eq}}{p_{ref}} \cdot \frac{1}{K_{INC,O_{Y\bar{S}Z}^{2-}}^{eq}} \cdot \frac{C_{O_{Y\bar{S}Z}^{2-}}}{C_{V_{O^{2-}}}^{\bullet}}} + \frac{1}{K_{INC,O_{Y\bar{S}Z}^{2-}}^{eq}} \cdot \frac{C_{O_{Y\bar{S}Z}^{2-}}}{C_{V_{O^{2-}}}^{\bullet}}} \right)^{-1} \quad (C.19)$$

Finally, the equilibrium constants of the charge transfer reactions (**ER1** and **ER2**) are obtained:

$$K_{ct,1-RED}^{eq} = \frac{\theta_{H_{Ni}}^{eq} \cdot \theta_{OH_{Y\bar{S}Z}}^{eq}}{\theta_{H_2O_{Ni}}^{eq} \cdot \theta_{Y\bar{S}Z}^{eq}} \exp\left(\frac{F}{RT} E^{eq}\right) \quad (C.20)$$

$$K_{ct,2-RED}^{eq} = \frac{\theta_{H_{Ni}}^{eq} \cdot \theta_{O_{Y\bar{S}Z}^{2-}}^{eq}}{\theta_{OH_{Y\bar{S}Z}}^{eq} \cdot \theta_{Ni}^{eq}} \exp\left(\frac{F}{RT} E^{eq}\right) \quad (C.21)$$

The diffusion of all the species involved in the reaction mechanism has been modeled according to eqs. (III-9) to (III-15) and using the diffusion coefficients reported in Table III-IV.

$$\varepsilon_{pores} \frac{dC_{H_2}}{dt} + \nabla \cdot (-D_{H_2}^{eff} \nabla C_{H_2}) = +v_{H_{2Ni}}^{DES} \quad (C.22)$$

$$\varepsilon_{pores} \frac{dC_{H_2O}}{dt} + \nabla \cdot (-D_{H_2O}^{eff} \nabla C_{H_2O}) = -v_{H_2O_{Y\bar{S}Z}}^{ADS} - v_{H_2O_{Ni}}^{ADS} \quad (C.23)$$

$$Sp_{Ni-Y\bar{S}Z} C_{dl} \frac{dE}{dt} = -\nabla \cdot (-\sigma_{el}^{eff} \nabla \varphi_{el}) + F(v_{RED}^{ct,1} + v_{RED}^{ct,2}) \quad (C.24)$$

$$-Sp_{Ni-Y\bar{S}Z} C_{dl} \frac{dE}{dt} = -\nabla \cdot (-\sigma_{io}^{eff} \nabla \varphi_{io}) - 2Fv_{O_{Y\bar{S}Z}^{2-}}^{INC} \quad (C.25)$$

$$Sp_{pores-Ni} \Gamma_{Ni} \frac{d\theta_{H_{Ni}}}{dt} + \nabla \cdot (-Sp_{pores-Ni} \Gamma_{Ni} D_{H_{Ni}} \nabla \theta_{H_{Ni}}) = -2v_{H_{2Ni}}^{DES} + v_{RED}^{ct,1} + v_{RED}^{ct,2} \quad (C.26)$$

$$Sp_{pores-Ni} \Gamma_{Ni} \frac{d\theta_{H_2O_{Ni}}}{dt} + \nabla \cdot (-Sp_{pores-Ni} \Gamma_{Ni} D_{H_2O_{Ni}} \nabla \theta_{H_2O_{Ni}}) = +v_{H_2O_{Ni}}^{ADS} - v_{RED}^{ct,1} \quad (C.27)$$

$$Sp_{Y\bar{S}Z-pores} \Gamma_{Y\bar{S}Z} \frac{d\theta_{H_2O_{Y\bar{S}Z}}}{dt} + \nabla \cdot (-Sp_{Y\bar{S}Z-pores} \Gamma_{Y\bar{S}Z} D_{H_2O_{Y\bar{S}Z}} \nabla \theta_{H_2O_{Y\bar{S}Z}}) = +v_{H_2O_{Y\bar{S}Z}}^{ADS} - v_{H_2O_{Y\bar{S}Z}}^{DISS} \quad (C.28)$$

$$Sp_{Y\bar{S}Z-pores} \Gamma_{Y\bar{S}Z} \frac{d\theta_{OH_{Y\bar{S}Z}}}{dt} + \nabla \cdot (-Sp_{Y\bar{S}Z-pores} \Gamma_{Y\bar{S}Z} D_{OH_{Y\bar{S}Z}} \nabla \theta_{OH_{Y\bar{S}Z}}) = +2v_{H_2O_{Y\bar{S}Z}}^{DISS} + v_{RED}^{ct,1} - v_{RED}^{ct,2} \quad (C.29)$$

$$Sp_{Y\bar{S}Z-pores} \Gamma_{Y\bar{S}Z} \frac{d\theta_{O_{Y\bar{S}Z}^{2-}}}{dt} + \nabla \cdot (-Sp_{Y\bar{S}Z-pores} \Gamma_{Y\bar{S}Z} D_{O_{Y\bar{S}Z}^{2-}} \nabla \theta_{O_{Y\bar{S}Z}^{2-}}) = -v_{H_2O_{Y\bar{S}Z}}^{DISS} + v_{RED}^{ct,2} - v_{O_{Y\bar{S}Z}^{2-}}^{INC} \quad (C.30)$$

Solving this set of partial differential equations with the boundary conditions reported in chapter III section III.1.1.5, it is possible to simulate the  $\eta$ -i curves and the impedance spectra.



# Bibliography

- [Adler 1998] Adler, S. B. (1998). *Mechanism and kinetics of oxygen reduction on porous LaSrCoO electrodes*. **Solid State Ionics**, 111, 125.
- [Adler 2004] Adler, S. B. (2004). *Factors governing oxygen reduction in solid oxide fuel cell cathodes*. **Chemical Reviews**, 104(10), 4791.
- [Adler 2000] Adler, S. B., Henderson, B. T., Wilson, M. A., Taylor, D. M., & Richards, R. E. (2000). *Reference electrode placement and seals in electrochemical oxygen generators*. **Solid State Ionics**, 134(1–2), 35.
- [Adler 1996] Adler, S. B., Lane, J. A., & Steele, B. C. H. (1996). *Electrode Kinetics of Porous Mixed-Conducting Oxygen Electrodes*. **Journal of Electrochemical Society**, 143(11), 3554.
- [Aicart 2014] Aicart, J., Laurencin, J., Petitjean, M., & Dessemond, L. (2014). *Experimental validation of two-dimensional H<sub>2</sub>O and CO<sub>2</sub> Co-electrolysis modeling*. **Fuel Cells**, 14(3), 430.
- [Aicart 2015] Aicart, J., Petitjean, M., Laurencin, J., Tallobre, L., & Dessemond, L. (2015). *Accurate predictions of H<sub>2</sub>O and CO<sub>2</sub> co-electrolysis outlet compositions in operation*. **International Journal of Hydrogen Energy**, 40(8), 3134.
- [Armstrong 1997] Armstrong, R., & Horrocks, B. R. (1997). *The double layer structure at the metal-solid electrolyte interface*. **Solid State Ionics**, 94, 181.
- [Arsalis 2019] Arsalis, A. (2019). *A comprehensive review of fuel cell-based micro-combined-heat-and-power systems*. **Renewable and Sustainable Energy Reviews**, 105, 391.
- [Atangulov 1993] Atangulov, R. U., & Murygin, I. V. (1993). *Gas electrode impedance with slow adsorption and surface diffusion*. **Solid State Ionics**, 67(1–2), 9.
- [Atkins 2006] Atkins, P., & de Paula, J. (2006). **PHYSICAL CHEMISTRY** (8th ed.). W.H. Freeman and Company.
- [Badwal 2001] Badwal, S. P. S. (2001). *Stability of solid oxide fuel cell components*. **Solid State Ionics**, 143(1), 39.
- [Banerjee 2017] Banerjee, A., & Deutschmann, O. (2017). *Elementary kinetics of the oxygen reduction reaction on LSM-YSZ composite cathodes*. **Journal of Catalysis**, 346, 30.
- [Baqué 2017] Baqué, L. C., Soldati, A. L., Teixeira-Neto, E., Troiani, H. E., Schreiber, A., & Serquis, A. C. (2017). *Degradation of oxygen reduction reaction kinetics in porous La<sub>0.6</sub>Sr<sub>0.4</sub>Co<sub>0.2</sub>Fe<sub>0.8</sub>O<sub>3-δ</sub> cathodes due to aging-induced changes in surface chemistry.pdf*. **Journal of Power Sources**, 337, 166.
- [Bard 2001] Bard, A. J., & Faulkner, L. R. (2001). **ELECTROCHEMICAL METHODS Fundamentals and Applications** (2nd ed.). John Wiley & Sons.

- [Basu 2012] Basu, S., Varma, S., Shirsat, A. N., Wani, B. N., Bharadwaj, S. R., Chakrabarti, A., Jha, S. N., & Bhattacharyya, D. (2012). *X-ray absorption spectroscopy of doped ZrO<sub>2</sub> systems*. **Journal of Applied Physics**, 111(5).
- [Baumann 2007] Baumann, F. S., Fleig, J., Cristiani, G., Stuhlhofer, B., Habermeier, H.-U., & Maier, J. (2007). *Quantitative Comparison of Mixed Conducting SOFC Cathode Materials by Means of Thin Film Model Electrodes*. **Journal of The Electrochemical Society**, 154(9), B931.
- [Baumann 2006] Baumann, F. S., Fleig, J., Habermeier, H. U., & Maier, J. (2006). *Impedance spectroscopic study on well-defined (La,Sr)(Co,Fe)O<sub>3-δ</sub> model electrodes*. **Solid State Ionics**, 177(11–12), 1071.
- [Bekale 2008] Bekale, V. M., Huntz, A. M., Legros, C., Sattonnay, G., & Jomard, F. (2008). *Impurity diffusion of cerium and gadolinium in single- and polycrystalline yttria-stabilized zirconia*. **Philosophical Magazine**, 88(1), 1.
- [Bernadet 2015] Bernadet, L., Gousseau, G., Chatroux, A., Laurencin, J., Mauvy, F., & Reyrier, M. (2015). *Influence of pressure on solid oxide electrolysis cells investigated by experimental and modeling approach*. **International Journal of Hydrogen Energy**, 40(38), 12918.
- [Bernadet 2017] Bernadet, L., Laurencin, J., Roux, G., Montinaro, D., Mauvy, F., & Reyrier, M. (2017). *Effects of Pressure on High Temperature Steam and Carbon Dioxide Co-electrolysis*. **Electrochimica Acta**, 253, 114.
- [Bertei 2017] Bertei, A., Carpanese, M. P., Clematis, D., Barbucci, A., Bazant, M. Z., & Nicolella, C. (2017). *Understanding the electrochemical behaviour of LSM-based SOFC cathodes. Part II - Mechanistic modelling and physically-based interpretation*. **Solid State Ionics**, 303, 181.
- [Bertei 2013] Bertei, A., Nucci, B., & Nicolella, C. (2013). *Microstructural modeling for prediction of transport properties and electrochemical performance in SOFC composite electrodes*. **Chemical Engineering Science**, 101, 175.
- [Bessler 2010] Bessler, W. G., Vogler, M., Störmer, H., Gerthsen, D., Utz, A., Weber, A., & Ivers-Tiffée, E. (2010). *Model anodes and anode models for understanding the mechanism of hydrogen oxidation in solid oxide fuel cells*. **Physical Chemistry Chemical Physics**, 12(42), 13888.
- [Bessler 2007] Bessler, W. G., Warnatz, J., & Goodwin, D. G. (2007). *The influence of equilibrium potential on the hydrogen oxidation kinetics of SOFC anodes*. **Solid State Ionics**, 177(39–40), 3371.
- [Bieberle 2000] Bieberle, A., & Gauckler, L. J. (2000). *Reaction mechanism of Ni pattern anodes for solid oxide fuel cells*. **Solid State Ionics**, 135(1–4), 337.
- [Bieberle 2002] Bieberle, A., & Gauckler, L. J. (2002). *State-space modeling of the anodic SOFC*

- system Ni, H2-H2O|YSZ. Solid State Ionics*, 146(1–2), 23.
- [Bieberle 2001] Bieberle, A., Meier, L. P., & Gauckler, L. J. (2001). *The Electrochemistry of Ni Pattern Anodes Used as Solid Oxide Fuel Cell Model Electrodes. Journal of The Electrochemical Society*, 148(6), A646.
- [Bishop 2009] Bishop, S. R., Duncan, K. L., & Wachsman, E. D. (2009). *Surface and Bulk Defect Equilibria in Strontium-Doped Lanthanum Cobalt Iron Oxide. Journal of The Electrochemical Society*, 156(10), B1242.
- [Blennow 2011] Blennow, P., Hjelm, J., Klemensø, T., Ramousse, S., Kromp, A., Leonide, A., & Weber, A. (2011). *Manufacturing and characterization of metal-supported solid oxide fuel cells. Journal of Power Sources*, 196(17), 7117.
- [Bleuet 2013] Bleuet, P., Audoit, G., Barnes, J. P., Bertheau, J., Dabin, Y., Dansas, H., Fabbri, J. M., Florin, B., Gergaud, P., Grenier, A., Haberfehlner, G., Lay, E., Laurencin, J., Serra, R., & Villanova, J. (2013). *Specifications for hard condensed matter specimens for three-dimensional high-resolution tomographies. Microscopy and Microanalysis*, 19(3), 726.
- [Blum 2016] Blum, L., de Haart, L. G. J., Malzbender, J., Margaritis, N., & Menzler, N. H. (2016). *Anode-Supported Solid Oxide Fuel Cell Achieves 70 000 Hours of Continuous Operation. Energy Technology*, 4(8), 939.
- [Blum 2020] Blum, L., Fang, Q., Groß-Barsnick, S. M., de Haart, L. G. J. (Bert., Malzbender, J., Menzler, N. H., & Quadackers, W. J. (2020). *Long-term operation of solid oxide fuel cells and preliminary findings on accelerated testing. International Journal of Hydrogen Energy*, 45(15), 8955.
- [Blum 2005] Blum, L., Meulenbergh, W. A., Nabielek, H., & Steinberger-Wilckens, R. (2005). *Worldwide SOFC technology overview and benchmark. International Journal of Applied Ceramic Technology*, 2(6), 482.
- [Boukamp 2006] Boukamp, B. A., Verbraeken, M., Blank, D. H. A., & Holtappels, P. (2006). *SOFC-anodes, proof for a finite-length type Gerischer impedance? Solid State Ionics*, 177, 2539.
- [Bouwmeester 2004] Bouwmeester, H. J. M., Den Otter, M. W., & Boukamp, B. A. (2004). *Oxygen transport in  $La_{0.6}Sr_{0.4}Co_{1-y}Fe_yO_{3-\delta}$ . Journal of Solid State Electrochemistry*, 8, 599.
- [Brandon 2017] Brandon, N. P., Ruiz-Trejo, E., & Boldrin, P. (2017). *Solid Oxide Fuel Cell Lifetime and Reliability* (1st ed.). Academic Press.
- [Bredikhin 2018] Bredikhin, S. I., Agarkov, D. A., Aronin, A. S., Burmistrov, I. N., Matveev, D. V., & Kharton, V. V. (2018). *Ion transfer in Ni-containing composite anodes of solid oxide fuel cells: A microstructural study. Materials Letters*, 216, 193.
- [Brisse 2008] Brisse, A., Schefold, J., & Zahid, M. (2008). *High temperature water electrolysis in*

- solid oxide cells*. **International Journal of Hydrogen Energy**, 33(20), 5375.
- [Burvall 2011] Burvall, A., Lundström, U., Takman, P. A. C., Larsson, D. H., & Hertz, H. M. (2011). *Phase retrieval in X-ray phase-contrast imaging suitable for tomography*. **Optics Express**, 19(11), 10359.
- [Butz 2012] Butz, B., Lefarth, A., Störmer, H., Utz, A., Ivers-Tiffée, E., & Gerthsen, D. (2012). *Accelerated degradation of 8.5 mol% Y2O3-doped zirconia by dissolved Ni*. **Solid State Ionics**, 214, 37.
- [Butz 2009] Butz, B., Schneider, R., Gerthsen, D., Schowalter, M., & Rosenauer, A. (2009). *Decomposition of 8.5 mol.% Y2O3-doped zirconia and its contribution to the degradation of ionic conductivity*. **Acta Materialia**, 57(18), 5480.
- [Cadi-Essadek 2016] Cadi-Essadek, A., Roldan, A., & de Leeuw, N. H. (2016). *Density functional theory study of the interaction of H2O, CO2 and CO with the ZrO2 (111), Ni/ZrO2 (111), YSZ (111) and Ni/YSZ (111) surfaces*. **Surface Science**, 653, 153.
- [Caliandro 2019] Caliandro, P., Nakajo, A., Diethelm, S., & Van herle, J. (2019). *Model-assisted identification of solid oxide cell elementary processes by electrochemical impedance spectroscopy measurements*. **Journal of Power Sources**, 436, 226838.
- [Chaopradith 2015] Chaopradith, D. T., Scanlon, D. O., & Catlow, C. R. A. (2015). *Adsorption of Water on Ytria-Stabilized Zirconia*. **The Journal of Physical Chemistry C**, 119(39), 22526.
- [Chase 1998] Chase, M. W. (1998). NIST-JANAF Thermochemical Tables (4th ed.).
- [Chen 2012] Chen, G., Guan, G., Kasai, Y., & Abudula, A. (2012). *Nickel volatilization phenomenon on the Ni-CGO anode in a cathode-supported SOFC operated at low concentrations of H2*. **International Journal of Hydrogen Energy**, 37(1), 477.
- [Chen 2011] Chen, K., & Jiang, S. P. (2011). *Failure mechanism of (La,Sr)MnO3 oxygen electrodes of solid oxide electrolysis cells*. **International Journal of Hydrogen Energy**, 36(17), 10541.
- [Chen 2016] Chen, K., & Jiang, S. P. (2016). *Review—Materials Degradation of Solid Oxide Electrolysis Cells*. **Journal of The Electrochemical Society**, 163(11), F3070.
- [Chen 2013] Chen, M., Liu, Y.-L., Bentzen, J. J., Zhang, W., Sun, X., Hauch, A., Tao, Y., Bowen, J. R., & Vang Hendriksen, P. (2013). *Microstructural Degradation of Ni/YSZ Electrodes in Solid Oxide Electrolysis Cells under High Current*. **Journal of the Electrochemical Society**, 160(8), 883.
- [Chen 2010] Chen, X., Zhen, Y., Li, J., & Jiang, S. P. (2010). *Chromium deposition and poisoning in dry and humidified air at (La0.8Sr0.2)0.9MnO3+δ cathodes of solid oxide fuel cells*. **International Journal of Hydrogen Energy**, 35(6), 2477.
- [Christensen 2001] Christensen, A., & Carter, E. A. (2001). *Adhesion of ultrathin ZrO2(111) films*

- on Ni(111) from first principles. **Journal of Chemical Physics**, 114(13), 5816.
- [Cloetens 1999] Cloetens, P., Ludwig, W., Baruchel, J., Van Dyck, D., Van Landuyt, J., Guigay, J. P., & Schlenker, M. (1999). *Holotomography: Quantitative phase tomography with micrometer resolution using hard synchrotron radiation x rays*. **Applied Physics Letters**, 75(19), 2912.
- [Connor 2018] Connor, P. A., Yue, X., Savaniu, C. D., Price, R., Triantafyllou, G., Cassidy, M., Kerherve, G., Payne, D. J., Maher, R. C., Cohen, L. F., Tomov, R. I., Glowacki, B. A., Kumar, R. V., & Irvine, J. T. S. (2018). *Tailoring SOFC Electrode Microstructures for Improved Performance*. **Advanced Energy Materials**, 8(23), 1.
- [Costamagna 1998] Costamagna, P., Costa, P., & Antonucci, V. (1998). *Micro-modelling of solid oxide fuel cell electrodes*. **Electrochimica Acta**, 43(3–4), 375.
- [Cucinotta 2011] Cucinotta, C. S., Bernasconi, M., & Parrinello, M. (2011). *Hydrogen oxidation reaction at the Ni/YSZ anode of solid oxide fuel cells from first principles*. **Physical Review Letters**, 107(20), 1.
- [Dasari 2013] Dasari, H. P., Park, S.-Y., Kim, J., Lee, J.-H., Kim, B.-K., Je, H.-J., Lee, H.-W., & Yoon, K. J. (2013). *Electrochemical characterization of Ni–yttria stabilized zirconia electrode for hydrogen production in solid oxide electrolysis cells*. **Journal of Power Sources**, 240, 721.
- [De Angelis 2018] De Angelis, S., Jørgensen, P. S., Tsai, E. H. R., Holler, M., Kreka, K., & Bowen, J. R. (2018). *Three dimensional characterization of nickel coarsening in solid oxide cells via ex-situ ptychographic nano-tomography*. **Journal of Power Sources**, 383, 72.
- [De Boer 1998] De Boer, B. (1998). *SOFC anode: hydrogen oxidation at porous nickel and nickel/zirconia electrodes*. **PhD Thesis**. <http://purl.utwente.nl/publications/9195>
- [De Nolf 2014] De Nolf, W., Vanmeert, F., & Janssens, K. (2014). *XRDUA: Crystalline phase distribution maps by two-dimensional scanning and tomographic (micro) X-ray powder diffraction*. **Journal of Applied Crystallography**, 47(3), 1107.
- [Deseure 2005] Deseure, J., Bultel, Y., Dessemond, L., & Siebert, E. (2005). *Modelling of dc and ac responses of a planar mixed conducting oxygen electrode*. **Solid State Ionics**, 176(3–4), 235.
- [Diard 2017] Diard, J. P., Le Gorrec, B., & Montella, C. (2017). *Handbook of Electrochemical Impedance Spectroscopy*. [www.bio-logic.net](http://www.bio-logic.net). <http://www.bio-logic.net/en/applications/eis>
- [Dinnebier 2008] Dinnebier, R. E., & Billinge, S. J. L. (2008). *Powder Diffraction: Theory and Practice*. RSC Publishing.
- [DOE 2020] U.S. Department of Energy. *Technical targets of fuel cell systems for stationary combined heat and power*. <https://www.energy.gov/eere/fuelcells/doe-technical-targets-fuel-cell-systems-stationary-combined-heat-and-power>
- [Dogdibegovic 2019a] Dogdibegovic, E., Wang, R., Lau, G. Y., Karimaghloo, A., Lee, M. H., &

- Tucker, M. C. (2019a). *Progress in durability of metal-supported solid oxide fuel cells with infiltrated electrodes*. **Journal of Power Sources**, 437, 226935.
- [Dogdibegovic 2019b] Dogdibegovic, E., Wang, R., Lau, G. Y., & Tucker, M. C. (2019b). *High performance metal-supported solid oxide fuel cells with infiltrated electrodes*. **Journal of Power Sources**, 410–411, 91.
- [Doppler 2018] Doppler, M. C., Fleig, J., Bram, M., & Opitz, A. K. (2018). *Hydrogen oxidation mechanisms on Ni/yttria stabilized zirconia anodes: Separation of reaction pathways by geometry variation of pattern electrodes*. **Journal of Power Sources**, 380, 46.
- [Dusastre 1999] Dusastre, V., & Kilner, J. A. (1999). *Optimisation of composite cathodes for intermediate temperature SOFC applications*. **Solid State Ionics**, 126(1), 163.
- [Ebbesen 2010] Ebbesen, S. D., & Mogensen, M. (2010). *Exceptional Durability of Solid Oxide Cells*. **Electrochemical and Solid-State Letters**, 13(9), B106.
- [Effori 2019] Effori, E., Moussaoui, H., Monaco, F., Sharma, R. K., Debayle, J., Gavet, Y., Delette, G., Si Larbi, G., Siebert, E., Vulliet, J., Dessemond, L., & Laurencin, J. (2019). *Reaction Mechanism and Impact of Microstructure on Performances for the LSCF-CGO Composite Electrode in Solid Oxide Cells*. **Fuel Cells**, 19(4), 429.
- [Endler 2010] Endler, C., Leonide, A., Weber, A., Tietz, F., & Ivers-Tiffée, E. (2010). *Time-Dependent Electrode Performance Changes in Intermediate Temperature Solid Oxide Fuel Cells*. **Journal of The Electrochemical Society**, 157(2), B292.
- [EU 2018] European Commission Report. *A Clean Planet for all: A European strategic long-term vision for a prosperous, modern, competitive and climate neutral economy*. [https://ec.europa.eu/clima/policies/strategies/2050\\_en](https://ec.europa.eu/clima/policies/strategies/2050_en)
- [Faes 2009] Faes, A., Hessler-Wyser, A., Presvytes, D., Vayenas, C. G., & Vanherle, J. (2009). *Nickel-zirconia anode degradation and triple phase boundary quantification from microstructural analysis*. **Fuel Cells**, 9(6), 841.
- [Fang 2015] Fang, Q., Blum, L., & Menzler, N. H. (2015). *Performance and Degradation of Solid Oxide Electrolysis Cells in Stack*. **Journal of The Electrochemical Society**, 162(8), F907.
- [Fang 2019] Fang, Q., Blum, L., & Stolten, D. (2019). *Electrochemical Performance and Degradation Analysis of an SOFC Short Stack Following Operation of More than 100,000 Hours*. **Journal of the Electrochemical Society**, 166(16), 1320.
- [Fang 2018] Fang, Q., Frey, C. E., Menzler, N. H., & Blum, L. (2018). *Electrochemical Performance and Preliminary Post-Mortem Analysis of a Solid Oxide Cell Stack with 20,000 h of Operation*. **Journal of The Electrochemical Society**, 165(2), F38.
- [FCU JH 2018] FUEL CELLS and HYDROGEN 2 JOINT UNDERTAKING. *Fuel Cells and*

*Hydrogen 2 Joint Undertaking - Addendum to the Multi-Annual Work Plan 2014-2020.*

- [Ferreira-Sanchez 2017] Ferreira-Sanchez, D., Grolimund, D., Hubert, M., Bleuet, P., & Laurencin, J. (2017). *A 2D and 3D X-ray  $\mu$ -diffraction and  $\mu$ -fluorescence study of a mixed ionic electronic conductor*. **International Journal of Hydrogen Energy**, 42(2), 1203.
- [Finsterbusch 2012] Finsterbusch, M., Lussier, A., Schaefer, J. A., & Idzerda, Y. U. (2012). *Electrochemically driven cation segregation in the mixed conductor  $\text{La}_{0.6}\text{Sr}_{0.4}\text{Co}_{0.2}\text{Fe}_{0.8}\text{O}_{3-\delta}$* . **Solid State Ionics**, 212, 77.
- [Fleig 2007] Fleig, J., Merkle, R., & Maier, J. (2007). *The  $p(\text{O}_2)$  dependence of oxygen surface coverage and exchange current density of mixed conducting oxide electrodes: model considerations*. **Physical Chemistry Chemical Physics**, 9(21), 2713.
- [Frey 2018] Frey, C. E., Fang, Q., Sebold, D., Blum, L., & Menzler, N. H. (2018). *A Detailed Post Mortem Analysis of Solid Oxide Electrolyzer Cells after Long-Term Stack Operation*. **Journal of The Electrochemical Society**, 165(5), F357.
- [Fu 2014] Fu, Z., Wang, M., Zuo, P., Yang, Z., & Wu, R. (2014). *Importance of oxygen spillover for fuel oxidation on Ni/YSZ anodes in solid oxide fuel cells*. **Physical Chemistry Chemical Physics**, 16, 8536.
- [Geary 2016] Geary, T. C., Lee, D., Shao-Horn, Y., & Adler, S. B. (2016). *Nonlinear Impedance Analysis of  $\text{La}_{0.4}\text{Sr}_{0.6}\text{Co}_{0.2}\text{Fe}_{0.8}\text{O}_{3-\delta}$  Thin Film Oxygen Electrodes*. **Journal of The Electrochemical Society**, 163(9), F1107.
- [Gewies 2008] Gewies, S., & Bessler, W. G. (2008). *Physically Based Impedance Modeling of Ni/YSZ Cermet Anodes*. **Journal of The Electrochemical Society**, 155(9), B937.
- [Ghatee 2009] Ghatee, M., Shariat, M. H., & Irvine, J. T. S. (2009). *Investigation of electrical and mechanical properties of 3YSZ/8YSZ composite electrolytes*. **Solid State Ionics**, 180(1), 57.
- [Godula-Jopek 2015] Godula-Jopek, A., Millet, P., Guillet, N., Laurencin, J., Mougín, J., Bourasseau, C., & Guinot, B. (2015). *Hydrogen Production by Electrolysis* (A. Godula-Jopek (ed.)). Wiley-VCH.
- [Gómez 2016] Gómez, S. Y., & Hotza, D. (2016). *Current developments in reversible solid oxide fuel cells*. **Renewable and Sustainable Energy Reviews**, 61, 155.
- [Gong 2012] Gong, M., Gemmen, R. S., & Liu, X. (2012). *Modeling of oxygen reduction mechanism for 3PB and 2PB pathways at solid oxide fuel cell cathode from multi-step charge transfer*. **Journal of Power Sources**, 201, 204.
- [Goodwin 2009] Goodwin, D. G., Zhu, H., Colclasure, A. M., & Kee, R. J. (2009). *Modeling Electrochemical Oxidation of Hydrogen on Ni-YSZ Pattern Anodes*. **Journal of The Electrochemical Society**, 156(9), B1004.

- [Gorski 2011] Gorski, A., Yurkiv, V., Starukhin, D., & Volpp, H. R. (2011). *H<sub>2</sub>O chemisorption and H<sub>2</sub> oxidation on yttria-stabilized zirconia: Density functional theory and temperature-programmed desorption studies*. **Journal of Power Sources**, 196(17), 7188.
- [Graves 2011] Graves, C., Ebbesen, S. D., Mogensen, M., & Lackner, K. S. (2011). *Sustainable hydrocarbon fuels by recycling CO<sub>2</sub> and H<sub>2</sub>O with renewable or nuclear energy*. **Renewable and Sustainable Energy Reviews**, 15(1), 1.
- [Grondin 2011] Grondin, D., Deseure, J., Ozil, P., Chabriat, J. P., Grondin-Perez, B., & Brisse, A. (2011). *Computing approach of cathodic process within solid oxide electrolysis cell: Experiments and continuum model validation*. **Journal of Power Sources**, 196(22), 9561.
- [Groß-Barsnick 2019] Groß-Barsnick, S. M., Fang, Q., Batfalsky, P., Niewolak, L., Blum, L., & Quadackers, W. J. (2019). *Post-test Characterization of Metallic Materials and Adjacent Components in an SOFC Stack After 34,000 h Operation at 700 °C*. **Fuel Cells**, 19(1), 84.
- [Grunbaum 2006] Grunbaum, N., Dessemond, L., Fouletier, J., Prado, F., & Caneiro, A. (2006). *Electrode reaction of Sr<sub>1-x</sub>La<sub>x</sub>Co<sub>0.8</sub>Fe<sub>0.2</sub>O<sub>3-δ</sub> with x = 0.1 and 0.6 on Ce<sub>0.9</sub>Gd<sub>0.1</sub>O<sub>1.95</sub> at 600 ≤ T ≤ 800 °C*. **Solid State Ionics**, 177(9–10), 907.
- [Grunbaum 2009] Grunbaum, N., Dessemond, L., Fouletier, J., Prado, F., Mogni, L., & Caneiro, A. (2009). *Rate limiting steps of the porous La<sub>0.6</sub>Sr<sub>0.4</sub>Co<sub>0.8</sub>Fe<sub>0.2</sub>O<sub>3-δ</sub> electrode material*. **Solid State Ionics**, 180(28–31), 1448.
- [Hagen 2006] Hagen, A., Barfod, R., Hendriksen, P. V., Liu, Y.-L., & Ramousse, S. (2006). *Degradation of Anode Supported SOFCs as a Function of Temperature and Current Load*. **Journal of The Electrochemical Society**, 153(6), A1165.
- [Hanna 2014] Hanna, J., Lee, W. Y., Shi, Y., & Ghoniem, A. F. (2014). *Fundamentals of electro- and thermochemistry in the anode of solid-oxide fuel cells with hydrocarbon and syngas fuels*. **Progress in Energy and Combustion Science**, 40(1), 74.
- [Hardy 2012] Hardy, J. S., Templeton, J. W., Edwards, D. J., Lu, Z., & Stevenson, J. W. (2012). *Lattice expansion of LSCF-6428 cathodes measured by in situ XRD during SOFC operation*. **Journal of Power Sources**, 198, 76.
- [Hartley 2000] Hartley, A., Sahibzada, M., Weston, M., Metcalfe, I. S., & Mantzavinos, D. (2000). *La<sub>0.6</sub>Sr<sub>0.4</sub>Co<sub>0.2</sub>Fe<sub>0.8</sub>O<sub>3</sub> as the anode and cathode for intermediate temperature solid oxide fuel cells*. **Catalysis Today**, 55(1–2), 197.
- [Hauch 2016] Hauch, A., Brodersen, K., Chen, M., & Mogensen, M. B. (2016). *Ni/YSZ electrodes structures optimized for increased electrolysis performance and durability*. **Solid State Ionics**, 293, 27.
- [Hauch 2008] Hauch, A., Ebbesen, S. D., Jensen, S. H., & Mogensen, M. (2008). *Solid Oxide*

- Electrolysis Cells: Microstructure and Degradation of the Ni/Yttria-Stabilized Zirconia Electrode. Journal of The Electrochemical Society*, 155(11), B1184.
- [Hauch 2006] Hauch, A., Jensen, S. H., Ramousse, S., & Mogensen, M. (2006). *Performance and Durability of Solid Oxide Electrolysis Cells. Journal of The Electrochemical Society*, 153(9), A1741.
- [Hauch 2011a] Hauch, A., Jørgensen, P. S., Brodersen, K., & Mogensen, M. (2011). *Ni/YSZ anode - Effect of pre-treatments on cell degradation and microstructures. Journal of Power Sources*, 196(21), 8931.
- [Hauch 2011b] Hauch, A., Mogensen, M., & Hagen, A. (2011). *Ni/YSZ electrode degradation studied by impedance spectroscopy - Effect of p(H<sub>2</sub>O). Solid State Ionics*, 192(1), 547.
- [Hendriks 2002a] Hendriks, M. G. H. M., Ten Elshof, J. E., Bouwmeester, H. J. M., & Verweij, H. (2002). *The defect structure of the double layer in yttria-stabilised zirconia. Solid State Ionics*, 154–155, 467.
- [Hendriks 2002b] Hendriks, M. G. H. M., Ten Elshof, J. E., Bouwmeester, H. J. M., & Verweij, H. (2002). *The electrochemical double-layer capacitance of yttria-stabilised zirconia. Solid State Ionics*, 146(3–4), 211.
- [Hino 2004] Hino, R., Haga, K., Aita, H., & Sekita, K. (2004). 38. *R&D on hydrogen production by high-temperature electrolysis of steam. Nuclear Engineering and Design*, 233(1–3), 363.
- [Hoerlein 2018] Hoerlein, M. P., Riegraf, M., Costa, R., Schiller, G., & Friedrich, K. A. (2018). *A parameter study of solid oxide electrolysis cell degradation: Microstructural changes of the fuel electrode. Electrochimica Acta*, 276, 162.
- [Holtappels 1999a] Holtappels, P., de Haart, L. G. J., & Stimming, U. (1999). *Reaction of Hydrogen/Water Mixtures on Nickel-Zirconia Cermet Electrodes: II. AC Polarization Characteristics. Journal of The Electrochemical Society*, 146(8), 2976.
- [Holtappels 1999b] Holtappels, P., de Haart, L. G. J., & Stimming, U. (1999). *Reaction of hydrogen water mixtures on nickel-zirconia cermet electrodes I. DC polarization characteristics. Journal of the Electrochemical Society*, 146(5), 1620.
- [Holzer 2011] Holzer, L., Iwanschitz, B., Hocker, T., Münch, B., Prestat, M., Wiedenmann, D., Vogt, U., Holtappels, P., Sfeir, J., Mai, A., & Graule, T. (2011). *Microstructure degradation of cermet anodes for solid oxide fuel cells: Quantification of nickel grain growth in dry and in humid atmospheres. Journal of Power Sources*, 196(3), 1279.
- [Holzer 2013] Holzer, L., Wiedenmann, D., Münch, B., Keller, L., Prestat, M., Gasser, P., Robertson, I., & Grobóty, B. (2013). *The influence of constrictivity on the effective transport properties of porous layers in electrolysis and fuel cells. Journal of Materials Science*, 48(7), 2934.

- [Huang 2007] Huang, Q. A., Hui, R., Wang, B., & Zhang, J. (2007). *A review of AC impedance modeling and validation in SOFC diagnosis*. **Electrochimica Acta**, 52(28), 8144.
- [Hubert 2018] Hubert, M. (2018). *Durability of Solid Oxide Cells: an experimental and modelling investigation based on synchrotron X-ray nano-tomography characterization*. **PhD Thesis**.
- [Hubert 2016] Hubert, M., Laurencin, J., Cloetens, P., da Silva, J. C., Lefebvre-Joud, F., Bleuet, P., Nakajo, A., & Siebert, E. (2016). *Role of microstructure on electrode operating mechanisms for mixed ionic electronic conductors: From synchrotron-based 3D reconstruction to electrochemical modeling*. **Solid State Ionics**, 294, 90.
- [Hubert 2018a] Hubert, M., Laurencin, J., Cloetens, P., Morel, B., Montinaro, D., & Lefebvre-Joud, F. (2018). *Impact of Nickel agglomeration on Solid Oxide Cell operated in fuel cell and electrolysis modes*. **Journal of Power Sources**, 397, 240.
- [Hubert 2017] Hubert, M., Laurencin, J., Cloetens, P., Mougin, J., Ferreira Sanchez, D., Pylypko, S., Morales, M., Morata, A., Morel, B., Montinaro, D., Siebert, E., & Lefebvre-Joud, F. (2017). *Solid Oxide Cell Degradation Operated in Fuel Cell and Electrolysis Modes: A Comparative Study on Ni Agglomeration and LSCF Destabilization*. **ECS Transactions**, 78(1), 3167.
- [Hubert 2018b] Hubert, M., Pacureanu, A., Guilloud, C., Yang, Y., Da Silva, J. C., Laurencin, J., Lefebvre-Joud, F., & Cloetens, P. (2018). *Efficient correction of wavefront inhomogeneities in X-ray holographic nanotomography by random sample displacement*. **Applied Physics Letters**, 112(20), 203704.
- [IEA 2019] International Energy Agency. *Electricity Statistics*. <https://www.iea.org/subscribe-to-data-services/electricity-statistics>
- [IEO 2019] U.S. Energy Information Administration. *International Energy Outlook*. <https://www.eia.gov/outlooks/ieo/>
- [Ingel 1986] Ingel, R. P., & Lewis, D. I. (1986). *Lattice Parameters and Density for Y<sub>2</sub>O<sub>3</sub>-Stabilized ZrO<sub>2</sub>*. **Journal of the American Ceramic Society**, 69(4), 325.
- [IPCC 2018] International Panel on Climate Change. *Global Warming of 1.5°C*. <https://www.ipcc.ch/sr15/>
- [Irshad 2016] Irshad, M., Siraj, K., Raza, R., Ali, A., Tiwari, P., Zhu, B., Rafique, A., Ali, A., Ullah, M. K., & Usman, A. (2016). *A brief description of high temperature solid oxide fuel cell's operation, materials, design, fabrication technologies and performance*. **Applied Sciences**, 6(3).
- [Irvine 2013] Irvine, J. T. S., & Connor, P. (2013). *Solid Oxide Fuels Cells: Facts and Figures*. In *Green Energy and Technology* (1st ed.). Springer.
- [Irvine 2016] Irvine, J. T. S., Neagu, D., Verbraeken, M. C., Chatzichristodoulou, C., Graves, C., &

- Mogensen, M. B. (2016). *Evolution of the electrochemical interface in high-temperature fuel cells and electrolyzers*. **Nature Energy**, 1, 1.
- [Jais 2017] Jais, A. A., Ali, S. A. M., Anwar, M., Rao Somalu, M., Muchtar, A., Wan Isahak, W. N. R., Yong Tan, C., Singh, R., & Brandon, N. P. (2017). *Enhanced ionic conductivity of scandia-ceria-stabilized-zirconia (10Sc1CeSZ) electrolyte synthesized by the microwave-assisted glycine nitrate process*. **Ceramics International**, 43(11), 8119.
- [Jamnik 1999] Jamnik, J. (1999). *Treatment of the Impedance of Mixed Conductors - Equivalent Circuit Model and Explicit Approximate Solutions*. **Journal of The Electrochemical Society**, 146(11), 4183.
- [Jiang 2003] Jiang, S. P. (2003). *Sintering behavior of Ni/Y2O3-ZrO2cermet electrodes of solid oxide fuel cells*. **Journal of Materials Science**, 38(18), 3775.
- [Jiang 2008] Jiang, S. P. (2008). *Development of lanthanum strontium manganite perovskite cathode materials of solid oxide fuel cells: A review*. **Journal of Materials Science**, 43, 6799.
- [Jiang 2017] Jiang, S. P. (2017). *Placement of Reference Electrode, Electrolyte Thickness and Three-Electrode Cell Configuration in Solid Oxide Fuel Cells: A Brief Review and Update on Experimental Approach*. **Journal of The Electrochemical Society**, 164(7), F834.
- [Jiang 2004] Jiang, S. P., & Chan, S. H. (2004). *A review of anode materials development in solid oxide fuel cells*. **Journal of Materials Science**, 39, 4405.
- [Jiang 2014] Jiang, S. P., & Chen, X. (2014). *Chromium deposition and poisoning of cathodes of solid oxide fuel cells - A review*. **International Journal of Hydrogen Energy**, 39(1), 505.
- [Jiao 2011] Jiao, Z., Takagi, N., Shikazono, N., & Kasagi, N. (2011). *Study on local morphological changes of nickel in solid oxide fuel cell anode using porous Ni pellet electrode*. **Journal of Power Sources**, 196(3), 1019.
- [Kanit 2003] Kanit, T., Forest, S., Galliet, I., Mounoury, V., & Jeulin, D. (2003). *Determination of the size of the representative volume element for random composites: Statistical and numerical approach*. **International Journal of Solids and Structures**, 40(13–14), 3647.
- [Kanno 2011] Kanno, D., Shikazono, N., Takagi, N., Matsuzaki, K., & Kasagi, N. (2011). *Evaluation of SOFC anode polarization simulation using three-dimensional microstructures reconstructed by FIB tomography*. **Electrochimica Acta**, 56(11), 4015.
- [Katamura 1995] Katamura, J., Seki, T., & Samuka, T. (1995). *The Cubic-Tetragonal Phase Equilibria in the ZrO2-R2O3 (R = Y, Gd, Sm, Nd) Systems*. **Journal of Phase Equilibria**, 16(4), 315.
- [Kawata 2006] Kawata, K., Maekawa, H., Nemoto, T., & Yamamura, T. (2006). *Local structure analysis of YSZ by Y-89 MAS-NMR*. **Solid State Ionics**, 177(19-25 SPEC. ISS.), 1687.

- [Kee 2003] Kee, R. J., Coltrin, M. E., & Glarborg, P. (2003). *Chemically Reacting Flow: Theory and Practice*. John Wiley & Sons.
- [Kek 2001] Kek, D., Mogensen, M., & Pejovnik, S. (2001). *A Study of Metal (Ni, Pt, Au)/Yttria-Stabilized Zirconia Interface in Hydrogen Atmosphere at Elevated Temperature*. **Journal of The Electrochemical Society**, 148(8), A878.
- [Kendall 2016] Kendall, K., & Kendall, M. (2016). *High-Temperature Solid Oxide Fuel Cells for the 21st Century - Fundamentals, Design and Applications*. Elsevier Ltd.
- [Kennouche 2016a] Kennouche, D., Chen-Wiegart, Y. C. K., Riscoe, C., Wang, J., & Barnett, S. A. (2016). *Combined electrochemical and X-ray tomography study of the high temperature evolution of Nickel - Yttria Stabilized Zirconia solid oxide fuel cell anodes*. **Journal of Power Sources**, 307, 604.
- [Kennouche 2016b] Kennouche, D., Chen-Wiegart, Y. C. K., Yakal-Kremiski, K. J., Wang, J., Gibbs, J. W., Voorhees, P. W., & Barnett, S. A. (2016). *Observing the microstructural evolution of Ni-Yttria-stabilized zirconia solid oxide fuel cell anodes*. **Acta Materialia**, 103, 204.
- [Khamidy 2020] Khamidy, N. I., Laurencin, J., Ferreira-Sanchez, D., Monaco, F., Charlot, F., & Djurado, E. (2020). *Durability of nanostructured  $LaPrNiO_{4+\delta}$  electrode for solid oxide cells: Electrochemical, microstructural, and structural investigation*. **Journal of Power Sources**, 450, 227724.
- [Khan 2016] Khan, M. S., Lee, S. B., Song, R. H., Lee, J. W., Lim, T. H., & Park, S. J. (2016). *Fundamental mechanisms involved in the degradation of nickel–yttria stabilized zirconia (Ni–YSZ) anode during solid oxide fuel cells operation: A review*. **Ceramics International**, 42(1), 35.
- [Khan 2018] Khan, M. Z., Mehran, M. T., Song, R. H., Lee, J. W., Lee, S. B., & Lim, T. H. (2018). *A simplified approach to predict performance degradation of a solid oxide fuel cell anode*. **Journal of Power Sources**, 391, 94.
- [Kharton 2004] Kharton, V. V., Marques, F. M. B., & Atkinson, A. (2004). *Transport properties of solid oxide electrolyte ceramics: A brief review*. **Solid State Ionics**, 174(1–4), 135.
- [Kieffer 2013] Kieffer, J., & Karkoulis, D. (2013). *PyFAI, a versatile library for azimuthal regrouping*. **Journal of Physics: Conference Series**, 425, 202012.
- [Kim 2017] Kim, Y. T., Jiao, Z., & Shikazono, N. (2017). *Evaluation of  $La_{0.6}Sr_{0.4}Co_{0.2}Fe_{0.8}O_{3-Gd_{0.1}Ce_{0.9}O_{1.95}}$  composite cathode with three dimensional microstructure reconstruction*. **Journal of Power Sources**, 342, 787.
- [Kishimoto 2012a] Kishimoto, H., Suzuki, A., Shimonosono, T., Brito, M. E., Yamaji, K., Horita, T., Munakata, F., & Yokokawa, H. (2012). *Agglomeration behavior of nickel particles on YSZ and*

- TiO<sub>2</sub>-doped YSZ electrolytes*. **Journal of Power Sources**, 199, 174.
- [Kishimoto 2012b] Kishimoto, H., Yashiro, K., Shimonosono, T., Brito, M. E., Yamaji, K., Horita, T., Yokokawa, H., & Mizusaki, J. (2012). *In situ analysis on the electrical conductivity degradation of NiO doped yttria stabilized zirconia electrolyte by micro-Raman spectroscopy*. **Electrochimica Acta**, 82, 263.
- [Knibbe 2011] Knibbe, R., Hauch, A., Hjelm, J., Ebbesen, S. D., & Mogensen, M. (2011). *Durability of Solid Oxide Cells*. **Green**, 1, 141.
- [Knibbe 2010a] Knibbe, R., Hjelm, J., Menon, M., Pryds, N., Søgaard, M., Wang, H. J., & Neufeld, K. (2010). *Cathode-electrolyte interfaces with CGO barrier layers in SOFC*. **Journal of the American Ceramic Society**, 93(9), 2877.
- [Knibbe 2010b] Knibbe, R., Traulsen, M. L., Hauch, A., Ebbesen, S. D., & Mogensen, M. (2010). *Solid Oxide Electrolysis Cells: Degradation at High Current Densities*. **Journal of The Electrochemical Society**, 157(8), B1209.
- [Kondoh 1998] Kondoh, J., Kikuchi, S., Tomii, V., & Ito, Y. (1998). *Effect of Aging on Yttria-Stabilized Zirconia - III. A Study of the Effect of Local Structures on Conductivity*. **Journal of Electrochemical Society**, 145(5), 1550.
- [Kostogloudis 2000] Kostogloudis, G. C., Tsiniarakis, G., & Ftikos, C. (2000). *Chemical reactivity of perovskite oxide SOFC cathodes and yttria stabilized zirconia*. **Solid State Ionics**, 135(1–4), 529.
- [Kournoutis 2009] Kournoutis, V. C., Tietz, F., & Bebelis, S. (2009). *AC impedance characterisation of a La<sub>0.8</sub>Sr<sub>0.2</sub>Co<sub>0.2</sub>Fe<sub>0.8</sub>O<sub>3-δ</sub> electrode*. **Fuel Cells**, 9(6), 852.
- [Kournoutis 2011] Kournoutis, V. C., Tietz, F., & Bebelis, S. (2011). *Cyclic voltammetry characterization of a La<sub>0.8</sub>Sr<sub>0.2</sub>Co<sub>0.2</sub>Fe<sub>0.8</sub>O<sub>3-δ</sub> electrode interfaced to CGO/YSZ*. **Solid State Ionics**, 197(1), 13.
- [Kresse 2000] Kresse, G., & Hafner, J. (2000). *First-principles study of the adsorption of atomic H on Ni (111), (100) and (110)*. **Surface Science**, 459(3), 287.
- [Krishna 1997] Krishna, R., & Wesselingh, J. A. (1997). *The Maxwell-Stefan approach to mass transfer*. **Chemical Engineering Science**, 52(6), 861.
- [Kröll 2017] Kröll, L., De Haart, L. G. J., Vinke, I., & Eichel, R. A. (2017). *Degradation Mechanisms in Solid-Oxide Fuel and Electrolyzer Cells: Analytical Description of Nickel Agglomeration in a Ni/YSZ Electrode*. **Physical Review Applied**, 7, 044007.
- [Kwakman 2011] Kwakman, L., Franz, G., Visser Taklo, M. M., Klumpp, A., & Ramm, P. (2011). *Characterization and Failure Analysis of 3D Integrated Systems using a novel plasma-FIB system*. **AIP Conference Proceedings**, 269, 1395.

- [Laguna-Bercero 2012] Laguna-Bercero, M. A. (2012). *Recent advances in high temperature electrolysis using solid oxide fuel cells: A review*. **Journal of Power Sources**, 203, 4.
- [Larminie 2003] Larminie, J., & Dicks, A. L. (2003). *Fuel Cell Systems Explained* (2nd ed.). Wiley and Sons.
- [Laurencin 2015] Laurencin, J., Hubert, M., Couturier, K., Le Bihan, T., Cloetens, P., Lefebvre-Joud, F., & Siebert, E. (2015). *Reactive Mechanisms of LSCF Single-Phase and LSCF-CGO Composite Electrodes Operated in Anodic and Cathodic Polarisation*. **Electrochimica Acta**, 174, 1299.
- [Laurencin 2017] Laurencin, J., Hubert, M., Sanchez, D. F., Pylypko, S., Morales, M., Morata, A., Morel, B., Montinaro, D., Lefebvre-Joud, F., & Siebert, E. (2017). *Degradation mechanism of La<sub>0.6</sub>Sr<sub>0.4</sub>Co<sub>0.2</sub>Fe<sub>0.8</sub>O<sub>3-δ</sub>/Gd<sub>0.1</sub>Ce<sub>0.9</sub>O<sub>2-δ</sub> composite electrode operated under solid oxide electrolysis and fuel cell conditions*. **Electrochimica Acta**, 241, 459.
- [Laurencin 2011] Laurencin, J., Kane, D., Delette, G., Deseure, J., & Lefebvre-Joud, F. (2011). *Modelling of solid oxide steam electrolyser: Impact of the operating conditions on hydrogen production*. **Journal of Power Sources**, 196(4), 2080.
- [Laurencin 2008] Laurencin, J., Lefebvre-Joud, F., & Delette, G. (2008). *Impact of cell design and operating conditions on the performances of SOFC fuelled with methane*. **Journal of Power Sources**, 177(2), 355.
- [Laurencin 2012] Laurencin, J., Quey, R., Delette, G., Suhonen, H., Cloetens, P., & Bleuet, P. (2012). *Characterisation of Solid Oxide Fuel Cell Ni-8YSZ substrate by synchrotron X-ray nanotomography: From 3D reconstruction to microstructure quantification*. **Journal of Power Sources**, 198, 182.
- [Lay-Grindler 2013] Lay-Grindler, E., Laurencin, J., Delette, G., Aicart, J., Petitjean, M., & Dessemond, L. (2013). *Micro modelling of solid oxide electrolysis cell: From performance to durability*. **International Journal of Hydrogen Energy**, 38(17), 6917.
- [Lay-Grindler 2014] Lay-Grindler, E., Laurencin, J., Villanova, J., Cloetens, P., Bleuet, P., Mansuy, A., Mougín, J., & Delette, G. (2014). *Degradation study by 3D reconstruction of a nickel-yttria stabilized zirconia cathode after high temperature steam electrolysis operation*. **Journal of Power Sources**, 269, 927.
- [Lee 2014] Lee, Y. H., Muroyama, H., Matsui, T., & Eguchi, K. (2014). *Degradation of nickel-yttria-stabilized zirconia anode in solid oxide fuel cells under changing temperature and humidity conditions*. **Journal of Power Sources**, 262, 451.
- [Lee 2009] Lee, Y. H., Sheu, H. S., Deng, J. P., & Kao, H. C. I. (2009). *Preparation and fluorite-pyrochlore phase transformation in Gd<sub>2</sub>Zr<sub>2</sub>O<sub>7</sub>*. **Journal of Alloys and Compounds**, 487(1–2),

595.

- [Lehner 2014] Lehner, M., Tichler, R., & Koppe, M. (2014). *Power-to-Gas : Technology and Business Models* (Springer). Springer.
- [Leib 2016] Leib, E. W., Pasquarelli, R. M., Blankenburg, M., Müller, M., Schreyer, A., Janssen, R., Weller, H., & Vossmeier, T. (2016). *High-Temperature Stable Zirconia Particles Doped with Yttrium, Lanthanum, and Gadolinium*. **Particle and Particle Systems Characterization**, 33, 645.
- [Leonide 2008] Leonide, A., Sonn, V., Weber, A., & Ivers-Tiffée, E. (2008). *Evaluation and Modeling of the Cell Resistance in Anode-Supported Solid Oxide Fuel Cells*. **Journal of The Electrochemical Society**, 155(1), B36.
- [Liu 2010a] Liu, B., Muroyama, H., Matsui, T., Tomida, K., Kabata, T., & Eguchi, K. (2010). *Analysis of Impedance Spectra for Segmented-in-Series Tubular Solid Oxide Fuel Cells*. **Journal of The Electrochemical Society**, 157(12), B1858.
- [Liu 2010b] Liu, D.-J., Almer, J., & Cruse, T. (2010). *Characterization of Cr Poisoning in a Solid Oxide Fuel Cell Cathode Using a High Energy X-ray Microbeam*. **Journal of The Electrochemical Society**, 157(5), B744.
- [Liu 1998a] Liu, M. (1998). *Equivalent Circuit Approximation to Porous Mixed-Conducting Oxygen Electrodes in Solid-State Cells*. **Journal of The Electrochemical Society**, 145(1), 142.
- [Liu 1998b] Liu, M. (1998). *Significance of interfaces in solid-state cells with porous electrodes of mixed ionic–electronic conductors*. **Solid State Ionics**, 107(1–2), 105.
- [Liu 1999] Liu, M., & Winnick, J. (1999). *Fundamental issues in modeling of mixed ionic-electronic conductors (MIECs)*. **Solid State Ionics**, 118(1–2), 11.
- [Liu 2008] Liu, S., Song, C., & Lin, Z. (2008). *The effects of the interconnect rib contact resistance on the performance of planar solid oxide fuel cell stack and the rib design optimization*. **Journal of Power Sources**, 183(1), 214.
- [Liu 2014] Liu, Y., Chen, K., Zhao, L., Chi, B., Pu, J., Jiang, S. P., & Jian, L. (2014). *Performance stability and degradation mechanism of  $\text{La}_{0.6}\text{Sr}_{0.4}\text{Co}_{0.2}\text{Fe}_{0.8}\text{O}_{3-\delta}$  cathodes under solid oxide fuel cells operation conditions*. **International Journal of Hydrogen Energy**, 39(28), 15868.
- [Liu 2012] Liu, Y. L., Thydén, K., Chen, M., & Hagen, A. (2012). *Microstructure degradation of LSM-YSZ cathode in SOFCs operated at various conditions*. **Solid State Ionics**, 206, 97.
- [Luo 2017] Luo, Y., Li, W., Shi, Y., Wang, Y., & Cai, N. (2017). *Reversible  $\text{H}_2/\text{H}_2\text{O}$  electrochemical conversion mechanisms on the patterned nickel electrodes*. **International Journal of Hydrogen Energy**, 42(40), 25130.
- [Luo 2019] Luo, Y., Shi, Y., Li, W., & Cai, N. (2019). *Mechanism of rate-limiting step switchover*

- for reversible solid oxide cells in H<sub>2</sub>/H<sub>2</sub>O atmosphere. **Electrochimica Acta**, 326, 135003.
- [Mahmoud 2017] Mahmoud, A., Daroukh, M. Al, Lipinska-Chwalek, M., Luysberg, M., Tietz, F., & Hermann, R. P. (2017). *A Mössbauer spectral study of degradation in La<sub>0.58</sub>Sr<sub>0.4</sub>Fe<sub>0.5</sub>Co<sub>0.5</sub>O<sub>3-x</sub> after long-term operation in solid oxide electrolysis cells*. **Solid State Ionics**, 312, 38.
- [Mai 2006] Mai, A., Becker, M., Assenmacher, W., Tietz, F., Hathiramani, D., Ivers-Tiffée, E., Stöver, D., & Mader, W. (2006). *Time-dependent performance of mixed-conducting SOFC cathodes*. **Solid State Ionics**, 177(19-25 SPEC. ISS.), 1965.
- [Marina 2007] Marina, O. A., Pederson, L. R., Williams, M. C., Coffey, G. W., Meinhardt, K. D., Nguyen, C. D., & Thomsen, E. C. (2007). *Electrode Performance in Reversible Solid Oxide Fuel Cells*. **Journal of The Electrochemical Society**, 154(5), B452.
- [Marinha 2012] Marinha, D., Dessemond, L., & Djurado, E. (2012). *Electrochemical investigation of oxygen reduction reaction on La<sub>0.6</sub>Sr<sub>0.4</sub>Co<sub>0.2</sub>Fe<sub>0.8</sub>O<sub>3-δ</sub> cathodes deposited by Electrostatic Spray Deposition*. **Journal of Power Sources**, 197, 80.
- [Matsui 2016] Matsui, T., Komoto, M., Muroyama, H., Kishida, K., Inui, H., & Eguchi, K. (2016). *Degradation factors in (La,Sr)(Co,Fe)O<sub>3-d</sub> cathode/Sm<sub>2</sub>O<sub>3</sub>-CeO<sub>2</sub> interlayer/Y<sub>2</sub>O<sub>3</sub>-ZrO<sub>2</sub> electrolyte system during operation of solid oxide fuel cells*. **Journal of Power Sources**, 312, 80.
- [Matsui 2019] Matsui, T., Li, S., Inoue, Y., Yoshida, N., Muroyama, H., & Eguchi, K. (2019). *Degradation Analysis of Solid Oxide Fuel Cells with (La,Sr)(Co,Fe)O<sub>3-δ</sub> Cathode/Gd<sub>2</sub>O<sub>3</sub>-CeO<sub>2</sub> Interlayer/Y<sub>2</sub>O<sub>3</sub>-ZrO<sub>2</sub> Electrolyte System: The Influences of Microstructural Change and Solid Solution Formation*. **Journal of The Electrochemical Society**, 166(4), F295.
- [Menzler 2018] Menzler, N. H., Sebold, D., & Guillon, O. (2018). *Post-test characterization of a solid oxide fuel cell stack operated for more than 30,000 hours: The cell*. **Journal of Power Sources**, 374, 69.
- [Menzler 2010] Menzler, N. H., Tietz, F., Uhlenbruck, S., Buchkremer, H. P., & Stöver, D. (2010). *Materials and manufacturing technologies for solid oxide fuel cells*. **Journal of Materials Science**, 45(12), 3109.
- [Mineshige 2005] Mineshige, A., Izutsu, J., Nakamura, M., Nigaki, K., Abe, J., Kobune, M., Fujii, S., & Yazawa, T. (2005). *Introduction of A-site deficiency into La<sub>0.6</sub>Sr<sub>0.4</sub>Co<sub>0.2</sub>Fe<sub>0.8</sub>O<sub>3-δ</sub> and its effect on structure and conductivity*. **Solid State Ionics**, 176, 1145.
- [Mitterdorfer 1999] Mitterdorfer, A., & Gauckler, L. J. (1999). *Reaction kinetics of the Pt, O<sub>2</sub>(g)|c-ZrO<sub>2</sub> system: precursor-mediated adsorption*. **Solid State Ionics**, 120(1), 211.
- [Mizusaki 1994a] Mizusaki, J., Tagawa, H., Saito, T., Kamitani, K., Yamamura, T., Hirano, K.,

- Ehara, S., Takagi, T., Hikita, T., Ippommatsu, M., Nakagawa, S., & Hashimoto, K. (1994). *Preparation of Nickel Pattern Electrodes on YSZ and Their Electrochemical Properties in H<sub>2</sub>-H<sub>2</sub>O Atmospheres*. **Journal of The Electrochemical Society**, 141(8), 2129.
- [Mizusaki 1994b] Mizusaki, J., Tagawa, H., Saito, T., Yamamura, T., Kamitani, K., Hirano, K., Ehara, S., Takagi, T., Hikita, T., Ippommatsu, M., Nakagawa, S., & Hashimoto, K. (1994). *Kinetic studies of the reaction at the nickel pattern electrode on YSZ in H<sub>2</sub>-H<sub>2</sub>O atmospheres*. **Solid State Ionics**, 70–71, 52.
- [Moçoteguy 2013] Moçoteguy, P., & Brisse, A. (2013). *A review and comprehensive analysis of degradation mechanisms of solid oxide electrolysis cells*. **International Journal of Hydrogen Energy**, 38(36), 15887.
- [Mogensen 2017] Mogensen, M. B., Hauch, A., Sun, X., Chen, M., Tao, Y., Ebbesen, S. D., Hansen, K. V., & Hendriksen, P. V. (2017). *Relation Between Ni Particle Shape Change and Ni Migration in Ni-YSZ Electrodes – a Hypothesis*. **Fuel Cells**, 17(4), 434.
- [Mogensen 2002] Mogensen, M., Jensen, K. V., Jorgensen, M. J., & Primdahl, S. (2002). *Progress in understanding SOFC electrodes*. **Solid State Ionics**, 150(1–2), 123.
- [Mohsenzadeh 2014] Mohsenzadeh, A., Bolton, K., & Richards, T. (2014). *DFT study of the adsorption and dissociation of water on Ni(111), Ni(110) and Ni(100) surfaces*. **Surface Science**, 627, 1.
- [Montinaro 2014] Montinaro, D., Contino, A. R., Dellai, A., & Rolland, M. (2014). *Determination of the impedance contributions in anode supported solid oxide fuel cells with (La,Sr)(Co,Fe)O<sub>3-δ</sub> cathode*. **International Journal of Hydrogen Energy**, 39(36), 21638.
- [Morales 2017] Morales, M., Miguel-Pérez, V., Tarancón, A., Slodczyk, A., Torrell, M., Ballesteros, B., Ouweltjes, J. P., Bassat, J. M., Montinaro, D., & Morata, A. (2017). *Multi-scale analysis of the diffusion barrier layer of gadolinia-doped ceria in a solid oxide fuel cell operated in a stack for 3000 h*. **Journal of Power Sources**, 344, 141.
- [Morel 2005] Morel, B., Laurencin, J., Bultel, Y., & Lefebvre-Joud, F. (2005). *Anode-Supported SOFC Model Centered on the Direct Internal Reforming*. **Journal of The Electrochemical Society**, 152(7), A1382.
- [Mortensen 2014] Mortensen, J. E., Søgaard, M., & Jacobsen, T. (2014). *Analytical, 1-Dimensional Impedance Model of a Composite Solid Oxide Fuel Cell Cathode*. **Journal of The Electrochemical Society**, 161(3), 161.
- [Moussaoui 2020] Moussaoui, H., Debayle, J., Gavet, Y., Cloetens, P., & Laurencin, J. (2020). *Particle-based model for functional and diffusion layers of solid oxide cells electrodes*. **Powder Technology**, 367, 67.

- [Moussaoui 2018] Moussaoui, H., Laurencin, J., Gavet, Y., Delette, G., Hubert, M., Cloetens, P., Le Bihan, T., & Debayle, J. (2018). *Stochastic geometrical modeling of solid oxide cells electrodes validated on 3D reconstructions*. **Computational Materials Science**, 143, 262.
- [Moussaoui 2019] Moussaoui, H., Sharma, R. K., Debayle, J., Gavet, Y., Delette, G., & Laurencin, J. (2019). *Microstructural correlations for specific surface area and triple phase boundary length for composite electrodes of solid oxide cells*. **Journal of Power Sources**, 412, 736.
- [Moussaoui 2019a] Moussaoui, H. (2019). *Microstructural optimization of Solid Oxide Cells: a coupled stochastic geometrical and electrochemical modeling approach applied to LSCF-CGO electrode*. **PhD Thesis**.
- [Munroe 2009] Munroe, P. R. (2009). *The application of focused ion beam microscopy in the material sciences*. **Materials Characterization**, 60(1), 2.
- [Nagata 2001] Nagata, S., Momma, A., Kato, T., & Kasuga, Y. (2001). *Numerical analysis of output characteristics of tubular SOFC with internal reformer*. **Journal of Power Sources**, 101(1), 60.
- [Nakajo 2020] Nakajo, A., Rinaldi, G., Caliandro, P., Jeanmonod, G., Navratilova, L., Cantoni, M., & Van herle, J. (2020). *Evolution of the Morphology Near Triple-Phase Boundaries in Ni–Yttria Stabilized Zirconia Electrodes Upon Cathodic Polarization*. **Journal of Electrochemical Energy Conversion and Storage**, 17(4), 1.
- [Nakamura 1986] Nakamura, A., & Wagner, B. (1986). *Defect Structure, Ionic Conductivity, and Diffusion in Yttria Stabilized Zirconia and Related Oxide Electrolytes with Fluorite Structure*. **Journal of The Electrochemical Society**, 133(8), 1542.
- [Nechache 2014] Nechache, A., Cassir, M., & Ringuedé, A. (2014). *Solid oxide electrolysis cell analysis by means of electrochemical impedance spectroscopy: A review*. **Journal of Power Sources**, 258, 164.
- [Nechache 2016] Nechache, A., Mansuy, A., Petitjean, M., Mougín, J., Mauvy, F., Boukamp, B. A., Cassir, M., & Ringuedé, A. (2016). *Diagnosis of a cathode-supported solid oxide electrolysis cell by electrochemical impedance spectroscopy*. **Electrochimica Acta**, 210, 596.
- [Nguyen 2013] Nguyen, V. N., Fang, Q., Packbier, U., & Blum, L. (2013). *Long-term tests of a Jülich planar short stack with reversible solid oxide cells in both fuel cell and electrolysis modes*. **International Journal of Hydrogen Energy**, 38(11), 4281.
- [Ni 2008] Ni, M., Leung, M. K. H., & Leung, D. Y. C. (2008). *Technological development of hydrogen production by solid oxide electrolyzer cell (SOEC)*. **International Journal of Hydrogen Energy**, 33(9), 2337.
- [Nielsen 2011] Nielsen, J., Jacobsen, T., & Wandel, M. (2011). *Impedance of porous IT-SOFC LSCF:CGO composite cathodes*. **Electrochimica Acta**, 56(23), 7963.

- [Oh 2012] Oh, D., Gostovic, D., & Wachsman, E. D. (2012). *Mechanism of La<sub>0.6</sub>Sr<sub>0.4</sub>Co<sub>0.2</sub>Fe<sub>0.8</sub>O<sub>3</sub> cathode degradation*. **Journal of Materials Research**, 27(15), 1992.
- [Ong 2017] Ong, K., Hanna, J., & Ghoniem, A. F. (2017). *Investigation of a Combined Hydrogen and Oxygen Spillover Mechanism for Syngas Electro-Oxidation on Ni/YSZ*. **Journal of The Electrochemical Society**, 164(2), F32.
- [Otsu 1979] Otsu, N. (1979). *A Threshold Selection Method from Gray-Level Histograms*. **IEEE Transactions on Systems, Man, and Cybernetics**, C(1), 62.
- [Paganin 2002] Paganin, D., Mayo, S. C., Gureyev, T. E., Miller, P. R., & Wilkins, S. W. (2002). *Simultaneous phase and amplitude extraction from a single defocused image of a homogeneous object*. **Journal of Microscopy**, 206(1), 33.
- [Pan 2016] Pan, W., Chen, K., Ai, N., Lü, Z., & Jiang, S. P. (2016). *Mechanism and Kinetics of Ni-Y<sub>2</sub>O<sub>3</sub>-ZrO<sub>2</sub> Hydrogen Electrode for Water Electrolysis Reactions in Solid Oxide Electrolysis Cells*. **Journal of The Electrochemical Society**, 163(2), F106.
- [Pecho 2015] Pecho, O. M., Stenzel, O., Iwanschitz, B., Gasser, P., Neumann, M., Schmidt, V., Prestat, M., Hocker, T., Flatt, R. J., & Holzer, L. (2015). *3D microstructure effects in Ni-YSZ anodes: Prediction of effective transport properties and optimization of redox stability*. **Materials**, 8(9), 5554.
- [Perona 1990] Perona, P., & Malik, J. (1990). *Scale-space and edge detection using anisotropic diffusion*. **IEEE Transactions on Pattern Analysis and Machine Intelligence**, 12(7), 629.
- [Ploner 2017] Ploner, A., Hagen, A., & Hauch, A. (2017). *Study of Operating Parameters for Accelerated Anode Degradation in SOFCs*. **Fuel Cells**, 17(4), 498.
- [Prestat 2007] Prestat, M., Koenig, J. F., & Gauckler, L. J. (2007). *Oxygen reduction at thin dense La<sub>0.52</sub>Sr<sub>0.48</sub>Co<sub>0.18</sub>Fe<sub>0.82</sub>O<sub>3-δ</sub> electrodes: Part I. Reaction model and faradaic impedance*. **Journal of Electroceramics**, 18(1–2), 87.
- [Primdahl 1997] Primdahl, S., & Mogensen, M. (1997). *Oxidation of Hydrogen on Ni/Yttria-Stabilized Zirconia Cermet Anodes*. **Journal of The Electrochemical Society**, 144(10), 3409.
- [Primdahl 1998] Primdahl, S., & Mogensen, M. (1998). *Gas Conversion Impedance: A Test Geometry Effect in Characterization of Solid Oxide Fuel Cell Anodes*. **Journal of The Electrochemical Society**, 145(7), 2431.
- [Quey 2013] Quey, R., Suhonen, H., Laurencin, J., Cloetens, P., & Bleuet, P. (2013). *Direct comparison between X-ray nanotomography and scanning electron microscopy for the microstructure characterization of a solid oxide fuel cell anode*. **Materials Characterization**, 78, 87.
- [Radhakrishnan 2005] Radhakrishnan, R., Virkar, A. V., & Singhal, S. C. (2005). *Estimation of*

- Charge-Transfer Resistivity of La<sub>0.8</sub>Sr<sub>0.2</sub>MnO<sub>3</sub> Cathode on Y<sub>0.16</sub>Zr<sub>0.84</sub>O<sub>2</sub> Electrolyte Using Patterned Electrodes.* **J. Electrochem. Soc.**, 152(1), A210.
- [Raz 2001] Raz, S., Sasaki, K., Maier, J., & Riess, I. (2001). *Characterization of adsorbed water layers on Y<sub>2</sub>O<sub>3</sub>-doped ZrO<sub>2</sub>.* **Solid State Ionics**, 143, 181.
- [Rebollo 2003] Rebollo, N. R., Fabrichnaya, O., & Levi, C. G. (2003). *Phase stability of Y + Gd co-doped zirconia.* **Zeitschrift Fuer Metallkunde/Materials Research and Advanced Techniques**, 94(3), 163.
- [Rinaldi 2017a] Rinaldi, G., Diethelm, S., Oveisi, E., Burdet, P., Van herle, J., Montinaro, D., Fu, Q., & Brisse, A. (2017). *Post-test Analysis on a Solid Oxide Cell Stack Operated for 10,700 Hours in Steam Electrolysis Mode.* **Fuel Cells**, 17(4), 541.
- [Rinaldi 2019] Rinaldi, G., Nakajo, A., Caliandro, P., Navratilova, L., & Van herle, J. (2019). *Effects of Polarization on the Microstructural Changes at the YSZ/Ni-YSZ Interface.* **ECS Transactions**, 91(1), 641.
- [Rinaldi 2017b] Rinaldi, G., Nakajo, A., Van herle, J., Burdet, P., Oveisi, E., & Cantoni, M. (2017). *Strontium Migration at the GDC-YSZ Interface of Solid Oxide Cells in SOFC and SOEC Modes.* **ECS Transactions**, 78(1), 3297.
- [Sasaki 2004] Sasaki, T., Matsunaga, K., Ohta, H., Hosono, H., Yamamoto, T., & Ikuhara, Y. (2004). *Atomic and electronic structures of Ni/YSZ(111) interface.* **Materials Transactions**, 45(7), 2137.
- [Schefold 2020] Schefold, J., & Brisse, A. (2020). *Solid Oxide Electrolyser Cell Testing up to the Above 30,000 h Time Range.* **ECS Transactions**, 97(7), 553.
- [Schefold 2017] Schefold, J., Brisse, A., & Poepke, H. (2017). *23,000 h Steam Electrolysis With an Electrolyte Supported Solid Oxide Cell.* **International Journal of Hydrogen Energy**, 42(19), 13415.
- [Schefold 2012] Schefold, J., Brisse, A., & Tietz, F. (2012). *Nine Thousand Hours of Operation of a Solid Oxide Cell in Steam Electrolysis Mode.* **Journal of The Electrochemical Society**, 159(2), A137.
- [Schuler 2012] Schuler, J. A., Wuillemin, Z., Hessler-Wyser, A., Comminges, C., Steiner, N. Y., & Van Herle, J. (2012). *Cr-poisoning in (La,Sr)(Co,Fe)O<sub>3</sub> cathodes after 10,000 h SOFC stack testing.* **Journal of Power Sources**, 211, 177.
- [Seenivasan 2017] Seenivasan, H., Jackson, B., & Tiwari, A. K. (2017). *Water dissociation on Ni(100), Ni(110), and Ni(111) surfaces: Reaction path approach to mode selectivity.* **Journal of Chemical Physics**, 146(7), 074705.
- [Shaikh 2015] Shaikh, S. P. S., Muchtar, A., & Somalu, M. R. (2015). *A review on the selection of*

- anode materials for solid-oxide fuel cells. Renewable and Sustainable Energy Reviews*, 51, 1.
- [Shimonosono 2012] Shimonosono, T., Kishimoto, H., Brito, M. E., Yamaji, K., Horita, T., & Yokokawa, H. (2012). *Phase transformation related electrical conductivity degradation of NiO doped YSZ. Solid State Ionics*, 225, 69.
- [Shimura 2019] Shimura, T., He, A., & Shikazono, N. (2019). *Evaluation of La<sub>0.57</sub>Sr<sub>0.38</sub>Co<sub>0.2</sub>Fe<sub>0.8</sub>O<sub>3-δ</sub> Electrode Performance Degradation Based on Three-Dimensional Microstructure Reconstruction and Electrochemical Simulation. Journal of The Electrochemical Society*, 166(12), F821.
- [Shin 2013] Shin, E. C., Ahn, P. A., Seo, H. H., Jo, J. M., Kim, S. D., Woo, S. K., Yu, J. H., Mizusaki, J., & Lee, J. S. (2013). *Polarization mechanism of high temperature electrolysis in a Ni-YSZ/YSZ/LSM solid oxide cell by parametric impedance analysis. Solid State Ionics*, 232, 80.
- [Shin 2016] Shin, E. C., Ahn, P. A., Seo, H. H., & Lee, J. S. (2016). *Application of a general gas electrode model to Ni-YSZ symmetric cells: Humidity and current collector effects. Journal of the Korean Ceramic Society*, 53(5), 511.
- [Shishkin 2010] Shishkin, M., & Ziegler, T. (2010). *Hydrogen Oxidation at the Ni/Yttria-Stabilized Zirconia Interface: A Study Based on Density Functional Theory. Journal of Physical Chemistry C*, 114, 11209.
- [Siebert 2013] Siebert, E., Boréave, A., Gaillard, F., & Pagnier, T. (2013). *Electrochemical and Raman study of La<sub>0.7</sub>Sr<sub>0.3</sub>Co<sub>0.8</sub>Fe<sub>0.2</sub>O<sub>3-δ</sub> reduction. Solid State Ionics*, 247–248, 30.
- [Siebert 2011] Siebert, E., Roux, C., Boréave, A., Gaillard, F., & Vernoux, P. (2011). *Oxido-reduction properties of La<sub>0.7</sub>Sr<sub>0.3</sub>Co<sub>0.8</sub>Fe<sub>0.2</sub>O<sub>3-δ</sub> perovskite oxide catalyst. Solid State Ionics*, 183(1), 40.
- [Simrick 2012] Simrick, N. J., Bieberle-Hütter, A., Ryll, T. M., Kilner, J. A., Atkinson, A., & Rupp, J. L. M. (2012). *An investigation of the oxygen reduction reaction mechanism of La<sub>0.6</sub>Sr<sub>0.4</sub>Co<sub>0.2</sub>Fe<sub>0.8</sub>O<sub>3</sub> using patterned thin films. Solid State Ionics*, 206, 7.
- [Skafté 2016] Skafté, T. L., Hjelm, J., Blennow, P., & Graves, C. (2016). *Quantitative review of degradation and lifetime of solid oxide cells and stacks. EFCF Proceedings, July*, B0501.
- [Skarmoutsos 2000] Skarmoutsos, D., Tsoga, A., Naoumidis, A., & Nikolopoulos, P. (2000). *5 mol% TiO<sub>2</sub>-doped Ni-YSZ anode cermets for solid oxide fuel cells. Solid State Ionics*, 135(1–4), 439.
- [Sogaard 2006] Sogaard, M., Hendriksen, P. V., Jacobsen, T., & Mogensen, M. (2006). *Modelling of the Polarization Resistance from Surface Exchange and Diffusion Coefficient Data. 7th European SOFC Forum, July*.
- [Sohal 2011] Sohal, M. S., O'Brien, J. E., Stoots, C. M., Sharma, V. I., Yildiz, B., & Virkar, A. (2011). *Degradation Issues in Solid Oxide Cells During High Temperature Electrolysis*.

- Journal of Fuel Cell Science and Technology**, 9(1), 011017.
- [Solé 2007] Solé, V. A., Papillon, E., Cotte, M., Walter, P., & Susini, J. (2007). *A multiplatform code for the analysis of energy-dispersive X-ray fluorescence spectra*. **Spectrochimica Acta - Part B Atomic Spectroscopy**, 62(1), 63.
- [Sonn 2008] Sonn, V., Leonide, A., & Ivers-Tiffée, E. (2008). *Combined Deconvolution and CNLS Fitting Approach Applied on the Impedance Response of Technical Ni8YSZ Cermet Electrodes*. **Journal of The Electrochemical Society**, 155(7), B675.
- [Suciu 2018] Suciu, C., Dorolti, E., & Hoffmann, A. C. (2018). *Physico-chemical properties of nanocrystalline YSZ powders as a function of doping level and electrical properties after sintering*. **Materials Science for Energy Technologies**, 1(2), 136.
- [Sun 2019] Sun, X., Hendriksen, P. V., Mogensen, M. B., & Chen, M. (2019). *Degradation in Solid Oxide Electrolysis Cells During Long Term Testing*. **Fuel Cells**, 19(6), 740.
- [Suwanwarangkul 2003] Suwanwarangkul, R., Croiset, E., Fowler, M. W., Douglas, P. L., Entchev, E., & Douglas, M. A. (2003). *Performance comparison of Fick's, dusty-gas and Stefan-Maxwell models to predict the concentration overpotential of a SOFC anode*. **Journal of Power Sources**, 122(1), 9.
- [Svensson 1998] Svensson, A. M., Sunde, S., & Nişancıoğlu, K. (1998). *Mathematical Modeling of Oxygen Exchange and Transport in Air-Perovskite-Yttria-Stabilized Zirconia Interface Regions II. Direct Exchange of Oxygen Vacancies*. **Journal of The Electrochemical Society**, 145(4), 1390.
- [Świerczek 2009] Świerczek, K., Dabrowski, B., Suescun, L., & Kolesnik, S. (2009). *Crystal structure and magnetic properties of high-oxygen pressure annealed  $Sr_{1-x}La_xCo_{0.5}Fe_{0.5}O_{3-\delta}$  ( $0 \leq x \leq 0.5$ )*. **Journal of Solid State Chemistry**, 182(2), 280.
- [Szász 2018] Szász, J., Wankmüller, F., Wilde, V., Störmer, H., Gerthsen, D., Menzler, N. H., & Ivers-Tiffée, E. (2018). *Nature and Functionality of  $La_{0.58}Sr_{0.4}Co_{0.2}Fe_{0.8}O_{3-\delta}/Gd_{0.2}Ce_{0.8}O_{2-\delta}/Y_{0.16}Zr_{0.84}O_{2-\delta}$  Interfaces in SOFCs*. **Journal of The Electrochemical Society**, 165(10), F898.
- [Tanasini 2009] Tanasini, P., Cannarozzo, M., Costamagna, P., Faes, A., Van Herle, J., Hessler-Wyser, A., & Comninellis, C. (2009). *Experimental and theoretical investigation of degradation mechanisms by particle coarsening in SOFC electrodes*. **Fuel Cells**, 9(5), 740.
- [Tao 1990] Tao, T., Ro, J., Melngailis, J., Xue, Z., & Kaesz, H. D. (1990). *Focused ion beam induced deposition of platinum*. **Journal of Vacuum Science & Technology B**, 8(6), 1826.
- [Tezyk 2019] Tezyk, V., Rossignol, C., Sergent, N., Djurado, E., Laurencin, J., & Siebert, E. (2019). *Cyclic voltammetry and high-frequency series resistance of  $La_{0.6}Sr_{0.4}Co_{0.2}Fe_{0.8}O_{3-\delta}$*

- electrode deposited on GDC: Effect of the electrode microstructure and the oxygen partial pressure. **Electrochimica Acta**, 304, 312.*
- [The 2015] The, D., Grieshammer, S., Schroeder, M., Martin, M., Al Daroukh, M., Tietz, F., Schefold, J., & Brisse, A. (2015). *Microstructural comparison of solid oxide electrolyser cells operated for 6100 h and 9000 h. **Journal of Power Sources**, 275, 901.*
- [Tietz 2006] Tietz, F., Haanappel, V. A. C., Mai, A., Mertens, J., & Stöver, D. (2006). *Performance of LSCF cathodes in cell tests. **Journal of Power Sources**, 156(1 SPEC. ISS.), 20.*
- [Tietz 2013] Tietz, F., Sebold, D., Brisse, A., & Schefold, J. (2013). *Degradation phenomena in a solid oxide electrolysis cell after 9000 h of operation. **Journal of Power Sources**, 223, 129.*
- [Todd 2002] Todd, B., & Young, J. B. (2002). *Thermodynamic and transport properties of gases for use in solid oxide fuel cell modelling. **Journal of Power Sources**, 110(1), 186.*
- [Trini 2020] Trini, M., Hauch, A., De Angelis, S., Tong, X., Hendriksen, P. V., & Chen, M. (2020). *Comparison of microstructural evolution of fuel electrodes in solid oxide fuel cells and electrolysis cells. **Journal of Power Sources**, 450, 227599.*
- [Trini 2019] Trini, M., Jørgensen, P. S., Hauch, A., Bentzen, J. J., Hendriksen, P. V., & Chen, M. (2019). *3D Microstructural Characterization of Ni/YSZ Electrodes Exposed to 1 Year of Electrolysis Testing. **Journal of The Electrochemical Society**, 166(2), F158.*
- [Tsoga 2000] Tsoga, A., Gupta, A., Naoumidis, A., & Nikolopoulos, P. (2000). *Gadolinia-Doped Ceria and Ytria Stabilized Zirconia Interfaces: Regarding Their Application for SOFC Technology. **Acta Materialia**, 48, 4709.*
- [Tsoga 1999a] Tsoga, A., Gupta, A., & Stöver, D. (1999). *Performance characteristics of composite film electrolytes for intermediate-temperature solid oxide fuel cells. **Ionics**, 5(3–4), 175.*
- [Tsoga 1999b] Tsoga, A., Naoumidis, A., Jungen, W., & Stöver, D. (1999). *Processing and characterisation of fine crystalline ceria gadolinia–yttria stabilized zirconia powders. **Journal of the European Ceramic Society**, 19, 907.*
- [Tsoga 1996a] Tsoga, A., Naoumidis, A., & Nikolopoulos, P. (1996). *Wettability and interfacial reactions in the systems Ni/YSZ and Ni/Ti-TiO<sub>2</sub>/YSZ. **Acta Materialia**, 44(9), 3679.*
- [Tsoga 1996b] Tsoga, A., Nikolopoulos, P., & Naoumidis, A. (1996). *Modified YSZ/Ni structures with improved stability. **Ionics**, 2(5–6), 427.*
- [Uhlenbruck 2009] Uhlenbruck, S., Moskalewicz, T., Jordan, N., Penkalla, H. J., & Buchkremer, H. P. (2009). *Element interdiffusion at electrolyte-cathode interfaces in ceramic high-temperature fuel cells. **Solid State Ionics**, 180(4–5), 418.*
- [Usseglio-Viretta 2014] Usseglio-Viretta, F., Laurencin, J., Delette, G., Villanova, J., Cloetens, P., & Leguillon, D. (2014). *Quantitative microstructure characterization of a Ni-YSZ bi-layer coupled*

- with simulated electrode polarisation. **Journal of Power Sources**, 256, 394.
- [Vaisakhan Thampi 2015] Vaisakhan Thampi, D. S., & Prabhakar R. P., A. Renju, U. A. (2015). *Influence of aliovalent cation substitution on structural and electrical properties of  $Gd_2(Zr_{1-x}M_x)_{2O_{7-\delta}}$  ( $M = Sc, Y$ ) systems*. **RSC Advances**, 5, 88675.
- [Villanova 2013] Villanova, J., Laurencin, J., Cloetens, P., Bleuet, P., Delette, G., Suhonen, H., & Usseglio Viretta, F. (2013). *3D phase mapping of solid oxide fuel cell YSZ/Ni cermet at the nanoscale by holographic X-ray nanotomography*. **Journal of Power Sources**, 243, 841.
- [Villanova 2019] Villanova, J., Schlabach, S., Brisse, A., & Léon, A. (2019). *X-ray fluorescence nano-imaging of long-term operated solid oxide electrolysis cells*. **Journal of Power Sources**, 421, 100.
- [Virkar 2010] Virkar, A. V. (2010). *Mechanism of oxygen electrode delamination in solid oxide electrolyzer cells*. **International Journal of Hydrogen Energy**, 35(18), 9527.
- [Virkar 2000] Virkar, A. V., Chen, J., Tanner, C. W., & Kim, J. W. (2000). *Role of electrode microstructure on activation and concentration polarizations in solid oxide fuel cells*. **Solid State Ionics**, 131(1), 189.
- [Vivet 2011] Vivet, N., Chupin, S., Estrade, E., Piquero, T., Pommier, P. L., Rochais, D., & Bruneton, E. (2011). *3D Microstructural characterization of a solid oxide fuel cell anode reconstructed by focused ion beam tomography*. **Journal of Power Sources**, 196(18), 7541.
- [Vogler 2009] Vogler, M., Bieberle-Hütter, A., Gauckler, L., Warnatz, J., & Bessler, W. G. (2009). *Modelling Study of Surface Reactions, Diffusion, and Spillover at a Ni/YSZ Patterned Anode*. **Journal of The Electrochemical Society**, 156(5), B663.
- [Volkert 2007] Volkert, C. A., & Minor, A. M. (2007). *Focused Ion Beam Micromachining*. **MRS Bulletin**, 32, 389.
- [Wankmüller 2017] Wankmüller, F., Szász, J., Joos, J., Wilde, V., Störmer, H., Gerthsen, D., & Ivers-Tiffée, E. (2017). *Correlative tomography at the cathode/electrolyte interfaces of solid oxide fuel cells*. **Journal of Power Sources**, 360, 399.
- [Wen 2002] Wen, T. L., Wang, D., Tu, H. Y., Chen, M., Lu, Z., Zhang, Z., Nie, H., & Huang, W. (2002). *Research on planar SOFC stack*. **Solid State Ionics**, 152–153, 399.
- [Wilde 2015] Wilde, V., Störmer, H., Szász, J., Wankmüller, F., Ivers-Tiffée, E., & Gerthsen, D. (2015). *Effect of  $Gd_{0.2}Ce_{0.8}O_2$  Sintering Temperature on Formation of a  $SrZrO_3$  blocking Layer between  $Y_{0.16}Zr_{0.84}O_2$ ,  $Gd_{0.2}Ce_{0.8}O_2$  and  $La_{0.58}Sr_{0.4}Co_{0.2}Fe_{0.8}O_3$* . **ECS Transactions**, 66(2), 103.
- [Wilde 2018] Wilde, V., Störmer, H., Szász, J., Wankmüller, F., Ivers-Tiffée, E., & Gerthsen, D. (2018).  *$Gd_{0.2}Ce_{0.8}O_2$  Diffusion Barrier Layer between  $(La_{0.58}Sr_{0.4})(Co_{0.2}Fe_{0.8})O_{3-\delta}$*

- Cathode and Y<sub>0.16</sub>Zr<sub>0.84</sub>O<sub>2</sub> Electrolyte for Solid Oxide Fuel Cells: Effect of Barrier Layer Sintering Temperature on Microstructure.* **ACS Applied Energy Materials**, 1(12), 6790.
- [Willmott 2011] Willmott, P. (2011). *An Introduction to Synchrotron Radiation: Techniques and Applications.* John Wiley & Sons.
- [Wuillemin 2008] Wuillemin, Z., Müller, A., Nakajo, A., Autissier, N., Diethelm, S., Molinelli, M., Van, J., & Favrat, D. (2008). *Investigation of Local Electrochemical Performance and Local Degradation in an Operating Solid Oxide Fuel Cell.* **EFCF Proceedings**, B1009.
- [Xu 2019] Xu, H., Cheng, K., Chen, M., Zhang, L., Brodersen, K., & Du, Y. (2019). *Interdiffusion between gadolinia doped ceria and yttria stabilized zirconia in solid oxide fuel cells: Experimental investigation and kinetic modeling.* **Journal of Power Sources**, 441, 227152.
- [Yamamura 2003] Yamamura, H., Nishino, H., Kakinuma, K., & Nomura, K. (2003). *Electrical conductivity anomaly around fluorite–pyrochlore phase boundary.* **Solid State Ionics**, 158, 359.
- [Yashiro 2011] Yashiro, K., Nakano, I., Kuhn, M., Hashimoto, S., Sato, K., & Mizusaki, J. (2011). *Electrical Conductivity and Oxygen Diffusivity of Perovskite-Type Solid Solution La<sub>0.6</sub>Sr<sub>0.4</sub>Co<sub>1-y</sub>FeyO<sub>3-δ</sub> (y=0.2, 0.4, 0.5, 0.6, 0.8).* **ECS Transactions**, 35(1), 1899.
- [Yokokawa 2008] Yokokawa, H., Tu, H., Iwanschitz, B., & Mai, A. (2008). *Fundamental mechanisms limiting solid oxide fuel cell durability.* **Journal of Power Sources**, 182(2), 400.
- [Yonekura 2011] Yonekura, T., Yachikawa, Y., Yoshizuma, T., Shiratori, Y., Ito, K., & Sasaki, K. (2011). *Exchange Current Density of Solid Oxide Fuel Cell Electrodes.* **ECS Transactions**, 35(1), 1007.
- [Yoshikawa 2017] Yoshikawa, M., Yamamoto, T., Yasumoto, K., & Mugikura, Y. (2017). *Degradation Analysis of SOFC Stack Performance – Durability Test and Verification of Improved SOFCs-.* **ECS Transactions**, 75(42), 23.
- [Yurkiv 2014] Yurkiv, V., Costa, R., Ilhan, Z., Ansar, A., & Bessler, W. G. (2014). *Impedance of the surface double layer of LSCF/CGO composite cathodes: An elementary kinetic model.* **Journal of The Electrochemical Society**, 161(4), F480.
- [Zhou 2004] Zhou, X. D., Scarfino, B., & Anderson, H. U. (2004). *Electrical conductivity and stability of Gd-doped ceria/Y-doped zirconia ceramics and thin films.* **Solid State Ionics**, 175(1–4), 19.
- [Zhu 2003] Zhu, H., & Kee, R. J. (2003). *A general mathematical model for analyzing the performance of fuel-cell membrane-electrode assemblies.* **Journal of Power Sources**, 117(1–2), 61.





## ***Analysis of the Degradation in Solid Oxide Cells Operated in Fuel Cell and Electrolysis Modes: Microstructural Evolution and Stability of the Electrodes Materials***

This work was dedicated to the analysis of the degradation of solid oxide cells operated in electrolysis and fuel cell modes. A threefold methodology has been applied by coupling (i) electrochemical tests, (ii) advanced post-test analyses and (iii) multi-scale modeling. Long-term durability experiments have been carried out on standard cells (Ni-YSZ/YSZ/GDC/LSCF) to investigate the performance loss as a function of the operating conditions. Specimens, which have been extracted from the pristine and aged samples, have been characterized to evaluate the microstructural and physico-chemical evolutions occurring at the two electrodes. In parallel, detailed micro-kinetic models for the hydrogen electrode (Ni-YSZ cermet) and for the oxygen electrode (LSCF/LSCF-GDC) have been developed and experimentally validated before being integrated into a macro-scale model for the complete cell. The multi-scale numerical tool has been used to propose a better understanding of the underlying forces driving the degradation. Moreover, the impact on the cell performances has been simulated and discussed as a function of the operating conditions. Based on the results presented in this work, it has been confirmed that the degradation of SOCs is significantly larger in electrolysis mode with respect to fuel cell operation under H<sub>2</sub>. On the one hand, it has been shown that the difference in durability behavior can be ascribed to the effect of the cathodic overpotential on the nickel instability in the hydrogen electrode. On the other hand, it has been observed and demonstrated that the destabilization of the LSCF is favored by both the anodic current and the high operating temperature.

## ***Analyse de la dégradation des cellules à oxydes solides fonctionnant en mode pile à combustibles et électrolyse : Évolution microstructurale et stabilité des matériaux d'électrodes***

Ce travail a été dédié à l'étude de la dégradation des piles à oxyde solide fonctionnant en mode électrolyse et pile à combustibles. Une approche intégrée couplant (i) des caractérisations électrochimiques, (ii) des analyses post-test avancées et (iii) une modélisation multi-échelle a été adoptée. Des tests de longue durée ont été menés avec des cellules standards (Ni-YSZ/YSZ/GDC/LSCF) pour évaluer la dégradation des performances en fonction des conditions de fonctionnement. Des échantillons, extraits de cellules initiales et après test, ont été finement caractérisés pour déterminer les évolutions microstructurales et physico-chimiques des deux électrodes en fonctionnement. En outre, des modèles de cinétiques élémentaires ont été développés et validés expérimentalement pour l'électrode à hydrogène (cermet Ni-YSZ) et pour l'électrode à oxygène (LSCF/LSCF-GDC) avant d'être intégrés dans un modèle de cellule à l'échelle macroscopique. L'outil numérique multi-échelle a été utilisé pour étudier les mécanismes sous-jacents contrôlant les phénomènes de dégradation. Par ailleurs, leurs effets sur les performances de la cellule en fonction des conditions de fonctionnement ont été évalués et discutés grâce au modèle. Sur la base des résultats présentés dans ce travail, il a été confirmé que la dégradation des SOCs est nettement plus importante en mode électrolyse par rapport à un fonctionnement en pile à combustibles fonctionnant sous H<sub>2</sub>. Cette différence peut être attribuée d'une part, à l'effet des surtensions cathodiques sur l'instabilité du nickel dans l'électrode à hydrogène. D'autre part, il a été observé et démontré que la déstabilisation du LSCF est favorisée sous fort courant anodique à haute température.